Large-scale hydrothermal dolomitisation in the southwestern Cantabrian Zone (NW Spain): causes and controls of the process and origin of the dolomitising fluids

INAUGURAL-DISSERTATION

zur

Erlangung der Doktorwürde

der

Naturwissenschaftlich-Mathematischen Gesamtfakultät

der

Ruprecht-Karls-Universität

Heidelberg

vorgelegt von

Marta Gasparrini (Geologa)

aus Salerno, Italien

- 2003 -

Gutachter: Prof. Dr. Thilo Bechstädt
Univ. Ass. Dr. Ronald J. Bakker

Tag der Promotionsprüfung: 20.06.2003

Sea Fever

I must go down to the seas again, to the lonely sea and the sky,
And all I ask is a tall ship and a star to steer her by,
And the wheel's kick and the wind's song and the white sail's shaking,
And a grey mist on the sea's face, and a grey dawn breaking.

I must go down to the seas again, for the call of the running tide
Is a wild call and a clear call that may not be denied;
And all I ask is a windy day with the white clouds flying,
And the flung spray and the blown spume, and the sea-gulls crying.

I must go down to the seas again, to the vagrant gypsy life,
To the gull's way and the whale's way where the wind's like a whetted knife;
And all I ask is a merry yarn from a laughing fellow-rover
And quiet sleep and a sweet dream when the long trick's over.

John Masefield (1878-1967)

A mia madre
e mio padre,
fonti inesuaribili di
affetto e sicurezza.

Thanks

To **Thilo Bechstädt** for introducing me to the geology of the Cantabrian Zone and for his critical review of the thesis. I also appreciated his ability in providing connections, essential for the good development of the survey, as well as additional funding when the project needed.

To **Ronald Bakker** of the University of Leoben (Austria) for introducing me to the "*fabelhafte Welt*" of the fluid inclusions and for his helpful review of the thesis. I thank him for the motivation he transmitted me during my stays in Leoben, and for the comfortable welcome of "Hotel Bakker". The "holiday" he spent in Heidelberg in November 2002 to discuss on my data made the difference between keep writing the thesis and quitting it: I will always be grateful to him for that.

To **Maria Boni** of the University of Naples (Italy) who was my connection to the University of Heidelberg. I thank her for giving me the chance to carry out this research project, for her helpful suggestions and for believing in my abilities since the beginning when nobody else did.

To **Fernando Ayllón**, my "unofficial" supervisor. His contagious enthusiasm, useful advice and frequent critics were of inestimable help for me. I thank him for the long discussions on geology, fluids and many other topics. It was nice to have him next door swearing in Spanish at every computer breakdown and to share with him good and bad moments of our life in Germany.

To **Hans Machel** of the University of Alberta (Canada) who helped me with the interpretation of the isotope geochemistry during his stay in Heidelberg and who readily answered to my frequent e-mails. To **Alessandro Iannace** of the University of Naples (Italy) for the pleasant and enlightening discussions on diagenesis. To **Dave Morrow** of the Geological Survey of Canada and **Gabi Gutiérrez-Alonso** of the University of Salamanca (Spain) who listened and supported "my dolomite story". To **Covadonga Brime** of the University of Oviedo (Spain) who was a friendly and helpful point of reference at the Department of Geology.

To the ***DFG*** *Graduierten-Kolleg Program 273* "Fluid-rock Interaction" for the three years of funding.

To **Michael Joachimski** of the University of Erlangen (Germany) for measuring the stable isotopes of my carbonates. To **Odile Wallerath** for quickly preparing all my sections. To **Johanna Kontny** for the most efficient "postal service" on New Year's Eve 2002. To **Kevin Carrière** who improved the English text. To **Roswitha Marioth** who constantly helped me since my first day in Germany and who corrected the final draft of the thesis. To the funny, incomprehensible **Francis Cueto** who was at the right time, in the right place and above all in the right mood to recover this thesis when my computer "died".

To all of my colleagues in Heidelberg for the friendly working environment and above all to **Zbynek Veselovsky** for his availability in solving most of my everyday life problems.

To **Juan Pérez-Claros**, **Andreas Tretner**, **Bernd Kober**, **Anja Schleicher**, **Heiko Hofmann**, **Laurence Warr**, **Margot Isenbeck-Schröter**, **Fabio Lapponi, Jochen Schneider**, **Gesine Lorenz, Michael Seeling** and **Christian Scholz**: this work would have never been finished without their psychological (psychiatric?) support and practical help.

To the families **Mayo** and **Martínez-Álvarez** from Villamanín, who contributed with their merriment to make the long months of field work in NW Spain an unforgettable time of my life.

To the "pupils" of the ***Seniorenzentrum Weststadt*** for the nice "Italian hours" spent together and for reminding me what the important things in life are.

To **Jochen Kühn** whose affection and comprehension during the years we spent together gave a deeper sense to my stay in Germany and encouraged me to go through the worst moments.

Last but not least, to **my parents** and **my sisters**, who are patiently waiting for me in Italy, just for being so unique.

List of abbreviations

CZ = Cantabrian Zone

N = North **E** = East **S** = South **W** = West

Fm. = formation

Ma = million years

CAI = conodont alteration index

CL = cathodoluminescence

XRD = X-ray diffraction

d = lattice spacing

OR = degree of order

ICP-ES = Inductively Coupled Plasma Atomic Emission Spectroscopy

k = element distribution coefficient

α = isotope fractionation coefficient

PDB = Pee Dee Belemnite

SMOW = Standard Mean Oceanic Water

FI = fluid inclusion

°**C** = degree Celsius

MPa = mega Pascals

Tt = trapping temperature

Pt = trapping pressure

Th = homogenisation temperature

$\mathbf{Tn}_{\mathbf{gas}}$ = gas nucleation temperature

$\mathbf{Tn}_{\mathbf{ice}}$ = ice nucleation temperature

Te = first melting or eutectic temperature

$\mathbf{Tm}_{\mathbf{final}}$ = final melting temperature

$\mathbf{Tm}_{\mathbf{ice}}$ = ice melting temperature

$\mathbf{Tm}_{\mathbf{hy}}$ = salt hydrate melting temperature

F = degree of fill

eq. wt % = equivalent weight percentage

H = host limestones

S = bedding parallel stylolites

CV = calcite veins

Dol A1 = dark mosaic dolomite

Dol A2 = main mosaic dolomite

Dol B1 = white sparry dolomite

Dol B2 = last crystal generation of Dol B1

Cal 1 = main blocky calcite

Cal 2 = late blocky calcite

Contents

Contents **1**

Abstract **5**

Chapter 1: Introduction **7**

1.1 Topic and aim of the survey 7

1.2 The “dolomite problem” 8

Chapter 2: Geological setting **13**

2.1 The Variscan Orogeny: an introduction 13

2.2 The Variscan Orogeny in the Iberian Peninsula 13

2.3 The Cantabrian Zone (CZ) 14

2.3.1 General features 14

2.3.2 Tectono-sedimentary evolution of the CZ 15

2.3.3 The CZ and the Variscan deformation 17

2.3.4 The CZ and the “Alpidic cycle” 18

2.3.5 Volcanism, magmatism, metamorphism and metallogenesis in the CZ 20

2.4 The Bodón Unit 21

2.4.1 General features of the Bodón Unit 22

2.4.2 Carboniferous rocks in the Bodón Unit 22

2.4.3 Structure and deformation age in the Bodón Unit 23

2.4.4 The León Fault 24

Chapter 3: Applied methods **25**

3.1 Field methods 25

3.2 Thin section microscopy 25

3.2.1 Transmitted light microscopy 25

3.2.2 Cathodoluminescence (CL) microscopy 25

3.3 Geochemical methods 26

3.3.1 Staining 26

3.3.2 X-ray diffraction (XRD) analyses 26

3.3.3 Minor and trace element analyses (ICP-ES) 28

3.3.4 O and C stable isotope analyses 29

3.3.5 Sr isotope analyses 31

3.4 Fluid Inclusion (FI) study 32

3.4.1 Microthermometry 32

3.4.2 Raman spectroscopy 33

3.4.3 Crush-leach analyses 34
3.4.4 Thermodynamic calculations and computer programs 34

Chapter 4: Field observations 37
4.1 Dolomite distribution 37
4.2 Dolomite macroscopic features 38
4.2.1 Colour, geometry and types 38
4.2.2 Dolomite porosity and zebra-structures 39
4.2.3 Dolomite and alternate bands 40
4.3 Dolomite and mineralisations 41
4.4 Dolomite and deformation 41
4.4.1 Dolomite and Variscan thrusts 41
4.4.2 Dolomite and Variscan folds 41
4.4.3 Dolomite and faults 42
4.5 Main diagenetic features of the precursor rocks 42
4.5.1 Stylolites 42
4.5.2 Calcite veins 42

Chapter 5: Thin section microscopy 43
5.1 Microscopic features of the precursor rocks 43
5.1.1 Primary and early diagenetic features 43
5.1.2 Bedding parallel stylolites (S) and calcite veins (CV) 44
5.2 Microscopic features of the dolomitised rocks 44
5.2.1 Dolomite A (replacive event) 44
5.2.2 Dolomite B (void-filling event) 47
5.3 Microscopic features of the late calcite phases 48
5.3.1 Calcite 1 48
5.3.2 Calcite 2 49

Chapter 6: Geochemical analyses 51
6.1 Results of staining 51
6.2 Results of XRD analyses 51
6.3 Results of ICP-ES analyses 55
6.3.1 Strontium (Sr) 56
6.3.2 Sodium (Na) 57
6.3.3 Iron (Fe) and Manganese (Mn) 59
6.4 Results of O and C stable isotope analyses 60
6.5 Results of Sr isotope analyses 63

Chapter 7: Fluid Inclusion (FI) study 67
7.1 FI petrography 67
7.1.1 FIs in the calcite veins (CV) 67
7.1.2 FIs in Dol A1 67
7.1.3 FIs in Dol A2 67
7.1.4 FIs in Dol B 67
7.1.5 FIs in Cal 1 68
7.1.6 FIs in Cal 2 69
7.2 Identification of the fluid system 69
7.3 FI microthermometry 71
7.3.1 Microthermometry results for type I FIs (Dol A2) 72
7.3.2 Microthermometry results for type III FIs (Dol B) 72
7.3.3 Microthermometry results for type IV FIs (Cal 1) 76
7.4 Regional comparison of microthermometry results 76
7.5 Preliminary conclusions from FI study 78
7.6 Case study 1: Dol B at Villanueva 79
7.6.1 Raman combined with microthermometry 80
7.6.2 Crush-leach analyses 83
7.7 Case study 2: Cal 1 at Mina Profunda 84
7.7.1 Raman combined with microthermometry 84
7.7.2 Crush-leach analyses 86
7.8 Salinity calculation 86
7.8.1 Salinity of type I (Dol A2) and type III (Dol B) FIs 86
7.8.2 Salinity of type IV FIs (Cal 1) 88
7.9 Bulk density and composition of FIs 90
7.10 P-T conditions during FI trapping 90
7.10.1 P-T trapping conditions for type I, type III and type IV FIs 92
7.10.2 Regional comparison of P-T trapping conditions (type III FIs) 92

Chapter 8: Discussion 95
8.1 Dolomite stoichiometry and degree of order (OR) 95
8.2 Minor and trace element geochemistry 96
8.2.1 Sr contents 96
8.2.2 Na contents 96
8.2.3 Fe and Mn contents 97
8.3 O and C stable isotope geochemistry 98
8.4 Sr isotope geochemistry 100

8.5 Origin of stylolites and calcite veins (CV) 101
8.6 Type of dolomitisation 102
8.7 Controls of the dolomitisation 103
8.8 Porosity development and dolomitisation 104
8.9 Origin of the zebra-structures 105
8.10 Timing and tectonic setting of the dolomitisation 106
8.11 “Openness” of the dolomitising system (water/rock ratio) 108
8.12 Thermal conditions of the dolomitising fluids 109
8.13 Nature of the dolomitising fluids 112
8.14 Replacive versus void-filling dolomitisation 115
8.14.1 Origin of Dol A1 and Dol A2 115
8.14.2 Origin of Dol B 117
8.14.3 Origin of Dol B2 “reentrants” 117
8.14.4 Origin of Dol B2 zones 118
8.15 “Hydrothermal” dolomitisation? 118
8.16 Comparison with dolomites from other tectonic units of the CZ 119
8.17 Origin of the calcite cements 121
8.17.1 Origin of Cal 1 121
8.17.2 Origin of Cal 2 123
8.18 Sequence of diagenetic events 124

Chapter 9: Model of dolomitisation 127
9.1 Thermal convection and dolomitisation 127
9.2 Proposed model of dolomitisation 128
9.3 Late to post-Variscan dolomites: a European perspective 130

References 131

Appendix 143
Appendix 1: Geological map of the central and eastern Bodón Unit 144
Appendix 2: Results of geochemical analyses 146
Appendix 3: Results of FI microthermometry 154

Plates of photos 165

Abstract

The Cantabrian Zone in NW Spain represents the foreland belt of the Variscan Iberian Massif and is made up of a Precambrian basement covered by Palaeozoic sediments. This succession was thrusted and folded in Late Carboniferous time during the Variscan Orogeny, resulting in several thin-skinned thrust units. The rocks underwent deformation, diagenetic to epizonal thermal events, and several episodes of fluid-flow. A spectacular product of fluid circulation in this area is a large-scale dolomitisation, mostly affecting the carbonates of the Late Carboniferous succession.

The aim of this work is to reconstruct the main episodes of late diagenesis in the Carboniferous carbonates of the Bodón thrust unit and to define the causes of the dolomitisation as well as the origin of the dolomitising fluids. Employed methods are transmitted light and cathodoluminescence microscopy, X-ray diffraction and ICP-ES analyses, O, C and Sr isotope geochemistry and fluid inclusion study, comprising microthermometry, Raman spectroscopy and crush-leach analyses.

The precursor carbonates underwent burial and deformation prior to dolomitisation, resulting in the development of bedding parallel stylolites and calcite veins. The dolomitisation post-dated the main Variscan compressinal event in the study area (Westphalian B - Stephanian B) and pre-dated the precipitation of ore minerals (~280-260 Ma).

The dolomite bodies display irregular morphology and are often associated with rock discontinuities, such as fault, bedding, lamination and stylolite planes. The dolomitisation consisted in two major events: the first replacive and the second void-filling. “Zebra-structures” are common. These are given by the repetition of mm-scale replacive and void-filling dolomite sheets and bear cavities locally filled by later calcite cements. The dolomites display features typical of burial dolomitisation, such as scarce preservation of precursor fabrics, coarse crystallinity, non-planar texture and abundant dolomite of the saddle type.

The replacive and void-filling dolomites have a very similar geochemical signature. They both have a dull red and unzoned CL and are nearly stoichiometric and well ordered. They display depletion in Sr, and enrichment in Fe and Mn relative to the precursor carbonates. They have wide-ranging $\delta^{18}O$ values (-3 to -12 ‰ PDB), distinctly lower than those of the precursors. On the contrary, the $\delta^{13}C$ values (1,7-5,4 ‰ PDB) were strongly buffered by the precursor carbonates. Both replacive and void-filling dolomites formed from hot (100-170 °C) and saline (19,0-22,6 eq. wt % $MgCl_2$) fluids, slightly radiogenic and strongly enriched in ^{18}O relative to Late Palaeozoic seawater.

A continuous dolomitisation process which evolved from a replacive stage towards a void-filling stage in a nearly isochemical system is postulated. The dolomitising fluids were hydrothermal and hypersaline brines, with isotopic signature of chemically modified Late Palaeozoic seawater.

The dolomitisation possibly occurred during the Early Permian, when predominantly extensional tectonics followed the main Variscan compression. During this period the Cantabrian Zone underwent crustal thinning, possibly accompanied by increased heat flow from the basement.

Shallow water sedimentation in semiarid climatic conditions occurred in isolated basins controlled by normal faults. Regional Variscan fractures (e.g. León Fault) were reactivated and controlled the occurrence of volcanic and magmatic phenomena.

It is proposed that Early Permian seawater, concentrated by evaporation, circulated downwards through fractures and mixed with formation waters. The latter carried abundant ^{18}O, radiogenic ^{87}Sr and high salinity, because of fluid-rock interaction with ambient rocks at high temperatures. Thermal convection, induced by the increased heat flow, homogenised the surface seawater and the subsurface formation waters and made them circulate through the permeable precursors. The concentrated seawater furnished continuous supply of Mg to the convecting system. Main pathways for the dolomitising fluids were Variscan thrust and fault planes. The León Fault possibly played a major role for fluid circulation as suggested by the almost complete dolomitisation in the region of the Bodón Unit closer to this fault.

The dolomitisation was followed by the precipitation of burial calcite from fluids of the same hydraulic system than the dolomites, but having higher salinities and slightly lower temperatures. Much later in the diagenetic history of the studied carbonates a low temperature calcite precipitated from fluids having a meteoric signature, suggesting the exposure of the study area.

Keywords: Variscan Orogeny, Cantabrian Zone, burial diagenesis, hydrothermal dolomitisation, zebra-structures, saddle dolomite, hypersaline brines, thermal convection.

Chapter 1: Introduction

1.1 Topic and aim of the survey

In the Variscan foreland fold and thrust belt of the Iberian Peninsula, the so-called Cantabrian Zone (CZ), a widespread dolomitisation affected different Palaeozoic carbonates ranging in age from Cambrian to Late Carboniferous. The lateral and vertical extension of the phenomenon, the presence of large dolomite bodies in most of the tectonic thrust units of the CZ, as well as the variety of lithologies affected by this process, are impressive. Consequently, one may suspect that a regional scale fluid-flow event affected the whole area.

This study deals with this widespread process of dolomitisation and focuses mainly on the Carboniferous carbonates of the southwestern CZ.

The origin of massive dolomite is still a matter of debate (see paragraph 1.2). Understanding the origin of dolomites is important since these rocks provide porous and permeable hosts for many hydrocarbon reservoirs and ore deposits. The dolomites from the CZ do not host hydrocarbons and only contain minor base-metal mineralisations. Nevertheless, understanding their origin and emplacement mechanism is important in interpreting similar dolomites economically more significant.

This study is a multidisciplinary approach, which combines field work and microscopy observations with geochemical data. The origin of the dolomites was investigated relative to the paragenetic sequence of different diagenetic phases, spatially or genetically related to the dolomitisation. The main target was to build a model by constraining both the age and tectonic setting of dolomitisation, and the temperature and composition of the dolomitising fluids.

Main macroscopic features of the studied dolomites are coarse crystallinity, destruction of the precursor rock fabrics, abundant dolomite cements of saddle nature and development of zebra-structures. Large occurrences of dolomites showing the same macroscopic features have been reported from several areas (e.g. Morrow et al. 1990, Wilson et al. 1990, Spencer-Cervato and Mullis 1992, Coniglio et al. 1994, Morrow and Aulstead 1995, Wendte et al. 1998, Boni et al. 2000). These dolomites are interpreted to have been formed by the convective circulation of hot (100-200 °C) fluids in the subsurface, regardless of the fluid origin. The final goal of this work was to verify the possibility of a similar origin for the dolomites of the southwestern Cantabrian Zone.

1.2 The “dolomite problem”

The mineral dolomite and the uncertainties which surround its origin have attracted the attention of earth scientists for over two centuries. Only few other geological processes boast such a wide number of publications, disagreements, debates and genetic models as the dolomitisation does. The complexity and incomprehensibility of this process led Fairbridge (1957) to define the “dolomite question”, later renamed the “dolomite problem” (McKenzie 1991).

The importance of the “dolomite problem” is due to the fact that dolomite together with calcite is the most abundant carbonate mineral. Additionally, since dolomite forms under various chemical and physical conditions, it occurs in a wide range of environments.

The core of the “dolomite problem” is the apparent paradox posed by the paucity of dolomite in modern marine depositional environments versus its relative abundance in the sedimentary record. Although the present day seawater is supersaturated with respect to dolomite, this mineral rarely precipitates from normal seawater.

An additional problem is the difficulty of studying dolomite formation in laboratory experiments, as dolomite is a highly ordered mineral and it requires time to precipitate. This is the reason why it has not yet been possible to synthesise dolomite crystals in a reasonably brief span of time, at sedimentary temperatures and using natural waters. The chemical controls on dolomite precipitation have thus been extrapolated from high temperature experiments (Gaines 1980, Morrow 1990a, Usdowski 1994).

In the past there has been much discussion over the “primary” (i.e. direct precipitation) versus replacement origin of many dolomites. At present it is believed that “primary” dolomite is rare and that most dolomites in the geological record are of replacement origin (e.g. Morrow 1990a, b, Tucker and Wright 1990, Purser et al. 1994a). However, it is largely accepted that dolomite cements are directly precipitated from pore-fluids during early and late diagenesis.

Various dolomitisation models have been proposed. A complete and exhaustive description of the different models can be found in Land (1985), Machel and Mountjoy (1986), Tucker and Wright (1990), Morrow (1990b, 1998) and Braithwaite (1991). Hundreds of case studies have been published and important compilations can be found in Zenger et al. (1980), Shukla and Baker (1988) and Purser et al. (1994b).

The dolomitisation models can be subdivided in three broad groups:

1. The evaporative and seepage-reflux dolomitisation models. These models explain the formation of massive dolomite by hypersaline brines.

   In the evaporative model (Fig. 1A) penecontemporaneous dolomites form by direct

precipitation in evaporitic environments like sabkhas (McKenzie 1981) and coastal evaporitic lakes (Von der Borch and Lock 1979). The amounts of dolomite formed in these environments are generally small.

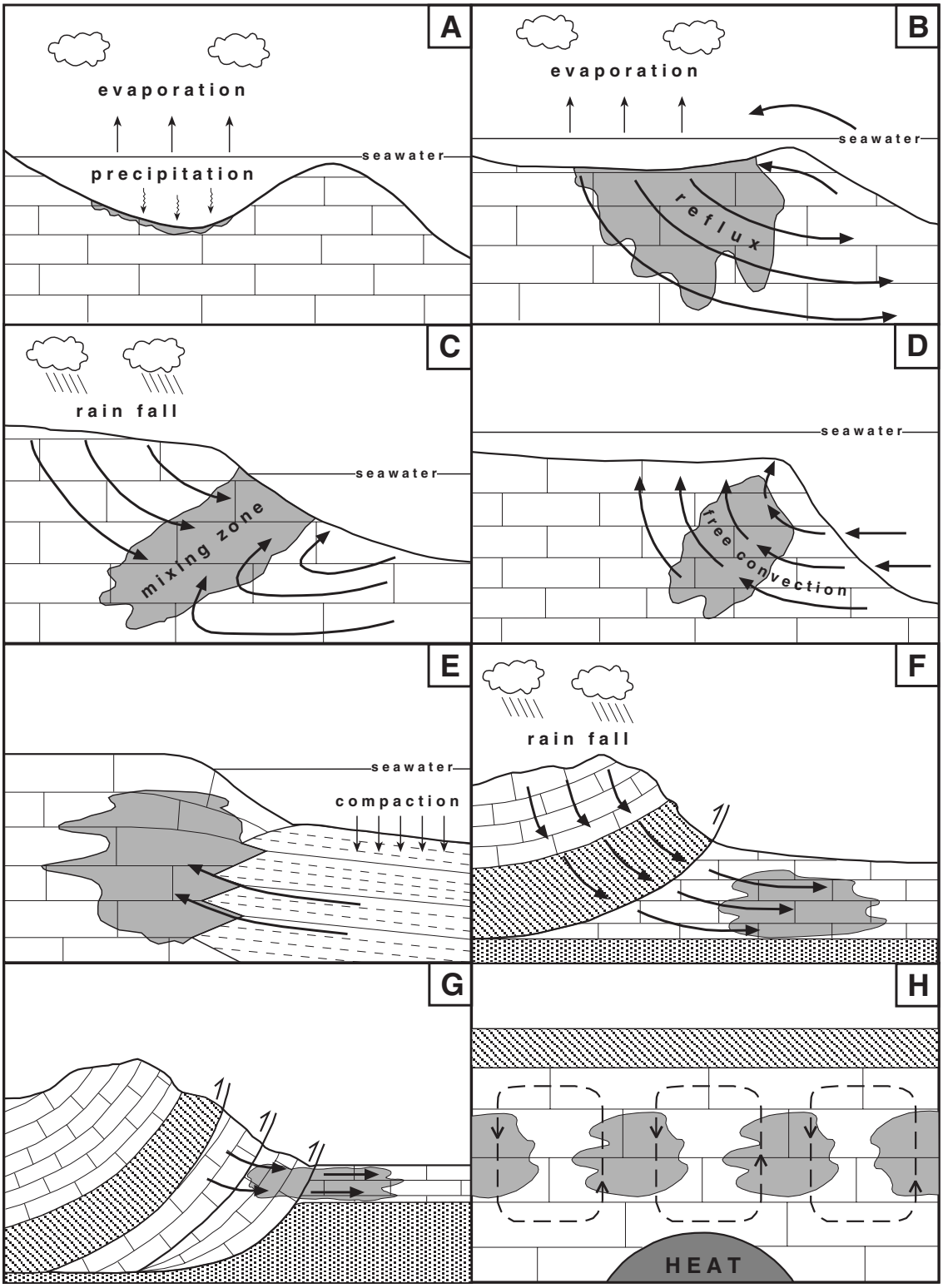

Fig. 1: Major dolomitisation models summarised in simplified cross sections. Grey areas = dolomite bodies. **A.** Evaporative model. **B.** Seepage-reflux model. **C.** Mixing-zone model. **D.** Kohout convection model. **E.** Burial compaction model. **F.** Topographic recharge model. **G.** Tectonic squeeze model. **H.** Thermal convection model.

The seepage-reflux model (Fig. 1B) requires the percolation and descent of concentrated seawater from coastal lagoons or sabkhas into the underlying carbonates (Adams and Rhodes 1960, Fisher and Rodda 1969). The downward fluid motion would be driven by the density contrast between the heavy, concentrated seawater and the lighter groundwater. This dolomitisation was thought to be restricted to the first meters of carbonate rocks immediately beneath the intertidal to supratidal settings. Recently, modelling by Jones et al. (2002, in press) suggests, however, the possibility of refluxing brines that penetrate the platform down to 1-2 km.

2. The mixing-zone and seawater models. This group of models is based on the hypothesis that highly concentrated fluids are not necessarily required for dolomitisation and that normal or even dilute seawater may generate dolomite as well.

   In the mixing-zone model (Fig. 1C) hyposaline solutions originate from the mixing of seawater and dilute groundwater (Hanshaw et al. 1971). The Mg/Ca ratio decreases relative to pure marine water but it can be kept high enough to cause dolomitisation. Concomitantly, kinetic obstacles of dolomitisation, such as the high ionic strength of seawater, are removed (Folk and Land 1975). However, not a single location has been unambiguously proven to have been dolomitised in a fresh water/seawater mixing zone in recent or ancient carbonates. In addition, the dolomitised rocks produced in such an environment are expected to be restricted only to the platform margins (Hardie 1987).

   The seawater models assume normal marine water, or seawater only slightly modified by water-rock interaction, as the most likely dolomitising fluids (Land 1985, Morrow 1990b). These fluids can be put into motion from different mechanisms, and various hydrologic systems have been proposed: seawater thermal convection or Kohout model (Sanford et al. 1998; Fig. 1D), seawater thermal convection combined with reflux of slightly evaporated seawater (Whitaker et al. 1994), or seawater circulation in the mixing-zone in response to partial platform exposure (Vahrenkamp et al. 1991).

   Early dolomite was noted in pelagic sediments, and it is thought to be linked to bacterial sulphate reduction and methanogenesis (Garrison et al. 1984, Kelts and McKenzie 1984, Burns and Baker 1987, Mazzullo 2000). SO_4^{2-} anions represent a kinetic obstacle to dolomite precipitation. Consequently, their removal by bacterial reduction favours dolomitisation. This “organogenic model” (after Compton 1988) accounts for small amounts of dolomite and its main requirements are seawater and organic-rich materials.

3. The burial (subsurface) dolomitisation models. This very broad group of models is based on the evidence that under moderate to deep burial conditions (after Choquette and Pray 1970) the kinetic requirements for dolomite formation are more easily satisfied than at surface. The increasing temperature with depth makes the burial environment suitable for dolomitisation,

since it reduces the proportion of hydrated Mg^{2+} and increases the dolomitisation rates. Four main types of burial models are distinguished based on the hydrologic drives of the fluid-flow (e.g. Morrow 1998): the compaction flow, the topography-driven flow, the tectonically-driven flow and the thermal convection flow.

The compaction-flow (Fig. 1E) is induced by the compaction of sediments under burial and consequent pore water squeezing (Illing 1959). This model never became popular, as the limited amounts of compaction water cannot account for large masses of dolomite.

The topography-driven flow (Garven and Freeze 1984) may take place in uplifted thrust belts exposed to meteoric recharge (Fig. 1F). The gravity-driven meteoric water is pumped through the basin in front of the thrust belt and during circulation it may pick up enough Mg to become a potential dolomitising fluid (e.g. Morrow 1998).

The tectonically-driven flow (Oliver 1986) is triggered by tectonic loading and compression during the development of orogenic thrust belts and causes the expulsion of metamorphic and/or basinal fluids towards the basin margins (Fig. 1G). This model has often been invoked (e.g. Qing and Mountjoy 1992, 1994a, Amthor et al. 1993, Drivet and Mountjoy 1997), even though fluxes of the tectonically-induced flow appear to be low (Machel et al. 2000).

The thermal convection of fluids can be driven by heat gradient in the crust (Wood and Hewett 1982, Wilson et al. 2001). In many cases a heat source, such as a magmatic intrusion, is invoked to generate the onset of convection cells (e.g. Morrow et al. 1990, Spencer-Cervato and Mullis 1992, Coniglio et al. 1994, Morrow and Aulstead 1995, Wendte et al. 1998). The genesis of high temperature dolomites, commonly called “hydrothermal dolomites”, is frequently linked to the thermal convection model (Fig. 1H). Well documented examples of these dolomites in regional fluid-flow systems are known (see Morrow 1998 and reference therein). Variants of this model have the potential to explain the occurrence of many regional late dolomites (Davies 1997).

Dolomitisation in burial environments may be related also to pressure-solution processes. Dolomite forms if Mg-bearing fluids react with limestones across pressure-solution surfaces. Precursor limestones, particularly if they are tight and fine-grained, may also release considerable quantities of autochthonous Mg upon dissolution (Wanless 1979). However, in order to form large amounts of dolomite other sources of Mg are required (Morrow 1990b).

Further discussions on dolomites derive from differences in terminology.

The term dolomite refers to the mineral whose ideal formula is $CaMg(CO_3)_2$, whereas dolostone is a rock that consists of >75% dolomite by volume. Nevertheless, dolostones are usually also called dolomites, and this terminology will be used throughout this work.

The commonly invoked “hydrothermal” origin for dolomites is controversial, since the term “hydrothermal” has at least three, partially contradictory definitions, as recently pointed out by

Machel and Lonnee (2002). These authors recommend the definition proposed by White (1957), who related the term “hydrothermal” to “aqueous solutions that are warm or hot relative to the surrounding environment”. This implies that a dolomite should be called “hydrothermal” only if it can be demonstrated to have formed at higher temperatures compared to the surrounding rocks at the time of dolomitisation, regardless of the absolute temperature of origin (Machel and Lonnee 2002). All of the other high temperature dolomites for which a “hydrothermal” origin cannot be proved, should be more conveniently called “hot dolomites”.

Chapter 2: Geological setting

2.1 The Variscan Orogeny: an introduction

The Variscan Orogeny resulted from Late Palaeozoic collision between two main continents: Gondwana in the S and Laurentia-Baltica in the N. The collision caused the closing of oceanic areas and intense deformation affected the borders of these continental masses.
The Variscan chain represents the pre-Mesozoic basement of most of western Europe. It crops out in several mountain belts: the Iberian and Armorican Massifs, the French Central Massif, the Ardennes, the Rhenohercynian and the Bohemian Massifs (e.g. Matte 1991), etc.

2.2 The Variscan Orogeny in the Iberian Peninsula

A segment of the European Variscides crops out in the western half of the Iberian Peninsula and forms the so called Iberian Massif (Fig. 2). In this location the main collisional events took place in the pre-Stephanian Carboniferous. Late- to post-Variscan tectonics affected the same areas in Stephanian and Permian times. As a consequence of extensive erosion most post-orogenic cover was removed and the pre- and syn-orogenic Palaeozoic sediments are well exposed (Dallmeyer and Martínez-García 1990).
Lotze (1945) distinguished several zones in the Iberian Massif, based on facies, structure, metamorphism and magmatism. This subdivision has slightly been modified by Julivert et al. (1972). From NE to SW the Iberian Massif includes the following zones (Fig. 2):

1. Cantabrian;
2. West Asturian-Leonese;
3. Central Iberian;
4. Ossa-Morena;
5. South Portuguese.

The first three zones occupy an autochthonous position relative to the chain suture and have thrusts and folds with predominant vergence towards the N (e.g. Aramburu and Bastida 1995). The Cantabrian Zone is the most external area, where the deformation affected higher crustal levels and magmatic/metamorphic phenomena are poorly developed. The West Asturian-Leonese and the Central Iberian zones represent more internal areas where intense deformation and important magmatic/metamorphic events developed (e.g. Fernández-Suárez et al. 2000).

The Ossa-Morena and South Portuguese zones are characterised by thrusts and folds with vergence towards the S (e.g. Aramburu and Bastida 1995).

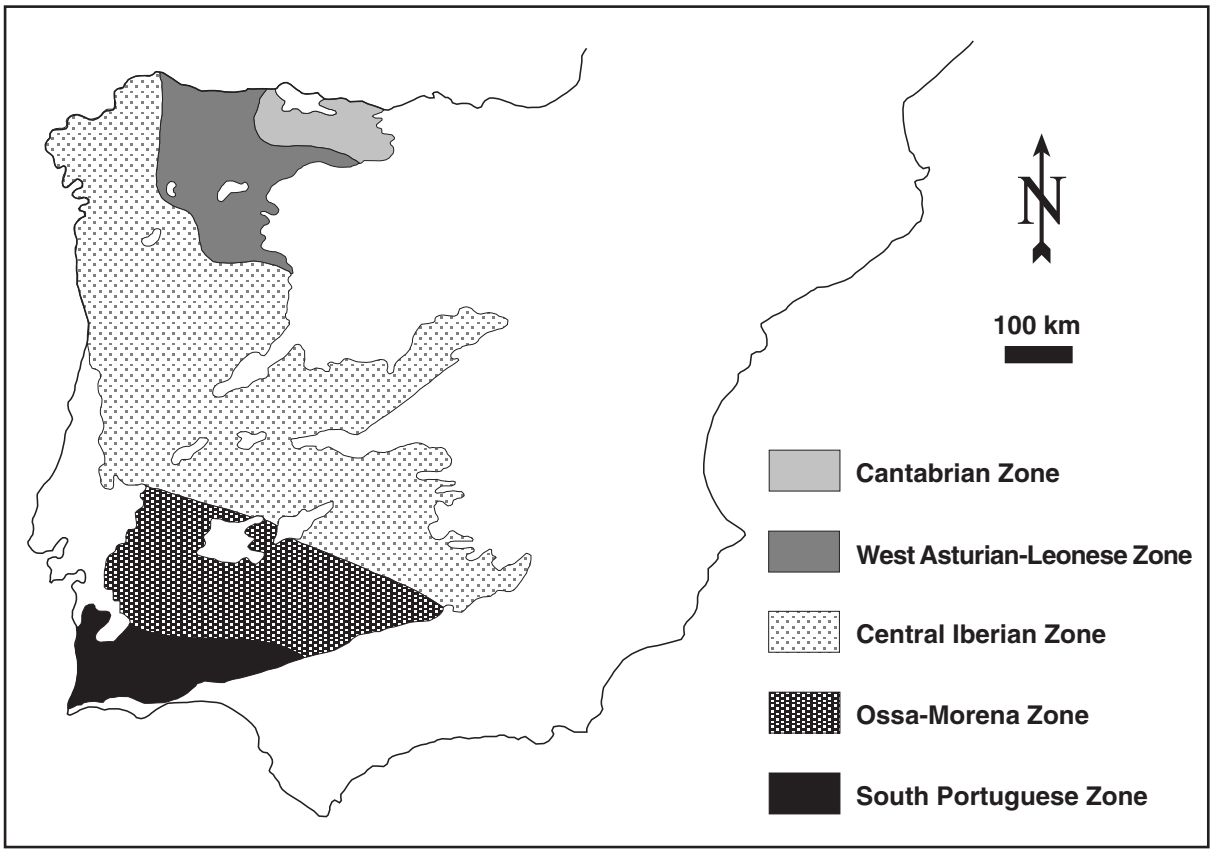

Fig. 2: The Iberian Massif and the location of the different zones (modified from Dallmayer and Martínez-García 1990).

2.3 The Cantabrian Zone (CZ)

2.3.1 General features

The Cantabrian Zone (CZ) represents the foreland of the Iberian Massif. The present structure and relief resulted, however, from the superposition of the Variscan and Alpidic orogenesis and intervening extensional tectonics.

Precambrian rocks of the Narcea Antiform separate the CZ from the more internal areas of the orogen (Fig. 3). Two stratigraphic domains are recognised in the CZ: the Asturian-Leonese and the Palentine. The former comprises the following thrust units: Somiedo-Correcilla, Sobia-Bodón, Aramo, Central Coal Basin, Ponga and Picos de Europa. The latter corresponds to the Pisuerga-Carrión Unit (Pérez-Estaún and Bastida 1990; Fig. 3).

The Palaeozoic rocks are divided into a pre-orogenic succession, deposited before the onset of the Variscan movements in the Late Carboniferous, a syn-orogenic succession, given by Upper

Carboniferous rocks, and a post-orogenic succession, comprising Stephanian and younger sediments (e.g. Julivert 1978, Marcos and Pulgar 1982).

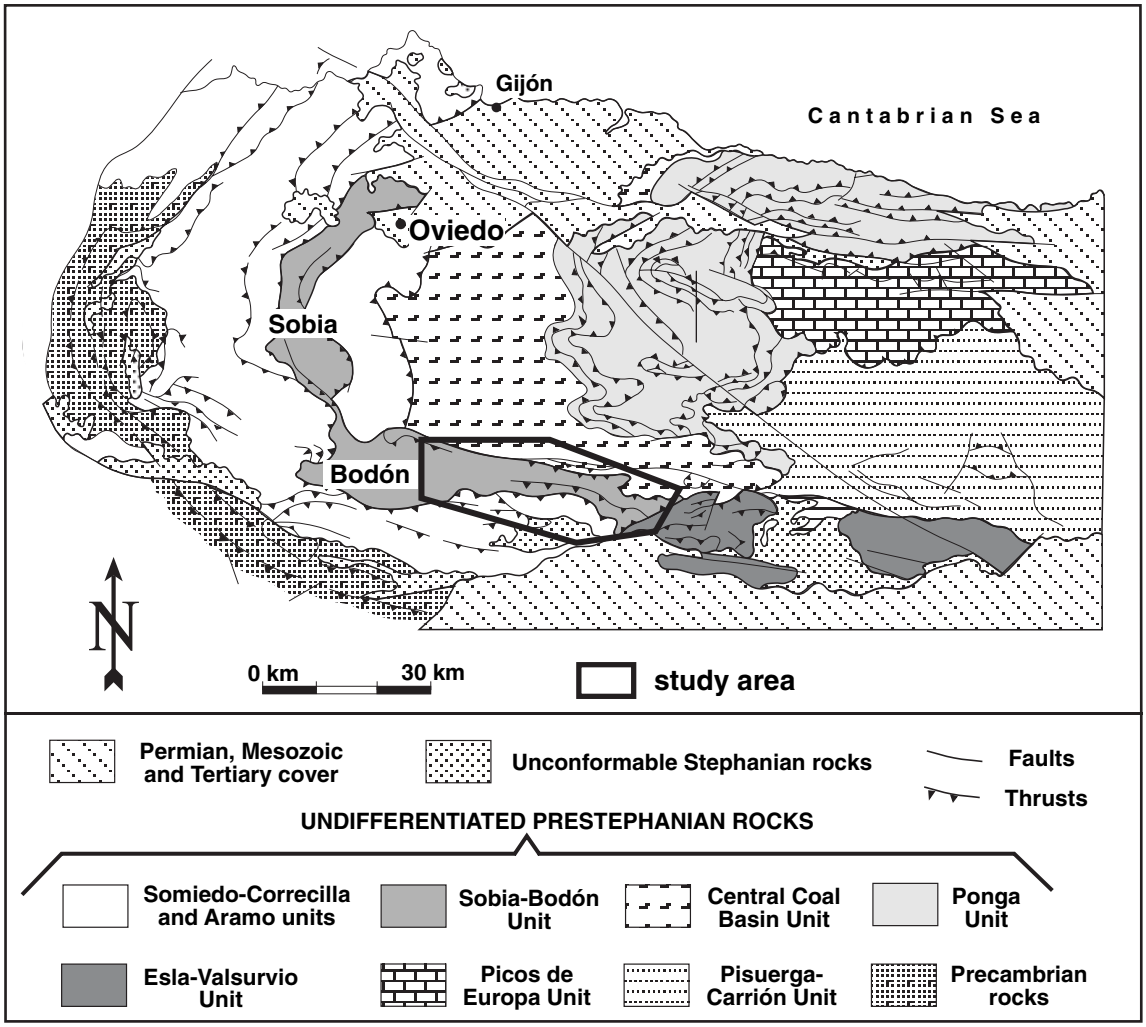

Fig. 3: Gelogical sketch map of the Cantabrian Zone showing the different thrust units and the location of the study area (modified from Pérez-Estaún and Bastida 1990).

2.3.2 Tectono-sedimentary evolution of the CZ

The Cambrian - Silurian succession is characterised by the predominance of sandstones and the abundance of stratigraphic hiatuses. Most of these sediments derived from the erosion of a source area in the E. At the beginning of the Devonian this source area was peneplained and did not supply much siliciclastic sediments to the basin. Consequently, during this period carbonate sedimentation predominated (Aramburu et al. 1992, Aramburu and Bastida 1995).

During the Carboniferous the Variscan compression caused the formation of a relief (the orogen) in the W and the inversion of the sediment provenance. Sedimentation in the Early Carboniferous formed the Baleas, Vegamián and Alba Fms. (Tournaisian - Viséan). These formations conformably overlie the Devonian rocks and display reduced thickness, facies regularity and significant lateral

extension. Late Carboniferous sedimentation reflected the influence of the Variscan Orogeny. The subsidence rate and the amount of sediments entering the basin increased. The basin geometry underwent continuous change. This resulted in a complex succession, which exhibits rapid lateral and vertical facies changes (e.g. Aramburu and Bastida 1995). The area of compression moved from the W to the E and gradually involved eastern areas of the foreland basin (Sánchez de la Torre et al. 1983, Colmenero et al. 1993).

During the Namurian A the sedimentary basin consisted of a large carbonate platform separated from the orogen by a foredeep (Fig. 4A). The sediments deposited in these two different environments gave origin to the carbonatic Barcaliente Fm. and the turbiditic Olleros Fm.

During the Namurian B - Westphalian A a less extensive carbonate platform developed and the more open marine Valdeteja Fm. was deposited (Fig. 4B). The foredeep gradually moved further

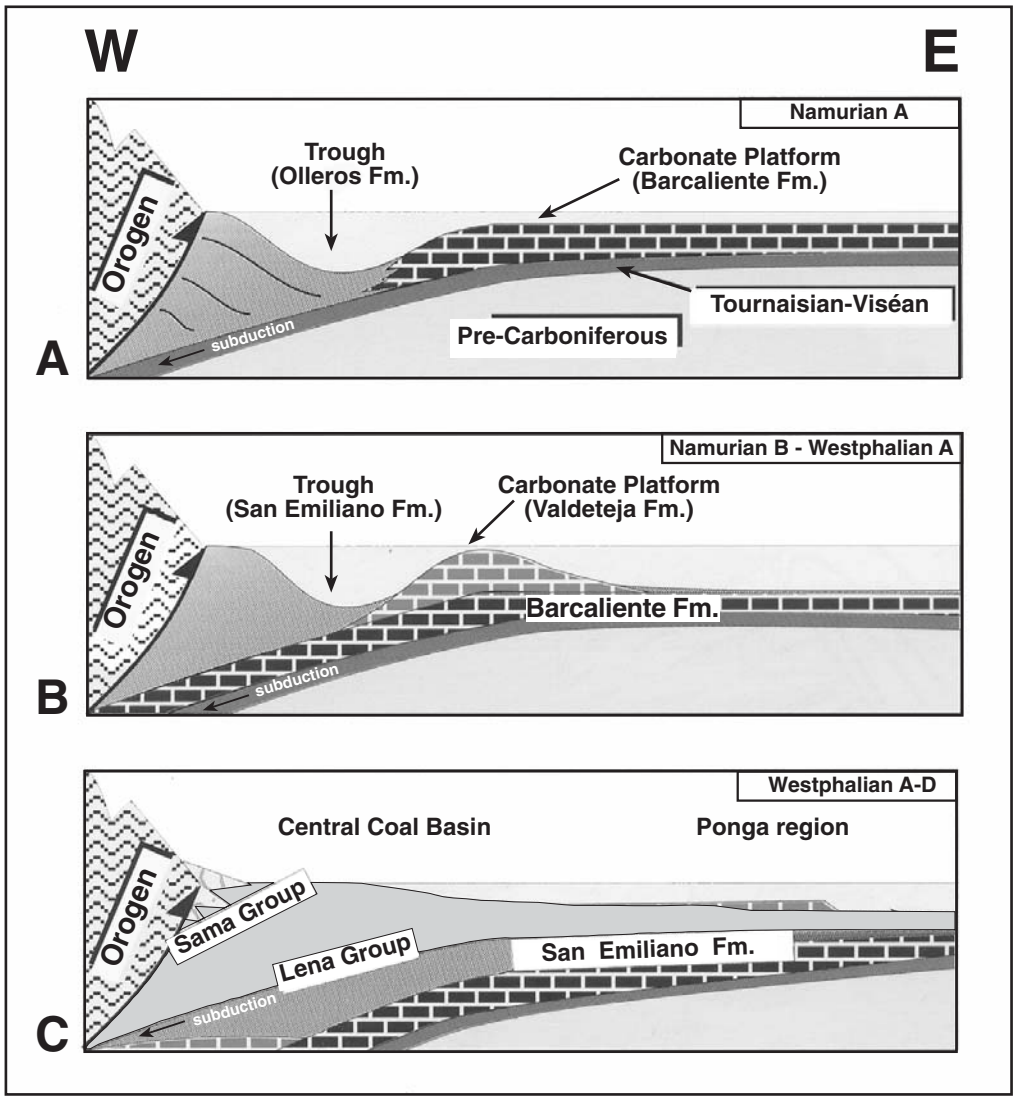

Fig. 4: Tectono-sedimentary evolution of the Variscan foreland basin during the Carboniferous (modified from Aramburu and Bastida 1995). The three sketches refer to areas of the CZ progressively involved in the Variscan tectonics. **A.** During Namurian A time. **B.** During Namurian B - Westphalian A time. **C.** During Westphalian A-D time.

to the E. The platform subsided and was covered by clastics.

In the Westphalian A the trough was filled and the terrigenous deposits replaced most of the carbonates (Fig. 4C). In the W these clastic sediments form the San Emiliano Fm. and the Lena and Sama groups. The latter reached the maximum thickness in the Central Coal Basin Unit. Only in the Picos de Europa Unit did carbonate sedimentation continued during all of the Westphalian and even into the Stephanian, with the development of the Picos de Europa Fm.

Stephanian deposits formed in isolated intramontaneous basins on deformed substrate. These deposits show mostly continental facies and unconformably overlie the western and southern nappes, whereas in the Picos de Europa Unit they show marine facies, involved in the thrust tectonics (Marquínez 1978, Martínez-García and Wagner 1982).

Permian deposits were strongly influenced by the predominance of extensional tectonics. They crop out in the northern CZ. The Autunian succession (Viñon Fm.) consists of shallow water limestones deposited in isolated basins controlled by normal faults. The limestones alternate with alkaline volcanic rocks, conglomerates and shales with some gypsum (Prado 1972, Sanchez de la Torre et al. 1977, Martínez-García 1983). The Saxonian succession (Villaviciosa Fm.) formed in a predominantly continental environment under semiarid conditions. It consists of conglomerates and sandstones, caliche limestones and shales containing gypsum (Sanchez de la Torre et al. 1977, Martínez-García 1983).

The transition to the Triassic was characterised by highly arid conditions. Brackish lagoons formed and evaporites with predominant gypsum were deposited together with shales and marls (Sánchez de la Torre et al. 1977, Gutiérrez-Claverol 1984, García-Mondéjar et al. 1986, Orti et al. 1996). In Jurassic and Cretaceous times the sea covered most of the territories, although continental exposure persisted locally. Mesozoic deposits crop out in the N, S and E of the CZ (Fig. 3).

The Permian – Mesozoic succession of the CZ cannot be reconstructed in detail because it has been intensively eroded.

2.3.3 The CZ and the Variscan deformation

In the CZ the Variscan tectonics affected the uppermost crust. Deformation resulted from the emplacement of regional thrusts and folds, followed by late fracturing (Julivert 1971, Julivert and Marcos 1973, Pérez-Estaún and Bastida 1990).

The main thrusts migrated from the hinterland towards the foreland in a forward-type sequence. The thrusts show features of thin-skinned tectonics with development of a ramp and flat "staircase" geometry (Pérez-Estaún and Bastida 1990, Alonso and Pulgar 1995). The thrusts bound allochthonous units (nappes), named after the basal thrust surface. The rearmost thrust units of Somiedo-Correcilla, Sobia-Bodón and Aramo were the first to move. The Central Coal Basin and the Ponga units followed. The Picos de Europa Unit was the last to be displaced.

Emplacement ages are Early Westphalian for the rearmost units and Early Stephanian for the foremost unit (Pérez-Estaún and Bastida 1990). The Pisuerga-Carrión Unit is considered relatively autochthonous. It is also characterised by shallow deformation and predominance of thrust tectonics, but it shows a higher metamorphic grade (Pérez-Estaún and Bastida 1990).

Regional folds nucleated together with the thrusts. The fold axes are mostly perpendicular to the thrust vergence (e.g. Julivert 1971, Julivert and Marcos 1973). These folds locally deformed the thrust fronts (Bastida et al. 1984, Aller 1986).

In addition to the faults that form the inner structure of each nappe, major faults, which crosscut several units and affect all of the preceding structures, are present. The faults in the southern CZ have an E-W trend (e.g. the León and Sabero-Gordón faults). They initially had strike-slip movements and were later reactivated mainly as reverse faults (Marcos 1968a, Julivert et al. 1971, Marcos et al. 1979, Heward and Reading 1980).

The CZ was classified by Carey (1955) as an orocline, defined as an original linear belt that underwent secondary curvature. Several tectonic models have been proposed for the formation of the arc (e.g. Matte and Ribeiro 1975, Ries et al. 1980, Pérez-Estaún et al. 1988). Recent structural and palaeomagnetic data point to a Late Stephanian – Early Permian age for the oroclinal bending around a vertical axis (Van der Voo et al. 1997, Weil et al. 2000, 2001, Gutiérrez-Alonso et al. submitted).

In Early Permian times the CZ was affected by predominantly extensional tectonics. During this period, crustal thinning, basin development, as well as volcanic, magmatic and metamorphic events occurred (see paragraph 2.3.5). The origin of this extensional phase has been traditionally related to the development of a continental rift (e.g. Martínez-García 1981, 1983, Lepvrier and Martínez-García 1990). Recently, it has been proposed that lithospheric thickening due to the oroclinal bending induced delamination beneath the orogenic belt (Fernández-Suárez et al. 2000, Gutiérrez-Alonso et al. submitted). Delamination commonly occurs during the final stages of collisional orogeny and consists in the peeling off of the mantle lithosphere from the crust. The delaminated lithosphere sinks into the underlying mantle and is replaced by hot and fast upwelling asthenosphere (e.g. Bird 1979, Nelson 1992, Schott and Schmeling 1998; Fig. 5A). The consequences for the overlying crust are rapid heating, uplift, extensional collapse and crustal thinning (Nelson 1992; Fig. 5B). However, no compelling evidence supporting either of the two models (i.e. rifting and delamination) has been presented yet.

2.3.4 The CZ and the “Alpidic cycle”

The Late Permian to Tertiary sedimentation and deformation define the so-called “Alpidic cycle”. This can be divided in two stages, the first one extensive and the second one compressive (Alvarado 1980, Alonso and Pulgar 1995).

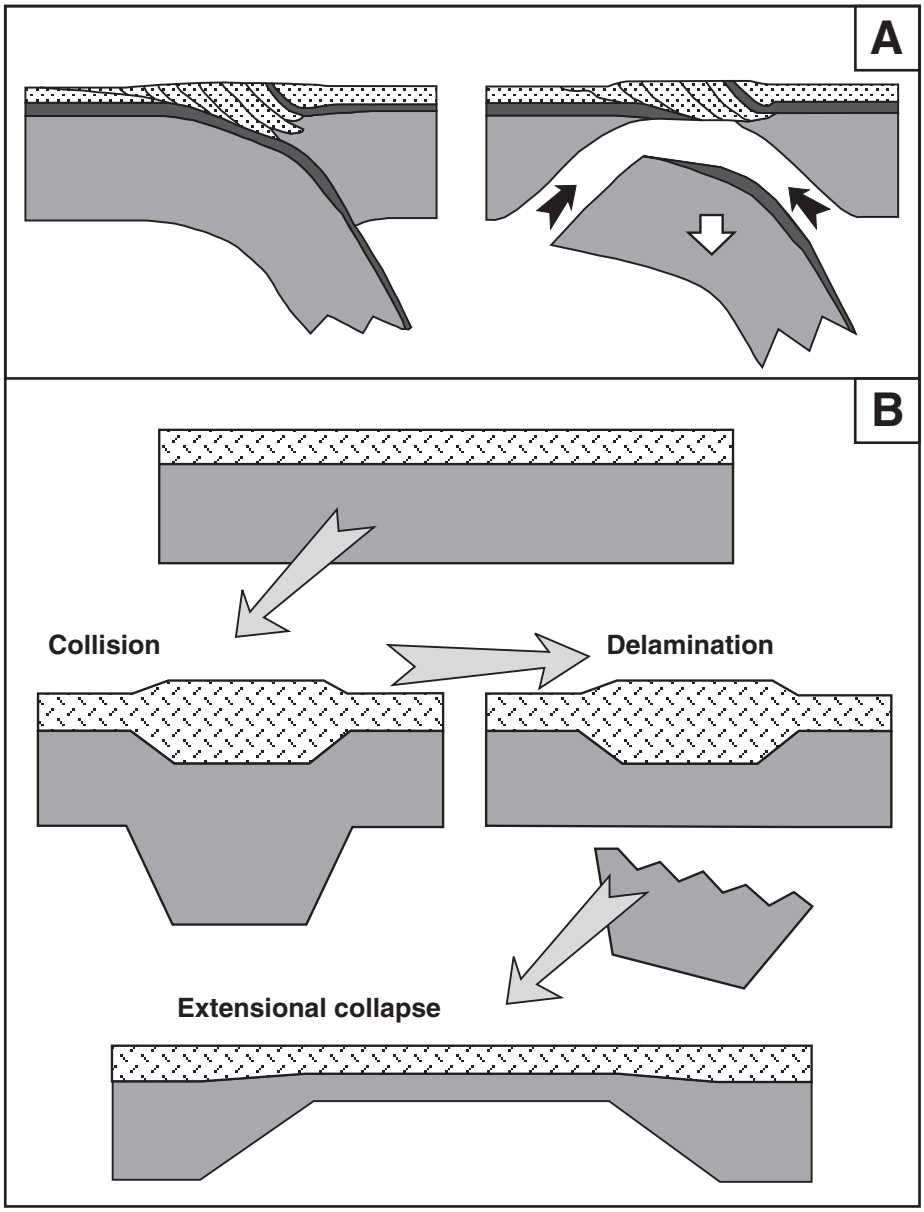

Fig. 5: **A.** Schematic sketch illustrating the process of delamination. Dash pattern = upper crust, dark grey = lower crust, light grey = mantle lithosphere, black arrows = asthenosphere upwelling (modified after Nelson 1992). **B.** Simplified model of collisional orogeny including collisional shortening, delamination and orogenic collapse. Dash pattern = crust, grey = mantle lithosphere (modified after Nelson 1992).

The first stage started with Late Permian and especially Triassic basin development (e.g. Espina 1992). In Jurassic and Cretaceous times extensional tectonics was related to the opening of the northern Atlantic Ocean and the Bay of Biscay (e.g. García-Mondejar et al. 1986). During these extensional periods Mesozoic basins possibly covered most of the CZ until tectonic inversion occurred in the Tertiary (Alonso et al. 1996).

The second stage developed as the Iberian plate and the European plate moved close together. In the CZ this compression began in the Late Eocene and had a southward vergence (Alonso

et al. 1996). The effects of this compressional phase were uplift of the basement, further N-S shortening of the chain, development of new faults, reactivation of some Variscan fractures and inversion of Permian - Mesozoic normal faults. In some places the deformation resulted in up to 30° of dip increase for the Variscan thrusts (Alonso et al. 1996, Pulgar et al. 1999).

2.3.5 Volcanism, magmatism, metamorphism and metallogenesis in the CZ

Volcanism. Alkaline volcanic rocks occur in the Middle Cambrian to Lower Ordovician succession. In the Permian an important alkaline volcanism developed (Corretgé and Suárez 1990).

Magmatism. In the CZ post-Variscan granitoid stocks are found. They have a tonalite-granodiorite-monzogranite composition and appear along with mafic to intermediate dykes (e.g. Fernández-Suárez et al. 2000). The granitoids formed by melting of lower crust with varying involvement of mantle derived melts. The mafic to intermediate dykes originated as mantle melts with some crustal contamination (Galán and Suárez 1989, Galán et al. 1996).

The largest granitoids are in the Pisuerga-Carrión Unit (e.g. Peña Prieta stock). In the westernmost CZ granodioritic to gabbroic stocks are also found (e.g. Arcellana and Carlés stocks). These intrusions are mostly located along deep, late-Variscan faults of considerable lateral extension (Julivert 1971, Loeschke 1982, Corretgé and Suárez 1990, Gallastegui et al. 1990).

Geochronological data for the igneous rocks of the CZ are scarce. In more internal zones of the Iberian Massif the main chronological peak for the post-tectonic plutons was reported at 295-285 Ma (Fernández-Suárez et al. 2000). In the CZ U-Pb dating of the Peña Prieta and Arcellana stocks gave ages of 293±2 Ma and 293±1 Ma respectively (Valverde-Vaquero et al. 1999).

Metamorphism. In most of the CZ diagenetic conditions were dominant. However, low grade metamorphism developed locally (Aller and Brime 1985, Aller 1986, Raven and Van der Pluijm 1986, Colmenero and Prado 1993, Keller and Krumm 1993, Bastida et al. 1999, García-López et al. 1997, 1999, Brime et al. 2001, Frings 2002).

Two distinct metamorphic events affected the CZ. The first event resulted from peak burial in the Westphalian and superimposed regional Variscan tectonic subsidence. It is exclusively manifested in the westernmost CZ. Metamorphic grade (up to epizone) is higher in older rocks. Cleavage is very sparse. The thermal peak coincided with the maximum thickness of the Palaeozoic succession. It developed previously and/or during the early stages of thrust motion, with little or no evidence of post-thrusting metamorphism from tectonic loading (Raven and Van der Pluijm 1986, Bastida et al. 1999, García-López et al. 1997, 1999, Brime et al. 2001).

The second event is late- to post-Variscan and is thought to be Late Stephanian - Early Permian in age (Aller 1986, García-López et al. 1999, Brime et al. 2001). It consists of two different manifestations. One is related to extensional tectonics and especially affected the southern Central Coal Basin and the Pisuerga-Carrión units (Aller 1986, Colmenero and Prado 1993,

García-López et al. 1999). It mostly developed anchizonal to epizonal conditions together with cleavage. The other manifestation developed contact aureoles between post-Variscan granitoids and the intruded rocks. These two manifestations are genetically related and frequently coexist, with the contact metamorphism representing the final stage of the process.

Metallogenesis. Over 300 mineralisations are known in the CZ. Most of them are hosted in Carboniferous rocks. Frequent deposit types are:

1. Cu-Co-Ni. These deposits are fault related, mostly found in the western CZ and hosted by intensively dolomitised Carboniferous carbonates (Ypma et al. 1968, Fernández et al. 1985, Paniagua et al. 1987, 1988a, 1993, 1995, Paniagua and Rodríguez-Pevida 1988, Paniagua 1989, 1993). Less frequently they are hosted in Carboniferous sediments near granodioritic to gabbroic intrusions (Loredo and García-Iglesias 1988, Cepedál et al. 1998);
2. Pb-Zn-Ba. These deposits are fault related and mainly found in dolomitised Carboniferous carbonates of the Picos de Europa Unit (Fernández 1985, Martínez-García 1981, Gómez-Fernández et al. 2000). Small showings are hosted in Lower Cambrian carbonates of the western and southern CZ (Paniagua 1993);
3. As-Sb-Au. These deposits are fault related and hosted by dolomitised Carboniferous carbonates near intermediate to basic dykes (Paniagua et al. 1996, Paniagua 1998, Crespo et al. 2000). Alternatively, they are hosted in basic igneous rocks close to major faults (Paniagua et al. 1988b, Gutiérrez et al. 1988, Loredo and García-Iglesias 1988);
4. Talc. These deposits are fault related and hosted in dolomitised Carboniferous carbonates of the eastern CZ (Galán-Huertos and Rodas 1973, Hardy et al. 1980, Tornos and Spiro 2000).

The major metallogenic feature of the southern CZ is the abundance of hydrothermal mineralisations related to regional fractures, such as the León, Tarna, Cofiñal, Polentinos and Ventaniella faults (Heward and Reading 1980, Luque and Martínez-García 1983, Luque et al. 1990). The deposits (mostly of the types 1. 2. and 3.) occur as veins, breccias or replacement bodies in pervasively dolomitised host carbonates (e.g. Paniagua 1993, Paniagua et al. 1993, 1996, Spiro et al. 1995).

2.4 The Bodón Unit

In the Bodón Unit (Fig. 3) extensive dolomitisation, the object of this study, is mainly found in Carboniferous carbonates. The central and eastern Bodón Unit was chosen as the main study area. A brief description of the Carboniferous rocks and of the main structural features of this unit is given in the following paragraphs.

2.4.1 General features of the Bodón Unit

The Bodón Unit consists of the Gayo, Bodón and Forcada nappes (Evers 1967, Marcos 1968b; Fig. 6). The Correcilla Thrust separates the Bodón Unit from the Correcilla Unit in the S. The Central Coal Basin Unit and the León Fault bound it to the N. The Porma Fault separates it from the Esla Unit in the E. The Bodón Unit passes into the Somiedo Unit in the W.

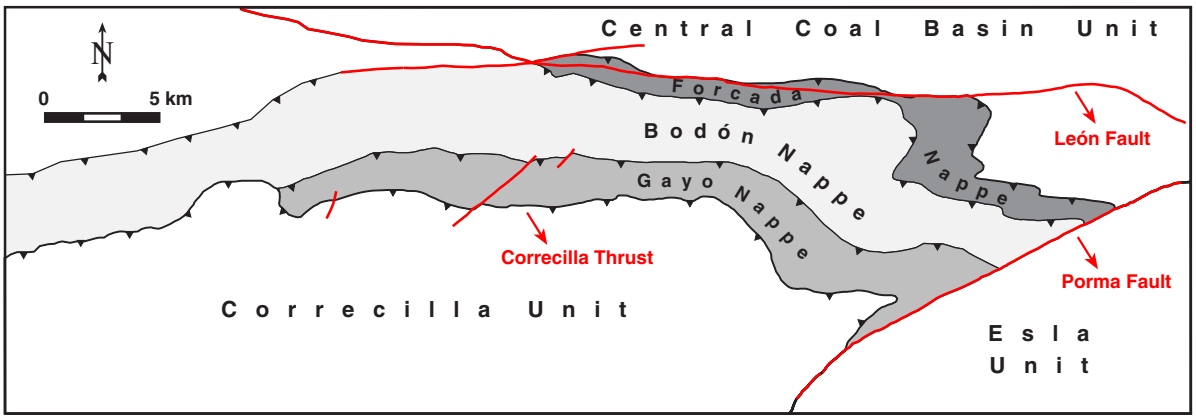

Fig. 6: Simplified tectonic sketch of the central and eastern Bodón Unit. Location of the Gayo, Bodón and Forcada nappes and of the major tectonic lineaments (modified from Marcos 1968b).

The Bodón Unit consists of a relatively complete Cambrian - Silurian, mainly siliciclastic succession, covered by Devonian rocks in which stratigraphic gaps occur. A thick Carboniferous pile of sediments (up to 2800 m) constitutes the top of the succession (see Appendix 1).

2.4.2 Carboniferous rocks in the Bodón Unit

The **Alba Fm.** (Viséan) is less than 30 m thick, has a wide extension and sharply overlies the older rocks. This formation consists of micritic, bioclastic and fossiliferous nodular limestones with a typical red to pinkish colour. The middle part of the formation contains red shales and red radiolarite horizons (Alonso et al. 1990). The Adrián Member is a dark grey limestone, which formed during Earliest Namurian time and represents the transition to the Barcaliente Fm. (Kullmann et al. 1977, Hemleben and Reuther 1980, Reuther 1980).

The **Barcaliente Fm.** (Namurian A) is 200-350 m thick. The transition to the Valdeteja or San Emiliano Fms. can be abrupt. This formation consists of dark grey to black, micritic, and bituminous limestones. Regular bedding and lamination are typical. The beds are tabular or wavy. Bioclastic and fossil content is generally very low (Wagner et al. 1971, Alonso et al. 1990). Normal gradation is the most common sedimentary structure at the base of the formation. In the middle part, lamination as well as bioturbation increase in importance. Towards the top bioturbation predominanates. In the uppermost part evaporitic intervals occur together with synsedimentary breccias (Reuther 1977, González-Lastra 1978, Hemleben and Reuther 1980). The uppermost

debris interval is named the Porma Breccia. The breccia clasts are a chaotic mixture of angular to sub-rounded and heterometric clasts, embedded in normal Barcaliente ground mass (Kullmann et al. 1977, Reuther 1977).

The Barcaliente Fm. possibly formed in a low energy, restricted environment, with euxinic bottom conditions and low rate of sedimentation (Evers 1967, Wagner et al. 1971).

The **Valdeteja Fm.** has a variable thickness (0 to 500 m) and a less continuous distribution than the Barcaliente Fm. The base of the formation is isochronous (Namurian A-B) whereas the top is strongly diachronous (Namurian B to Westphalian A; Lobato et al. 1984, Alonso et al. 1990). The transition to the San Emiliano Fm. is generally gradual. The Valdeteja Fm. consists of different lithologies, dominated by light grey, massive limestones, with some intercalations of better stratified limestones and marls. Various faunas exist with algae forming bioherms being dominant (Wagner et al. 1971).

The Valdeteja Fm. formed in a shallow neritic environment (Evers 1967, Eichmüller 1985).

The **San Emiliano Fm.** is 1000 to 2000 m thick. Its uppermost part is eroded. It consists of a terrigenous succession with carbonate intercalations and thin coal seams. The formation is divided in three members. The base is diachronous with the Valdeteja or Barcaliente Fms. whereas the top is Westphalian B in age (Lobato et al. 1984, Alonso et al. 1990).

The **Lena** and **Sama** groups (Namurian C - Westphalian D) are typical of the succession of the Central Coal Basin Unit, but also occur in the Forcada Nappe. The Lena Group consists mainly of limestones, heteropic with the first two members of the San Emiliano Fm. The Sama Group contains abundant sandstones and coal seams with rare limestones and corresponds to the uppermost member of the San Emiliano Fm. (Lobato et al. 1984, Alonso et al. 1990).

Post-orogenic Stephanian B sediments are found along the León Fault and consist of conglomerates, sandstones and shales with abundant coal seams (Lobato et al. 1984).

2.4.3 Structure and deformation age in the Bodón Unit

As mentioned already, the Bodón Unit consists of three thrust nappes (Fig. 6).

The **Gayo Nappe**, the uppermost of the pile, is bound by the Correcilla Thrust in the S and by the Gayo Thrust in the N (Fig. 6). The latter is at the base of the Cambrian Láncara Fm (see Appendix 1). The succession of this nappe is over 1700 m thick (Evers 1967, Lobato et al. 1984).

The **Bodón Nappe** occurs between the Gayo Thrust and the Bodón Thrust (Fig. 6). It has a stratigraphic thickness of 1900-2300 m (Evers 1967). The Bodón Thrust developed at the base of the Cambrian Herrería Fm. in the E and at the base of the Láncara Fm. in the W. N of Millaró the Bodón Nappe is in fault contact with the Lena Group of the Central Coal Basin Unit (see Appendix 1). E of Millaró a Variscan fault runs through the Barcaliente and Valdeteja carbonates controlling the location of several mineralisations (Lobato et al. 1984, Alonso et al. 1990).

The **Forcada Nappe**, the lowermost of the pile, occurs between the Bodón Thrust and the Forcada Thrust (Fig. 6). It has a thickness of 500-800 m (Evers 1967). The Forcada Thrust occurs mostly at the base of the Láncara Fm. In the E it coincides with the León Fault.

The first pulse of Variscan tectonism in the Bodón Unit took place in the Namurian A (Kullmann et al. 1977, Reuther 1977, 1980). The emplacement of the main thrusts occurred in the Westphalian B (Marcos 1968b). Regional folds locally affected the thrust fronts. This compressional event continued until the Stephanian B (Evers 1967, Marcos 1968b, Lobato et al. 1984).

2.4.4 The León Fault

The León Fault extends for 150 km with a predominantly E-W orientation. The eastern part of the fault is found nearly continuously within Stephanian sediments. The western part intersects the Bodón and Forcada thrusts and then continues to the NW (Fig. 6). This fault has a steep dip and is associated with a zone of brecciation and fracturing, several tens of meters wide. In the E the fault also controls the location of dykes of gabbrodioritic to gabbroic composition (Corretgé and Suárez 1990).

The first activation of the León Fault occurred with the development of the Central Coal Basin and Ponga units in the Late Westphalian (Julivert 1967). During this phase the León Fault was probably a sinistral strike-slip fault. Stephanian movements, mostly as reverse fault, were related to the emplacement of the Picos de Europa Unit. Fault reactivation occurred again in the Permian (Marcos 1968a, Marcos et al. 1979). Rejuvenation of the León Fault during the Alpidic Orogenesis is ambiguous (Pulgar et al. 1999).

The interference between the León Fault and the Bodón Unit gave rise to an E-W oriented brittle shear zone of about 100 km in extension, formed by a sequence of several shear duplexes. Associated with this shear zone, two different dolomite-hosted mineralisations are distinguished (Paniagua 1993, Paniagua et al. 1993). Within the shear duplexes a number of Cu deposits (with significant Ni-Co-U-As-Au contents) are found, representing the inner mineralised zone. The two most important mineralisations are those of Mina Profunda and Mina Providencia. To the S several Pb-Zn and As-Sb deposits constitute the outer mineralised zone. The most important Pb-Zn deposit is the one of Mina Fontún.

Chapter 3: Applied methods

3.1 Field methods

The spatial distribution of the dolomite bodies in the study area was reported in order to evaluate the extension of the dolomitisation phenomenon. Over 200 rock samples were collected in a region of about 500 km^2. Most of the samples come from the central and eastern Bodón Unit (Fig. 3). These samples were taken along seven profiles approximately perpendicular to the strike direction of the three formations of interest: the Alba, Barcaliente and Valdeteja Fms. From W to E the sampled profiles are named: Caldas, Cubillas, Villanueva, Millaró, Mina Profunda, Cármenes and Nocedo (see Appendix 1). Other sampled points of the Bodón Unit are named: Villamanín, Canseco, Montuerto and Valdecastillo (see Appendix 1).

Some Carboniferous samples were also taken from the Correcilla Unit at the locality Piedrasecha and Valporquero. A few samples from the Cambrian Láncara Fm. were collected at the base of the Correcilla Thrust.

Precursor rock samples as close as possible to the dolomite samples were collected, as well.

3.2 Thin section microscopy

3.2.1 Transmitted light microscopy

From the most representative samples of both dolomite and precursor limestone 119 polished and/or unpolished thin sections (50-60 μm) were prepared. The sections were observed under transmitted light, using a Leica MPV-SP microscope. Fluid inclusion petrography was accomplished on the polished thin sections.

The crystal size of the various carbonate phases is reported as diameter in μm. The crystal size characterisation refers to the classification proposed by Folk (1965).

3.2.2 Cathodoluminescence (CL) microscopy

The principle of cathodoluminescence (CL) is based on the property of many minerals, which luminesce under electron bombardment. Luminescing conditions occur in impure crystalline substances, where guest ions act either as activators or inhibitors of luminescence.

Electron bombardment of minerals causes excitement of ions which “jump” to a state of higher energy. After a short delay time the excited ions return to their former energy state and emit

radiation. Emission in the visible spectrum is responsible for the luminescence to occur. The term “cathodoluminescence microscopy” refers to the microscopic observation of minerals in thin section while under electron bombardment (e.g. Miller 1988).

Even if the causes of CL emission are still not fully understood (Machel et al. 1991, Pagel et al. 2000), most authors attribute the CL of carbonates to the presence of Mn^{2+} as main activator ion, whereas Fe^{2+} is believed to be the most important quencher ion (e.g. Long and Agrell 1965, Sommer 1972, Ebers and Kopp 1979, Pierson 1981). Minor CL activators are REEs like Sm^{3+}, Eu^{2+} and Eu^{3+}, whereas Co^{2+}, Ni^{2+} and Fe^{3+} have a quencher function. Machel and Burton (1991) identified 26 factors, which govern the CL of diagenetic carbonates, but they also agree that almost all CL is caused by trace elements.

CL microscopy was carried out for all of the prepared thin sections in order to better characterise the growth features and relations of the different mineral phases. The minerals were distinguished in extinct and luminescing. The latter were further characterised based on their CL colour, intensity and zoning.

A Citl cold cathode apparatus of the type CCL 8200mk3 was used. Thin sections were placed on a tray controlled by X-Y manipulators in a vacuum chamber with an upper window for microscopic observations. An electron beam was deflected on the sections by means of an obliquely arranged gun. A beam voltage of 20 kV and a current of 400 to 600 µA were used.

3.3 Geochemical methods

3.3.1 Staining

A potassium ferricyanide staining solution was prepared following the procedure of Dickson (1966). 14 previously polished rock slices were stained in order to roughly estimate the Fe content of the different carbonate phases. Ferroan calcites and dolomites display a characteristic blue colour after treatment with this staining solution for standard 40 seconds (Dickson 1966).

3.3.2 X-ray diffraction (XRD) analyses

In order to perform XRD analyses high-energy electrons are generated and bombard a Cu anode, which reacts by emitting X-rays. This radiation is directed on the sample, which rotates at a regular speed. When the mineral phases in the sample reach an appropriate angle, they will cause the diffraction of the X-rays according to Bragg’s Law:

$$n\lambda = 2d \sin\theta \qquad (1)$$

where n is an integer, λ is the X-ray wavelength, d is the lattice spacing and θ is the diffraction angle.

Output from a diffractometer is a strip chart of the X-ray diffraction pattern where the horizontal scale is calibrated in °2θ and the vertical scale shows the intensity of the diffracted peaks. Minerals can be identified by comparison of the obtained peaks to a set of standard patterns compiled by the Joint Committee on Powder Diffraction Standards (JCPDS). Then the peaks can be measured in terms of °2θ and automatically converted in lattice spacing (d) by means of the Bragg's equation ($d = \lambda/2\sin\theta$).

In the "ideal" dolomite there is an equal number of Ca and Mg ions, arranged in separate sheets with CO_3^{2-} planes in between. The "ideal" dolomite has therefore molar ratio of Ca:Mg=50:50 and is stoichiometric. Departure from this molar ratio is a measure of nonstoichiometry, commonly expressed as mol % $CaCO_3$ in the dolomite lattice. Most natural dolomites are not stoichiometric: they commonly have an excess of Ca, and less commonly an excess of Mg (e.g. Tucker and Wright 1990).

The effect of Ca substitution for Mg is to increase the lattice spacing since Ca^{2+} is a larger ion than Mg^{2+} (ionic radii 0,99 and 0,80 Å respectively). This can be detected by X-ray diffraction since the lattice reflections occur at lower °2θ angles as the Ca content increases. The stoichiometry of a dolomite can then be determined by evaluating the displacement of the measured d_{104} reflection relative to the d_{104} of the ideal dolomite (2,886 Å based on Goldsmith and Graf 1958). The greater the displacement of this peak towards higher d values, the more Ca is present in the dolomite structure (Hardy and Tucker 1988).

The Ca excess of dolomites can be calculated from the equation of Lumsden (1979) that relates mol % $CaCO_3$ (N_{CaCO3}) to the d_{104} spacing measured in Ångstrom units (d):

$$N_{CaCO3} = Md + B \qquad (2)$$

where M is 333,333 and B is –911,99.

XRD analyses also give information on the ordering of the dolomite crystals. Superstructure reflections corresponding to d_{021}, d_{015} and d_{101} are revealed by XRD analyses on dolomites. The sharpness and relative intensities of these peaks give information on the cation ordering of the dolomite crystals. The ratio of the heights between the peak (015) and the peak (110) is calculated: the greater the ratio, the higher the degree of order (OR), with the ideal dolomite having a ratio equal to 1 (Hardy and Tucker 1988).

XRD analyses were performed at the Geological-Palaeontological Institute of the University of Heidelberg (Germany), in order to determine bulk mineralogy, stoichiometry and ordering of the different dolomite phases, previously identified by means of other methods.

35 powder samples were analysed. Care has been taken to avoid contamination between the adjacent phases. In order to obtain granulometrically homogeneous powders, the samples were first ground in a mortar and pestle and then in a motor driven mill.

Quartz powder was added to the dolomite powders as internal standard in order to correct the position of the peaks, mostly shifted relative to the real position, by referring to the known d_{101} reflection of the internal quartz standard.

The analyses were performed on a Bragg-Brentano-Diffractometer of the type Siemens D 500, with a Cu Röntgen X-ray tube (CuKa) and graphite monochromator. The diffractometer operated at 40 kV and 30 mA and scanned the samples in the 2θ range from 2.0° to 70.0° with increments of 0,02°[2θ]/sec. Aperture diaphragm and detector diaphragm were respectively 1° and 0,15°.

For each sample the analyses were replicated four times under the same measuring conditions and by refilling every time the sample holder in order to minimise both the instrumental and preparation error. The PC-program Siemens Diffrac AT enabled the determination of bulk mineralogy, stoichiometry and degree of order.

3.3.3 Minor and trace element analyses (ICP-ES)

Minor and trace elements occur in natural minerals. They can be incorporated in the mineral lattice as guest ions, which substitute for host ions of similar charge and radius. They may also occur interstitially between lattice planes and along crystal boundaries. Additionally, they may occupy lattice defects or be included as solid or liquid inclusions.

When a compatible trace element substitutes for a host element in the lattice, the incorporation of the trace element into the solid from the mother liquid can be described by the Homogeneous Distribution Equation (McIntyre 1963). This is expressed as:

$$\left(\frac{{}^{m}X_T}{{}^{m}X_H}\right)_{solid} = k \cdot \left(\frac{{}^{m}X_T}{{}^{m}X_H}\right)_{liquid} \qquad (3)$$

where m is the molar concentration, X_T is the trace element, X_H is the host element and k is the distribution coefficient.

The distribution coefficient k can be used to predict the element partitioning. For k>1, the guest ion will be partitioned preferentially into the solid. For k<1, the ratio of the guest to host ions in the solid is less than the same ratio in the fluid. For k=1 no partitioning occurs, and the guest to host ratio will be the same in the solid and in the fluid.

There has been much discussion over the real values of k in carbonates (e.g. Brand and Veizer 1980, Kretz 1982, Veizer 1983). The main problem is that theoretical k only apply to trace elements in lattice sites. As previously mentioned, there are however other modalities in which

trace elements can be incorporated into crystals. Furthermore, the experimental values of k for dolomites are difficult to obtain. Consequently, accurate estimation of the geochemistry of the dolomitising fluids is difficult. The minor and trace element geochemistry of dolomites is thus mostly used to distinguish between different dolomite types, and to obtain general information on the nature of the dolomitising fluids (Brand and Veizer 1980, Land 1980, Kretz 1982, Veizer 1983, Machel 1988). The elements usually studied are Sr, Na, Fe and Mn.

48 samples of carbonates were analysed for minor and trace elements by Inductively Coupled Plasma Atomic Emission Spectroscopy (ICP-ES) at the ACME Analytical Laboratories Ltd. in Vancouver, Canada. A minimum of 0,5 g of carbonate powder was obtained using a dental-drill. A 15% HCl solution was used to dissolve carbonate powder traces from the drill point, in order to avoid contamination between subsequently drilled samples.

Aqua regia, a 2:2:2 mixture of HCl, concentrated HNO_3 and de-mineralised H_2O, was added to each sample. Samples were digested for one hour in a hot water bath (>95 °C). After digestion the sample solutions were aspirated into a Jarrel Ash AtomComp 800 ICP emission spectrograph to determine element concentrations.

3.3.4 O and C stable isotope analyses

Isotopes of the same element have differences in mass and energy, which cause differences in physical and chemical properties. In a molecule where two isotopes of the same element are present, the isotope with lighter mass is more reactive than the heavier isotope. A change in the ratio of the two isotopes during a reaction from phase A to phase B, such as the mineral precipitation, is called “fractionation”. Each isotope reaction is defined by the temperature dependent fractionation coefficient α:

$$\alpha_{A-B} = \frac{R_A}{R_B} \qquad (4)$$

where R_A and R_B are the ratios of the heavy to light isotopes in phase A and phase B respectively.

Only a few of the lighter elements, such as O and C, have isotopes with sufficient relative mass difference to cause detectable fractionation in nature. The two most abundant stable isotopes of oxygen are ^{16}O and ^{18}O. The two stable isotopes of carbon are ^{12}C and ^{13}C. $^{18}O/^{16}O$ and $^{13}C/^{12}C$ isotope ratios are widely used to define the conditions of carbonate diagenesis. Their application in Earth Sciences is exhaustively discussed in Tucker and Wright (1990), Clauer and Chaudhuri (1992) and Hoefs (1997).

The O and C isotope composition of a sample (x) is expressed relative to a standard (std) of known isotopic composition, by means of the $\delta^{18}O$ and $\delta^{13}C$ notations. These are calculated as:

$$\delta^{18}O = \left[\frac{\left(\frac{^{18}O}{^{16}O}\right)_x - \left(\frac{^{18}O}{^{16}O}\right)_{std}}{\left(\frac{^{18}O}{^{16}O}\right)_{std}} \right] . 10^3 \quad (5)$$

and

$$\delta^{13}C = \left[\frac{\left(\frac{^{13}C}{^{12}C}\right)_x - \left(\frac{^{13}C}{^{12}C}\right)_{std}}{\left(\frac{^{13}C}{^{12}C}\right)_{std}} \right] . 10^3 \quad (6)$$

The $\delta^{18}O$ of a carbonate strongly depends on the isotope composition of the fluid from which it precipitated and on the fractionation coefficient α between the fluid and the solid. The primary O isotope signature of carbonates is very often altered during diagenesis. The extent of this alteration may be used to discriminate the $\delta^{18}O$ value and/or temperature of the diagenetic fluid, including a possible distinction between meteoric, marine and/or evaporitic waters.

The $\delta^{13}C$ of a carbonate is closely related to the $\delta^{13}C$ of the bicarbonate dissolved in the fluid from which the mineral precipitated. Alteration of the primary $\delta^{13}C$ may or may not occur during diagenesis, depending on the amount of C present in the diagenetic fluids. The $\delta^{13}C$ of the carbonates can be used for instance to identify, whether meteoric water (carrying soil CO_2) was involved, or whether CO_2 from organic matter maturation was available during diagenesis.

138 carbonate samples were analysed for O and C isotope ratios at the Geological Institute of the University of Erlangen (Germany). Carbonate powders were extracted from rock slices drilled by means of a dental-drill. Contamination between samples was avoided as for ICP-ES powder preparation. Sample weights were as small as 0,2 mg.

$^{18}O/^{16}O$ and $^{13}C/^{12}C$ ratios were measured at the same time on CO_2 gas produced from carbonate powder digestion. The powders were reacted with 100% phosphoric acid at 75 °C (Wachter and Hayes 1985) in an online carbonate preparation line, connected to a Finnigan Mat 252 mass spectrometer. Calibration was accomplished by assigning a $\delta^{18}O$ value of –2,20‰ and a $\delta^{13}C$ value of 1,95‰ to the NBS-19 standard. All of the $\delta^{18}O$ and $\delta^{13}C$ values for carbonates were reported in conventional per mil (‰) relative to the PDB international standard. This is the isotope ratio of a belemnite (*Belemnitella americana*) from the Cretaceous Pee Dee Formation of South Carolina. Reproducibility was checked by replicate analysis of laboratory standards and is better than ±0,02. As suggested by Land (1980), the $\delta^{18}O$ values of dolomite samples were not corrected for the phosphoric acid fractionation.

The O isotope composition of fluids was expressed relative to the SMOW (Standard Mean Oceanic Water) international standard. This represents the average O isotope composition of present day seawater (0‰). A fluid with positive $\delta^{18}O$ value is enriched in ^{18}O relative to SMOW, whereas negative values indicate relative depletion of the fluid in the heavy isotope. The conversion equations of $\delta^{18}O_{PDB}$ versus $\delta^{18}O_{SMOW}$ and vice versa (Coplen et al. 1983) are:

$$\delta^{18}O_{SMOW} = 1{,}03091\ \delta^{18}O_{PDB} + 30{,}91 \quad (7)$$

and

$$\delta^{18}O_{PDB} = 0{,}97002\ \delta^{18}O_{SMOW} - 29{,}98 \quad (8)$$

3.3.5 Sr isotope analyses

Heavy isotopes such as ^{86}Sr and ^{87}Sr do not fractionate as strongly as the light isotopes of O and C. The relative mass difference is simply not sufficient for ^{86}Sr to fractionate from ^{87}Sr as mineral precipitation takes place. Consequently, a mineral bears rather the same Sr isotope composition as its mother fluid (e.g. Clauer and Chaudhuri 1992, Hoefs 1997).

^{86}Sr is not part of any decay series and its abundance is constant, whereas ^{87}Sr generates by radioactive decay of ^{87}Rb and its abundance increases with time. Carbonates can host large amounts of Sr, but they exclude Rb from their structure. Consequently, the amount of ^{87}Sr in a carbonate phase does not vary with time and the $^{87}Sr/^{86}Sr$ ratio remains relatively constant. Therefore, the Sr isotope ratios of carbonates reflect the composition either of the fluids from which they precipitated, or of the fluids with which they subsequently reequilibrated.

The Sr isotope composition of dolomites is an excellent parameter to deduce the composition and nature of dolomitising fluids.

16 carbonate samples were analysed for Sr isotope ratios at the Department of Geology of the University of Alberta (Canada). A minimum of 0,3 g of carbonate powder was provided for each sample, using the same procedure as for C and O isotope powder preparation.

Isotopic measurements were performed on Sr extracted from HCl solution using standard cation exchange procedures (Baadsgaard et al. 1986). $^{87}Sr/^{86}Sr$ ratios were measured on a VG 354 thermal ionisation mass spectrometer. The samples were loaded as a phospho-tantalate gel on a single Re ribbon bead assembly. Precision of individual runs was better than 0.00004 (2). The measured $^{87}Sr/^{86}Sr$ ratios were normalised to $^{87}Sr/^{86}Sr = 0.1194$, in order to correct for variable mass fractionation in the mass spectrometer. Repeated measurements of NBS SRM-987 gave a long term laboratory average of 0.710235 throughout the course of this study.

3.4 Fluid Inclusion (FI) study

Fluid inclusions (FIs) are mineral imperfections, consisting in microcavities sealed within crystals. During crystal growth, small droplets of the mother solution may be trapped in these cavities. These FIs are named primary. FIs trapped in the crystals in a later stage from crack-healing mechanism are named secondary. The study of FIs may give useful information on temperature and composition of the fluids which precipitated or reequilibrated with the mineral phases.
The techniques of FI study and their applications in Earth Sciences are exhaustively discussed in Roedder (1984), Shepherd et al. (1985) and Goldstein and Reynolds (1994).

3.4.1 Microthermometry

The principle of FI microthermometry is based on phase changes, which occur when heating and cooling FIs. Microthermometry of aqueous FIs allows to measure several parameters.
The temperature at which the fluid was occluded in the host crystal is called trapping temperature (Tt) and represents the precipitation temperature of the host mineral. Fluids trapped under elevated pressure and temperature may develop a gas bubble when they approach surface conditions. During heating runs of these FIs the homogenisation temperature (Th), i.e. the temperature at which gas and liquid phases homogenise, can be measured. The homogenisation may occur into the gas or the liquid state. Th represents the minimum Tt of the FIs and gives an indication of the bulk fluid density.
During cooling runs the temperature of gas nucleation (Tn_{gas}) and the temperature of “ice” nucleation (Tn_{ice}) can be determined. Tn_{gas} is the temperature at which the gas bubble nucleates within the liquid, after homogenisation in the liquid phase. Tn_{ice} is the temperature at which ice-like phases (i.e. ice and salt hydrates) nucleate. Both Tn_{gas} and Tn_{ice} generally occur at temperatures lower than those derived according to thermodynamic equilibria (Roedder 1984). This delay in gas and ice nucleation is a measure of metastability, which in turn depends on the shape, salinity, and density of the FIs.
When 2-phase aqueous FIs are frozen they can be heated again and the following temperatures can be measured: first melting or eutectic temperature (Te) and final melting temperature (Tm_{final}). Te is the temperature at which the first liquid forms and the ice-like phases start to melt. Tm_{final} is the temperature at which the ice-like phases completely melt. Depending on FI composition, Te and Tm_{final} may correspond to the melting of ice (Tm_{ice}) or salt hydrate (Tm_{hy}). If the liquid phase contains a complex mixture of salts, also intermediate (peritectic) melting temperatures can be measured.

10 double polished thick sections (100-120 µm) were prepared and used for FI investigation. The sections were prepared by means of cold technique reaching the maximal temperature of 35 °C, in order to prevent reequilibration and/or decripitation of the FIs by overheating.

Microthermometric measurements were carried out at the Geological-Palaeontological Institute of the University of Heidelberg (Germany) using a Linkam TH 600 stage and at the Institute of Geosciences of the University of Leoben (Austria) using a Linkam MDS 600 stage. Both stages were calibrated using chemical standards and polished quartz wafers containing synthetic FIs. Calibration curves were constructed by measuring the following temperatures:

- Triple point of CO_2 (-56,6 °C);
- Triple point of H_2O (0,0 °C);
- Pure $C_{14}H_{10}$ melting point at 1 bar (99,2 °C);
- Pure $AgNO_3$ melting point at 1 bar (212,0 °C);
- Critical point of H_2O at 220 bar (374,1 °C).

Thick section chips were placed on a sample port, controlled by X-Y manipulators, which rests directly on a silver block within the stage chamber. The silver block can be heated by thermal conduction and cooled by a constant flux of N_2 through the chamber, in order to accomplish high and low temperature measurements respectively.

A video camera was mounted onto the microscope and connected to a computer screen in order to facilitate FI observation. The volumetric proportion of the liquid phase relative to the total volume of the FI, referred as the degree of fill (F), was calculated from screen images at room temperature by measuring areas. The basic assumption is that area-fractions are equal to volume-fractions.

The Linksys PC-program enabled all of the operations for FI petrography and microthermometry.

3.4.2 Raman spectroscopy

The Raman spectroscopy is a nondestructive technique, which permits compositional analyses of FIs without opening the vacuoles. The laser Raman microprobe is an instrument that focuses a laser through an optical microscope into a single FI. Scattered laser radiation is produced by the vibration of bonds between atoms and molecules and is restricted to polyatomic species. Monoatomic ions in aqueous solution (e.g. Na^+, Cl^-) do not produce the Raman effect, nor do monoatomic gases (e.g. Ar, Xe). Excitation of a sample will produce scattered light radiation with frequencies characteristic of the polyatomic bonds which are present. This radiation is detected by a spectrometer and characteristic spectra from many polyatomic species can be obtained (e.g. Wopenka et al. 1990, Burke 2001).

Identification of solid and fluid species in the studied FIs was carried out with a Raman microprobe Dilor LABRAM HR-800. A wavelength of 532,2 nm (green laser) was used for the radiation on both

calcite and dolomite samples. The measurements were preferentially performed on FIs as close as possible to the sample surface, because of the low penetration capacity of the laser in depth. The main peaks of the obtained spectra were compared with already compiled tables for the most common substances (Bakker, pers. commun.).

Raman measurements combined with low temperature microthermometry were accomplished. A Linkam TMS 93, calibrated as the other microthermometry stages (see paragraph 3.4.1), was attached to the Raman microprobe. The method described by Dubessy et al. (1982) and Bakker (2001a, 2002) was applied. This method allowed the identification of ice and salt hydrates, formed in FIs during cooling runs. Additionally, it enabled a more precise estimation of melting temperatures of the different phases than microthermometry alone could achieve. Measurements for the identification of ice-like phases were mostly performed at temperatures lower than -150 °C. This is because the quality of the Raman spectra is temperature dependent: at lower temperatures the Raman spectra have better defined peaks.

All of the operations for Raman spectroscopy were enabled by the LABSPEC 2.08 PC-program.

3.4.3 Crush-leach analyses

The crush-leach is a destructive technique. It allows the chemical analysis of the fluid released from FIs by bulk sample crushing, i.e. the analysis of a large number of FIs. Consequently, it is preferably applied to those samples containing only one type of FIs, homogeneous in composition. The presence of more than one generation of FIs in the sample would result in the characterisation of an artificially mixed fluid, with no geological relevance (e.g. Banks and Yardley 1992).

Dolomite and calcite samples, showing consistent microthermometric data, were analysed with the crush-leach method to get information on the bulk ion concentration in the FIs. The analyses were performed at the Institute of Geosciences of the University of Leoben (Austria). The samples were crushed under water and the resulting solution (the “leachate”), consisting in the inclusion contents diluted with leach water, was chemically analysed (e.g. Banks and Yardley 1992).

3.4.4 Thermodynamic calculations and computer programs

The microthermometry, Raman spectroscopy and crush-leach data were used to determine composition and density of the fluids trapped in the inclusions. The computer package FLUIDS (Bakker 2001b, Bakker 2003), including the programs AQSO1, AQSO2, AQSO3, BULK and LONER 32, was used.

The programs AQSO1 and AQSO3 were used to calculate salinities in the binary H_2O-NaCl system (Bodnar 1993) and H_2O-$MgCl_2$ system (Dubois and Marignac 1997), respectively. The program AQSO2 was used to calculate salinities in the ternary H_2O-$CaCl_2$-NaCl system (Naden 1996). Salinities were obtained by introducing the melting temperatures of ice-like phases.

The program BULK was used to calculate bulk fluid properties of individual FIs. Bulk density and composition of FIs were calculated using a purely empirical thermodynamic model. Calculation of FI properties at 20 °C was accomplished using the equation of state for aqueous systems of Krumgalz et al. (1996) and the volume fractions of the liquid phase of FIs at room temperature.
The program LONER 32 was used to calculate the isochore slope for the different types of FIs. Main requirement of this program is the knowledge of Th and salinity of the FIs, according to the model of Bodnar and Vityk (1994). As the calculation of isochore slopes by means of this program is possible only for the H_2O-NaCl system, the salinity of the different types of FIs was converted in eq. wt % NaCl.

Chapter 4: Field observations

4.1 Dolomite distribution

Extensive occurrences of apparently the same type of dolomite were observed in most of the tectonic thrust units of the CZ (Somiedo-Correcilla, Sobia-Bodón, Aramo, Central Coal Basin, Ponga and Picos de Europa units; Fig. 3). The most affected areas are the southern part of the Picos de Europa Unit and the central part of the Bodón Unit. In the latter the dolomitisation is more pervasive than elsewhere.

In the studied area (Fig. 3) the dolomitisation is rare in the sediments of the Cambrian to Devonian succession. In these rocks the dolomite bodies rarely exceed a few tens of cubic meters. Among these lithologies, the Cambrian Láncara Fm. contains the largest volumes of dolomite, located at the base of the Correcilla Thrust. A few minor dolomite occurrences have been reported in Devonian carbonates of the Correcilla Unit. In the Bodón Unit only the La Vid Fm. shows meter-sized patches of dolomitised rocks in the area E of Millaró.

The sediments most affected by dolomitisation are the Carboniferous Barcaliente and Valdeteja Fms. Less extensive dolomite occurrences are found in the underlying Alba Fm., and especially in its uppermost part.

Dolomitisation was not observed in the sediments of the late syn-orogenic and post-orogenic successions. Dolomites were neither found in the carbonate levels of the San Emiliano Fm., nor in the carbonate lenses of the Lena and Sama groups located N of the working area. No dolomitisation was observed in the carbonate conglomerates of the Stephanian basins, S of the Bodón Unit.

In the three tectonic nappes of the Bodón Unit the distribution of dolomite bodies is not uniform. In the Gayo Nappe dolomites are abundant only at Nocedo de Curueño, at Getino and in the area E of Villamanín (see Appendix 1). The Bodón Nappe is the most affected: widespread dolomitisation occurs in the central and western part of the E-W oriented Carboniferous carbonate ridge. N of Villanueva de la Tercia the dolomitisation is so pervasive that outcrops of precursor limestones are rarely found. Towards the eastern parts of the nappe the amounts of dolomite decrease and remnants of unaffected limestones become gradually more frequent. In the Forcada Nappe dolomite only occurs as small meter-sized bodies at Canseco and E of Lugueros.

4.2 Dolomite macroscopic features

4.2.1 Colour, geometry and types

The recognition of dolomite from limestone in the field was facilitated by the clear colour contrast existing between their external surfaces: limestones are light grey, whereas dolomites are yellowish-brown to dark grey (Plate 1, Ph. 1). The dolomites show on the contrary a lighter colour when sampled in fresh cuts (Plate 1, Ph. 2). The same observation has been reported by Crespo et al. (2000) for dolomite outcrops further to the E of the study area. The darker surface colour of dolomites is likely due to weathering and to the cover of lichen colonies, which preferentially grow on the dolomite surface.

The geometry of the dolomites in the field varies widely. They sometimes form extremely irregular masses, which enclose remnants of undolomitised limestone as relic bodies (Plate 1, Ph. 1). In other cases the dolomites occur as sub-vertical bodies with a dyke-like geometry at centimetric to decametric scale (Plate 1, Ph. 3).

The recognition of dolomite in the field was also facilitated by the more brittle behaviour of dolomite relative to limestone. Consequently, the dolomite is more intensively fractured. The dolomite-limestone contacts are very sharp and abrupt, and the transition from limestone to dolomite occurs in a few centimetres or even less (Plate 1, Phs. 4 and 5). These contacts are rarely concordant with the stratification and generally cut both bedding planes and sedimentary structures (Plate 1, Ph. 5).

Dolomite bodies at metric scale may be spatially related to 10-30° dipping faults (Plate 1, Ph. 6).

In some partly dolomitised outcrops the dolomitisation may appear restricted to discontinuities like bedding, lamination and/or stylolite planes. Only a few centimetres (or even less) of the host rock on both sides of the discontinuities are dolomitised (Plate 2, Phs. 1-3).

Locally, a halo of yellowish and coarse dolomite crystals may be found at the contact between limestone and massive dolomite (Plate 2, Ph. 4). These crystals also occur as clusters or isolated crystals floating within the limestone mud (Plate 2, Ph. 5).

The dolomitisation strongly overprints the precursor rocks. Sedimentary structures and fossils are rarely preserved. Locally, relics of fossils are recognisable although they show a strong degree of recrystallisation. In some fully dolomitised crinoidal limestones of the Valdeteja Fm. the matrix and the crinoids are still distinguishable due to their different colour (Plate 2, Ph. 6).

In some outcrops of Porma Breccia the dolomitisation preferably affected the carbonate matrix of the breccia, whereas many breccia clasts remained undolomitised (Plate 2, Ph. 7). Crinoidal limestones of the Valdeteja Fm. locally show similar features, as undolomitised crinoids appear embedded in a dolomitic matrix.

Two main dolomite types can be recognised in the field: a mosaic dolomite and a sparry dolomite. The mosaic dolomite is the most abundant. It is frequently the only dolomite type to be recognised with the naked eye. It consists of a mosaic of dolomite crystals whose colour varies from dark to light grey, brown to yellowish, and even pinkish. In the Valdeteja Fm. the most common colours for the mosaic dolomite are pink and light grey, whereas in the Barcaliente Fm. this dolomite is normally dark grey or yellowish. Mosaic dolomites in the Alba Fm., due to its lithologic heterogeneities, show strongly differing colours. The sparry dolomite is found along fractures, or as pore filling. This phase is milky white to light pink, coarser crystalline and mostly of the saddle type as indicated by curved crystal faces. There is apparently no correlation between the sparry dolomite colour and the protolith lithology.

The mosaic dolomite is a replacive phase as it locally preserves the primary features of the precursor carbonate. Moreover its colour is strongly influenced by the composition and/or colour of the precursors. The sparry dolomite is a cement as no primary structures were ever seen in this phase and it occurs in voids. Moreover, its colour is independent from the composition and/or colour of the host lithology.

4.2.2 Dolomite porosity and zebra-structures

The precursor limestones are fully cemented, showing no visible porosity. In contrast, the dolomites display an important porosity consisting of fairly widespread cavities, linear to roundish in shape (Plate 3, Phs. 1 and 2). The inner part of these cavities is lined by the milky white sparry dolomite. Similar cavities were never observed in the parent limestones.

The two mentioned dolomite types commonly form well documented banded structures. These are frequently reported in dolomites and are commonly named zebra-structures or zebra-dolomites (e.g. Wallace et al. 1994, Zeeh 1995, Nielsen et al. 1998).

The zebra-dolomites from the studied area are given by the rhythmic repetition of mm-scale mosaic dolomite and sparry dolomite sheets, with open space between two subsequent sparry dolomite sheets (Plate 3, Phs. 3 and 4). From the geometric point of view, the most typical feature of these structures is the bipolarity of the sparry dolomite, which grew in opposing direction on both sides of the mosaic dolomite sheet. The resulting sequence is thus given by the following alternation: mosaic dolomite – sparry dolomite - open space - sparry dolomite – mosaic dolomite (Plate 3, Phs. 3 and 4) and so on.

The sparry dolomite sheets are generally less thick than those of the mosaic dolomite. Geopetal features are not observed in the cavities and white sparry dolomite sheets show the same thickness above as well as below the central open space.

In the examples described, the cavities are still open and contain no later cement. In other cases, the sparry dolomite crystals, which grew from the cavity walls, have terminations which meet

halfway and fill completely the cavities. Elsewhere the remaining voids are filled by different types of coarse crystalline calcite, transparent to white in colour (Plate 3, Phs. 5 and 6). These calcite cements are never encountered in the precursor limestones.

Evidence of primary depositional rhythmicity at the zebra scale is not found in the precursor limestones. In addition the zebras and associated cavities are often unconformable with the sub-vertical to overturned bedding of the host rocks (Plate 3, Phs. 1, 3 and 4). The cavities do not display a constant orientation. They are mostly sub-horizontally aligned where the dolomitisation affected well bedded or laminated sediments of the Barcaliente and Alba Fms. (Plate 3, Phs. 1, 3 and 4). The cavities are on the contrary variously oriented where the dolomitisation affected the massive limestones of the Valdeteja Fm. (Plate 3, Ph. 2).

The sub-horizontal cavities often follow fissure planes (Plate 3, Ph. 3). Fractures with the same inclination (0-20°) are frequently reported in the parent limestones all over the studied area.

Sparry dolomite sheets are locally associated with sub-vertical veins. The veins are less than 1 mm in thickness. They are filled with apparently the same white sparry dolomite which forms the zebras (Plate 3, Ph. 7).

4.2.3 Dolomite and alternate bands

Some of the dolomitised outcrops especially from the lower Barcaliente Fm. show a banding given by light grey to brown or even pink bands alternated with dark grey bands (Plate 4, Ph. 1). The bands are roughly parallel to the bedding, even though they are not straight but wavy. Typically the dark bands are arranged on both sides of stratification, lamination or stylolite planes, whereas the light bands occupy the middle part of the layers between two subsequent discontinuities. The dark bands are volumetrically less important than the light ones and have a variable thickness, which ranges from less than one mm to several cm.

Both light and dark bands consist of a mosaic of dolomite crystals. However, the colour change may correspond to a textural change. The light bands consist mostly of anhedral crystals, corresponding to the mosaic dolomite previously described. They commonly host cavities partly filled with sparry dolomite. The dolomite of the dark bands shows various crystal coarseness. It consists of anhedral to subhedral crystals and hosts no cavities (Plate 4, Phs. 2-5).

The transition from dark to light bands may be abrupt (Plate 4, Ph. 2) or gradual (Plate 4, Ph. 5). In the latter case dark dolomite crystals occur between two subsequent dark bands, floating within the mosaic of lighter dolomite crystals.

Sparry dolomite veins crosscut both dolomite types forming the bands (Plate 4, Phs. 2 and 4).

4.3 Dolomite and mineralisations

As already underlined in Chapter 2 some ore deposits, presently non-economic, are found in the study area. The ores are commonly hosted in dolomitised Carboniferous carbonates and consist mostly of sulphides (Cu-Co-Ni-Cr and Zn-Pb-Ba). They occur mainly in veins which cut the studied dolomites and are embedded in a gangue of dolomite, calcite and quartz (Ypma et al. 1968, Fernández et al. 1985, Paniagua et al. 1987, Paniagua and Rodríguez-Pevida 1988, Paniagua 1989, Paniagua 1993, Paniagua et al. 1995). Only the products of supergene alteration of the ores (e.g. marcasite, azurite, malachite, cuprite and tenorite) are observed at surface. These minerals are locally found in the studied dolomites, filling pores and cavities (Plate 4, Ph. 6).

4.4 Dolomite and deformation

Some significant examples of the relationships between dolomite occurrences and structural features of the studied area are reported in the following paragraphs.

4.4.1 Dolomite and Variscan thrusts

S of Poladura de la Tercia, the Correcilla Thrust puts in contact the carbonates of the Láncara Fm. and the black shales of the siliciclastic San Emiliano Fm. (see Appendix 1). The dolomites occur in the Láncara carbonates directly in correspondence of the thrust plane (Plate 5, Ph. 1) and become gradually less abundant at greater distance from it. The mosaic dolomite appears undeformed and hosts open cavities, partly filled with sparry dolomite. On the contrary, the black shales of the San Emiliano Fm. are highly deformed and display a foliated character, curved shear planes and glassy appearance.

4.4.2 Dolomite and Variscan folds

At Piedrasecha in the Correcilla Unit a folded outcrop of pervasively dolomitised Barcaliente limestone (Plate 5, Ph. 2) displays zebra-structures and sheet-like cavities. The latter have a sub-horizontal orientation independent from the dip direction of the fold limbs. Where the host layers are sub-horizontal the cavities follow the sub-horizontal alignment of bedding and lamination planes (Plate 5, Ph. 3). Where the same host layers have a sub-vertical dip direction, the cavities follow the orientation of sub-horizontal fissures (Plate 5, Ph. 4).

4.4.3 Dolomite and faults

The dolomite bodies from the study area are undeformed also when they occur spatially related to fault planes. Only two exceptions were reported:

1. At Villanueva de la Tercia a fault contact between Valdeteja and San Emiliano Fms. is observed. The sandstones and shales of the clastic unit abruptly stop against the pervasively dolomitised carbonate sequence. A planar and striated slickenside surface is developed in the dolomite at the contact with the clastics (Plate 6, Ph. 1).
2. At Getino a large occurrence of dolomitised crinoidal limestone is affected by faulting. The dolomite is highly deformed: it is dusty and cataclastic, and displays several generations of curved, glassy and striated slickenside surfaces (Plate 6, Ph. 2).

4.5 Main diagenetic features of the precursor rocks

In the undolomitised Carboniferous carbonates from the study area the most evident diagenetic products are stylolites and calcite veins. Their relationships with the dolomites of interest are described in the following paragraphs.

4.5.1 Stylolites

In the Barcaliente Fm. stylolites are abundant. They are mostly arranged parallel to the stratification and may coincide with lamination planes. They have an important persistence (several meters or more) along the same layer and are easily recognised because of dark mineral residue trapped along them. The same type of stylolites is also abundant in the Alba Fm. In the Valdeteja Fm. they are only locally developed, and are less uniform in shape and lateral extension.

Stylolites regularly occur in the dolomitised rocks. Here they show the same orientation as in the precursor limestones. Some of the dolomite fronts are constrained by these stylolites (Plate 2, Ph. 3), which locally occur along with the dark dolomite bands (Plate 4, Phs. 2 and 5).

4.5.2 Calcite veins

Multiple generations of calcite-filled veins occur in all of the investigated Carboniferous carbonates. They are variously oriented and range from less than 1 mm to about 5 mm in thickness (Plate 6, Ph. 3).The calcite veins propagate through the stylolites. Similar veins are never seen in the dolomitised rocks. Commonly, the trace of the calcite veins stops at the contact with the dolomite front (Plate 2, Ph. 5 and Plate 6, Ph. 4). Dolomite crystals are found both in the host limestone and in the calcite of the veins.

Chapter 5: Thin section microscopy

5.1 Microscopic features of the precursor rocks

Thin section microscopy of the undolomitised carbonates suggests that all of the three Carboniferous formations of interest underwent a complex diagenesis, ranging from early to late. The main primary features and diagenetic products of these carbonates are briefly described in the following paragraphs.

5.1.1 Primary and early diagenetic features

The upper part of the Alba Fm. shows flaser structures with streaky pseudo-parallel layers of micrite and clay. Fossil shells and moulds occur in the micrite. Early calcite cementing fossil shells is abundant as well as spheroidal chert aggregates. Compaction of the micrite grains is locally observed.

The Barcaliente Fm. consists of a quite monotonous assemblage of dark to light brown micrite with abundant organic matter. The original grain size of the micrite is rarely identifiable since the limestones are recrystallised. Allochemical grains are represented by intraclasts, pellets, scarce oolites and scarce fossil fragments. Normal gradation is frequent and wavelike structures are also typical. Rounded to elliptical patches of microcrystalline sparry calcite, with sharp boundaries are enclosed in the micrite. Compaction is evident in the deformation of pellets. Silicified horizons are found especially in the lower part of the formation. They consist of roundish aggregates of quartz. Compaction patterns show that these aggregates formed during early diagenesis as the bedding is deformed around them. Much of this quartz was later recrystallised as calcite pseudomorphs (Hemleben and Reuther 1980). In few sections from the top of the Barcaliente Fm., elongated crystals of sulphates may be abundant. Small and disseminated euhedral to subhedral crystals of pyrite, sometimes partially oxidised, have been identified, too.

The carbonates of the Valdeteja Fm. are mainly composed of medium to coarse-grained, sorted biosparites and oosparites. They show various textures, which indicate different diagenetic environments (see Eichmüller 1985). Samples of bioclastic limestone display intergranular fibrous cementation of skeletal pores by early calcites.

All of these carbonates will be indicated throughout this work with the symbol H, standing for host. They mostly show a dull orange to red and unzoned CL with slight variation from one formation to another. Only slight differences in CL colour and intensity are observed between the matrix and the allochems of these rocks.

5.1.2 Bedding parallel styolites (S) and calcite veins (CV)

As pointed out in paragraph 4.5, most of the studied Carboniferous carbonates are affected by bedding parallel stylolitisation and host widespread calcite veins.

The bedding parallel stylolites (S) mostly coincide with lamination and bedding planes. They truncate both carbonate grains and interparticle early calcite cements. Their architecture is either very irregular or displays a saw-tooth type waveform. They exhibit opaque phases along their trace. These phases consist of clays accumulated along the stylolites as insoluble residue, framboidal pyrite and the products of pyrite oxidation (Plate 7, Ph. 1). The axes of the stylolite peaks are mostly perpendicular to the plane of stylolites and consequently to the lamination and bedding planes of the host limestones. The amplitude of the peaks rarely exceeds 2 mm, suggesting a little amount of dissolution across the stylolite planes (Choquette and James 1990). Under CL the opaque phases along the stylolites are always extinct.

The calcite veins (CV) are variously oriented (Plate 6, Ph. 3) and crosscut the stylolites (Plate 7, Ph. 1). The vein-filling calcite crystals are locally twinned, but do not show features of deformation contemporaneous to their growth. Locally, the crystal size distribution is typical of a free-growth phase as the crystals become coarser from the walls towards the vein centre (Plate 7, Ph. 2). The absolute crystal size depends on the vein thickness, with coarser crystals occurring in thicker veins. The contacts between CV and host limestone are commonly irregular.

The vein-filling calcite displays a dull orange to red and unzoned CL, almost indistinguishable from the one of the host limestones (Plate 7, Ph. 3).

5.2 Microscopic features of the dolomitised rocks

A common paragenesis of the dolomite phases can be established for all of the three studied formations. Different dolomite types were distinguished by macroscopic observation of dolomite in hand specimens (see Chapter 4). Transmitted light and CL microscopy enabled further distinction. The different occurring phases are sketched in Fig. 7.

5.2.1 Dolomite A (replacive event)

Field observations indicated that a regular banding, parallel to the main discontinuities is present mostly in the lower Barcaliente Fm. (Plate 4, Ph. 1-5). The dolomites of the dark and light bands show some microscopic differences which allow to consider them separately. They are both replacive in origin and were named respectively dolomite A1 (Dol A1) and dolomite A2 (Dol

A2). Dol A1 is distinctly less abundant than Dol A2 and shares some of the Dol A2 microscopic features. For this reason Dol A2 will be described first.

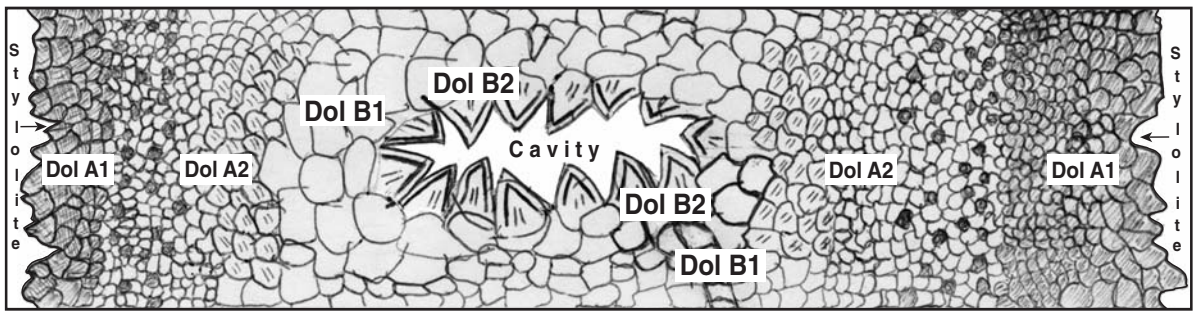

Fig. 7: Simplified sketch, showing the spatial relationships of the different dolomite phases. The scale is arbitrary.

Dol A2. This dolomite corresponds to the volumetrically most abundant mosaic dolomite described in paragraph 4.2.3. It displays a variety of fabrics and crystal forms. In most of the samples Dol A2 consists of a mosaic of fine to coarse sized interlocked crystals. Coarser crystals show a slight undulose extinction under crossed-polarised light, typical of saddle dolomite (Radke and Mathis 1980, Spötl and Pitman 1998). On the contrary, finer crystals extinguish faintly.

Subhedral and anhedral crystals may coexist together. However, anhedral and closely packed crystals with lobate or curved intercrystalline boundaries are the most common (Plate 7, Ph. 4A). According to the dolomite texture classification proposed by Sibley and Gregg (1987) this phase can be classified as non-planar.

The crystal size distribution is mostly unimodal. Locally polymodal crystal distribution occurs: because of the presence of fossils and other allochems in the host limestones, the dolomite crystals replacing these components can be significantly coarser than those replacing the limestone mud.

Brown to yellowish amorphous material is found as intra- and inter-crystalline phase and coats irregularly the Dol A2 crystals. This material represents the residue of leaching of the precursor limestones during dolomitisation.

The Dol A2 crystals are cloudy because of an abundance of fluid inclusions and micropores (Plate 7, Ph. 4A).

In most of the samples twinned crystals were not observed. The samples from the fault zone near Getino are the only exception (Plate 6, Ph. 1), as they consist of twinned and highly deformed dolomite crystals.

Dol A2 has a mottled dull red and unzoned CL, characterised by numerous micron-sized brighter red spots (Plate 7, Ph. 4B). The latter likely represent crystallographically coherent planar defects (Barber et al. 1985). Only very slight variations in CL colour or intensity were observed for Dol A2 all over the studied area.

The yellowish dolomite crystals locally observed at the transition from massive dolomite to host limestone (Plate 2, Phs. 4 and 5) consist of subhedral rhombs floating within the limestone matrix (Plate 7, Ph. 5). They share most microscopic features of Dol A2 crystals, although their borders are coated by a ferroan phase.

Regardless of the crystal shape, Dol A2 is strongly fabric destructive. It obliterated depositional and diagenetic features of the precursor limestones. Stylolites are still recognisable but their suture trace is smoothened (Plate 7, Ph. 6). In the dolomitised Barcaliente Fm. elongated pseudomorphic moulds of sulphate minerals are locally observed. Fossils are only locally preserved as recrystallised relics. Skeletal fabrics observed in hand specimens are hardly recognisable in thin section. In hand specimens of fully dolomitised crinoidal limestones, crinoids and matrix were easily distinguished (Plate 2, Ph. 6). In thin section the distinction is made only by the different crystal size: the matrix is fine to medium crystalline, whereas the recrystallised crinoids consist of a single and coarse dolomite crystal (Plate 8, Ph. 1).

Pyrite and hematite are commonly found scattered within the Dol A2 as intra- and inter-crystalline phases. The pyrite is fine crystalline and exhibits framboidal shape (Plate 8, Ph. 2). Less frequently, octahedral or dodecahedral crystal shapes are observed. The hematite crystals are mostly grouped in clusters and exhibit a reddish-brown colour.

Aggregates of microcrystalline quartz may be abundant. They form patches irregularly distributed in the Dol A2 crystal mosaic. The quartz crystals have a light yellow colour in plane light (Plate 8, Ph. 3A) and first order interference colours in cross-polarised light (Plate 8, Ph. 3B).

Quartz aggregates, pyrite and hematite crystals are always extinct under CL.

Dol A1. This dolomite forms the already described dark bands on both sides of discontinuity planes, and mainly along stylolites (Plate 4, Phs. 1-5). Stylolites are still recognisable within Dol A1. They are never obliterated by Dol A1 crystals, but their profile may be strongly smoothened (Plate 8, Ph. 4).

According to the dolomite texture classification of Sibley and Gregg (1987) Dol A1 is mostly non-planar. In plane light the crystals display a yellowish to light brown colour (Plate 8, Ph. 4). The crystals are cloudy due to the presence of fluid inclusions and micropores. Zonation, sweeping extinction and twins are never observed.

The crystal size ranges from very fine to coarse crystalline. A common crystal size distribution consists of fine crystals which may become coarser towards the stylolite planes (Plate 8, Ph. 5). Therefore, the crystal size distribution of Dol A1 may be polymodal.

Dol A1 crystals are microscopically distinguishable from Dol A2 crystals only by the darker colour, the crystal size distribution and the alignment along discontinuity planes. Additionally, pyrite, hematite and quartz crystals, typical of Dol A2 are rarely observed in Dol A1.

The transition from Dol A1 to Dol A2 is mostly gradual: Dol A1 crystals become less abundant

with increasing distance from the stylolites until they appear scattered within the mosaic of Dol A2 (Plate 8, Ph. 6). However, an abrupt transition from Dol A1 to Dol A2 may also occur.
Dol A1 has the same CL as Dol A2: dull red, unzoned and with micron-sized brighter red spots.

5.2.2 Dolomite B (void filling event)

The void filling event consists in the precipitation of the white sparry dolomite (see Chapter 4), which fills voids and cavities. This phase was named dolomite B (Dol B). It is mostly hosted in Dol A2, whereas it is rarely found in Dol A1.
As for the replacive dolomites, the crystals of Dol B are interlocked, but are coarser and clearer since impurity coatings are less frequent. Host limestone features are never recognised in this phase. Fossil relics or evaporitic moulds, for instance, are missing. Stylolites, which persisted in the replacive dolomite, are obliterated by Dol B crystals (Plate 8, Ph. 7). The quartz patches typical of Dol A2 are never seen. Pyrite, oxides and opaque minerals can be locally abundant as intra- and inter-crystalline phases.
Dol B crystal size increases from the first crystal generation, following the replacive dolomite (mostly Dol A2), towards the last crystal generation, close to the cavities. This crystal size increase can be gradual or abrupt. The former case is more frequent. The contact between replacive and void-filling dolomites never corresponds to a reaction border.
The described crystal size distribution can thus be considered polymodal and allows the distinction of Dol B in two sub-phases. These are named dolomite B1 (Dol B1) and dolomite B2 (Dol B2) respectively (Fig. 7). The former develops from the contact with the replacive dolomite towards the cavities. The latter consists in the last crystal generation of Dol B (Plate 9, Phs. 1 and 2). Although Dol B1 and Dol B2 seem to represent only different growth stages of the same dolomite phase, they show some microscopic differences. For this reason Dol B1 and Dol B2 will be described separately.
Dol B1. The crystals of Dol B1 are medium to very coarse crystalline, non-planar to planar-s (sensu Sibley and Gregg 1987). They display undulose extinction of saddle dolomite. The crystals may be uniformly cloudy. Locally, they are cloudy in the inner part, whereas the peripheral part is limpid.
The dolomite veins which crosscut the replacive phases (Plate 3, Ph. 7) are filled with a medium to coarse crystalline, non-planar, saddle dolomite, which shares most microscopic features of Dol B1 (Plate 9, Ph. 3). The contact between replacive and vein dolomite is not sharp. In the veins, no crystal size variation is seen. The veins are locally connected with the zebra-sheets. In such cases, it is possible to trace the vein propagation into the zebra sheets without any obvious discontinuity.
Dol B1, both filling veins and cavities, has the same CL of the replacive dolomite phases.

Dol B2. The crystals of Dol B2 are coarse to very coarse crystalline and display planar-s textures (xenotopic-C texture after Gregg and Sibley 1984) and undulose extinction (Plate 9, Phs. 1 and 2). The crystal shape ranges through increasing face curvature from rhombohedral with straight boundaries, to symmetrical saddle forms. In the latter case the crystals also display curved cleavage traces.

The crystals have inclusion rich cores and clear, almost inclusion-free external rims (Plate 9, Ph. 4). Locally, a more complex concentric zonation has been observed, and the crystals exhibit a regular alternation of inclusion–rich and inclusion-free zones always parallel to the crystal borders (Plate 9, Ph. 5). In other cases the outermost part of the Dol B2 crystals consists of brownish hydroxides, likely goethite or limonite (Plate 9, Ph. 6). Less frequently the Dol B2 crystal terminations exhibit an alternation of dolomite and hydroxide zones (Plate 9, Ph. 7).

The terminations of Dol B2 crystals locally have a stepwise shape: adjacent segments of the same crystal are minimally offset (Plate 9, Phs. 6 and 7). These “reentrants” most commonly affect only the outermost part of the Dol B2 crystals.

Dol B2 is characterised by the same dull red CL as Dol B1 but shows a zonation pattern at the extremity of the crystals. The most common type of zonation consists of one darker red zone, parallel to the crystal growth planes. This zone frequently corresponds to an inclusion-free rim or to a hydroxide zone (Plate 10, Ph. 1).

The darker red CL of the Dol B2 crystal terminations is observed also in samples where the hydroxide zones are not developed (Plate 10, Ph. 2).

5.3 Microscopic features of the late calcite phases

As observed in Chapter 4 calcite cements may occur associated with dolomites (Plate 3, Phs. 5 and 6). They post-date the dolomites as they fill the cavities between two Dol B sheets. Transmitted light and CL microscopy permitted to distinguish two calcite types named Calcite 1 (Cal 1) and Calcite 2 (Cal 2).

5.3.1 Calcite 1

Cal 1 is a xenotopic blocky calcite. Crystal size ranges from coarse to very coarse. Compromise boundaries between adjacent crystals are common. Cal 1 is locally twinned and has a sharp extinction. No reaction borders are observed between this calcite and Dol B2 crystals (Plate 9, Phs. 2 and 4).

Cal 1 commonly displays an unzoned and bright orange CL (Plate 10, Phs. 1-2). Locally, it shows a concentric zonation consisting of orange zones of variable intensity (Plate 10, Ph. 3). This calcite

mainly fills the cavities lined by the Dol B but also fills tiny veins which propagate from the cavities through the dolomites (Plate 10, Ph. 3).

Minor sulphides, oxides and Cu-carbonates locally occur together with Cal 1 within the dolomite cavities (Plate 10, Phs. 4 and 5).

5.3.2 Calcite 2

Cal 2 is a coarse to very coarse crystalline, blocky and xenotopic calcite. The crystals are commonly not twinned and have a sharp extinction. Sulphides, oxides and Cu-carbonates are never seen together with this phase.

Under CL Cal 2 shows an intense concentric zonation, which consists of thick non-luminescent and very thin bright orange zones (Plate 11, Phs. 1 and 2).

At the contact between Cal 2 and Dol B2 reaction borders are observed and the dolomite crystal terminations appear corroded.

Chapter 6: Geochemical analyses

6.1 Results of staining

The dolomite samples treated with potassium ferricyanide staining solution for standard 40 seconds (Dickson 1966) did not show any coloration. Leaving the samples in the staining solution for other 2 minutes the terminations of Dol B2 crystals acquired a deeper blue colour relative to the other dolomite phases (Plate 11, Ph. 3).

Cal 1 and Cal 2 did not acquire any coloration when treated with the potassium ferricyanide staining solution, regardless of the time of reaction.

6.2 Results of XRD analyses

Most of the dolomite samples analysed to determine bulk mineralogy, stoichiometry and degree of order (OR) come from the Bodón Unit. They belong to the Alba, Barcaliente and Valdeteja Fms. and correspond to: 4 Dol A1, 18 Dol A2, and 13 Dol B. Since the Dol B sub-phases (Dol B1 and Dol B2) could not be separated without contamination, they were measured together. We will refer therefore to Dol B without any further specification. The results for mol % $CaCO_3$ and OR are reported in Appendix 2.

The X-ray patterns obtained for the different dolomites do not show remnants of the precursor limestone calcite. Among the non-carbonate phases, minor quartz, pyrite and hematite have been detected. Therefore, considering only the carbonate phases, the composition of the analysed samples approximates 100% dolomite.

All of the dolomite samples analysed for stoichiometry and OR exhibit sharp diffraction peaks.

The values of d_{104} are quite constant and range between 2,8827 and 2,8894 Å. These d_{104} values correspond to a Ca content between 48,9 and 51,1 mol % $CaCO_3$ (Figs. 8 and 9). The Ca content of most of the dolomite samples fall within the narrower range 48,9-50,1 mol % $CaCO_3$. Only two dolomite samples display higher Ca contents (Figs. 8 and 9). The OR varies between 0,54 to 1 with most of the samples having values in the range 0,75-1 (Figs. 8 and 9).

Neither the Ca content nor the OR follows a geographical trend, as samples from different localities plot in the same broad area (Fig. 8). The three dolomite phases analysed plot within overlapping fields and do not show any strong difference in stoichiometry nor in OR (Fig. 9), regardless of the microscopic differences underlined in Chapter 5.

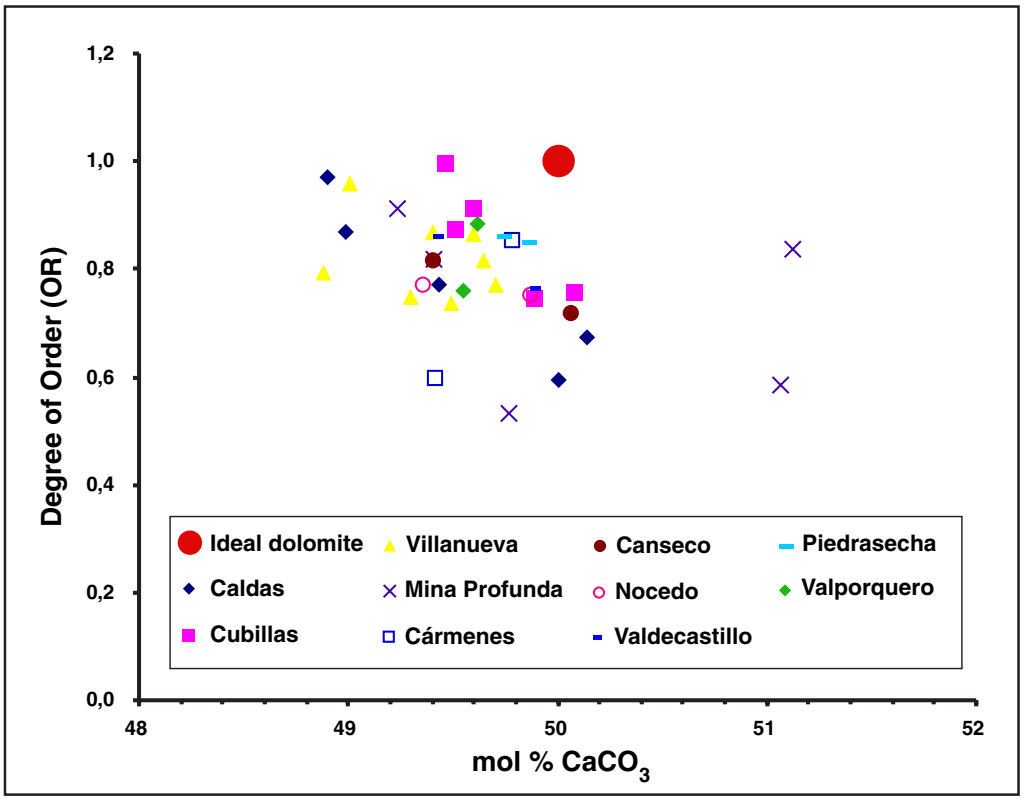

Fig. 8: XRD results for dolomite samples from different localities. Stoichiometry (as mol % $CaCO_3$) is plotted against the degree of order (OR). The composition of the "ideal" dolomite is also reported.

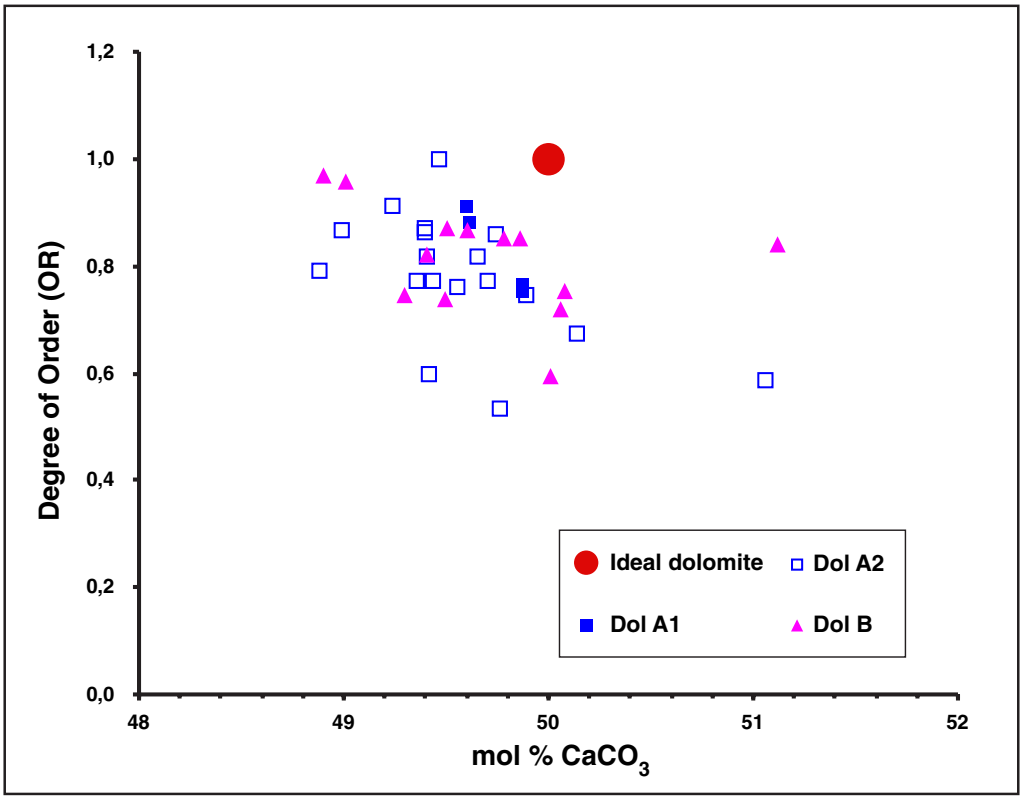

Fig. 9: The same plot as in Fig. 8 (stoichiometry versus ordering). The different dolomite phases (Dol A1, Dol A2 and Dol B) are differentiated.

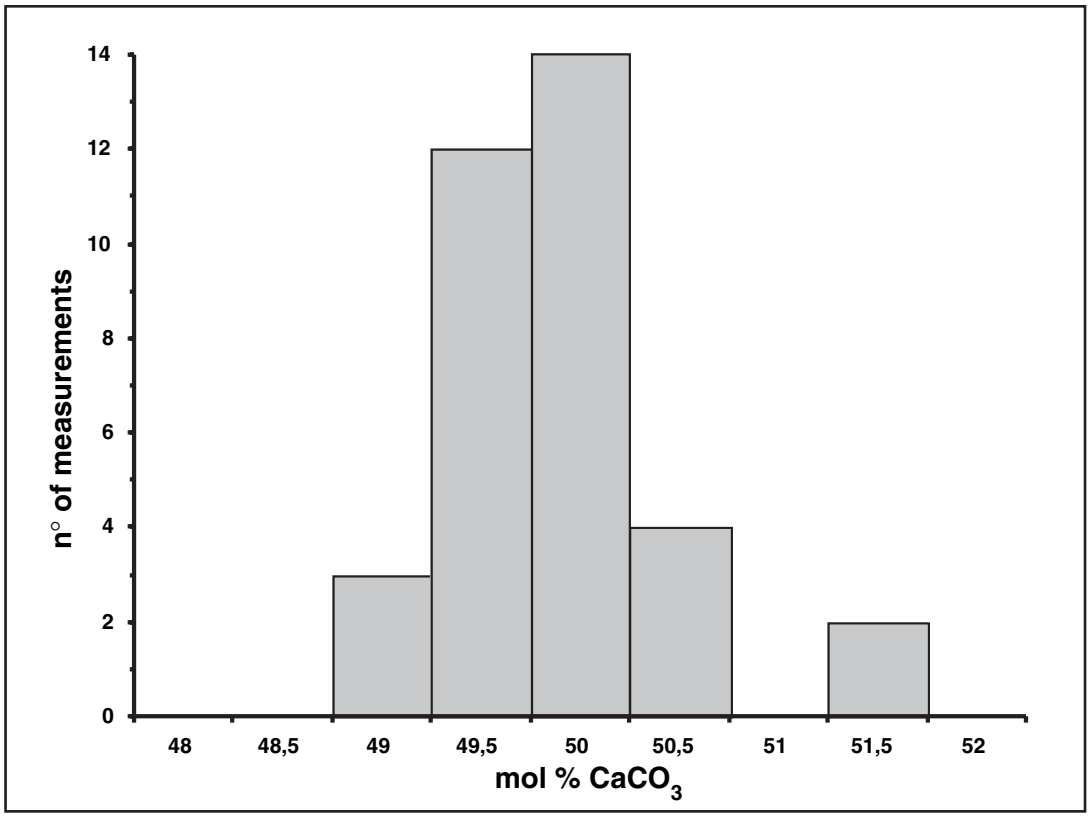

Fig. 10: Frequency histogram for mol % $CaCO_3$ based on analyses of both replacive and cement dolomites. Note the broad mode composition at 50 mol % $CaCO_3$.

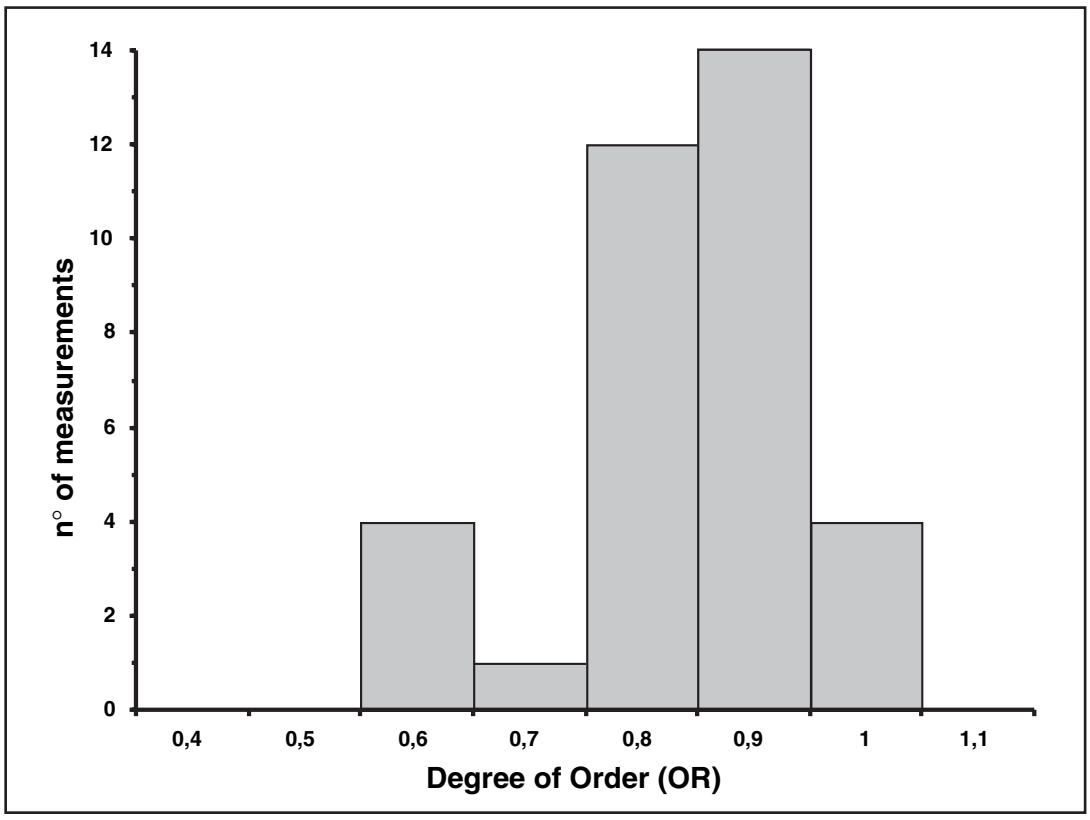

Fig. 11: Frequency histogram for OR based on analyses of both replacive and cement dolomites. A broad mode composition is observed at 0,9.

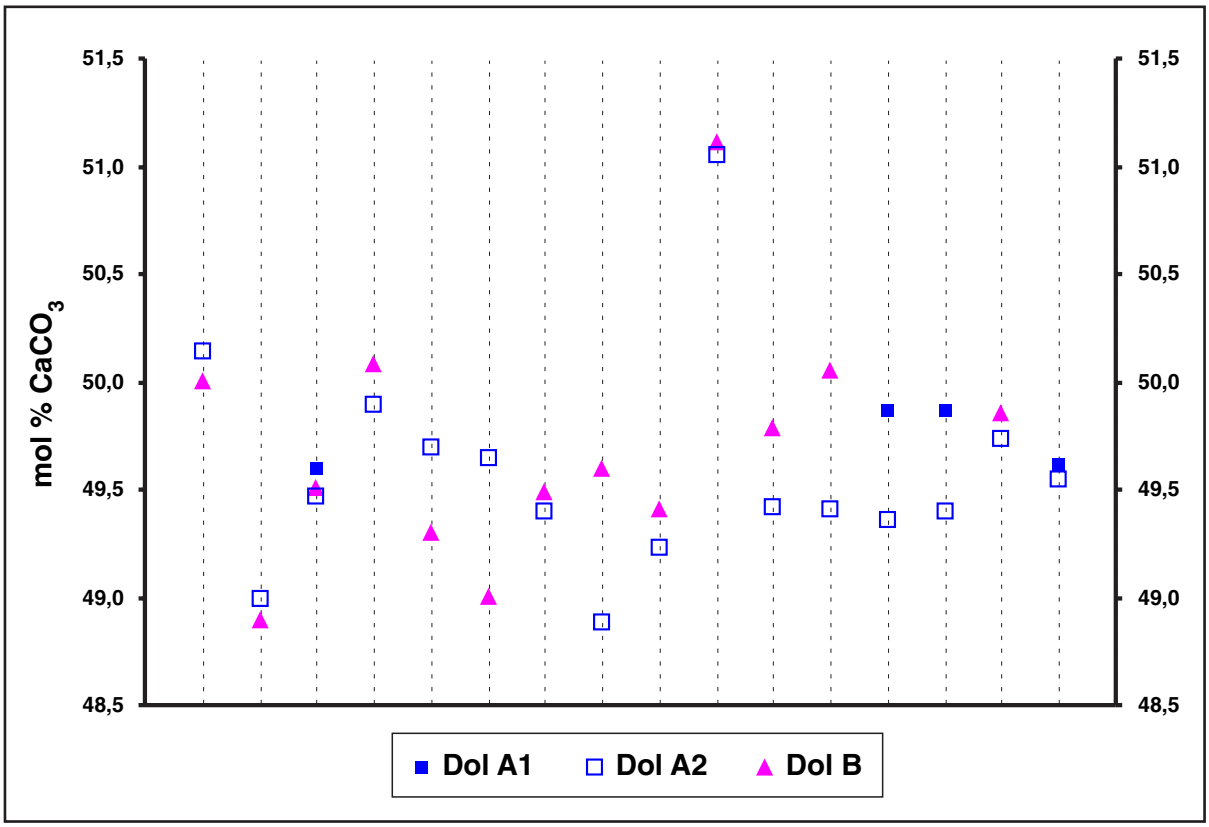

Fig. 12: Stoichiometry trend in single rock samples. Each vertical dashed line represents a rock sample and the dots on this line refer to the different dolomite phases in that sample.

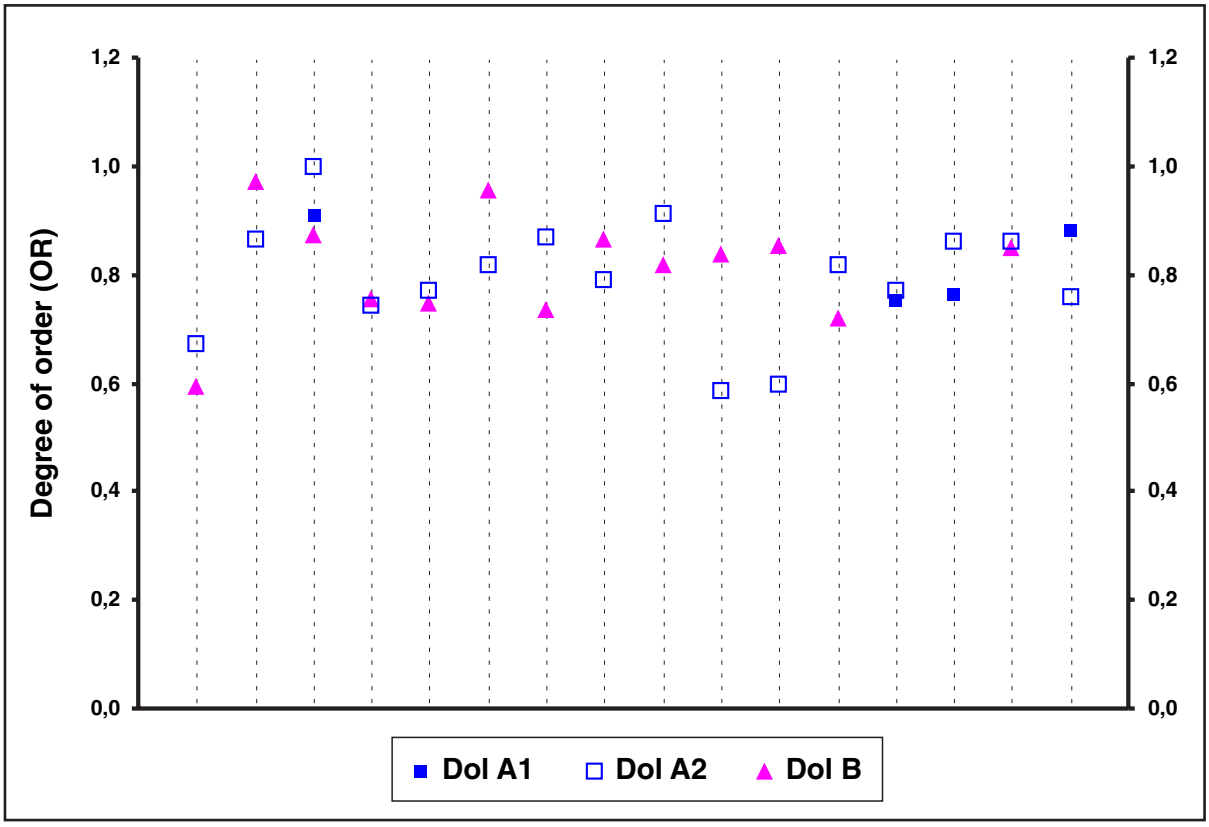

Fig. 13: Ordering trend in single rock samples. Each vertical dashed line represents a rock sample and the dots on this line refer to the different dolomite phases in that sample.

The frequency histogram for mol % $CaCO_3$ shows a normal distribution of data, with mode at about 50 mol % $CaCO_3$ (Fig. 10). The frequency histogram for the OR indicates a broad mode at about 0,9 (Fig. 11).

Ca content and OR of the different dolomite phases belonging to the same rock sample were also compared (Figs. 12 and 13). The Ca content of Dol A1 and Dol B, apart from two exceptions, is either very close or higher than the one of Dol A2 from the same rock sample (Fig. 12). On the other hand, no trend can be established for the OR, when comparing different dolomite phases from individual samples (Fig. 13).

6.3 Results of ICP-ES analyses

The samples analysed by means of ICP-ES belong mostly to the Bodón Unit and correspond to: 15 host limestones (H), 3 Dol A1, 16 Dol A2 and 14 Dol B. No separation could be accomplished between Dol B1 and Dol B2 sub-phases. All of the analysed samples (host limestones and dolomites) belong to the Barcaliente Fm. The results for Ca, Mg, Sr, Na, Fe and Mn are reported in Appendix 2. The statistic parameters of the concentrations of these elements in the different mineral phases are summarised in Table 1.

Phase		Ca (%)	Mg (%)	Sr (ppm)	Na (ppm)	Fe (ppm)	Mn (ppm)
Host (15)	min.	32.57	0.04	179	100	<100	8
	mean	36.95	0.23	598	227	847	81
	max.	39.95	0.45	950	400	3100	463
	Std. Dev.	2.42	0.11	257	103	871	114
Dol A1 (3)	min.	17.21	10.22	20	200	1400	222
	mean	19.04	10.44	26	267	2933	418
	max.	21.90	10.56	30	300	5200	716
	Std. Dev.	2.51	0.19	5	58	2003	263
Dol A2 (16)	min.	17.43	9.89	12	200	800	167
	mean	18.84	11.00	20	356	2069	354
	max.	20.61	12.25	41	500	6100	814
	Std. Dev.	0.87	0.57	7	121	1361	163
Dol B (14)	min.	17.48	10.16	12	100	600	213
	mean	19.25	10.81	24	300	2400	400
	max.	22.73	11.69	102	600	5500	901
	Std. Dev.	1.22	0.47	23	130	1542	187

Table 1: Elemental geochemistry from ICP-ES analyses. The statistic parameters of the concentrations of Ca, Mg, Sr, Na, Fe and Mn are reported for the different mineral phases analysed. In parenthesis is the number of measured samples. Min. = minimum value, mean = mean value, max. = maximum value, Std. Dev. = standard deviation.

Samples coming from different localities display similar contents of Ca, Mg, Sr, Na, Fe and Mn. Therefore, no geographical trend can be recognised in the elemental composition of the analysed mineral phases.

6.3.1 Strontium (Sr)

The Sr contents in the host limestones are quite variable and range between 179 and 950 ppm, with mean at 598 ppm.

The different dolomite phases have fairly consistent Sr concentrations. Dol A1 has Sr contents in the range 20-30 ppm. The mean content is 26 ppm. Dol A2 has Sr contents in the range 12-41 ppm. The mean value is 20 ppm. Dol B has Sr contents which vary between 12 and 102 ppm, with mean at 24 ppm. 95% of the analysed dolomite samples have Sr concentrations comprised between 12 and 30 ppm.

Sr contents of the different dolomite phases from the same rock sample were compared. When available, the Sr contents of the correspondent host limestones were reported as well (Fig. 14).

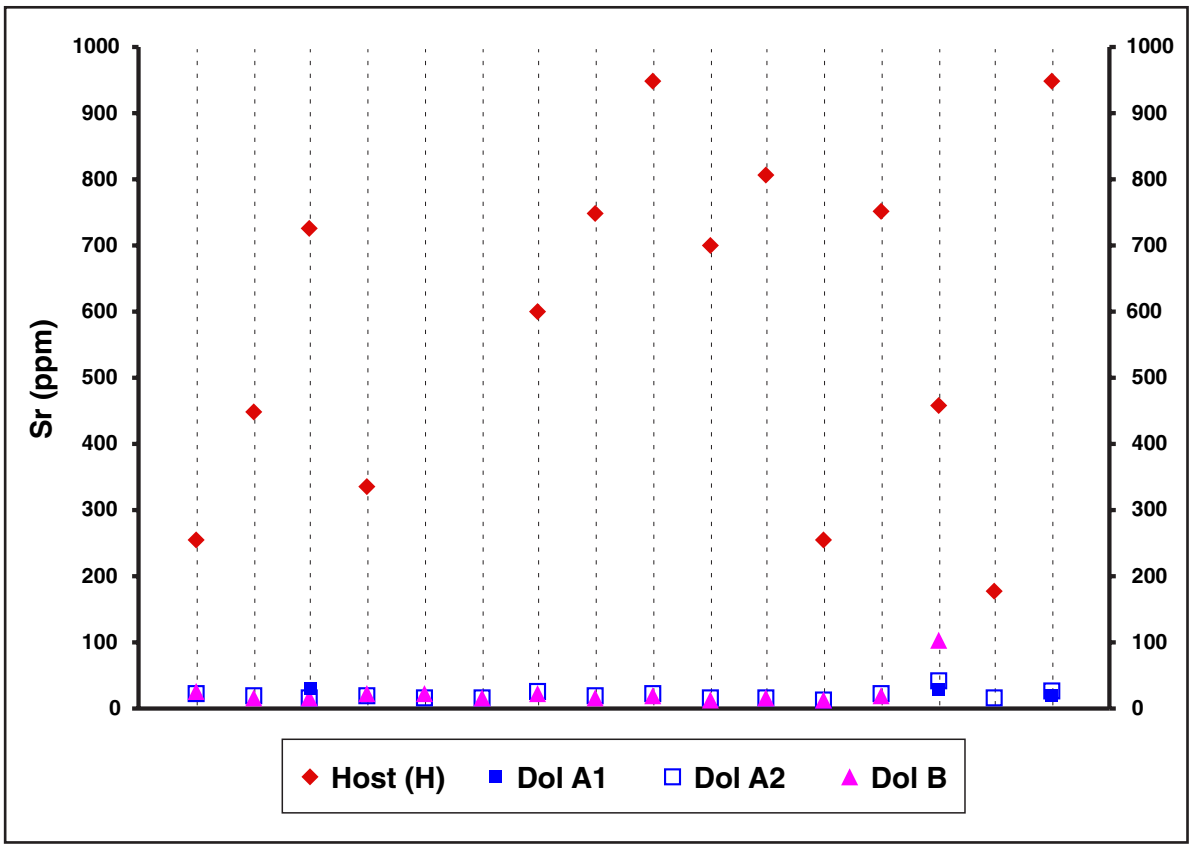

Fig. 14: The trend of Sr concentrations in single sampled sites. Sr contents of different dolomite phases from the same rock sample are plotted on the same vertical dashed line together with the Sr contents of the correspondent host limestone.

The different dolomite phases from the same rock sample have very similar Sr contents. It is evident that Dol A1, Dol A2 and Dol B are consistently depleted in Sr relative to the correspondent host limestones.

6.3.2 Sodium (Na)

The host limestones have Na contents in the range 100-400 ppm, with mean at 227 ppm.

Na concentrations of Dol A1, Dol A2 and Dol B samples are very similar and range between 200 and 600 ppm. The Na mean contents are respectively 267 ppm in Dol A1, 356 ppm in Dol A2, and 300 ppm in Dol B.

The Na contents of the different dolomite phases from the same rock sample were compared and reported relative to the Na contents of the correspondent host limestones (Fig. 15).

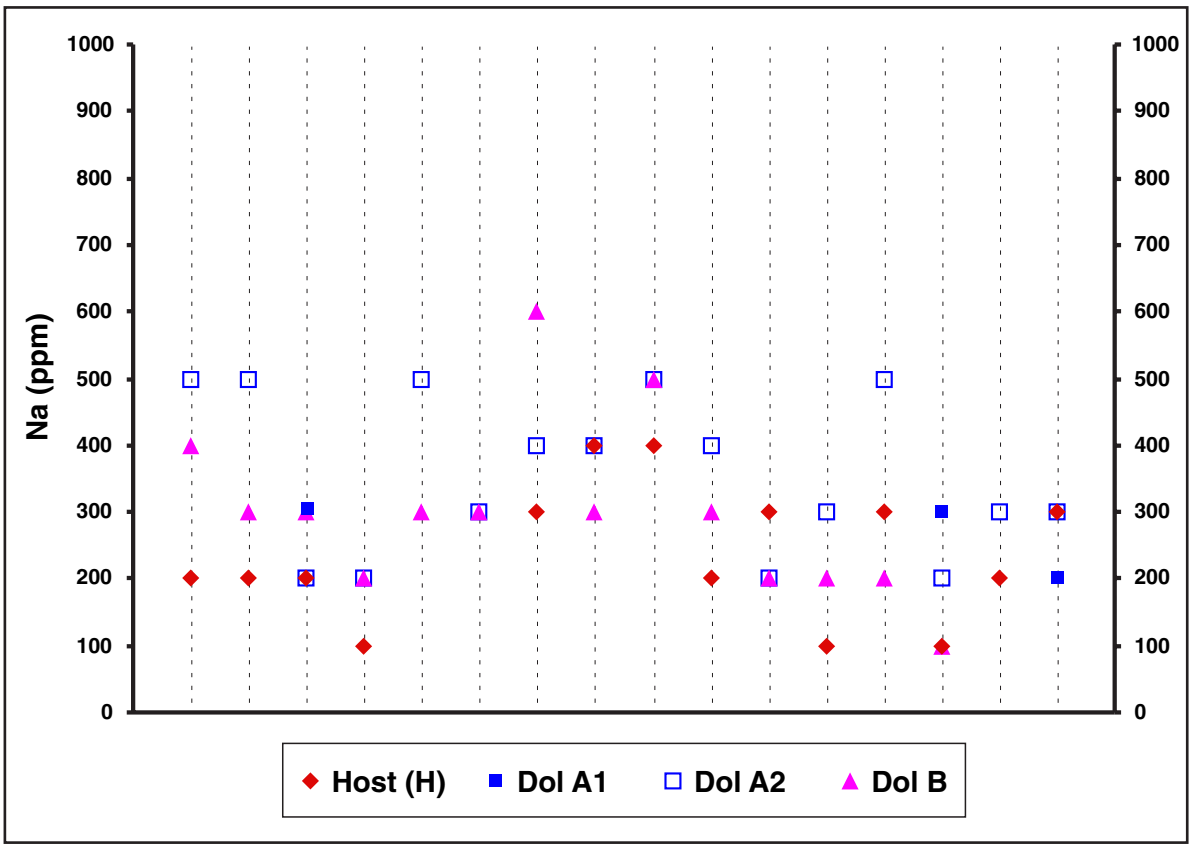

Fig. 15: The trend of Na concentrations in single sampled sites. Na contents of different dolomite phases from the same rock sample are plotted on the same vertical dashed line together with the Na contents of the correspondent host limestone.

The different dolomite phases from the same rock sample do not show any consistent trend in Na concentrations. The dolomites are either slightly enriched or depleted in Na, relative to the correspondent host limestones.

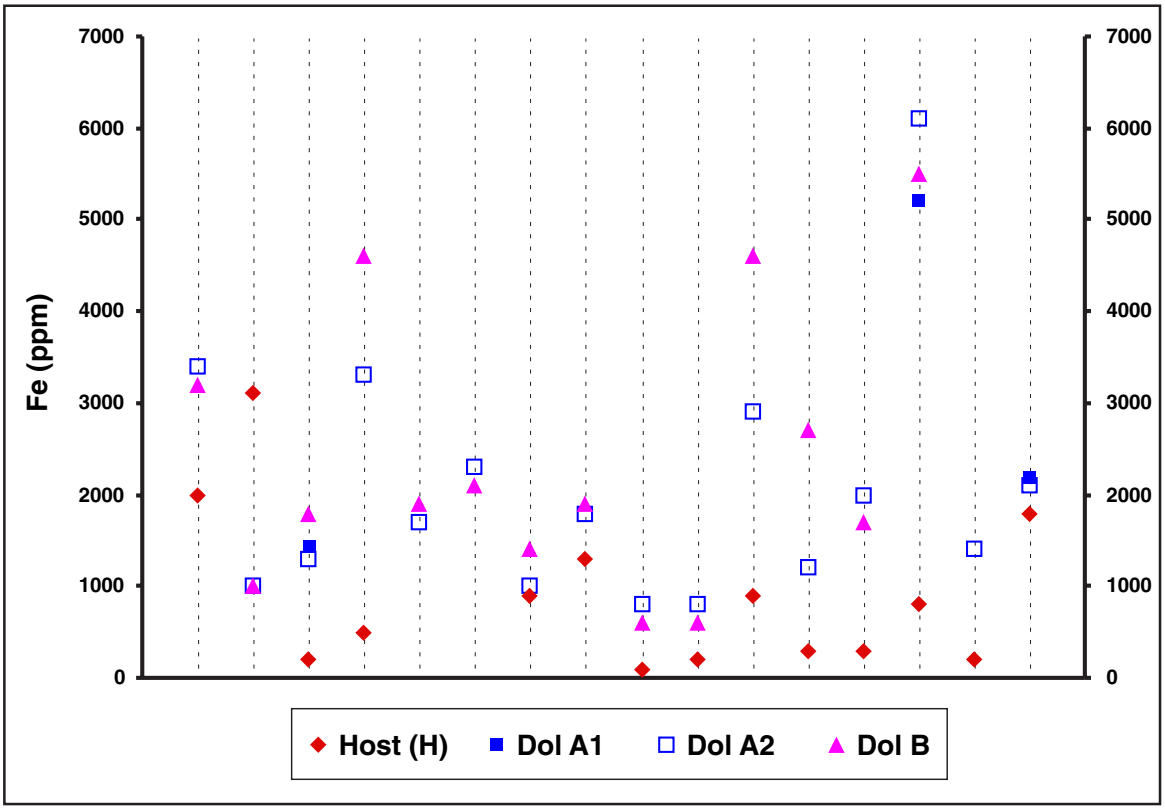

Fig. 16: The trend of Fe concentrations in single sampled sites. Fe contents of different dolomite phases from the same rock sample are plotted on the same vertical dashed line together with the Fe contents of the correspondent host limestone.

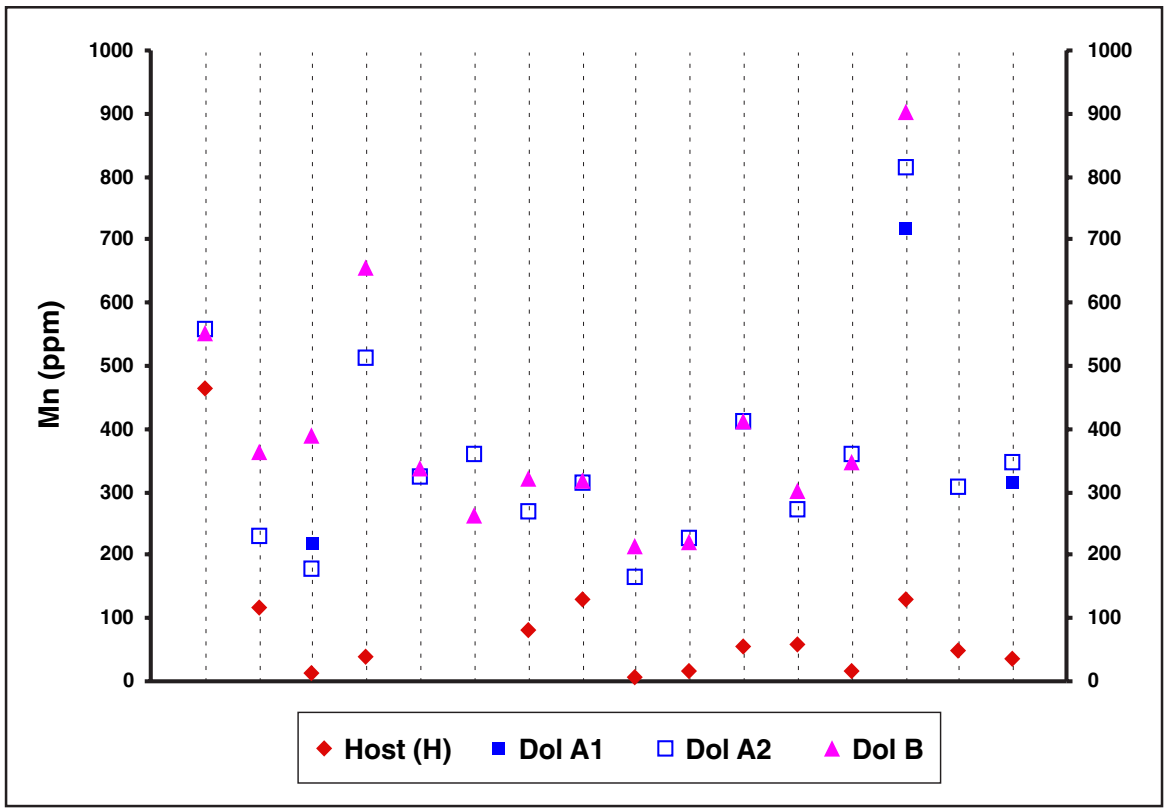

Fig. 17: The trend of Mn concentrations in single sampled sites. Mn contents of different dolomite phases from the same rock sample are plotted on the same vertical dashed line together with the Mn contents of the correspondent host limestone.

6.3.3 Iron (Fe) and Manganese (Mn)

The host limestones show variable concentrations of Fe and Mn. Fe varies between <100 and 3100 ppm (mean 847 ppm), whereas Mn varies between 8 and 463 ppm (mean 81 ppm).

Also Dol A1, Dol A2 and Dol B have variable Fe and Mn contents. The Fe mean contents are respectively 2933 ppm in Dol A1, 2069 ppm in Dol A2 and 2400 ppm in Dol B. The Mn mean contents are respectively 418 ppm in Dol A1, 354 ppm in Dol A2 and 400 ppm in Dol B. Therefore, all of the three dolomite phases display higher Fe and Mn mean contents relative to the host limestones.

Fe and Mn contents of the different dolomite phases from the same rock sample were compared and reported relative to the Fe and Mn contents of the correspondent host limestones. The different dolomite phases from the same rock sample do not show any consistent trend in the concentrations of these two elements (Figs. 16 and 17). On the other hand, both Fe and Mn contents consistently increase from the host limestones towards the correspondent dolomites (Figs. 16 and 17). Only one exception to this rule is reported in the trend of Fe (Fig. 16).

The dolomites exhibit a statistically significant positive covariation between Fe and Mn contents (Fig. 18). The degree of confidence (R^2) of the Fe-Mn covariation was calculated by means of linear interpolation of the data. R^2 is 0,99 for Dol A1, 0,96 for Dol A2 and 0,72 for Dol B.

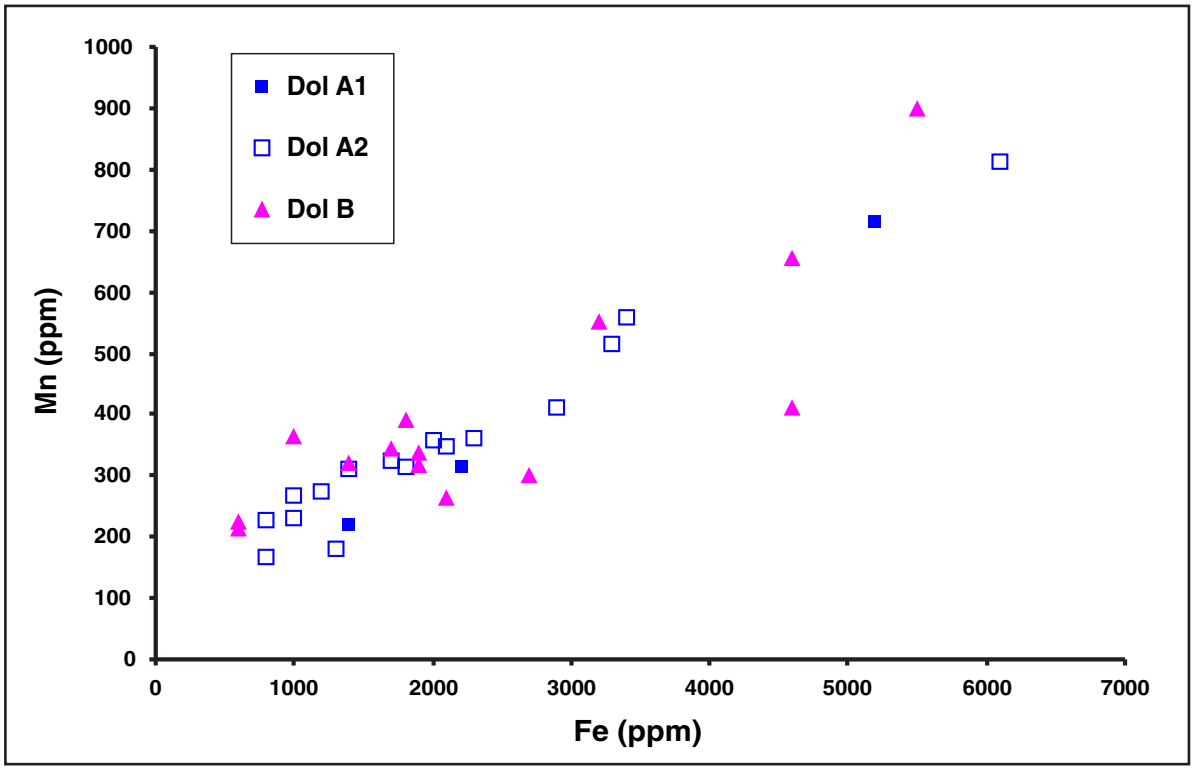

Fig. 18: Covariation between the Fe and Mn contents in the different dolomite phases. The degree of confidence (R^2) is 0,99 for Dol A1, 0,96 for Dol A2 and 0,72 for Dol B.

6.4 Results of O and C stable isotope analyses

Most of the samples analysed for $^{18}O/^{16}O$ and $^{13}C/^{12}C$ ratios were collected in the Bodón Unit. The samples belong to the Alba, Barcaliente and Valdeteja Fms. and correspond to: 32 host limestones (H), 9 calcite veins (CV), 10 Dol A1, 37 Dol A2, 30 Dol B, 9 Cal 1 and 11 Cal 2. No separation was made between Dol B1 and Dol B2 sub-phases. The results are reported in per mil (‰) relative to the PDB standard in Appendix 2. The statistic parameters of $\delta^{18}O$ and $\delta^{13}C$ for the different mineral phases are listed in Table 2. In Fig. 19 the mean values of $\delta^{18}O$ and $\delta^{13}C$ for the different analysed phases are plotted, together with the standard deviation range ($\pm 1\sigma$).

Phase		$\delta^{18}O$	$\delta^{13}C$
Host (32)	min.	-7.7	3.1
	mean	-2.1	4.3
	max.	2.1	5.3
	Std. Dev.	2.5	0.6
CV (9)	min.	-14.8	2.1
	mean	-9.2	3.4
	max.	-6.4	4.5
	Std. Dev.	2.7	0.8
Dol A1 (10)	min.	-10.5	3.5
	mean	-5.8	4.6
	max.	-3.0	5.3
	Std. Dev.	2.1	0.6
Dol A2 (37)	min.	-11.9	1.9
	mean	-7.0	4.2
	max.	-3.0	5.4
	Std. Dev.	2.1	0.7
Dol B (30)	min.	-12.0	1.7
	mean	-7.7	3.8
	max.	-4.2	5.3
	Std. Dev.	1.9	0.9
Cal 1 (9)	min.	-15.4	-2.6
	mean	-11.2	0.6
	max.	-8.1	2.5
	Std. Dev.	2.8	1.6
Cal 2 (11)	min.	-13.5	-7.9
	mean	-9.8	-4.6
	max.	-6.8	-1.8
	Std. Dev.	2.3	2.2

Table 2: O and C isotope geochemistry. The statistic parameters of $\delta^{18}O$ and $\delta^{13}C$ (‰ PDB) are reported for the different mineral phases analysed. In parenthesis is the number of measured samples. Min. = minimum value, mean = mean value, max. = maximum value, Std. Dev. = standard deviation.

No systematic variation of the O and C isotope ratios was observed for the different phases relative to the geographic location of the samples.

The host limestones (H) show $\delta^{18}O$ values which vary between –7,7 and 2,1‰. The mean value is –2,1‰. The $\delta^{13}C$ values for the host limestones are always positive and range between 3,1 and 5,3‰. The mean value is 4,3‰.

The calcite veins (CV) show widespread $\delta^{18}O$ values in the range –14,8 to -6,4‰, with mean at –9,2‰. $\delta^{13}C$ values are less variable. They range from 2,1 to 4,5‰, with mean at 3,4‰. All of the analysed CV samples have lower $\delta^{18}O$ values than the corresponding host limestones. On the other hand, only a slight depletion in ^{13}C is observed in the CV relative to the corresponding hosts.

The $\delta^{18}O$ values for Dol A1 range between –10,5 and –3,0‰, with mean at –5,8‰. The $\delta^{13}C$ values vary between 3,5 and 5,3‰, with mean at 4,6‰. The $\delta^{18}O$ values for Dol A2

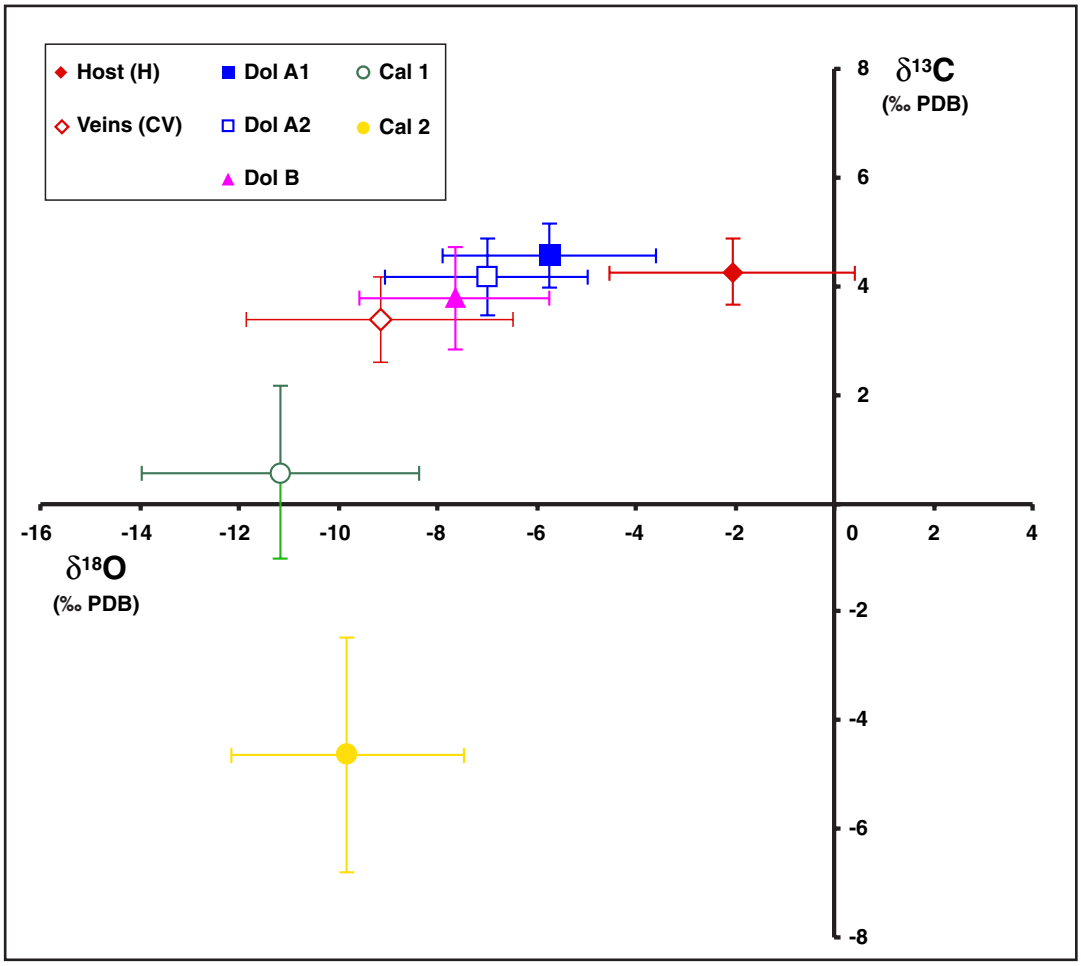

Fig. 19: O and C isotope composition of the different carbonate phases analysed. For each phase the mean values of $\delta^{18}O$ and $\delta^{13}C$ are reported, together with the standard deviation range ($\pm 1\sigma$).

range between –11,9 and –3,0‰, with mean at –6,9‰. The $\delta^{13}C$ values are comprised between 1,9 and 5,4‰, with mean at 4,2‰. The $\delta^{18}O$ values for Dol B range between –12,0 and –4,2‰, with mean at –7,7‰. The $\delta^{13}C$ values vary between 1,7 and 5,3‰ with mean at 3,8‰.

The different dolomite phases have therefore $\delta^{18}O$ and $\delta^{13}C$ values which cluster in the same broad area. The latter is characterised by a large spread in the $\delta^{18}O$ values and quite consistent $\delta^{13}C$ values. The $\delta^{18}O$ values for the different dolomites are distinctly more negative than those of the host limestones, whereas the $\delta^{13}C$ values are very similar (Fig. 19).

The $\delta^{18}O$ and $\delta^{13}C$ values of different dolomite phases from the same rock sample were compared and reported relative to those of the correspondent host limestones (Figs. 20 and 21).

A trend towards more negative $\delta^{18}O$ values is observed from the limestones towards the correspondent dolomites (Fig. 20). No consistent trend is observed in the $\delta^{13}C$ values as the dolomites are either slightly enriched or slightly depleted in ^{13}C relative to the hosts (Fig. 21).

$\delta^{18}O$ and $\delta^{13}C$ values of Dol A1 and Dol A2 from the same rock sample either overlap or are very similar. Dol B is in most cases depleted in ^{18}O relative to the replacive dolomites of the same

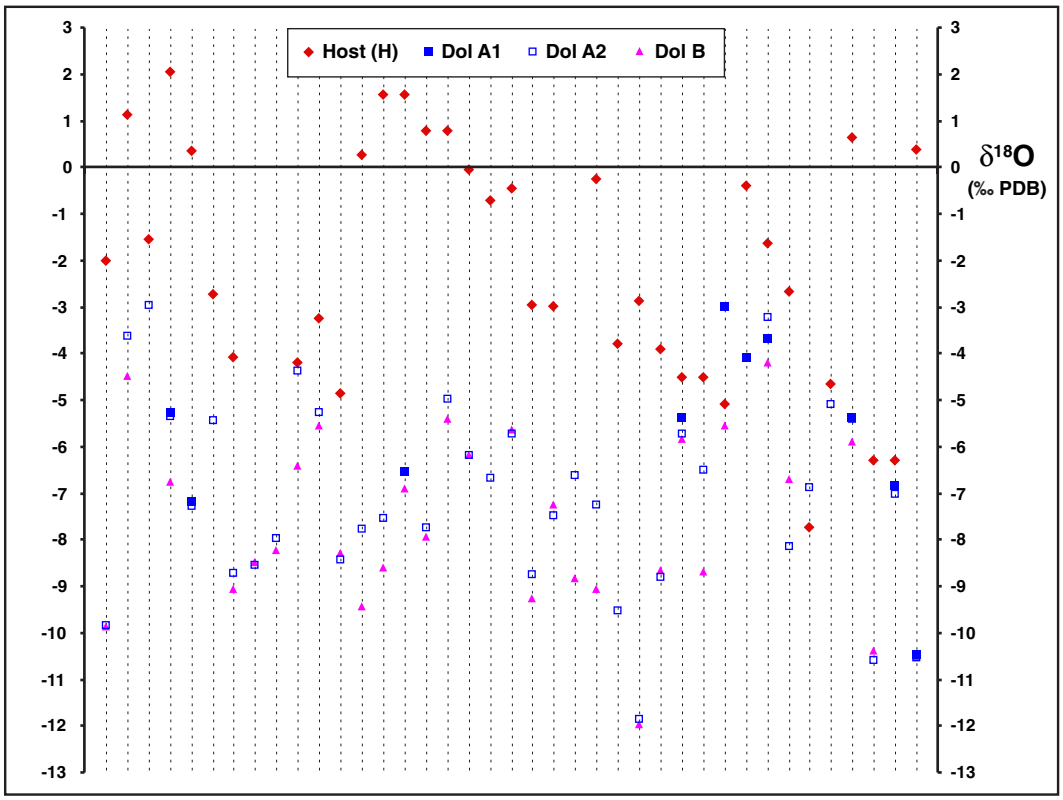

Fig. 20: The trend of O isotope composition in single sampled sites. $\delta^{18}O$ values of different dolomite phases from the same rock sample are plotted on the same vertical dashed line together with the $\delta^{18}O$ value of the correspondent host limestone.

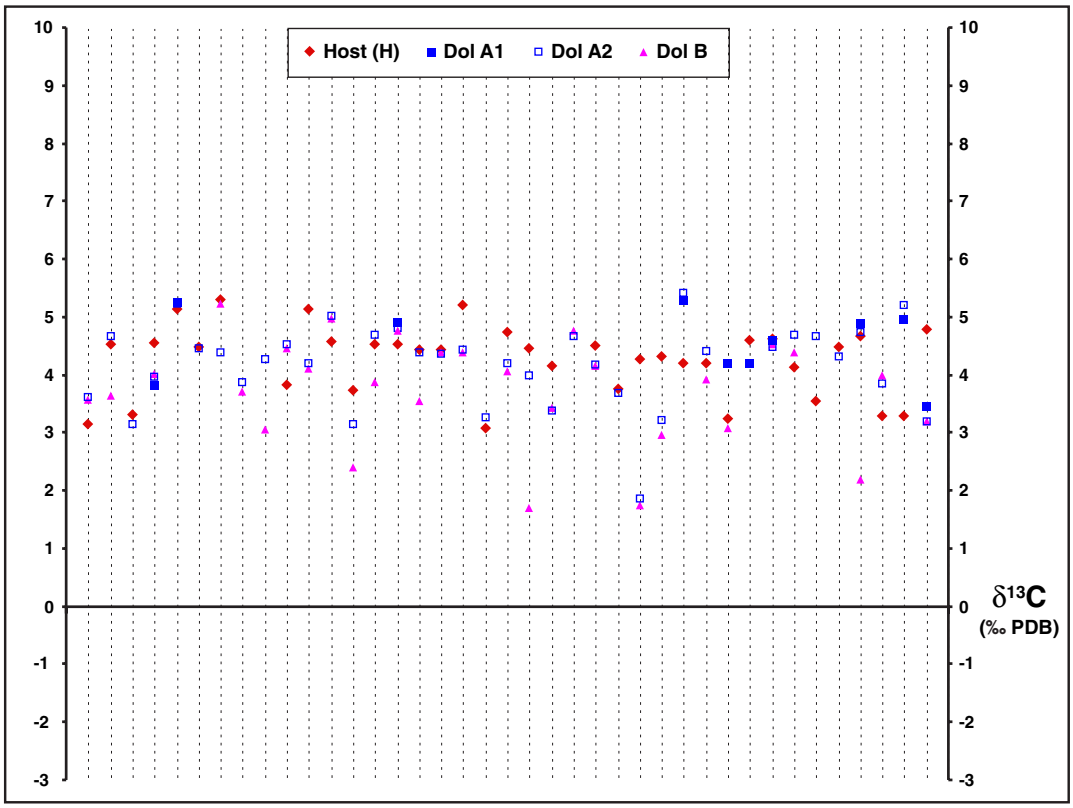

Fig. 21: The trend of C isotope composition in single sampled sites. $\delta^{13}C$ values of different dolomite phases from the same rock sample are plotted on the same vertical dashed line together with the $\delta^{13}C$ value of the correspondent host limestone.

rock sample. Only five exceptions to this rule are reported (Fig. 20). No trend in the $\delta^{13}C$ values is observed when comparing Dol B to the replacive dolomites of the same rock sample (Fig. 21).

Samples of Cal 1 have negative $\delta^{18}O$ values falling between –15,4 and –8,1‰. The mean value is –11,2‰. The $\delta^{13}C$ values vary between –2,6 and 2,5‰, with mean value at 0,6‰ (Fig. 19).

Samples of Cal 2 have negative $\delta^{18}O$ values, which range from –13,5 to –6,8‰, with mean at –9,8‰. The $\delta^{13}C$ values are always negative and range between –7,9 and –1,8‰, with mean at –4,6‰ (Fig. 19).

Therefore, the main feature of Cal 1 and Cal 2 is a significant depletion in ^{18}O and ^{13}C relative to the other considered carbonate phases. In particular, Cal 1 has the most negative $\delta^{18}O$ values, whereas Cal 2 has the most negative $\delta^{13}C$ values.

6.5 Results of Sr isotope analyses

Sr isotope analyses were performed on samples from the Bodón Unit. All of the analysed samples (host limestones and diagenetic phases) belong to the Barcaliente Fm. and correspond to: 4 host limestones (H), 1 Dol A1, 4 Dol A2, 4 Dol B, 2 Cal 1 and 1 Cal 2. No separation was made between Dol B1 and Dol B2 sub-phases.

The results are reported as $^{87}Sr/^{86}Sr$ ratios in Appendix 2. The statistic parameters of $^{87}Sr/^{86}Sr$ ratios in the different mineral phases analysed are listed in Table 3.

The host limestones have very consistent $^{87}Sr/^{86}Sr$ ratios comprised between 0,708082 and 0,708147, with mean at 0,708118.

The $^{87}Sr/^{86}Sr$ ratio for one sample of Dol A1 is 0,708910. The samples of Dol A2 have $^{87}Sr/^{86}Sr$ ratios between 0,708397 and 0,709207, with mean at 0,708734. $^{87}Sr/^{86}Sr$ ratios for Dol B samples range between 0,708458 and 0,708841, with mean at 0,708841. The different dolomite phases have therefore $^{87}Sr/^{86}Sr$ mean values slightly higher than those of the host limestones. This

Phase		$^{87}Sr/^{86}Sr$
Host (4)	min.	0.708082
	mean	0.708118
	max.	0.708147
	Std. Dev.	0.000030
Dol A1 (1)		0.708910
Dol A2 (4)	min.	0.708397
	mean	0.708734
	max.	0.709207
	Std. Dev.	0.000340
Dol B (4)	min.	0.708458
	mean	0.708841
	max.	0.708841
	Std. Dev.	0.000384
Cal 1 (2)	min.	0.708502
	mean	0.708620
	max.	0.708738
	Std. Dev.	0.000167
Cal 2 (1)		0.708416

Table 3: Sr isotope geochemistry. The statistic parameters of $^{87}Sr/^{86}Sr$ ratios are reported for the different mineral phases analysed. In parenthesis is the number of measured samples. Min. = minimum value, mean = mean value, max. = maximum value, Std. Dev. = standard deviation.

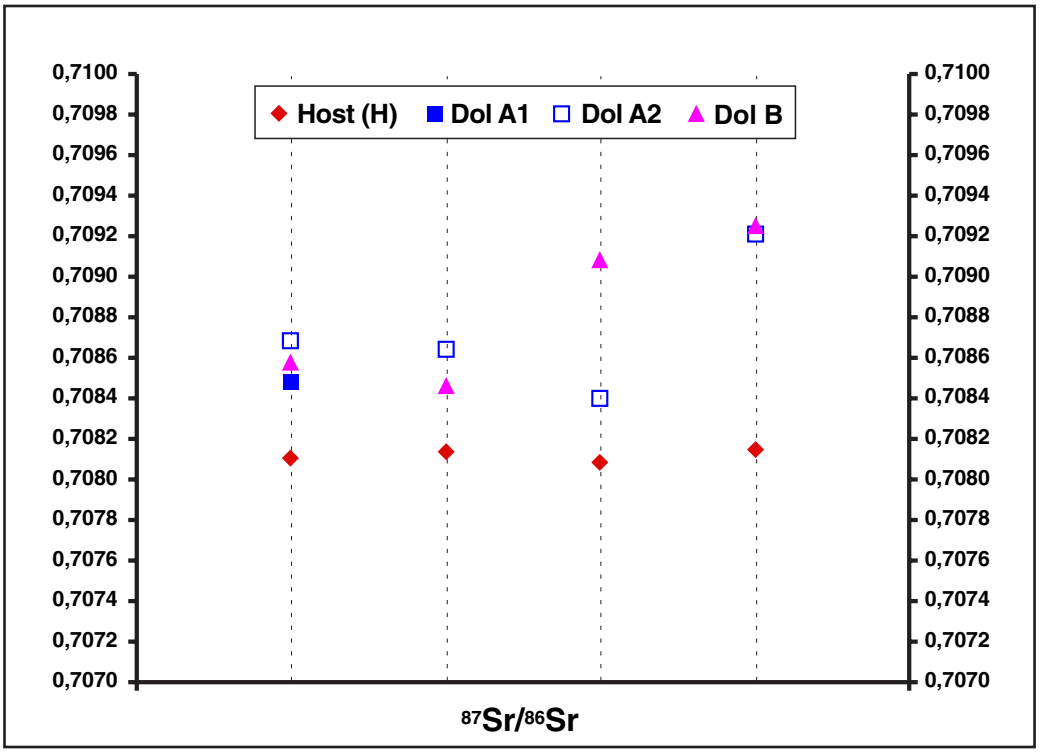

Fig. 22: The trend of Sr isotope composition in single sampled sites. $^{87}Sr/^{86}Sr$ ratios of different dolomite phases from the same rock sample are plotted on the same vertical dashed line, together with the $^{87}Sr/^{86}Sr$ ratios of the correspondent host limestone.

trend towards higher ratios is also evident when comparing dolomites from the same rock sample with the correspondent host limestones (Fig. 22). The dolomites always display an increase in $^{87}Sr/^{86}Sr$ relative to the host limestones by 0,0003 to 0,0011. Dol A1, Dol A2 and Dol B from the same rock sample mostly have similar $^{87}Sr/^{86}Sr$ ratios. Only in one sample Dol B has distinctly higher Sr isotope ratio than Dol A2 (Fig. 22). Therefore, the different dolomite phases from the same rock sample do not show any consistent trend in the $^{87}Sr/^{86}Sr$ ratios.

The two samples of Cal 1 display consistent $^{87}Sr/^{86}Sr$ ratios with mean of 0,708620. The $^{87}Sr/^{86}Sr$ ratio for one sample of Cal 2 is 0,708416. Both Cal 1 and Cal 2 have therefore Sr isotope ratios slightly higher than those of the host limestones. These values fall within the range of ratios reported for the dolomites.

The dolomite phases do not show any evident grouping in the plot Sr contents versus $^{87}Sr/^{86}Sr$ ratios (Fig. 23). The slight enrichment in ^{87}Sr in the various dolomite phases relative to the host limestones is accompanied by a larger depletion in Sr contents.

The plots $\delta^{18}O$ versus $^{87}Sr/^{86}Sr$ and $\delta^{13}C$ versus $^{87}Sr/^{86}Sr$ (Figs. 24 and 25) do not display any significant grouping between the different dolomite phases. Inverse covariation between $\delta^{18}O$ and $^{87}Sr/^{86}Sr$ values from the host limestones towards the diagenetic phases (both dolomites and calcites) is observed (Fig. 24). No covariation is seen between $\delta^{13}C$ and $^{87}Sr/^{86}Sr$ values from the host limestones towards the dolomites (Fig. 25). On the contrary, inverse covariation between $\delta^{13}C$ and $^{87}Sr/^{86}Sr$ values is observed from the host limestones towards the calcites (Fig. 25).

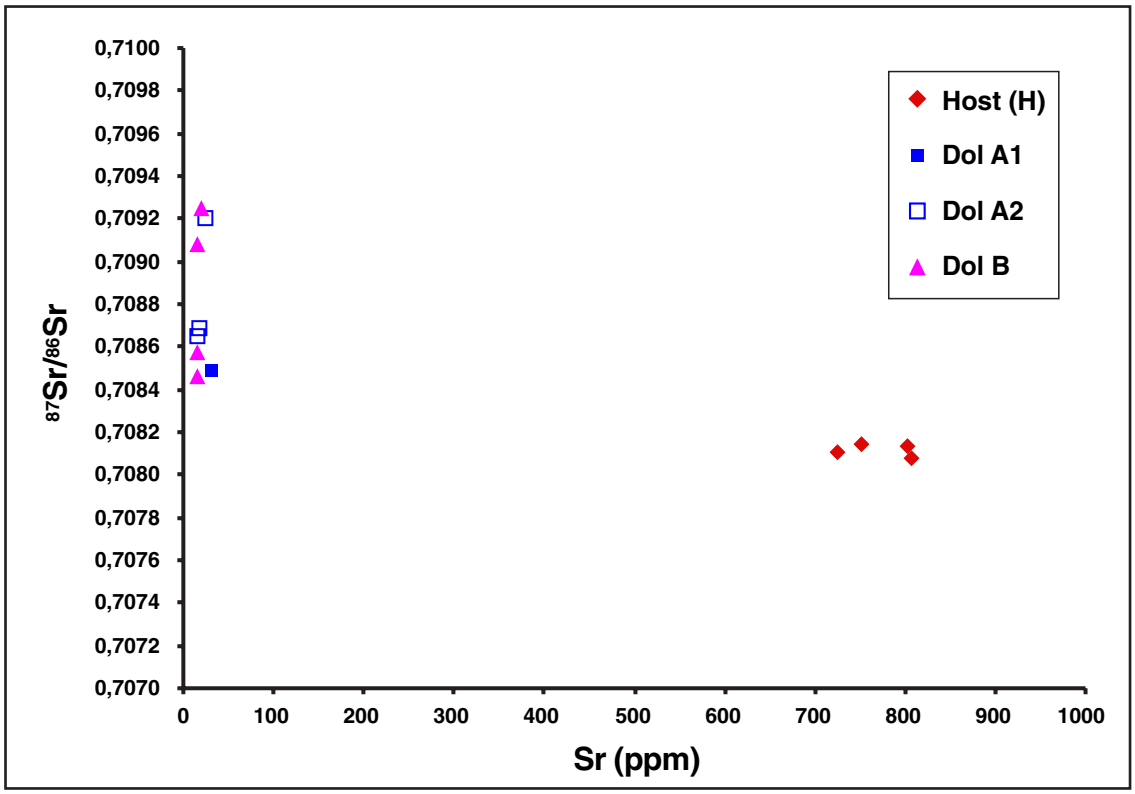

Fig. 23: Covariation plot between Sr contents and $^{87}Sr/^{86}Sr$ ratios for host limestones and dolomites.

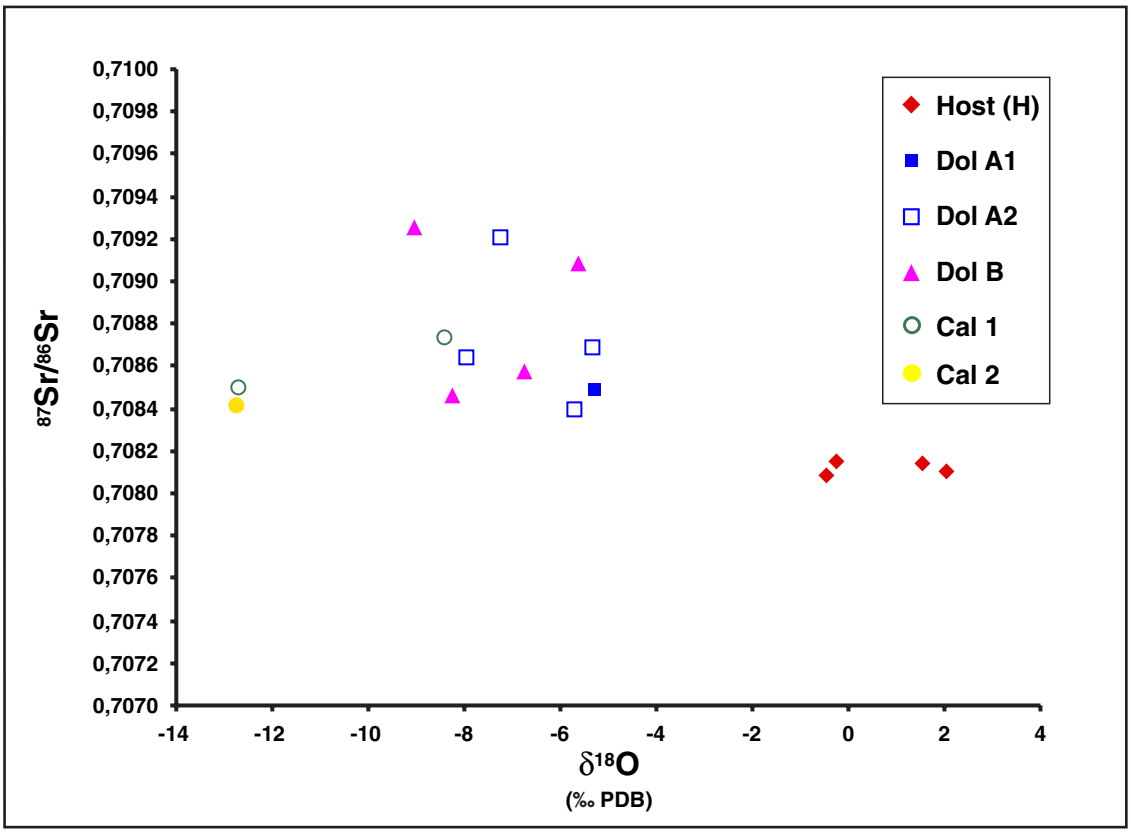

Fig. 24: Covariation plot between $\delta^{18}O$ and $^{87}Sr/^{86}Sr$ ratios for the studied mineral phases.

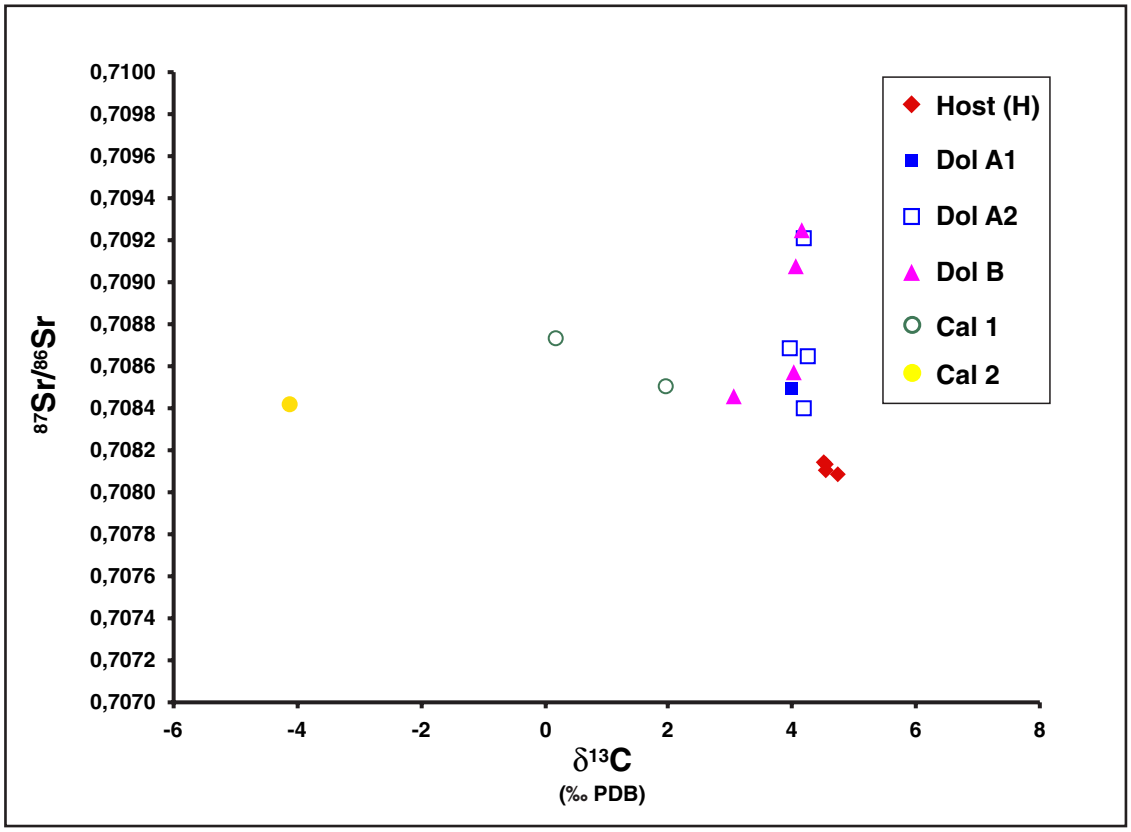

Fig. 25: Covariation plot between $\delta^{13}C$ and $^{87}Sr/^{86}Sr$ ratios for the studied mineral phases.

Chapter 7: Fluid Inclusion (FI) study

7.1 FI petrography

A detailed petrographic study of the previously described mineral phases (see Chapter 5) revealed the presence of many different types of primary and secondary FIs, which are described in the following paragraphs. A sketch illustrating the spatial distribution of the FIs in the different mineral phases is given in Fig. 26. The petrographic features of the main types of FIs are summarised in Table 4.

7.1.1 FIs in the calcite veins (CV)

In most of the examined samples the vein calcites do not contain FIs. In few instances small FIs (<1 μm) were observed along trails, suggesting that they are secondary in origin (Fig. 26A). Neither phase description, nor microthermometric measurements could be accomplished.

7.1.2 FIs in Dol A1

The Dol A1 crystals display a uniform cloudiness due to the presence of small (<1 μm) and possibly primary FIs (Fig. 26B). These are densely distributed throughout individual crystals. The darkness of the crystals and the small size of the FIs prevented any further characterisation. FIs suitable for microthermometric measurements were not found.

7.1.3 FIs in Dol A2

FIs in Dol A2 are densely distributed in three dimensions and are mainly concentrated in the crystal cores (Fig. 26C). This is the most common occurrence of primary FIs in dolomite (Goldstein and Reynolds 1994). The FIs (type I) are up to 5 μm in length and have an irregular shape (Plate 12, Ph. 1). Alternatively, they have negative crystal shape and mimic the crystallographic directions of the host crystal (Plate 12, Ph. 2). Type I FIs are 2-phase, liquid-rich (Fig. 26C). The degree of fill (F) ranges between 0,83 and 0,94.

Less commonly, primary, 1-phase, all liquid FIs (type II) are observed. They coexist together with type I FIs (Plate 12, Ph. 2). Type I and type II FIs have similar size and shape.

7.1.4 FIs in Dol B

Dol B commonly host FIs (Type III) uniformly distributed in the crystals. Locally, the crystals have inclusion-rich cores and clear inclusion-free rims (Plate 12, Ph. 3). The larger FIs (up to 15 μm)

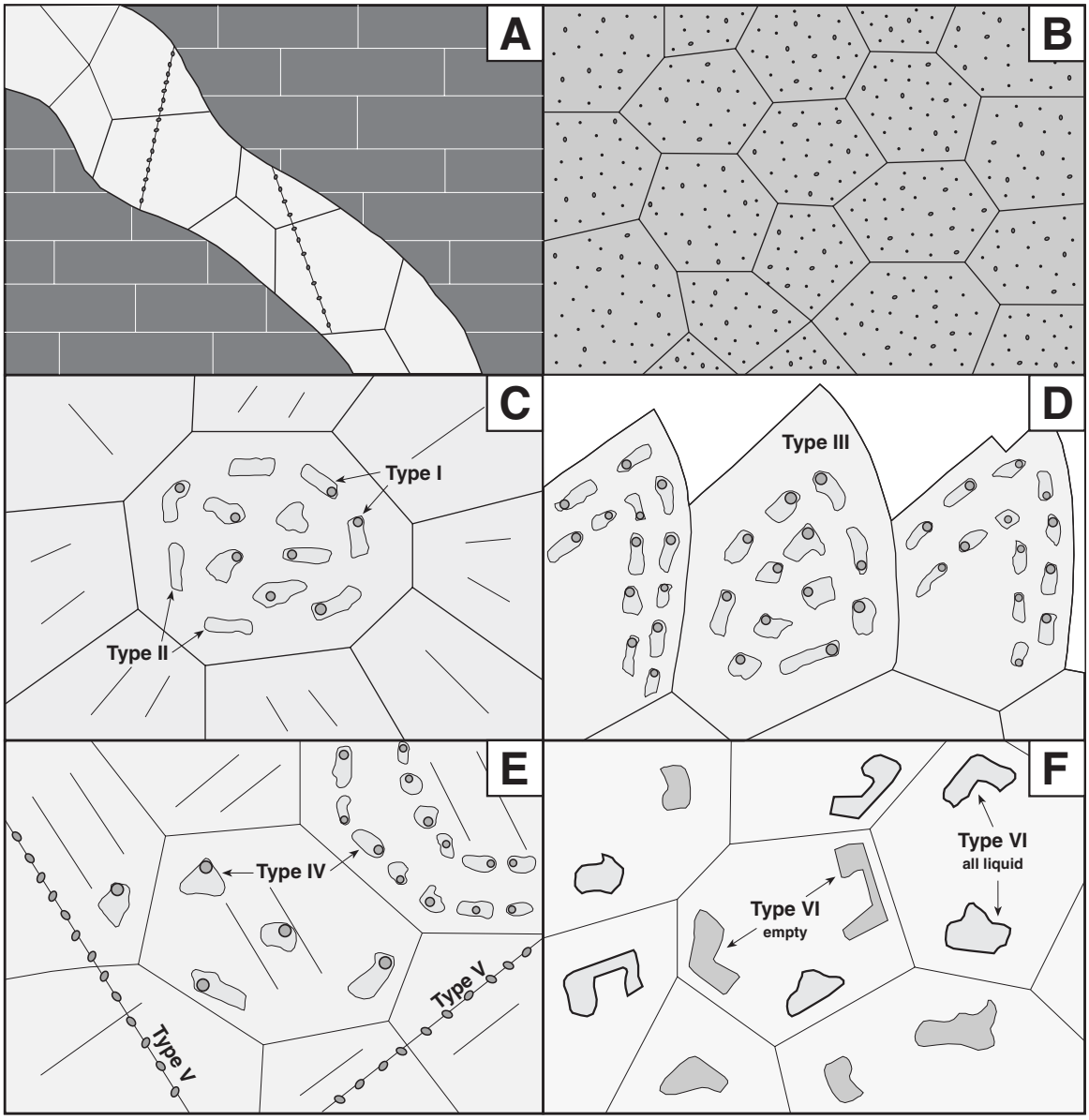

Fig. 26: Sketch illustrating the location and distribution of the different FIs in the studied mineral phases. The scale is arbitrary. **A.** FIs in CV. **B.** FIs in Dol A1. **C.** FIs in Dol A2. **D.** FIs in Dol B2. **E.** FIs in Cal 1. **F.** FIs in Cal 2.

are located in the last crystal generation of Dol B (the so-called Dol B2). These are preferentially grouped in the crystal cores or along crystal growth zones (Fig. 26D). Type III FIs have an irregular to lobate shape and are 2-phase, liquid-rich (Plate 12, Ph. 4). F ranges between 0,78 and 0,97.

7.1.5 FIs in Cal 1

Cal 1 is characterised by abundant FIs (type IV) mostly confined by growth-zone boundaries (Plate 12, Ph. 5). They also occur isolated or grouped in clusters (Fig. 26E) and are primary in origin. Type IV FIs are up to 20 µm in length and are spheroidal to oblate in shape (Plate 12, Ph. 6). They are 2-phases, liquid-rich. F ranges between 0,85 and 0,97.

Secondary FIs (type V) are less frequently observed (Fig. 26E). They are located along trails and sealed fractures, especially in those crystals which are heavily twinned. They are less than 2 µm in length, 1-phase all liquid and spheroidal in shape. Type V FIs were not considered in the present study.

7.1.6 FIs in Cal 2

FIs in Cal 2 (type VI) are isolated and do not occur along growth zones or along trails (Fig. 26F). Type VI FIs are 1-phase, all liquid, but they frequently appear empty. They mostly have an irregular shape (Plate 12, Ph. 7), but negative crystal shapes are also common. In the latter case FI walls are crystallographically controlled (Plate 12, Ph. 8). Type VI FIs are possibly primary and up to 30 µm in length.

7.2 Identification of the fluid system

The FIs described in the previous paragraph do not emit fluorescence under UV light, indicating absence of oil (e.g. Shepherd et al. 1985). This suggests an aqueous composition for the FIs.

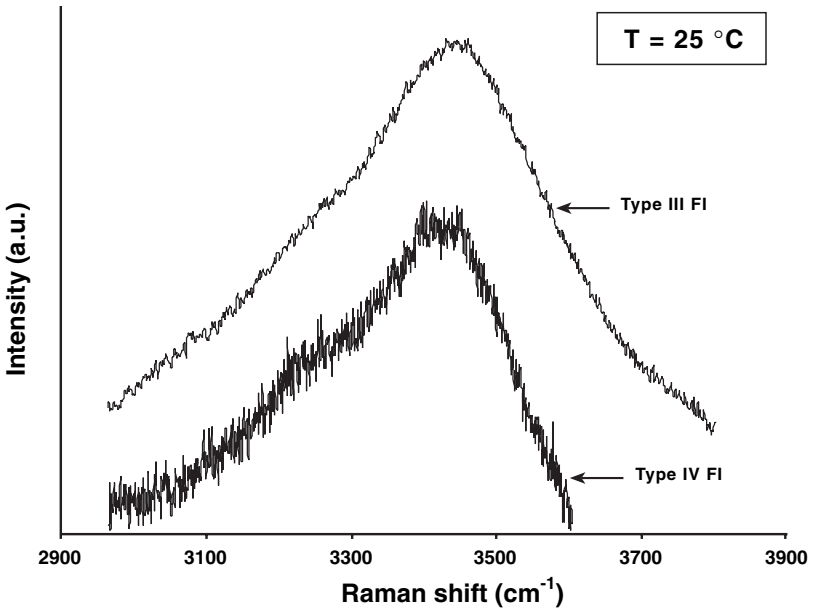

Fig. 27: Raman spectra at room temperature for the liquid phase of type III and type IV FIs. Both FI types show a spectrum typical for liquid water.

The presence of aqueous solutions was confirmed by Raman measurements accomplished on liquid phases of several type III and type IV FIs. Although liquid water is usually difficult to recognise in carbonate crystals due to the high background signal of the host, FIs close to the sample surface revealed a typical "water hill" between 3000 and 3700 cm^{-1} (Fig. 27). Raman measurements on the gas bubbles could not detect gases, such as CO_2, CH_4 and N_2. The gas bubbles possibly consist of water vapour. Therefore, the composition of the described FIs can be characterised in H_2O-salt fluid systems.

Mineral phase	Type	Phases	Shape	Size	F	Th (°C)		T_{liq} (°C)		Tm_{ice} (°C)	
						mode	range	mode	range	mode	range
Dol A2	I	aqueous liquid + vapour bubble	irregular to negative crystal	<5 μm	0,83 to 0,94	130-140 (26)	78,8 to 196,5	-48 (7)	-31,0 to -51,5	-34 (19)	-32,0 to -36,5
	II	aqueous liquid	irregular to negative crystal	<5 μm	1	-	-	-	-	-	-
Dol B	III	aqueous liquid + vapour bubble	irregular to lobate	up to 15 μm	0,78 to 0,97	130 (147)	93,1 to 205,5	-40 (58)	-32,5 to -52,8	-34 (119)	-27,1 to -39,5
Cal 1	IV	aqueous liquid + vapour bubble	spheroidal to lobate	up to 20 μm	0,83 to 0,97	115 (32)	100,0 to 145,6	-34 (15)	-28,5 to -46,9	-24 (28)	-19,5 to -26,5
	V	aqueous liquid	spheroidal (along trails)	<2 μm	1	-	-	-	-	-	-
Cal 2	VI	aqueous liquid (or empty)	irregular to negative crystal	up to 30 μm	1	-	-	-	-	-	-

Table 4: Petrographic features of the main types of FIs. The size of FIs is given as length in μm. F stands for degree of fill. The table also summarises the main results of microthermometry performed on type I, type III and type IV FIs. The range and mode values of Th, T_{liq} and Tm_{ice} are reported. In parenthesis is the number of measurements accomplished for each of these three parameters.

7.3 FI microthermometry

Microthermometry was accomplished on type I, type III and type IV FIs. The results of all measurements are reported in Appendix 3. The main results are summarised in Table 4.

The all liquid type II and type VI FIs could not be investigated by means of microthermometry, as they did not nucleate vapour bubbles even after cooling down to –190 °C, and the formation of ice-like phases was not observed.

In most type I, type III and type IV FIs homogenisation measurements were carried out before freezing runs, to avoid stretching of FIs by expanding ice. All of the three FI types homogenised in the liquid phase.

After total homogenisation, FIs were cooled and Tn_{gas} as well as Tn_{ice} were reported.

In type I and type III FIs nucleation of vapour bubble and ice-like phases was affected by significant metastability. The vapour bubble was metastably absent at room temperature. Ice nucleation could not be observed during the first cooling run down to –150 °C. Ice most commonly formed when the FIs after super cooling were slowly heated towards -60 °C. When heating runs were accomplished first to reach homogenisation, vapour bubble and ice-like phases occasionally nucleated together during the first cooling run at temperatures between –60 and –90 °C. However, in many FIs metastability was so high that ice-like phases did not nucleate even after several cycles of cooling and heating at temperatures below –60 °C. For these FIs only high temperature measurements could be accomplished.

Also Type IV FIs displayed metastability in the nucleation of vapour bubble and ice-like phases. After homogenisation only few type IV FIs nucleated the vapour bubble at temperatures above 0 °C. In the majority of them vapour and ice nucleated together at temperatures below -60 °C.

The appearance of a mosaic texture and consequent darkening of the FIs indicated the nucleation of the ice-like phases, which was commonly accompanied by a sudden contraction of the vapour bubble.

Due to the small size of the FIs and their metastable behaviour, low temperature measurements were problematic for all the of the investigated FI types. The real first melting temperature (Te) could not be determined. The values reported in Table 4 as T_{liq} refer to the temperatures at which the presence of liquid was indicated by an abrupt movement or a gradual expansion of the vapour bubble. Therefore, these temperatures represent only upper constrains to the real Te.

Many phase changes at low temperature (i.e. melting of salt hydrates) could not be identified and in most FIs only the melting temperatures of ice (Tm_{ice}), often corresponding to the final melting temperatures (Tm_{final}), were measured. In small FIs the melting of the last ice crystal could not be

seen and the Tm_{ice} was taken as the temperature at which, upon rapid cooling of the FIs, a last sudden movement of the vapour bubble was observed.

7.3.1 Microthermometry results for type I FIs (Dol A2)

High temperature measurements on type I FIs were performed on samples from Caldas, Villanueva and Canseco (see Appendix 3). Th was measured for a total of 26 FIs and ranges between 78,8 and 196,5 °C. 23 of 26 measurements, corresponding to 92,3% of the data, fall in the range 100-140 °C. The frequency histogram for Th shows an asymmetric distribution of data with mode between 130 and 140 °C (Fig. 28A).

Low temperature measurements were possible only on samples from Caldas and Villanueva (see Appendix 3). Appearance of first liquid (T_{liq}) was observed on 7 FIs at temperatures comprised between –31,0 and –51,5 °C. The mode value for T_{liq} is –48 °C.

Tm_{ice} corresponding to the Tm_{final} was measured on 19 FIs and ranges between –32,0 and –36,5 °C. The frequency histogram for Tm_{ice} shows a normal distribution of data. All of the values fall into a narrow range, with one pronounced mode at –34 °C (Fig. 29A).

The Th-Tm_{ice} plot for these FIs shows a distribution of data, which suggests a nearly constant salinity for a range of Th (Fig. 30A).

7.3.2 Microthermometry results for type III FIs (Dol B)

High temperature measurements on type III FIs were performed on samples from Caldas, Cubillas, Villanueva, Mina Profunda, Cármenes, Canseco and Nocedo (see Appendix 3).

Th was measured for a total of 147 FIs and ranges between 93,1 and 205,5 °C. 139 of 147 measurements, corresponding to 94,6% of the data, fall in the range 100-150 °C. The frequency histogram for Th shows a normal distribution of data with a broad mode at about 130 °C. A second mode may be suspected at 110 °C (Fig. 28B).

Low temperature measurements were accomplished on samples from the already mentioned localities, with the exception of Cármenes and Canseco where the FIs could not be frozen (see Appendix 3). Appearance of the first liquid (T_{liq}) was observed in 58 FIs at temperatures comprised between –32,5 and –52,8 °C. The mode value for T_{liq} is -40 °C.

Ice is the last phase to melt. Tm_{ice} was measured on 119 FIs and ranges between –27,1 and –39,5 °C. 116 of 119 measurements, corresponding to 97,5% of the data, fall in the range –30 to –36 °C. The frequency histogram for Tm_{ice} shows a normal distribution of data with one well-defined mode at –34 °C (Fig. 29B).

The Th-Tm_{ice} plot for type III FIs shows a distribution of data, which suggests a nearly constant salinity for a range of Th (Fig. 30B), just as observed for type I FIs.

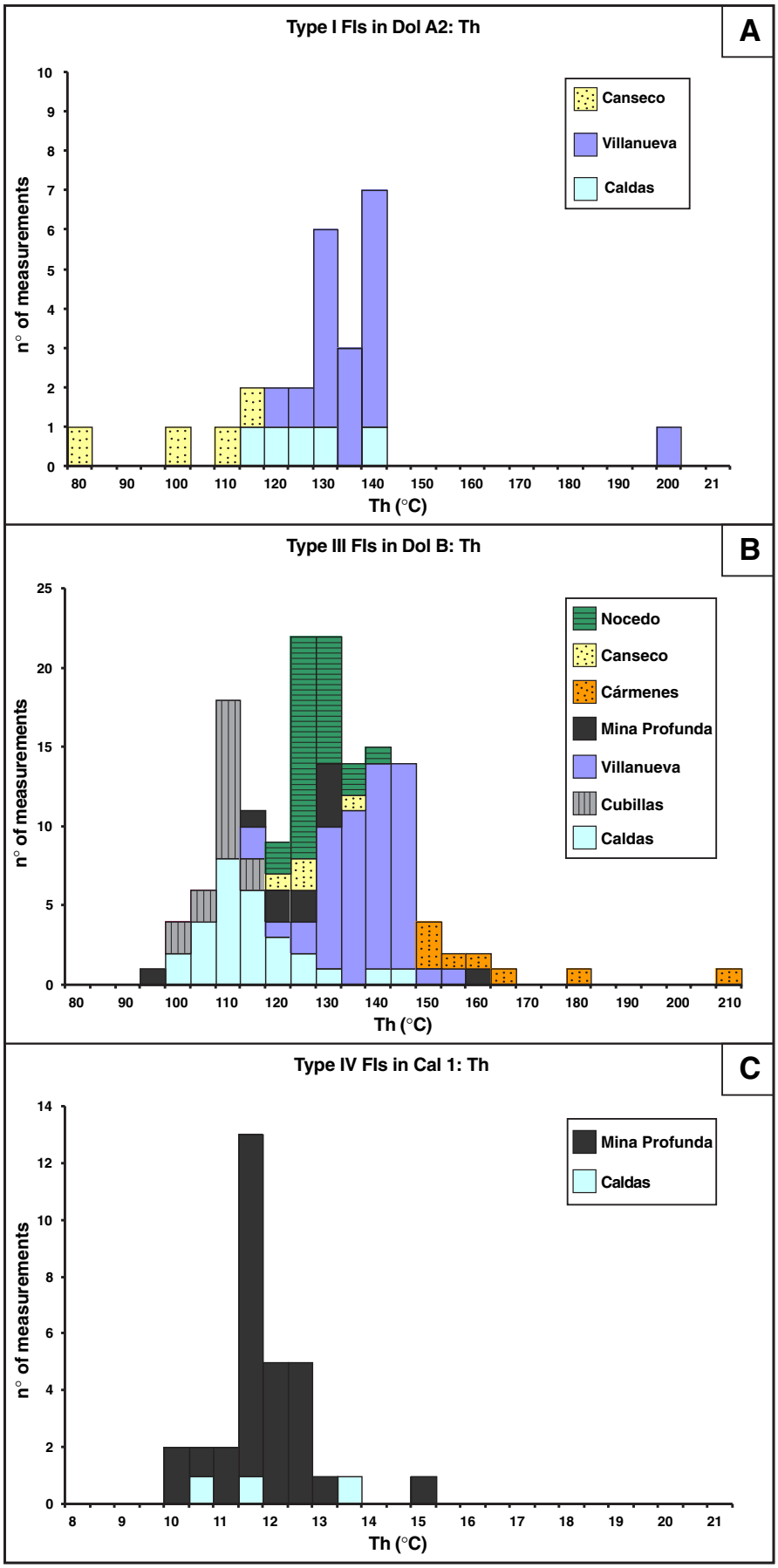

Fig. 28: Histograms showing the frequency distribution of Th values. **A.** Type I FIs in Dol A2. **B.** Type III FIs in Dol B. **C.** Type IV FIs in Cal 1.

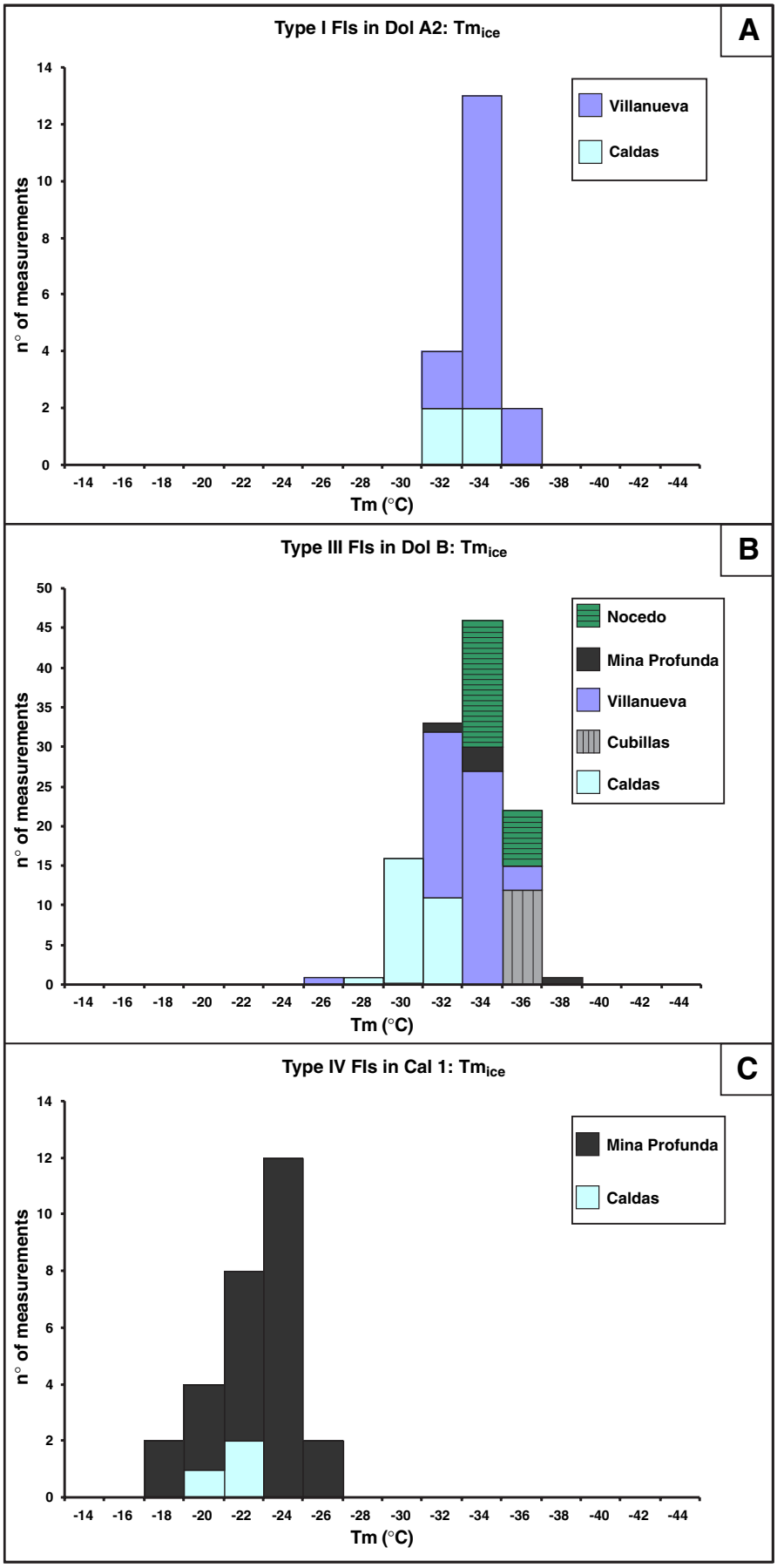

Fig. 29: Histograms showing the frequency distribution of Tm_{ice} values **A.** Type I FIs in Dol A2. **B.** Type III FIs in Dol B. **C.** Type IV FIs in Cal 1.

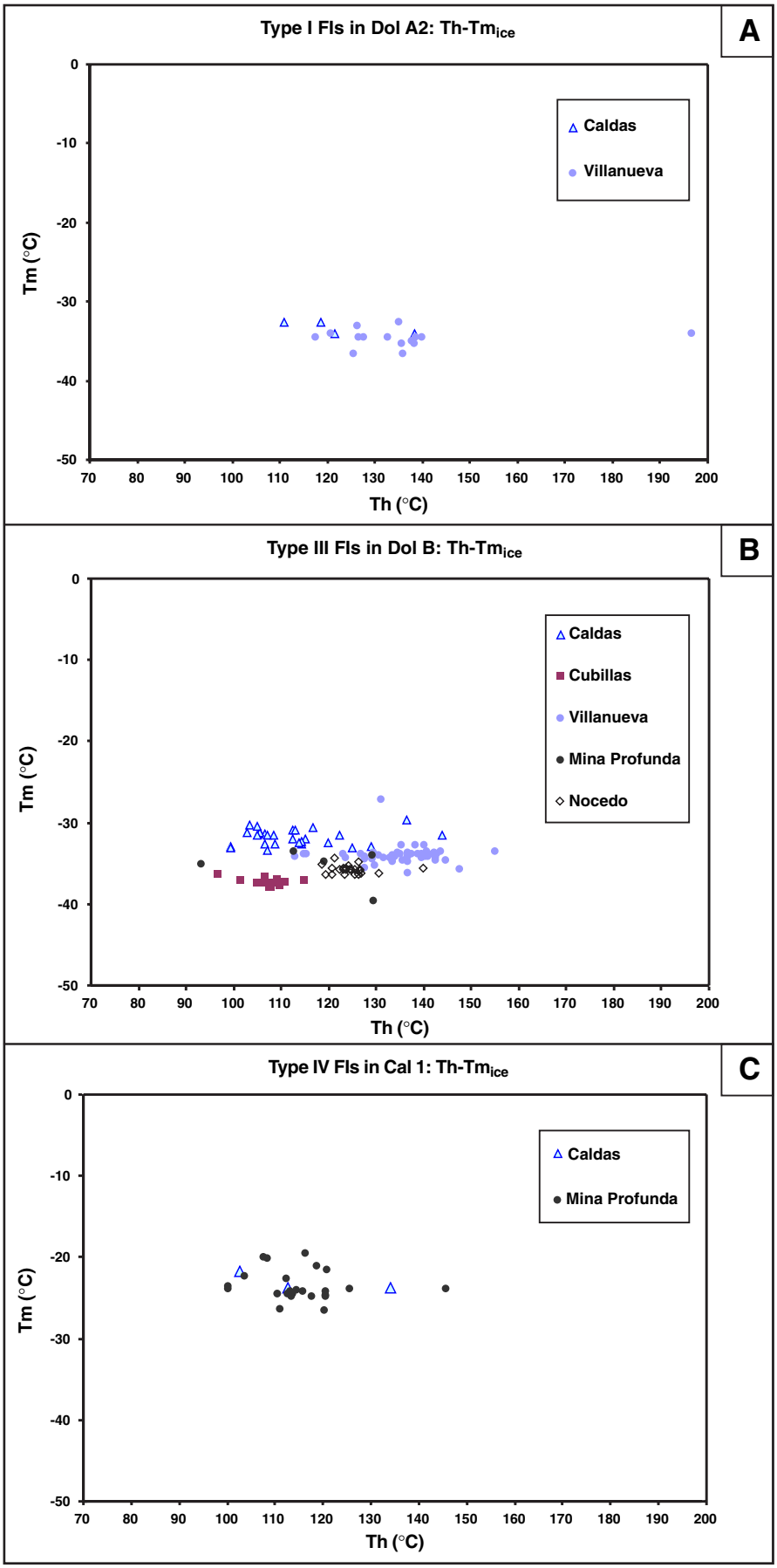

Fig. 30: Bivariate plots showing the covariance between Th and Tm_{ice} data. **A.** Type I FIs in Dol A2. **B.** Type III FIs in Dol B. **C.** Type IV FIs in Cal 1.

7.3.3 Microthermometry results for type IV FIs (Cal 1)

High temperature measurements on type IV FIs were performed on samples from Caldas and Mina Profunda (see Appendix 3). Th was measured for a total of 32 FIs and ranges between 100,0 and 145,6 °C. 30 of 32 measurements, corresponding to 93,8% of the data, fall in the range 100-130 °C. The frequency histogram for Th shows a normal distribution of data with a well-defined mode at 115 °C (Fig. 28C).

Low temperature measurements were accomplished on samples from both mentioned localities (see Appendix 3). Appearance of the first liquid (T_{liq}) was observed in 15 FIs at temperatures comprised between –28,5 and –46,9 °C. The mode value for T_{liq} is –34 °C.

Tm_{ice}, in most cases corresponding to Tm_{final}, was measured on 28 FIs and ranges between –19,5 and –26,5 °C. 25 of 28 measurements, corresponding to 89,3% of the data, fall in the range –20 to –26 °C. The frequency histogram for Tm_{ice} shows a normal distribution of data with a well-defined mode at –24 °C (Fig. 29C).

The Th-Tm_{ice} plot for type IV FIs (Fig. 30C) shows a distribution of data similar to the one reported for type I and types III FIs.

7.4 Regional comparison of microthermometry results

Microthermometry measurements performed on the different types of FIs refer to samples from different localities of the study area. Table 5 summarises the results for each locality.

Type I FIs display only slight variations in Th from one locality to another (Fig. 28A). Lower Th values were reported from Canseco, whereas higher values were reported from Villanueva.

Tm_{ice} values for type I FIs from Caldas and Villanueva overlap (Fig. 29A).

Type III FIs show more significant differences in Th from one locality to another (Fig. 28B). In particular higher Th values were measured in samples from Cármenes (range 146,0-205,5 °C and mode at 150 °C), Villanueva (range 113,0-155,0 °C and mode at 140 °C) and Mina Profunda (range 93,1-158,8 °C and mode at 130 °C). These three localities are in the middle of the study area (see Appendix 1). Lower Th values were measured in samples from Caldas (range 99,2-143,7 °C and mode at 110 °C), Cubillas (range 95,8-114,9 °C and mode at 110 °C) and Nocedo (range 118,5-139,8 °C and mode at 125 °C). These localities are in the western (Caldas and Cubillas) and the southeastern (Nocedo) parts of the study area (see Appendix 1).

Slight variation in Tm_{ice} is observed in type III FIs (Fig. 29B). Higher Tm_{ice} values were reported in samples from Caldas (range –29,85 to –33,3 °C and mode at –30 °C). Lower Tm_{ice} were reported from Cubillas (range –36,3 to –37,8 and mode at –36 °C) and Nocedo (range –34,2 to –36,3 °C

	Type I FIs (Dol A2)		Type III FIs (Dol B)		Type IV FIs (Cal 1)	
	Th (°C)	Tm_{ice} (°C)	Th (°C)	Tm_{ice} (°C)	Th (°C)	Tm_{ice} (°C)
Caldas	110.8 to 138.3 no mode (5)	-34.3 to -32.5 no mode (4)	99.2 to 143.7 mode 110 (28)	-33.3 to -29.5 mode -30 (28)	102,6 to 133,9 no mode (3)	-23,7 to -21,6 mode -22 (3)
Cubillas	-	-	95.8 to 114.9 mode 110 (16)	-37.8 to -36.3 mode -36 (12)	-	-
Villanueva	117,5 to 196.5 mode 130-140 (17)	-36.5 to -31,0 mode -34 (14)	113,0 to 155,0 mode 140 (53)	-37,1 to -27,1 mode -34 (52)	-	-
Mina Profunda	-	-	93,1 to 158,8 mode 130 (11)	-39,5 to -33,5 mode -34 (5)	100,0 to 145,6 mode 115 (29)	-26,5 to -19,5 mode -24 (25)
Cármenes	-	-	146,0 to 205,5 mode 150 (8)	-	-	-
Canseco	78,8 to 111,0 no mode (4)	-	118,5 to 133,0 mode 125 (4)	-	-	-
Nocedo	-	-	118,5 to 139,8 mode 125 (27)	-36,3 to -34,2 mode -34 (23)	-	-

Table 5: Main results of microthermometry are summarised by distinguishing samples coming from different localities of the study area. The range and the mode values of Th and Tm_{ice} for the different FI types are reported. In parenthesis is the number of measurements accomplished for each of the two parameters.

and mode at –34 °C).

Type IV FIs do not show any significant difference in Th and Tm_{ice} between the two localities (Caldas and Mina Profunda) where the analysed samples came from (Figs. 28C and 29C).

The Th-Tm_{ice} plots show a horizontal distribution of data in all of the localities and for all of the three considered FI types (Fig. 30).

7.5 Preliminary conclusions from FI study

Type I and type III FIs do not show any significant difference. They have a consistent degree of fill in a similar range and show metastability in the nucleation of vapour and ice-like phases. Both FI types have low T_{liq} and display similar final melting temperatures in the ice field. They homogenise in the liquid phase and the measured Th values fall in overlapping ranges. These facts suggest that type I and type III FIs formed from homogeneous fluids of similar composition and under similar thermal conditions.

Type II FIs in Dol A2 lack a vapour bubble. This could be the result of low trapping temperature, since vapour bubble nucleation does not occur in FIs trapped at temperatures lower than 50 °C. Alternatively, type II FIs did not nucleate the vapour bubble because of significant metastability (e.g. Roedder 1984). This second alternative is most possibly the case. As described in paragraph 7.3 type I FIs, which are brought to room temperature after homogenisation, may lack the vapour bubble. According to this interpretation the two types of FIs in Dol A2 formed by the same fluid under similar conditions. Type II FIs would thus correspond to type I FIs in which the vapour bubble is metastably absent and are filled with “stretched” liquid (Goldstein and Reynolds 1994).

Type IV FIs are also characterised by consistent degree of fill. They have slightly higher T_{liq} and lower Th relative to type I and type III FIs. This indicates that type IV FIs formed from a homogeneous fluid having composition and possibly temperature different from the fluids which formed type I and type III FIs.

T_{liq} values reported for type I, type III and type IV FIs suggest that the FIs contain a multicomponent salt system (Goldstein and Reynolds 1994).

Type VI FIs in Cal 2 are all liquid and do not coexist with any 2-phase FIs. Possibly, they formed at low temperatures (below 50 °C). This suggests a shallow environment (vadose zone) for their entrapment (e.g. Goldstein et al. 1990, Goldstein and Reynolds 1994). The empty type VI FIs possibly record leakage of the liquid phase by mechanical stress applied to the host crystals.

The Th-Tm_{ice} plots for type I, type III and type IV FIs display a similar distribution of data, which suggests a nearly constant salinity for relatively variable Th (Fig. 30). Variability in Th values is observed for each of the localities where the measured samples came from.

Such a distribution of data could be due to stretching by overheating and consequent thermal reequilibration of FIs (e.g. Presbindowski and Larese 1987, Goldstein and Reynolds 1994). In this case only the lower Th values would be representative of the thermal conditions at the time of FI trapping, whereas the higher Th values would possibly record the FI reequilibration. Thermal reequilibration can be the result of: 1) induced overheating by sample preparation or 2) natural

overheating of the samples due to later thermal events. In the studied samples overheating by sample preparation can be excluded because of the cold technique applied to prepare the thick sections (see paragraph 3.4.1).

The type of data distribution may be relevant to interpret the reported Th variability. Th data for the investigated FIs approximate either a normal distribution (Fig. 31A), or have an asymmetric distribution, with most of the values falling into the higher part of the range (Fig. 31B). On the contrary, Th data which refer to FIs affected by thermal reequilibration would have an asymmetric distribution, with most of the data falling into the lower part of the range (Fig. 31C). This excludes the hypothesis of thermal reequilibration for the studied FIs.

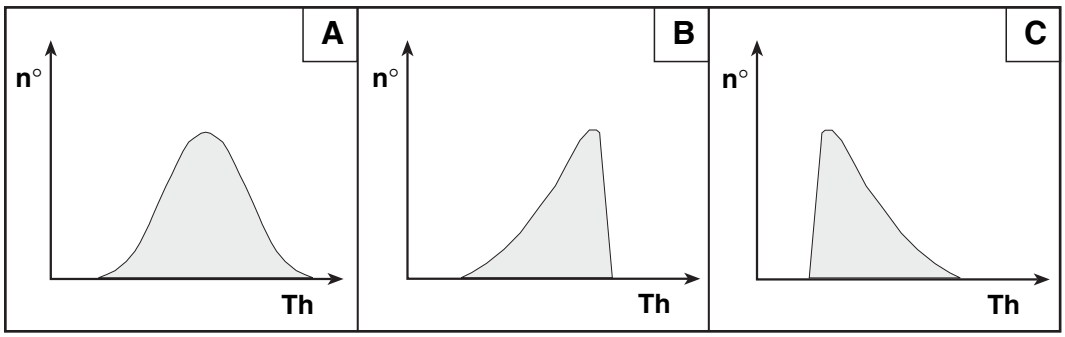

Fig. 31: Histograms showing three different frequency distributions of Th values. **A.** Normal distribution. **B.** Asymmetric distribution with most of the data falling in the higher part of the range. **C.** Asymmetric distribution with most of the data falling in the lower part of the range (thermal reequilibration).

Variability in Th values may be related also to the FI distribution in the crystals. Differences in Th between FIs of the same type but having a different location in the crystal (i.e. the centre and the border) are frequent. The same has been reported from FIs in different growth zones, as well as in the same growth zone of a crystal (Goldstein and Reynolds 1994). Therefore, the Th variability reported for the studied FIs could likely reflect slight variations in the crystal growth conditions.

7.6 Case study 1: Dol B at Villanueva

In most of the investigated dolomite samples, the FIs were too small and flat to accomplish Raman measurements at low temperatures. In the rock sample VCBD1B from Villanueva Dol B is fairly coarse crystalline and type III FIs reach the size of 15 µm. Many FIs from this sample were investigated by means of microthermometry (see Appendix 3). Raman combined with microthermometry was carried out on FIs from this sample. In addition, bulk sample analysis of FI composition was obtained by means of crush-leach on Dol B crystals.

7.6.1 Raman combined with microthermometry

Raman measurements at low temperatures were performed on 5 FIs. After a first rapid cooling the FIs persisted in the liquid state and the Raman spectra displayed a broad peak at about 3457 cm^{-1}, which is typical of liquid water (Fig. 32, spectrum a). Cycles of cooling and heating at temperatures below –60 °C were necessary to nucleate ice. After the FIs were frozen they were further cooled. The Raman spectra obtained at –120 °C indicated the presence of the main ice peak at 3111 cm^{-1}. In the region between 3300 and 3600 cm^{-1}, where the principal hydrate peaks should occur, the spectra were either relatively flat, or more commonly, showed a very broad peak centred between 3435 to 3445 cm^{-1}, indicating the presence of a metastable aqueous liquid (Fig. 32, spectrum b). No salt hydrate peak could be recognised. In order to induce the nucleation of salt hydrates,

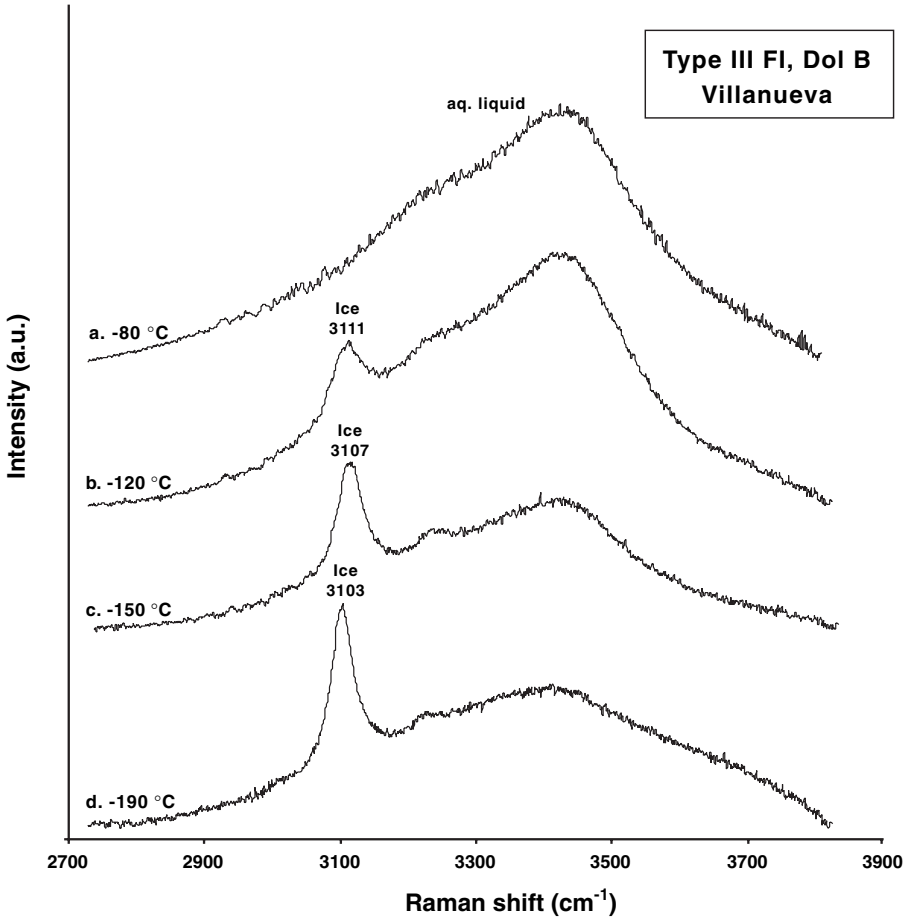

Fig. 32: Raman spectra of a type III FI at different temperatures, illustrating metastability of ice-like phases. At –80 °C (a) during the first cooling run the FI is not yet frozen. A broad peak typical of an aqueous liquid is observed. At –120 °C (b) after nucleation of solid phases. The main ice peak and the broad peak of an aqueous liquid are seen. At –150 °C (c) and –190 °C (d) ice and aqueous liquid still coexist. The main ice peak is sharper and shifted to the left relative to the one at –120 °C. The broad peak of the aqueous liquid is flatter.

the FIs were further cooled down to –150 and –190 °C. The obtained Raman spectra indicated the presence of only ice and a metastable aqueous liquid, without appearance of salt hydrates (Fig. 32, spectra c, d). At these lower temperatures the main ice peak became sharper and more intense and is shifted to the left relative to the one obtained at –120 °C. Contemporaneously, the broad peak of the aqueous liquid became flatter.

The described behaviour indicates metastable absence of the salt hydrates. This could depend on the rapidity with which the FIs are cooled, as recently reported in natural and synthetic aqueous FIs (Samson and Walker 2000, Bakker in press).

The metastable aqueous liquid which coexists together with ice crystals in the investigated FIs, is a hypersaline brine, in which the total amount of salts is concentrated. This residual brine has Raman spectra which resemble those of the undersaturated aqueous liquid at room temperature.

In FI 16 (see Appendix 3) the salt hydrates could be nucleated (Figs. 33 and 34). After ice nucleation the FI 16 was cooled down to –190 °C and subsequently slowly heated up to –60 °C. The FI was kept at this temperature until the salt hydrate nucleation occurred. This was indicated by the appearance of specific peaks in the region of the Raman spectra comprised between 3200 and 3550 cm^{-1}.

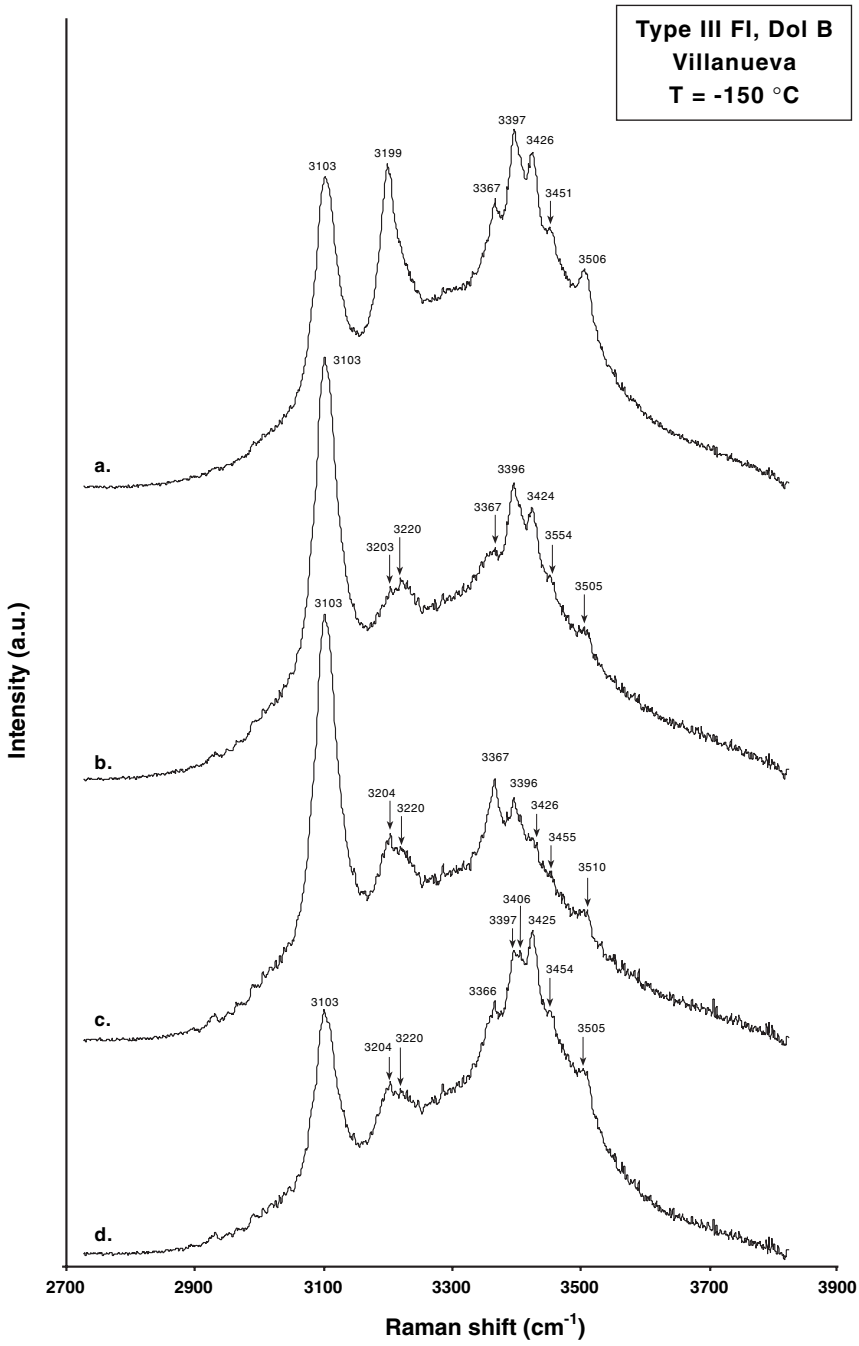

Fig. 33: Raman spectra of FI 16 (type III) at –150 °C. All of the four spectra (a, b, c, d) show the coexistence of ice and a complex mixture of salt hydrates.

Once the salt hydrate nucleated, the FI 16 was further cooled. Different Raman spectra were obtained at –150 and –190 °C (Figs. 33 and 34). The main ice peak is recognised at 3103 cm^{-1} in the spectra obtained at –150 °C (Fig. 33) and at 3096 cm^{-1} in the spectra obtained at –190 °C (Fig. 34). Therefore, the main ice peak is shifted to the left by 7 cm^{-1} in the spectra obtained at lower temperatures. In most of the spectra also the second ice peak can be seen at about 3220 cm^{-1} (Fig. 33, spectra b, c, d and Fig. 34, spectra c, d). Additionally, several salt hydrate peaks can be observed. The Raman shift of the two ice peaks (Ice1 and Ice 2) and of the six main peaks of the salt hydrates (S1 to S6) are summarised in Table 6. The Raman shift of the main peaks for the most common salt hydrates yet investigated by means of Raman spectroscopy are listed in Table 7. The peaks S1 and S6 of FI 16 (Table 6) are comparable to the first and the sixth peak of $MgCl_2$-hydrate (Table 7). S4 approximates the Raman shift of the main peak of NaCl-hydrate. The other peaks cannot be unambiguously interpreted and are possibly the result of a complex mixture of salt hydrates, whose spectra interfere with each other.

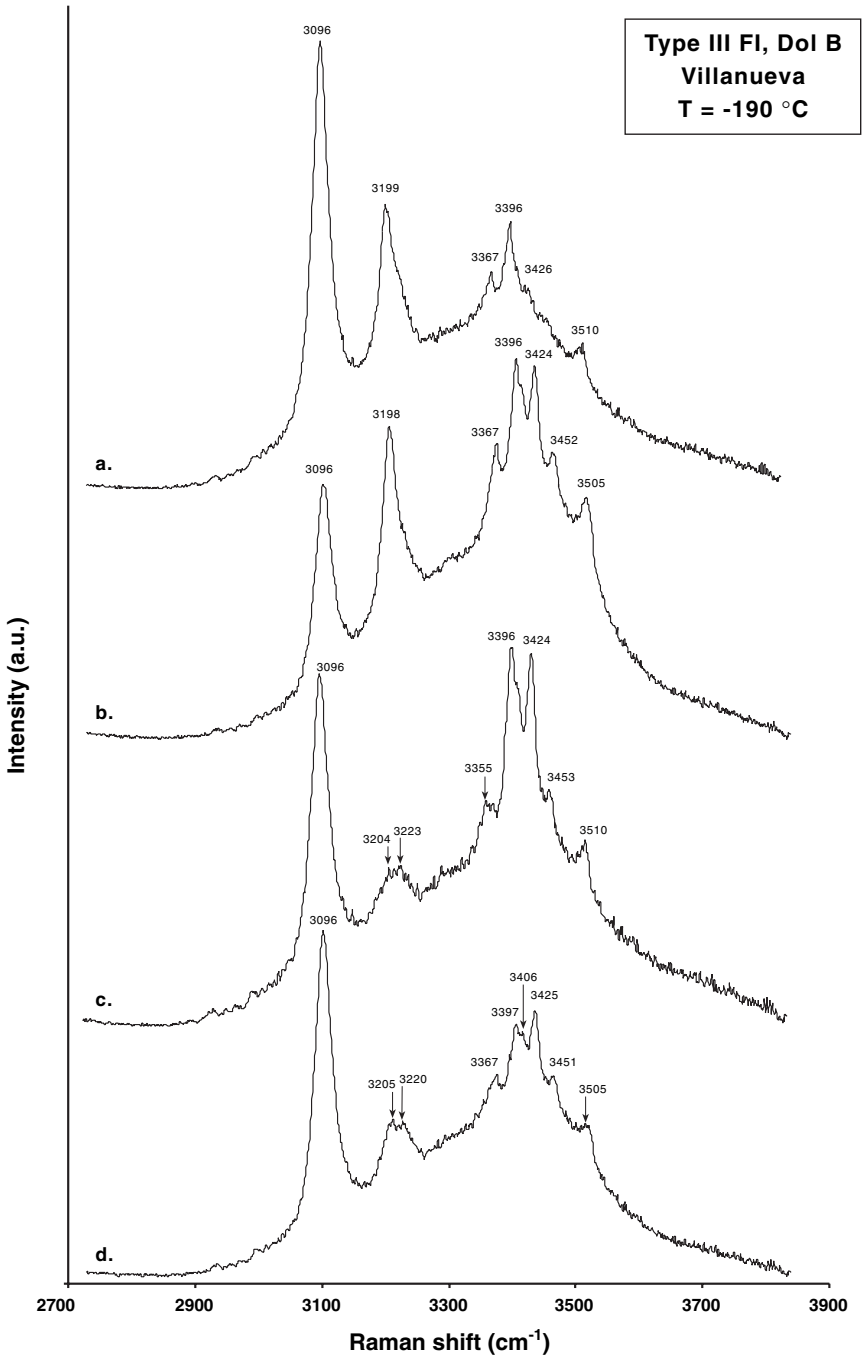

Fig. 34: Raman spectra of FI 16 (type III) at –190 °C. All of the four spectra (a, b, c, d) show the coexistence of ice and a complex mixture of salt hydrates.

All of the salt hydrate peaks maintained a constant position with only slight shift from one spectrum

to the other, regardless of the temperature at which the measurements were performed. On the contrary, a variety of intensities for individual peaks at a selected temperature was observed (Figs. 33 and 34). This could be explained by the salt hydrates having a coarse crystalline structure. The different crystallographic orientation of coarse salt-hydrate crystals relative to the Raman beam may cause the variability in peak intensity (Bakker, pers. commun.).

Raman measurements on FI 16 during reheating enabled the determination of Te at –51,6 °C. On further heating ice and salt hydrate crystals could be visually distinguished in the FI. The last salt hydrate crystal melted at 43,2 °C. The final melting occurred in the ice field at –34,4 °C. The sequence of phase changes in FI 16 during a heating/freezing cycle in shown in Plate 13.

	Raman shift (cm^{-1}) at -150 °C	Raman shift (cm^{-1}) at -190 °C
Ice 1	**3102 - 3103**	**3096**
Ice 2	**3220**	**3220 - 3223**
S1	**3199 - 3204**	**3199 - 3205**
S2	**3366 - 3367**	**3355 - 3367**
S3	**3396 - 3397**	**3396 - 3397**
S4	**3424 - 3426**	**3424 - 3426**
S5	**3451 - 3455**	**3451 - 3453**
S6	**3505 - 3510**	**3505 - 3510**

Table 6: Range of the Raman shift of the peaks corresponding to ice (Ice 1 and Ice 2) and salt hydrates (S1 to S6), as indicated by measurements at -150 and -190 °C on a type III FI.

Salt hydrate	Peak 1	Peak 2	Peak 3	Peak 4	Peak 5	Peak 6
$NaCl \cdot 2H_2O$	3325	3405	**3422**	3436	3538	
$CaCl_2 \cdot 6H_2O$	3243	3406	**3432**			
$CaCl_2 \cdot xH_2O$	3388	3402	3412	**3432**		
$MgCl_2 \cdot 12H_2O$	3191	3325	**3402**	3465	3485	3515
$FeCl_2 \cdot 4H_2O$	3174	**3392**	**3410**			
$FeCl_2 \cdot xH_2O$	3379	**3417**	3433			

Table 7: Raman shift of the peaks for the most common salt hydrates (Bakker, pers. commun.). The size of the characters is proportional to the intensity of the peaks.

7.6.2 Crush-leach analyses

The results of crush-leach analyses obtained from Dol B crystals are listed in Table 8. Mg^{2+} is the most abundant cation. Na^{+} and Ca^{2+} are relatively important cations as well, whereas K^{+} is present only in minor amounts. The Mg^{2+}/Na^{+} ratio is 2,03. The Ca^{2+}/Na^{+} and K^{+}/Na^{+} ratios are 0,83 and 0,28 respectively.

Assuming that the FIs contain a solution which consists of a $MgCl_2$-NaCl-$CaCl_2$-KCl mixture, the relative proportions of these salts (as molar weight per cent) would be 49,1%, 24,1%, 20,1% and 6,7% respectively.

Mineral phase	Li^+ (ppm)	Na^+ (ppm)	K^+ (ppm)	Mg^{2+} (ppm)	Ca^{2+} (ppm)	F^- (ppm)	Cl^- (ppm)	Br^- (ppm)	SO_4^{2-} (ppm)
Dol B	13	19205	5368	39122	16036	99	65747	1199	996
Cal 1	6	17043	2237	3211	21488	30	50567	753	501

Table 8: Results of crush-leach analyses on Dol B and Cal 1 crystals from the localities of Villanueva and Mina Profunda respectively.

7.7 Case study 2: Cal 1 at Mina Profunda

In the rock sample MBPD2M from Mina Profunda, type IV FIs in Cal 1 may reach the size of 20 µm. Many FIs from this sample were investigated by means of microthermometry (see Appendix 3). Raman combined with microthermometry was also performed. Additionally, bulk sample analysis of FI composition was obtained by means of crush-leach on Cal 1 crystals.

7.7.1 Raman combined with microthermometry

Raman measurements at low temperature were performed on 6 FIs. Ice-like phases nucleated during the first cooling run at temperatures below –60 °C. The FIs were kept for a few minutes at temperatures as low as –60 °C in order to induce coarse crystallinity of the ice-like phases. Subsequently, they were cooled down to –150 °C to accomplish Raman measurements. The spectra indicated the presence of the main ice peak at about 3103 cm^{-1}. The second ice peak, although very weak, could be seen at 3221 cm^{-1} (Fig. 35, spectrum a). In the region between 3300 and 3600 cm^{-1} the spectra showed two prominent peaks at 3422 and 3536 cm^{-1} and two weaker peaks at 3405 and 3436 cm^{-1}. Frequently, a much weaker peak at 3320 cm^{-1} was observed as well (Fig. 35, spectrum a). These peaks can be ascribed to the NaCl-hydrate (see Table 7), otherwise referred as hydrohalite (HH).

T_{liq} values for type IV FIs (mode at –34 °C, see Table 4) are much lower than Te for the binary H_2O-NaCl system (i.e. –21,2 °C). This suggests the presence of at least a second salt, other than NaCl, dissolved in the aqueous liquid. However, only ice and hydrohalite could be detected. The other salt hydrates are possibly present only in small amounts and could not be identified by means of Raman spectroscopy.

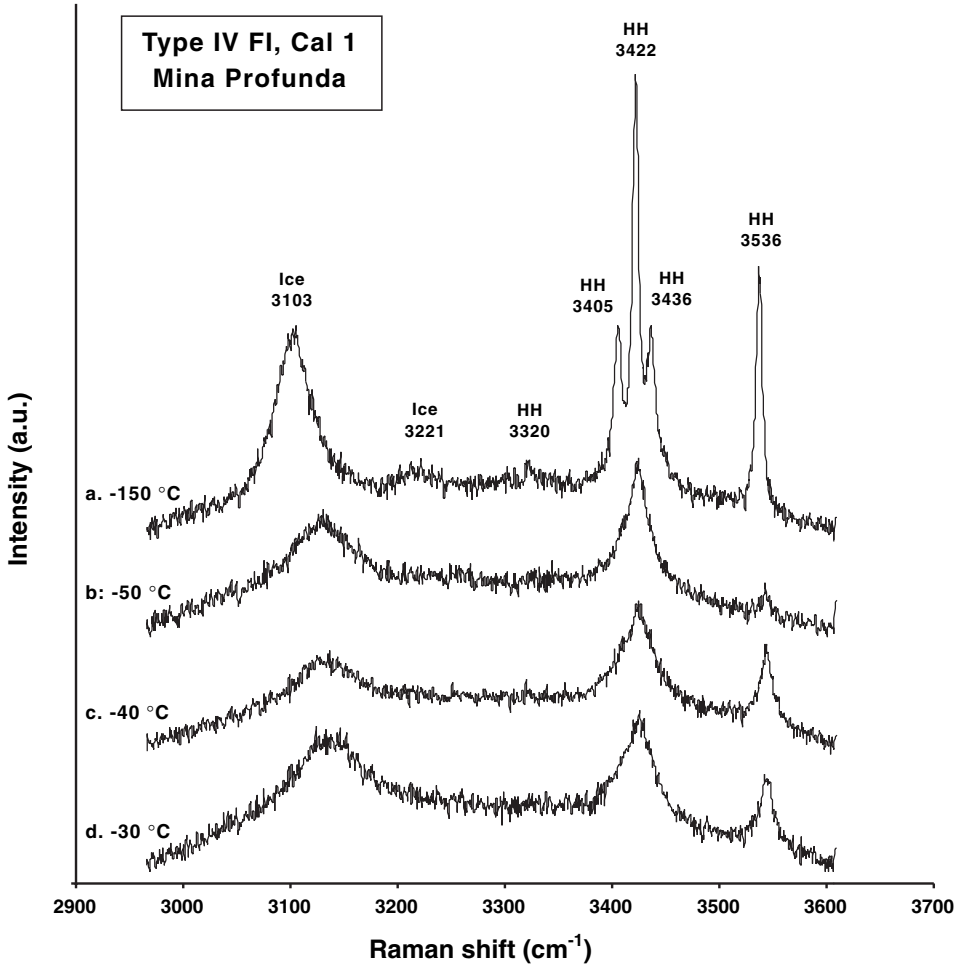

Fig. 35: Raman spectra of a type IV FI at different temperatures. At –150 °C (a) clear peaks of ice and hydrohalite (HH) are recognised. At –50 °C (b), –40 °C (c) and –30 °C (d) ice and hydrohalite are still recognisable. Some of their typical peaks merged, whereas others are less intense than they were at –150 °C.

Raman measurements on these FIs during reheating determined the first melting at lower temperatures (between –46 and –50 °C) than obtained by optical means (see Table 4). At T>Te ice and hydrohalite still coexisted (Fig. 35, spectra b, c, d). This implies that salt-hydrates other than hydrohalite melted at the eutectic point. At these higher temperatures some typical peaks of ice and hydrohalite merged, whereas others became less intense than they were at –150 °C. This is a consequence of the temperature dependence of the Raman spectra.

In these FIs ice and hydrohalite crystals could be optically distinguished and both ice and hydrohalite melting points could be measured (see Appendix 3). Ice crystals typically melted first at temperatures between –21,5 and –24,7 °C. The final melting mostly occurred in the hydrohalite field at temperatures between –16,3 and –24,0 °C.

The sequence of phase changes in one of these FIs during a heating/freezing cycle is shown in Plate 14.

7.7.2 Crush-leach analyses

The results of crush-leach analyses obtained from Cal 1 crystals are listed in Table 8. The most abundant cations are Ca^{2+} and Na^{+}. Only minor Mg^{2+} and K^{+} contents were detected. The Mg^{2+}/Na^{+} ratio is 0,19. The Ca^{2+}/Na^{+} and K^{+}/Na^{+} ratios are 1,26 and 0,13 respectively.

Assuming that the FIs contain a solution which consists of a $MgCl_2$-NaCl-$CaCl_2$-KCl mixture, the relative proportions of these salts (as molar weight per cent) would be 7,3%, 38,8%, 48,8% and 5,1% respectively.

7.8 Salinity calculation

7.8.1 Salinity of type I (Dol A2) and type III (Dol B) FIs

Results of microthermometry indicate a similar composition for type I and type III FIs. This allows to calculate salinities for both FI types in the same fluid system, by making the same assumptions.

In order to understand the melting behaviour of these FIs in the real fluid system, the melting path of an imaginary FI in the H_2O-$MgCl_2$-NaCl system is outlined in Fig. 36A. The results of Raman and crush-leach analyses (see paragraph 7.6) justify the choice of this system.

At low temperatures, the imaginary FI consists of vapour and a solid assemblage given by ice, hydrohalite and $MgCl_2$-hydrate. At the eutectic temperature of –35 °C one of the two salt hydrates (e.g. $MgCl_2$-hydrate) melts resulting in a FI containing vapour, hydrohalite, ice and an aqueous liquid (point A, Fig. 36A). As warming proceeds, the composition of the liquid develops along the cotectic line A-B (Fig. 36A), which separates the hydrohalite + liquid and the ice + liquid stability fields. Hydrohalite and ice contemporaneously melt whereas the proportion of liquid progressively increases, until one of the two solid species (e.g. hydrohalite) melts in point C (Fig. 36A). In this point the FI consists of vapour, ice and aqueous liquid. As warming continues, ice keeps melting and the composition of the liquid will evolve towards the H_2O apex of the diagram on the line C-D (Fig. 36A). This line defines the relative proportions of $MgCl_2$ and NaCl in the FI. In the point of intersection between the line C-D and the isotherm for Tm_{ice} (point E, Fig. 36A) the last ice crystal melts. This point gives the proportions of the three species in the FIs.

Type I and type III FIs have in reality T_{liq} values much lower than Te of the H_2O-$MgCl_2$-NaCl system (i.e. -35 °C). Even Tm_{ice} for many of these FIs occur at temperatures lower than –35 °C. Te as low as -51,6 °C has been measured on FI 16 (see paragraph 7.6.1). A more complex mixture of salts is possibly present in these FIs as suggested by Raman spectra (Figs. 33 and 34). As Ca^{2+} is the third most important cation in the aqueous solution of these FIs (see paragraph 7.6.2), it is reasonable to assume the H_2O-$MgCl_2$-(NaCl+$CaCl_2$) system as the one which better approximates

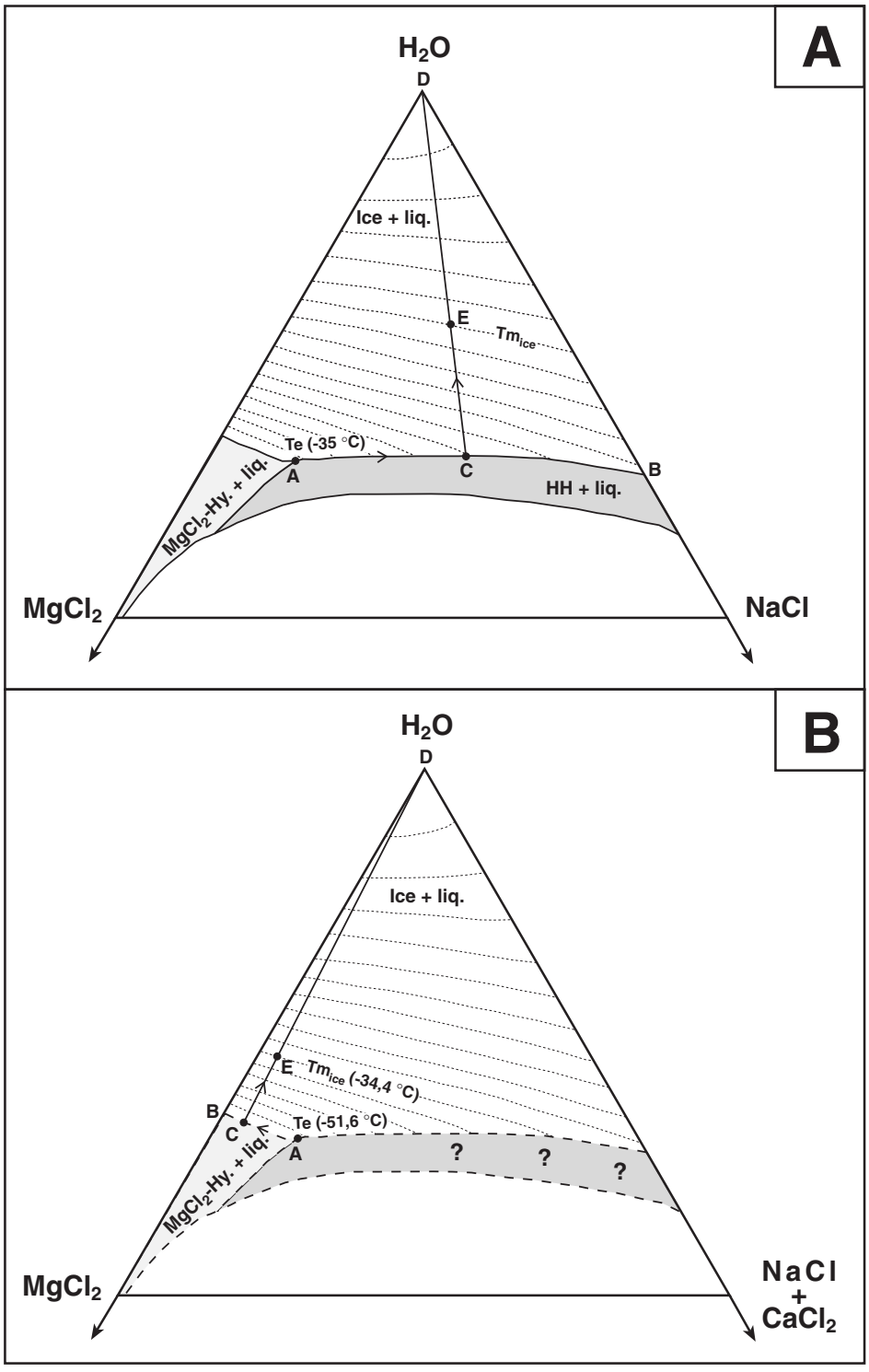

Fig. 36: **A.** H_2O-$MgCl_2$-NaCl ternary system showing phase boundaries and the melting path of an imaginary FI with final melting in the ice field. **B.** H_2O-$MgCl_2$-($NaCl+CaCl_2$) system showing hypothetical phase boundaries and the possible melting path of FI 16 (type III), with final melting in the ice field.

the composition of type I and type III FIs.

The melting path of one of these FIs can be sketched in such a system by using the known melting temperatures of FI 16 (Fig. 36B) and assuming that $MgCl_2$-hydrate is the last salt-hydrate to melt. At low temperatures, the FI consists of a vapour bubble and a solid assemblage given

by ice, $MgCl_2$-hydrate, hydrohalite and $CaCl_2$-hydrate (antarcticite). Upon heating Te is reached at about –51,6 °C (point A, Fig. 36B). Hydrohalite and antarcticite melt, whereas $MgCl_2$-hydrate, ice and aqueous liquid still coexist with the vapour bubble. The composition of the fluid on further heating evolves along the cotectic line A-B (Fig. 36B), which separates the ice + liquid and the $MgCl_2$-hydrate + liquid stability fields. When the melting point of the $MgCl_2$-hydrate is reached in the point C (-43,2 °C) the fluid will evolve towards the H_2O apex of the diagram along the line C-D. The point E at the intersection between the line C-D and the isotherm of Tm_{ice} (-34,4 °C) defines the composition of the FI.

The system H_2O-$MgCl_2$-($NaCl$+$CaCl_2$) is very complex. Salinity calculation in such a system is not possible as no equation of state is available. The predominance of Mg^{2+} ions in the analysed leachate (see paragraph 7.6.2) lets one assume that type I and type III FIs have composition close to the system H_2O-$MgCl_2$. Therefore, the salinity of individual type I and type III FIs was calculated in this binary system. For those FIs which have final melting at temperatures lower than Te of this system (i.e. -33 °C) the used equation of state was extended into the stability field of ice and $MgCl_2$-hydrate.

Both type I and type III FIs have consistent salinity values (see Appendix 3). The salinity of type I FIs varies in the narrow range 20,5–21,8 eq. wt % $MgCl_2$. Type III FIs have salinity in the slightly broader range 19,0–22,6 eq. wt % $MgCl_2$. For both types of FIs the salinity mode value is 22 eq. wt % $MgCl_2$.

7.8.2 Salinity of type IV FIs (Cal 1)

At least two salt species are dissolved in the aqueous liquid of type IV FIs. The results of Raman spectroscopy and crush-leach analyses (see paragraphs 7.7.2 and 7.7.3) indicate that the H_2O-$CaCl_2$-$NaCl$ ternary system is the one which better approximates the composition of type IV FIs.

The melting path and correspondent phase changes of these FIs upon heating can be schematically followed in Fig. 37. At low temperatures, an imaginary FI consists of vapour, and a solid assemblage given by ice, hydrohalite and antarcticite. At -52 °C (eutectic point of the system) antarcticite melts and the FI consists of vapour, ice, hydrohalite and an aqueous liquid. On further heating more liquid forms and evolves in composition following the cotectic line A-B (Fig. 37), which separates the ice + liquid and the hydrohalite + liquid stability fields. The fluid evolution along the line A-B continues until one of the two solid phases (i.e. ice or hydrohalite) melts in point C. In case ice is the first phase to melt, vapour, hydrohalite and aqueous liquid coexist in the FI. The composition of the fluid will evolve towards the hydrohalite (Point D, Fig. 37) along the line C-D, until hydrohalite is completely molten (point E, Fig. 37). The point E at the intersection between the line C-D and the isotherm of Tm_{HH} gives the composition of the fluid. If hydrohalite is the phase

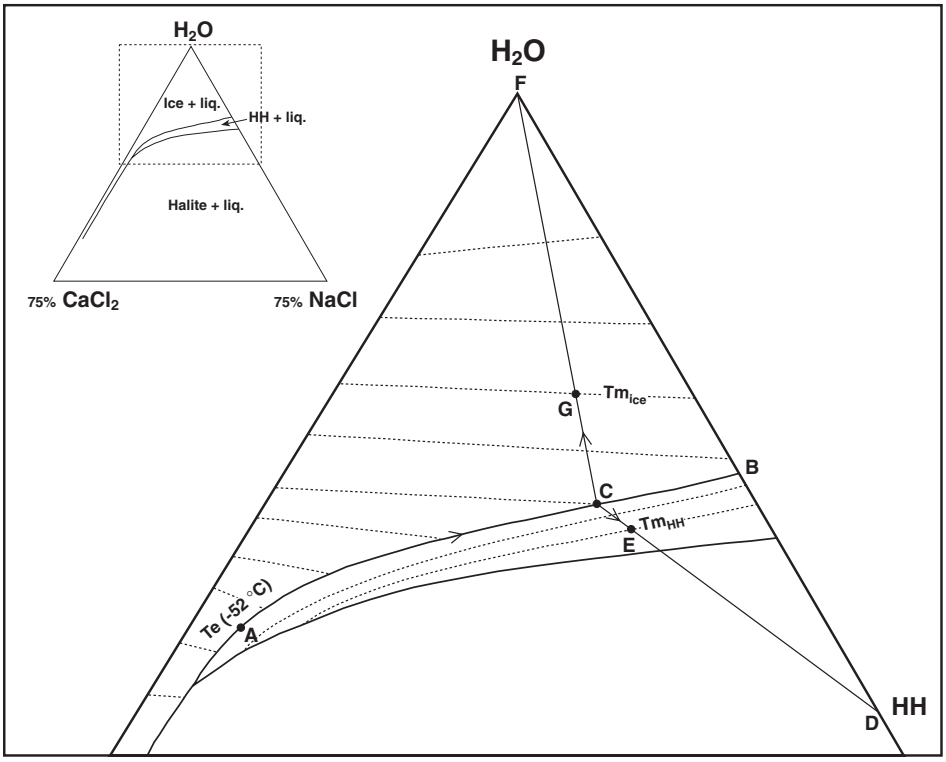

Fig. 37: H_2O-$CaCl_2$-NaCl ternary system showing phase boundaries and melting paths of imaginary FIs, with final melting occurring in the hydrohalite and ice fields respectively.

which melts in point C, the FI will consist of vapour, ice and aqueous liquid. The composition of the fluid will evolve towards the H_2O apex of the diagram along the line C-F until Tm_{ice} is reached (point G, Fig. 37). The point G at the intersection between the line C-F and the isotherm of Tm_{ice} gives the composition of the fluid.

The salinities of those type IV FIs in which both ice and hydrohalite melting points could be observed was calculated in the ternary H_2O-$CaCl_2$-NaCl system. NaCl ranges between 16,1 and 17,8 wt %, whereas $CaCl_2$ ranges between 1,0 and 10,0 wt %. The total salinity, calculated as the sum of the two salt species, ranges between 22,0 and 27,4 wt %.

However, for the majority of type IV FIs only the final melting of ice could be observed. The salinity of these FIs was calculated in the binary H_2O-NaCl system. For those FIs having final melting lower than Te of this system (i.e. -21,2 °C), the used equation of state was extended into the stability field of ice and hydrohalite. Salinity of these FIs ranges between 22,0 and 26,5 eq. wt % NaCl.

The total salinity of type IV FIs is therefore more variable and distinctly higher than the salinity reported for type I and type III FIs.

7.9 Bulk density and composition of FIs

Bulk density and composition of type I, type III and type IV FIs were calculated as described in paragraph 3.4.4. The molar volume and the mole fractions of the different species present (i.e. H_2O, Mg^{2+}, Na^{+}, Ca^{2+}, Cl^{-}) are reported for individual FIs in Appendix 3.
The molar volume of type I FIs ranges between 17,59 and 20,03 cm^3/mol. Type III FIs have molar volume which ranges between 17,07 and 20,40 cm^3/mol. Type IV FIs have molar volume in the range 17,08-19,58 cm^3/mol.

7.10 P-T conditions during FI trapping

At the time of trapping, type I, type III and type IV FIs consisted of a single homogeneous liquid phase. When they were brought to surface conditions as a consequence of uplift or erosion, the vapour bubble developed. Therefore, the measured Th values represent the minimum temperature of FI entrapment. It is crucial to evaluate the difference between the measured Th and the true trapping temperature (Tt). This temperature difference, referred as the “pressure correction”, depends on the composition and density of FIs.
The cooling path of an imaginary FI from trapping conditions (Pt-Tt) towards surface conditions (P_{room}-T_{room}) is schematically explained in Fig. 38. During cooling from Tt (point A) towards Th (point B) the FI consists of one homogeneous liquid phase. The P-T conditions of the FI are constrained by an isochore. This is a line of constant volume which originates at homogenisation condition on the liquid-vapour curve. In point B the FI segregates a vapour bubble. During further cooling from Th towards T_{room} (point C) the volume fraction of the liquid phase decreases and the P-T conditions of the FI are constrained by the liquid-vapour curve.
Therefore, the trapping temperature (Tt) of a FI with known Th can be derived by proceeding up the isochore until the presumed trapping pressure (Pt). However, in most cases Pt cannot be constrained from independent methods. Here, the hydrostatic and lithostatic thermobaric gradients supposed to have existed at the time of FI trapping can be used. Their points of intersection with the calculated isochore (points D and E, Fig. 38) define the possible P-T conditions of FI trapping in hydrostatic and lithostatic regimes respectively. This method may lead to significant error and cause underestimation as well as overestimation of Tt, depending on the choice of the gradient.
In the present paragraph the results of FI investigation are used to constrain the P-T trapping conditions of type I, type III and type IV FIs. Since there is no independent way to estimate the

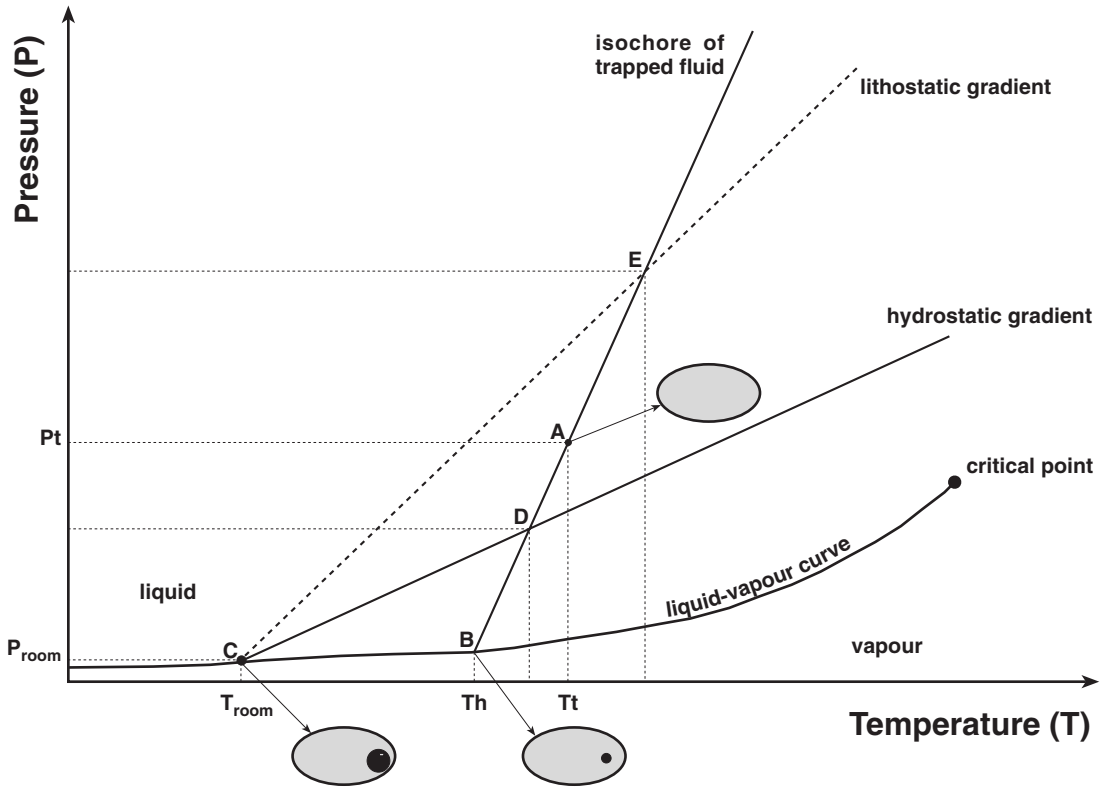

Fig. 38: P-T plot showing the cooling path of an imaginary FI from trapping conditions (Pt-Tt) towards surface conditions (P_{room}-T_{room}).

pressure at which the different host minerals have formed, the following calculations only attempt to define the trapping conditions of the studied FIs.

The hydrostatic and lithostatic thermobaric gradients were constructed using a geothermal gradient of 35 °C/km and geobarometric gradients of 10,1 and 27,1 MPa/km for hydrostatic and lithostatic conditions respectively. The surface temperature was taken at 20 °C. Both lithostatic and hydrostatic gradients were calculated making the assumption of linear proportionality between pressure (i.e. depth) and temperature.

Isochores were constructed for FIs of known salinity which have the minimum and maximum Th respectively, without considering those FIs having anomalous Th values (i.e. too low or too high relative to the normal distribution of data). Additionally, isochores were constructed for the Th mode values of each FI type (Fig. 28), using the correspondent salinity mode values. The intersection points of these isochores with the hydrostatic and lithostatic gradients allowed to correct the pressure for hydrostatic and lithostatic regimes respectively and to obtain FI trapping conditions.

The possible trapping depth (Dt) of the FIs was calculated from the obtained pressures and the assumed geobarometric gradients.

7.10.1 P-T trapping conditions for type I, type III and type IV FIs

Trapping conditions for type I, type III and type IV FIs were calculated in hydrostatic and lithostatic regimes respectively by means of isochores constructed for the minimum, the mode and the maximum Th values of each FI type (Table 9).

		Hydrostatic			Lithostatic		
		Tt (°C)	Pt (Mpa)	Dt (Km)	Tt (°C)	Pt (Mpa)	Dt (Km)
Type I (Dol A2)	**Th_{min} 110,8**	122	29	2,9	150	100	3,7
	Th_{mode} 140	156	39	3,9	198	137	5,0
	Th_{max} 139,7	156	39	3,9	198	137	5,0
Type III (Dol B)	**Th_{min} 99,2**	109	25	2,5	131	85	3,1
	Th_{mode} 130	145	35	3,5	181	124	4,6
	Th_{max} 155	175	44	4,4	226	159	5,9
Type IV (Cal 1)	**Th_{min} 100**	110	26	2,6	133	87	3,2
	Th_{mode} 115	127	31	3,1	157	106	3,9
	Th_{max} 133,9	149	37	3,7	188	129	4,8

Table 9: Trapping conditions for type I, type III and type IV FIs in hydrostatic and lithostatic regimes respectively. Temperature (Tt), pressure (Pt) and depth (Dt) of trapping were calculated by means of isochores constructed for the minimum, the mode and the maximum Th values of each FI type.

The isochore constructed for the Th mode value of type I FIs (140 °C, Fig. 28A) crosses the hydrostatic gradient at 156 °C and 39 MPa, and the lithostatic gradient at 198 °C and 137 MPa (Fig. 39A). This corresponds to a depth of about 3,9 and 5,0 km respectively.

The isochore constructed from the Th mode value of type III FIs (130 °C, Fig. 28B) intersects the hydrostatic gradient at 145 °C and 35 MPa and the lithostatic gradient at 181 °C and 124 MPa (Fig. 39B), corresponding respectively to 3,5 and 4,6 km of depth.

The isochore constructed from the Th mode value of type IV FIs (115 °C, Fig. 28C) crosses the hydrostatic gradient at 127 °C and 31 MPa and the lithostatic gradient at 157 °C and 106 MPa (Fig. 39C). This corresponds to a depth of 3,1 and 3,9 km respectively.

7.10.2 Regional comparison of P-T trapping conditions (type III FIs)

As already underlined in paragraph 7.4 type III FIs in samples coming from different localities of the study area may show slight differences in Th. The aim of the present paragraph is to constrain

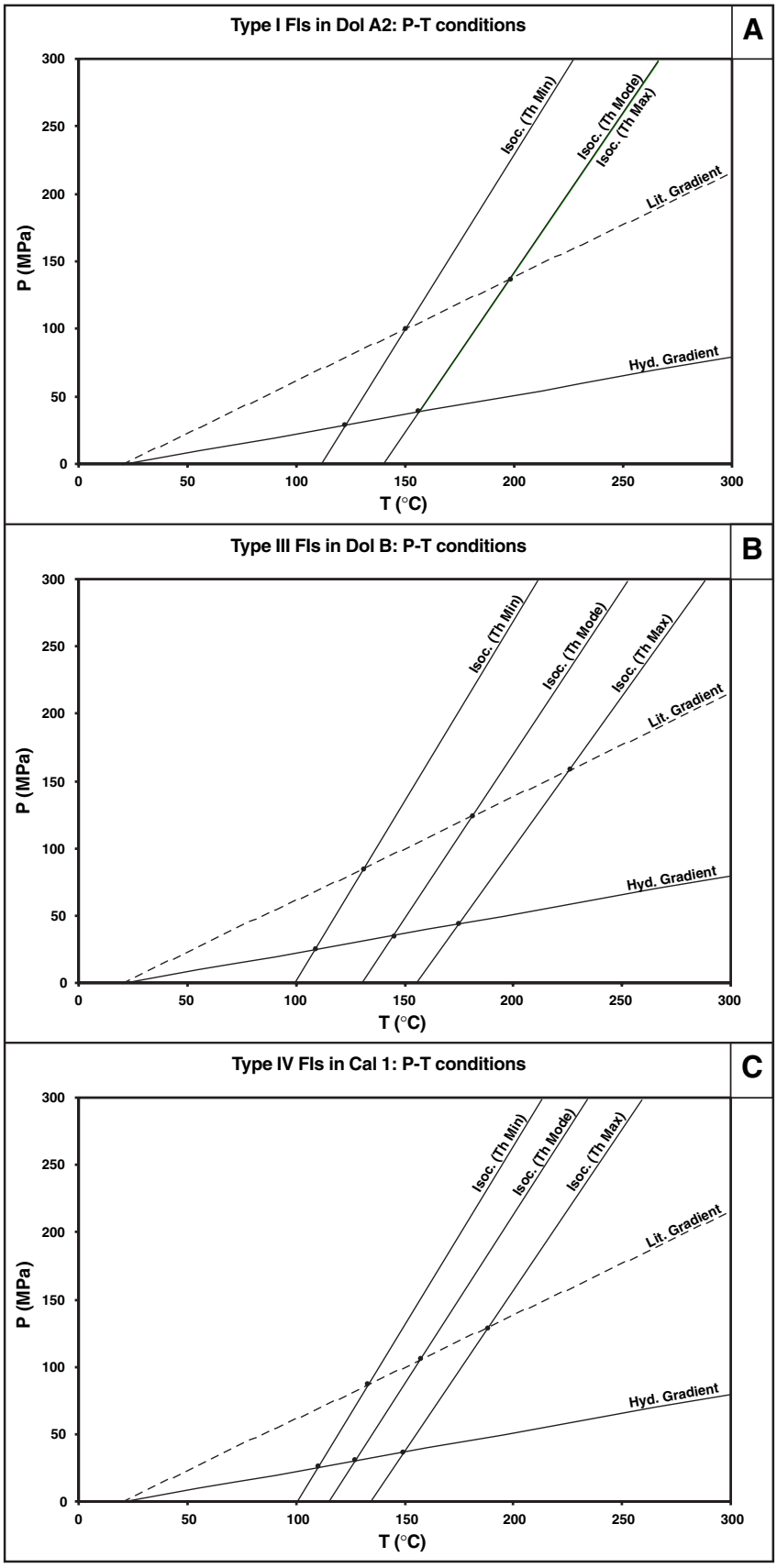

Fig. 39: P-T plots showing the hydrostatic and lithostatic gradients and their intersection points with isochores constructed from the minimum, the maximum and the mode Th values. **A.** Type I FIs in Dol A2. **B.** Type III FIs in Dol B. **C.** Type IV FIs in Cal 1.

the P-T trapping conditions of these FIs in the following three localities: Caldas (in the W), Villanueva (in the centre) and Nocedo (in the SE). Isochores were constructed for the Th mode values of type III FIs corresponding to each of these three localities (Fig. 40).

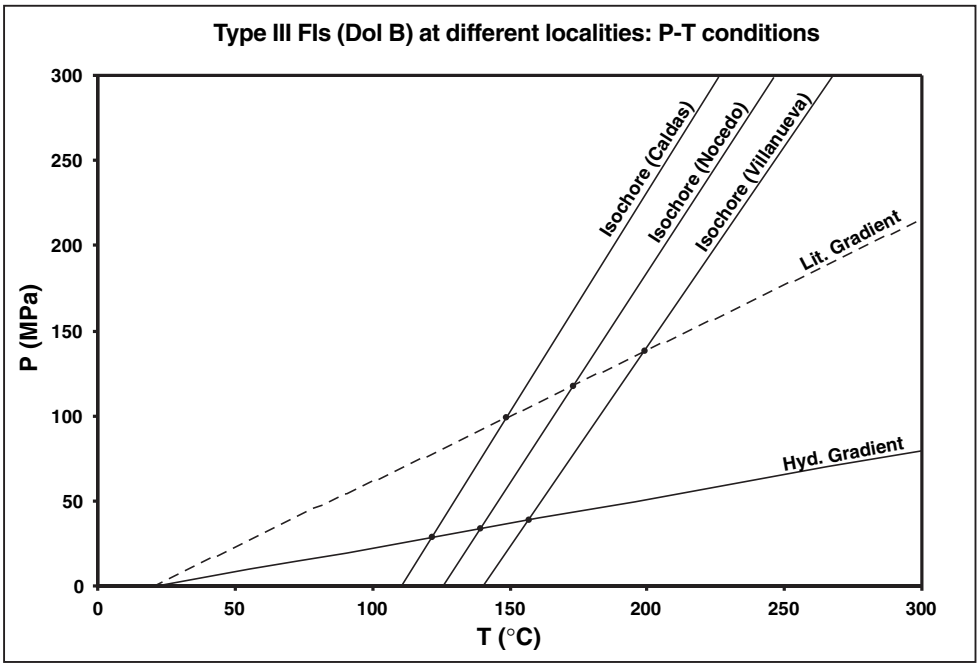

Fig. 40: P-T plot showing the hydrostatic and lithostatic gradients, and their intersection points with isochores constructed for the Th mode values of type III FIs from three different localities: Caldas, Villanueva and Nocedo.

The isochore constructed for Caldas using a Th mode value of 110 °C (see Fig. 28B) intersects the hydrostatic gradient at 121 °C and 29 MPa and the lithostatic gradient at 148 °C and 99 MPa, corresponding to a depth of 2,9 and 3,7 km respectively.

The isochore constructed for Villanueva using a Th mode value of 140 °C (see Fig. 28B) intersects the hydrostatic gradient at 156 °C and 39 MPa and the lithostatic gradient at 198 °C and 138 MPa, corresponding to a depth of 3,9 and 5,1 km respectively.

The isochore constructed for Nocedo using a Th mode value of 125 °C (see Fig. 28B) intersects the hydrostatic gradient at 139 °C and 34 MPa and the lithostatic gradient at 173 °C and 118 MPa, corresponding to a depth of 3,4 and 4,4 km respectively.

These results indicate that higher P-T conditions characterised the trapping of type III FIs in samples from the middle of the study area.

Chapter 8: Discussion

8.1 Dolomite stoichiometry and degree of order (OR)

The results for Ca content and OR reported in paragraph 6.2 suggest that most of the dolomite samples analysed approximate the stoichiometry and the ordering of the “ideal” dolomite. No significant difference between the replacive and cement dolomites has been observed: the three analysed dolomite phases (Dol A1, Dol A2 and Dol B) are nearly stoichiometric and well ordered.

The trend towards more stoichiometric composition in Dol A1 and Dol B relative to Dol A2 from the same rock sample could be the result of the coarser crystallinity, which frequently characterises Dol A1 and Dol B crystals. Several authors (e.g. Füchtbauer and Goldsmith 1965, Sperber et al. 1984) reported a broad correlation between increasing stoichiometry and increasing crystal size. Stoichiometry and ordering are commonly used to distinguish between different dolomite types. Three broad dolomite groups have been identified based on stoichiometry, texture, and possible association with evaporites (Morrow 1978, 1990b, Lumsden and Chimahusky 1980):

1. Coarsely crystalline, sucrosic dolomites which are generally nearly stoichiometric (mode at 50,0–51,0 mol % $CaCO_3$);
2. Fine crystalline dolomites associated with evaporites which are also nearly stoichiometric (mode at 51,0–52,0 mol % $CaCO_3$);
3. Fine crystalline dolomites not associated with evaporites which are generally Ca-rich (mode at 54,0–56,0 mol % $CaCO_3$).

Group 1 dolomites are commonly of late diagenetic burial origin, whereas group 2 and group 3 dolomites are early diagenetic and near surface in origin. The cause of these associations is thought to be the salinity and the Mg/Ca ratio of the dolomitising fluids, with a climatic control important for groups 2 and 3 (Folk and Land 1975, Morrow 1978).

The dolomites investigated in this study are nearly stoichiometric. From the mentioned systematics it results that only group 1 and group 2 dolomites have nearly stoichiometric composition. The hypothesis of evaporative origin (group 2) can be ruled out, as the studied dolomites mostly exhibit coarse crystallinity and are not associated with evaporites. Furthermore, dolomites forming in modern evaporative settings are characterised by low OR of less than 0,4 (e.g. Patterson 1972). This is inconsistent with the high OR reported for the studied samples (Figs. 9 and 11). Ca contents and OR similar to those reported in this study have been measured in burial dolomites developed along joints (Hird 1986). Therefore, all of the three analysed dolomite phases could

belong only to the late burial dolomites of group 1.

The near stoichiometry and high OR of group 1 dolomites is interpreted as the result of slow crystal growth, possibly aided by elevated temperatures (Morrow 1978, Morrow 1990b).

8.2 Minor and trace element geochemistry

The studied dolomites have relatively low concentrations of minor and trace elements. This is consistent with their nearly stoichiometric composition and high degree of cation order.

8.2.1 Sr contents

There is disagreement over the theoretical k for Sr in carbonates. However, this is thought to be less than 1. This means that during carbonate diagenesis Sr will be lost (Veizer and Demovic 1974, Jacobson and Usdowsky 1976, Brand and Veizer 1980, Kretz 1982, Veizer 1983).

The Sr content of dolomites can be used to distinguish between early and late dolomitisation and to constrain the composition of the dolomitising fluids. As a general rule early diagenetic dolomites have higher Sr contents than late diagenetic dolomites (Brand and Veizer 1980, Dunham and Olson 1980, Land 1980, M'Rabet 1981, Machel 1988).

Dolomites directly precipitated from seawater typically have Sr contents of several hundred ppm (Baker and Burns 1985, Carballo et al. 1987). Dolomites with more Sr than this precipitates from hypersaline fluids, where strong evaporation and gypsum precipitation have elevated the Sr/Ca ratio (Butler and Burns 1969, Behrens and Land 1972).

Sr contents in the range 10-152 ppm have been reported in saddle dolomites from several districts (see Spötl and Pitman 1998 and reference therein). Nielsen et al. (1998) reported Sr concentrations of 33 ppm (mean value) in both replacive and void-filling burial dolomites forming zebra-structures. Other authors reported Sr concentrations of a few tens of ppm in burial diagenetic dolomites (e.g. Mattes and Mountjoy 1980, Morrow et al. 1990, Barnaby and Read 1992, Montañez 1994).

All of the investigated dolomite samples have low Sr contents (see paragraph 6.3.1), which are incompatible with an origin as early dolomites directly precipitated from normal marine or evaporitic water. These low Sr contents suggest a late burial origin for both the replacive (Dol A1 and Dol A2) and the void-filling (Dol B) phases.

8.2.2 Na contents

A rigorous calculation of the theoretical k for Na in carbonates is unfeasible because variable amounts of Na are contained in carbonates as liquid and solid inclusions (Bein and Land 1983).

However, the k for Na in carbonates is thought to be very low (Land and Hoops 1973, Veizer et al. 1977, Brand and Veizer 1980, Veizer 1983).

As for Sr, Na contents can be used to distinguish between different dolomite types. In general early diagenetic dolomites have higher Na contents than late diagenetic dolomites (Brand and Veizer 1980, Land 1980, M'Rabet 1981). The high Na concentration of seawater may account for high Na contents in dolomites directly precipitated from seawater. Land and Hoops (1973) reported 1000-3000 ppm Na in modern dolomites from Florida, Bahamas, Arabian Gulf and Baffin Bay. On the other hand, late dolomites have typically only a few hundred ppm Na. Nielsen et al. (1998) reported 336 and 314 ppm Na (mean values) respectively in replacive and void-filling dolomites forming zebra-structures of late burial origin. Mattes and Mountjoy (1980) reported Na concentrations of 300 to 400 ppm in burial dolomites.

The low Na contents which characterise Dol A1, Dol A2 and Dol B from the study area (see paragraph 6.3.2) bear out a late origin for these phases in the burial environment.

8.2.3 Fe and Mn contents

The theoretical k for Fe and Mn in carbonates is greater than 1. This means that Fe and Mn tend to be picked up by carbonates during diagenesis (e.g. Brand and Veizer 1980, Veizer 1983). The studied dolomites have higher Fe and Mn contents than the host limestones (see paragraph 6.3.3). This is consistent with k for these two elements greater than 1 and with a diagenetic origin for the dolomites.

The positive covariation between Fe and Mn contents observed in the different dolomite phases (Fig. 18) is frequently reported in literature (e.g. Pierson 1981, Taylor and Sibley 1986, Barnaby and Read 1992). This covariation might reflect parallel changes of Fe and Mn concentrations in the dolomitising fluids.

The redox potential of the fluids is an important factor controlling the availability of Fe and Mn: reducing conditions favour the occurrence of these two elements in the fluids (Barnes and Back 1964, Edmunds et al. 1984, Barnaby and Rimstidt 1989). Consequently, early near surface dolomites commonly have very low Fe and Mn contents, since most near surface fluids are oxidising. On the other hand, late burial dolomites may have higher Fe and Mn contents, since most subsurface fluids are reducing (e.g. Land 1980, M'Rabet 1981, Barnaby and Read 1992, Morrow 1990a).

In conclusion, the reported Fe and Mn contents suggest a late burial origin for the studied dolomite phases, in a reducing environment.

The data also suggest that the dolomites are non-ferroan although they show an enrichment in Fe relative to the host limestones, because ferroan dolomites have Fe contents which exceed 10000 ppm (e.g. Morrow 1990a, Tucker and Wright 1990). This is consistent with the results of staining

(see paragraph 6.1) and with the dolomite CL pattern (see paragraph 5.2). Ferroan dolomites typically acquire a blue stain when treated for standard 40 seconds with potassium ferricyanide (Dickson 1966), and are non-luminescent regardless of their Mn contents (Pierson 1981). The terminations of Dol B2 crystals record the highest Fe contents, as they acquire a deeper blue colour after long duration staining (Plate 11, Ph. 3), and display a weaker CL (Plate 10, Ph. 1-3).

8.3 O and C stable isotope geochemistry

Secular variations in O and C isotope geochemistry of carbonates are well documented (e.g. Veizer and Hoefs 1976, Veizer et al. 1986, 1999, Grossmann 1994). An estimation of the isotope composition of Carboniferous seawater is necessary in order to interpret the isotope data of the studied carbonates. Grossmann (1994) published stable isotope ratios after Popp et al. (1986), measured in brachiopod calcite shells from the Upper Carboniferous of Spain. These ratios reflect the isotope composition of seawater, which precipitated the calcite shells. The calcite shells have $\delta^{18}O$ values (PDB) between –0,8 and –2,5‰ and $\delta^{13}C$ values between 5,2 and 6,1‰ (Fig. 41).
The host limestones analysed in this study approximate the $\delta^{13}C$ signature of Late Carboniferous seawater with only a slight depletion in ^{13}C. The large spread in the $\delta^{18}O$ values of the host limestones could reflect the effects of diagenesis: the $\delta^{18}O$ of marine carbonates is much more susceptible to changes during diagenesis than the $\delta^{13}C$ (e.g. Banner and Hanson 1990).
The calcite veins (CV) have $\delta^{13}C$ values buffered by the host limestones. The negative $\delta^{18}O$ values are typical of carbonates formed at high temperatures during burial (compare with Choquette and James 1990).
Theoretically, the $\delta^{18}O$ of dolomites which precipitate directly from seawater should be about 3‰ heavier than coeval marine calcites (Land 1980, 1985). Taking the $\delta^{18}O$ values of calcite shells precipitated from Late Carboniferous seawater (Grossmann 1994) and adding 3‰ to these values, the hypothetical isotope composition of marine dolomites precipitated from the same seawater is obtained. All of the dolomite samples investigated in this study are significantly depleted in ^{18}O relative to the hypothetical Upper Carboniferous marine dolomites (Fig. 41). Therefore, none of them represents a direct precipitate of Late Carboniferous seawater.
The $\delta^{18}O$ values of the different studied dolomite phases are comparable to those reported by several authors for late burial dolomites (e.g. Mattes and Mountjoy 1980, Zenger 1983, Gregg 1985, Taylor and Sibley 1986, Lee and Friedman 1987, Aulstead et al. 1988, Barnaby and Read 1992, Spencer-Cervato and Mullis 1992, Coniglio et al. 1994, Mountjoy et al. 1994, Qing and Mountjoy 1994b, Simo et al. 1994, Morrow and Aulstead 1995, Drivet and Mountjoy 1997, Nielsen

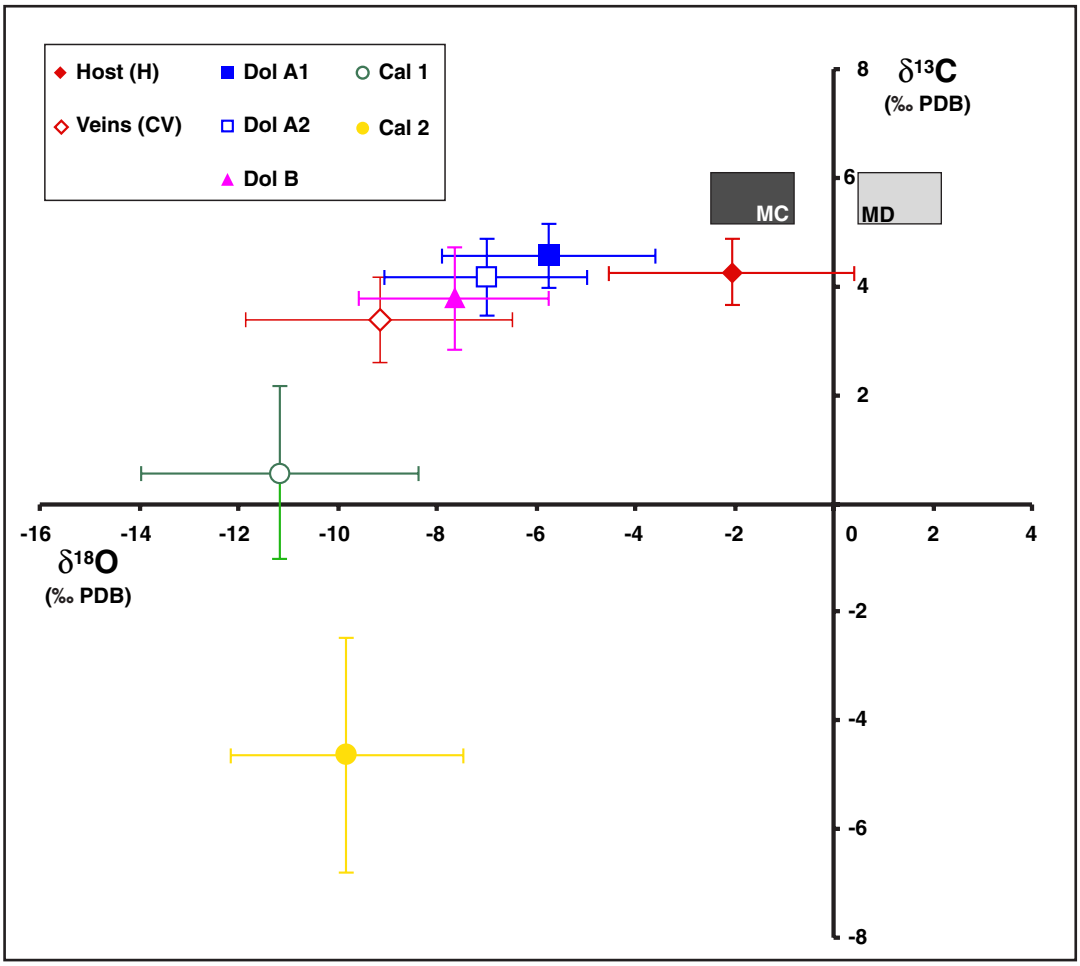

Fig. 41: O and C isotope composition of the different carbonate phases analysed. The isotope composition of Upper Carboniferous marine calcites (MC) from Spain (Grossman 1994) is reported together with the hypothetical isotope composition of coeval marine dolomites (MD). The composition of MD was inferred from MC by assuming a 3‰ difference in $\delta^{18}O$ between calcite and dolomite (Land 1980, 1985).

et al. 1998, Wendte et al. 1998, Boni et al. 2000). It can be concluded that the analysed dolomites are consistent with a burial diagenetic origin.

The dolomites have $\delta^{13}C$ values clearly buffered by the host limestones. This is the result of low concentrations of dissolved HCO_3^- in the dolomitising fluids and of the dominance of HCO_3^- derived by the dissolution of limestone calcite (Land 1985). There was no introduction of organic carbon during dolomitisation because dolomites associated with organic diagenetic processes have extremely variable $\delta^{13}C$ compositions (<-20 to 21‰ PDB; e.g. Kelts and McKenzie 1984, Burns and Baker 1987).

Cal 1 and Cal 2 exhibit wide-ranging and lower $\delta^{13}C$ values compared to the previously mentioned carbonates. This might reflect varying contributions of light organic C.

8.4 Sr isotope geochemistry

The $^{87}Sr/^{86}Sr$ ratios of seawater varied with time as a result of variation in Sr supply from different sources. The two main sources of Sr responsible for the $^{87}Sr/^{86}Sr$ variation in seawater are (Brass 1976, Elderfield 1986):

1. The hydrothermal alteration of basalts near the mid-oceanic ridge which provides Sr with relatively low isotope ratio of about 0,702;
2. The subaerial alteration of Rb-rich continental rocks which provides Sr with a higher isotope ratio (up to 0,718).

Several attempts have been done to reconstruct the variation of Sr isotope composition in seawater throughout the Phanerozoic by measuring the $^{87}Sr/^{86}Sr$ ratios of unaltered calcite shells of known age (e.g. Veizer and Compton 1974, Burke et al. 1982, Denison et al. 1994, Smalley et al. 1994, Veizer et al. 1999). The measured $^{87}Sr/^{86}Sr$ ratios are plotted against the time. The obtained curves illustrate the $^{87}Sr/^{86}Sr$ ratios of seawater of different ages. The most commonly used curves are those reconstructed by Burke et al. (1982) and Smalley et al. (1994).

In order to interpret the Sr isotope composition of the samples analysed in this study the measured $^{87}Sr/^{86}Sr$ ratios have to be compared with those of seawater.

The Sr isotope ratios of the analysed limestones from the Barcaliente Fm. fall within the range of $^{87}Sr/^{86}Sr$ ratios of Late Carboniferous seawater (Fig. 42). This means that the Barcaliente limestones effectively formed from marine water and any subsequent recrystallisation process occurred either with water of similar Sr isotope composition, or in a closed system relative to Sr (e.g. Banner et al. 1988, Banner 1995).

The $^{87}Sr/^{86}Sr$ ratios for Dol A1, Dol A2 and Dol B are mostly higher than those of Late Carboniferous seawater. This excludes the possibility of direct precipitation of the dolomites from Late Carboniferous seawater. Furthermore, the dolomites have $^{87}Sr/^{86}Sr$ ratios higher than those of seawater of most geological times (Fig. 42). Therefore, a radiogenic nature for the dolomitising fluids can be inferred.

Potential sources of radiogenic ^{87}Sr are detrital and igneous silicate minerals with high Rb/Sr ratios (Faure et al. 1963, Perry and Turekian 1974). The decay of ^{87}Rb to ^{87}Sr produces elevated $^{87}Sr/^{86}Sr$ ratios in these minerals. Release of radiogenic ^{87}Sr may occur as a result of albitisation or dissolution of alkali feldspar, dissolution of mica, conversion of smectite to illite, and interlayer cation exchange (Stueber et al. 1987, Chaudhuri and Clauer 1993).

The $^{87}Sr/^{86}Sr$ ratios of Cal 1 and Cal 2 are slightly higher than those of the host limestones and higher than seawater $^{87}Sr/^{86}Sr$ ratios of most geological times (Fig. 42). Therefore, a slight radiogenic nature could be inferred also for the fluids, which precipitated the calcites.

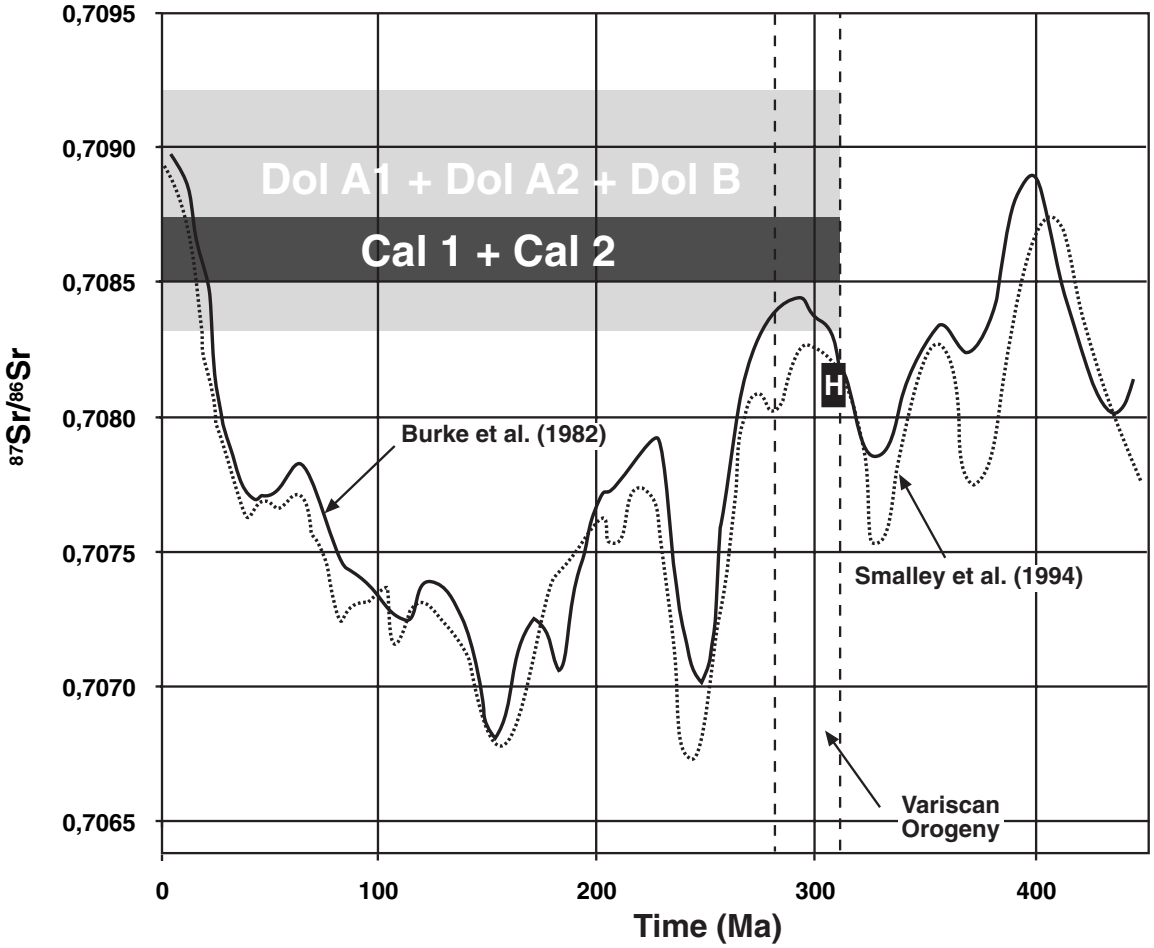

Fig. 42: $^{87}Sr/^{86}Sr$ variations of seawater throughout the Phanerozoic from Burke et al. (1982) and Smalley et al. (1994). The $^{87}Sr/^{86}Sr$ ratios measured in the Namurian host limestones of the Barcaliente Fm. are reported (black rectangle) together with the ratios measured in dolomites and calcites (grey bands).

8.5 Origin of stylolites and calcite veins (CV)

Three important factors could explain the occurrence of persistent stylolites especially in the Barcaliente and Alba Fms.: grain size, clay and organic content of the host limestones. Stylolites develop more uniformly in well bedded, fine grained limestones. Insolubles, such as clay and organic material, enhance chemical compaction in fine grained carbonates (Weyl 1959, Choquette and James 1990, Bathurst 1995). Organic matter and clays are abundant in the Barcaliente and Alba Fms. The massive, bioclastic, less bituminous and less argillaceous character of the Valdeteja limestones possibly prevented stylolite development.

The orientation of the stylolite peaks indicates that the axis of the principal stress responsible for the pressure-solution was perpendicular to the bedding planes. Therefore, the stylolitisation was

not related to tectonic compression, which would have produced stylolites with a more variable orientation and eventually several generations of them (e.g. Machel 1993, Bathurst 1995). It can be concluded that the stylolites developed prior to the onset of Variscan movements in the study area. They formed upon the natural lithostatic overburden, possibly at burial depths greater than 600-900 m (compare with Dunnington 1967, Choquette and James 1990).

The CV observed in the study area post-dated the stylolitisation (Plate 7, Ph. 1) and resulted from crack-seal mechanism. Their orientations vary widely (Plate 6, Ph. 3), indicating that at the time of crack opening the stress propagated from different directions (Ramsay 1980). The crack opening was likely related to the onset of Variscan movements. The cracks were filled by calcite and formed CV. This calcite precipitated in the burial environment as suggested by the low $\delta^{18}O$ values. The calcite and the host limestones have very similar C isotope composition (Fig. 41) and CL (Plate 7, Ph. 3). This suggests that the calcite precipitated from fluids strongly buffered by the host limestones.

Variously oriented calcite-filled cracks are reported from several Variscan areas of Europe. They are thought to be related to migration of fluids during compressional events of the Variscan tectonics (e.g. Muchez et al. 1995). A similar origin is proposed for the CV observed in the study area.

8.6 Type of dolomitisation

The studied dolomites are fabric destructive as demonstrated by the strongly overprinted precursor limestones, whose primary sedimentary structures and fossils are only locally recognised (Plate 2, Ph. 6).

The irregular morphology of the dolomite bodies (Plate 1, Phs. 1 and 3), which are often associated with discontinuities (Plate 1, Ph. 6), and the sharp limestone-dolomite contacts mostly cutting stratification and sedimentary structures (Plate 1, Phs. 4 and 5) suggest a late origin for the dolomites.

A burial origin is suggested by the presence of features commonly accepted as criteria for burial dolomitisation (e.g. Gregg and Sibley 1984, Gregg 1985, Taylor and Sibley 1986, Lee and Friedman 1987, Mountjoy and Amthor 1994), such as coarse crystallinity, non-planar texture and abundant saddle dolomite cements (see paragraph 5.2).

A late burial origin for the studied dolomites is confirmed by their geochemical signature as already discussed in paragraphs 8.1, 8.2 and 8.3.

Two main types of dolomitisation are recognised: a widespread replacive and a volumetrically minor void-filling. The replacive dolomitisation originated by the replacement of precursor

limestones. This is indicated by the halos of dolomite crystals scattered within the limestone mud at the contact with the massive dolomite (Plate 2, Phs. 4 and 5). This feature clearly demonstrates that the dolomite replaced the limestone, precluding the possibility that it is a neomorphic modification of earlier dolomites (compare with Mazzullo 1992, Montañez and Read 1992). The void-filling dolomitisation consisted in the precipitation of sparry dolomite, which filled cavities and fractures.

The dolomitising process was very effective. This is suggested by thin section microscopy indicating that the dolomite crystals do not contain mineral relics of the precursor limestones. Also the dolomite bulk mineralogy obtained by means of XRD analyses suggests that no calcitic fraction of the precursor limestones exists in the different dolomite phases.

8.7 Controls of the dolomitisation

Several authors reported a strict tectonic control on the dolomite occurrences of the CZ (Martínez-García 1981, Paniagua and Rodriguez-Pevida 1988, Gómez-Fernández et al. 1993, 2000, Crespo et al. 2000, Grimmer 2000, Tornos and Spiro 2000). However, they mostly refer to dolomites located in areas of the CZ away from the studied one. In the study area a tectonic control on the dolomite distribution is not so obvious where the dolomitisation affected large volumes of rocks. On the contrary, this is evident from less extensive dolomitised outcrops where the dolomite bodies occur directly on one or both sides of tectonic lineaments (Plate 1, Ph. 6). A clear structural control on dolomitisation is seen in the outcrops close to the Correcilla Thrust (Plate 5, Ph. 1), which possibly acted as a conduit for the dolomitising fluids. Occurrences of the studied dolomites may be controlled also by other rock discontinuities such as bedding, lamination and stylolite planes (Plate 2, Phs. 1-3). These facts support the idea that the dolomitising fluids migrated and spread through the sedimentary pile along discontinuities. Fluid migration was controlled firstly by the main tectonic lineaments of the area and then by bedding, lamination and stylolite planes of the precursor rocks.

The type of rock that comes in contact with the dolomitising fluids may also control the dolomitisation process (Murray and Lucia 1967, Bullen and Sibley 1984). In this case the physical and chemical features of the precursors control the dolomite distribution. Physical factors are for instance permeability, which influences the volume of fluid flowing through the pores, and particle size, which determines the amount of surface area available for fluid-rock interaction. Chemical factors, such as the solubility of carbonate minerals, may play a significant role as well.

In the study area the dolomitisation was also rock controlled: relatively pure limestones were preferentially dolomitised, whereas carbonates with siliciclastic rich intervals commonly escaped

the dolomitisation. This suggests that the permeability and the primary mineralogy of the precursors were outstanding factors, controlling the distribution of dolomitisation.

Some outcrops of dolomitised Porma Breccia give an example of rock controlled dolomitisation at the scale of hand specimens. The dolomitisation preferably affected the carbonate matrix of the breccia, whereas the breccia clasts are only sometimes affected and many of them remained undolomitised (Plate 2, Ph. 7). The carbonate matrix was finer grained, more porous and possibly more permeable than the embedded compact limestone clasts. Consequently, the matrix permitted the dolomitising fluids to flow more effectively and offered a greater active surface for the dolomitisation reaction to be triggered.

Dolomitised crinoidal limestones of the Valdeteja Fm. locally confirm the rock controlled character of the dolomitisation, as undolomitised crinoids may occur embedded in a dolomitic matrix. The phenomenon can be explained by the difference in grain size (i.e. porosity) between crinoids and limestone matrix (compare with Murray and Lucia 1967, Bullen and Sibley 1984).

8.8 Porosity development and dolomitisation

The relationship between porosity development and dolomitisation has widely been discussed because of the important role played by dolomites as reservoir rocks (Moore 1989, Dravis and Muir 1992, Purser et al. 1994a, c and references therein). At present most authors support the idea that dolomitisation “may generate, preserve or destroy porosity, depending on the fabrics and textures of the carbonates being replaced, rate, fluid composition, water-rock system and duration of the process” (Purser et al. 1994c).

Two main factors are considered responsible for the positive or negative effect of dolomitisation on porosity development: 1) the dissolution phenomena during dolomitisation, and 2) the precipitation of dolomite cements. 1) Porosity in dolomite rocks via dissolution is frequently formed, but its origin is not always contemporaneous or genetically related to the dolomitisation itself. Dissolution may pre-date dolomitisation (Sun 1992, Qing and Mountjoy 1994b) as well as post-date it (Barnaby and Read 1992, Dravis and Muir 1992). In both cases the dolomitisation is not responsible for the porosity enhancement. 2) Dolomite cements, by definition, have negative effects on the overall porosity development as they occlude pore spaces (Moore 1989, Purser et al. 1994c).

The porosity development in the studied dolomitised carbonates may be outlined considering the contribution of the different dolomite phases. In the closely packed mosaic of Dol A1 and Dol A2 only a minor intercrystalline porosity is created relative to the host limestones. On the other hand, an important vuggy porosity is formed, especially in the Dol A2 crystal mosaic. Thus, the porosity development in the replacive dolomites depended mostly on the process of dissolution which

created the vugs. This process affected only those parts of the carbonate sequence that have been dolomitised. It can be excluded that the dissolution took place prior to dolomitisation because in this case similar voids would be expected to occur also in the undolomitised parts of the sequence. The possibility of a dissolution process which took place after Dol A2 formation can be excluded as well. This is because reaction borders and corroded crystals are not present at the contact between Dol A2 and the subsequently precipitated Dol B (Plate 9, Phs. 1 and 2). In conclusion, the replacive dolomitisation and the dissolution process likely occurred contemporaneously. Therefore, the formation of Dol A2 had a positive effect on the porosity development. Subsequently, Dol B cements precipitated in cavities and fractures. Locally, this cementing event continued to the point that almost no vuggy porosity was left in the dolomitised rocks. Therefore, the amount of Dol B which precipitated after cavity development was an important factor controlling the whole rock porosity. However, the complete process of dolomitisation, comprising replacive and void-filling events, led to porosity and permeability enhancement relative to the tight precursor carbonates.

8.9 Origin of the zebra-structures

Banded structures like those observed in the studied dolomites are reported in literature with a variety of names: zebra-structures or zebra-dolomites (Beales and Hardy 1980, Wallace et al. 1994, Zeeh 1995, Nielsen et al. 1998, Boni et al. 2000), zebroid fabrics (Zenger 1983, Suchy et al. 1996), zebra-banding (Lugli et al. 2000), diagenetic crystallisation rhythmites (Fontboté and Amstutz 1983, Martín et al. 1987, Arne and Kissin 1989, Fontboté and Gorzawski 1990, Fontboté 1993) and banded or ribbon ores (Sass-Gustkiewicz et al. 1982, Tompkins et al. 1994).

These structures occur in various environments and they are often associated with carbonate-hosted sulphide deposits. Their origin is still controversial and interpretations vary from synsedimentary (e.g. Fontboté and Amstutz 1983) to early diagenetic (e.g. Beales and Hardy 1980, Martín et al. 1987), to late diagenetic (e.g. Zenger 1983, Arne and Kissin 1989, Fontboté and Gorzawski 1990, Fontboté 1993, Wallace et al. 1994, Suchy et al. 1996, Nielsen et al. 1998, Boni et al. 2000).

Many zebra-structures reported in literature are sub-horizontally aligned and concordant with the host rock stratification (Beales and Hardy 1980, Fontboté and Amstutz 1983, Zenger 1983, Martín et al. 1987, Fontboté and Gorzawski 1990, Suchy et al. 1996, Nielsen et al. 1998, Tompkin et al. 1994). A strict sedimentary facies control on the development of the zebra-structures has been reported from several authors (Beales and Hardy 1980, Martín et al. 1987, Tompkin et al. 1994). In the latter case the thickness and orientation of the zebra-structures were controlled by laminated layers, algal mats or evaporite laminae of the precursor limestones. In other cases the rhythmic

banding was not inherited from a former depositional rhythmicity (Arne and Kissin 1989, Fontboté and Gorzawski 1990, Fontboté 1993, Wallace et al. 1994, Suchy et al. 1996, Nielsen et al. 1998, Boni et al. 2000).

In the study area the host limestones lack former depositional rhythmicity at the zebra scale. Additionally, the described zebra-structures are often unconformably oriented relative to the bedding of the hosts (Plate 3, Phs. 1, 3 and 4). These facts exclude the possibility of a facies control on the formation of the zebra-structures. On the contrary, the orientation of the zebras is frequently controlled by fissures mainly sub-horizontally aligned (Plate 3, Ph. 3). Wallace et al. (1984) proposed the preferential formation of zebras along pre-existing fissure planes. The latter represent a “weakened” part of the rock through which fluids can more easily circulate. This interpretation matches the observations reported in the studied samples.

8.10 Timing and tectonic setting of the dolomitisation

Bedding parallel stylolites are never seen to affect dolomite crystals. Additionally, the stylolite traces are smoothened in the replacive mosaics of Dol A1 (Plate 7, Ph. 7) and Dol A2 (Plate 8, Ph. 4) and are commonly truncated by the void-filling Dol B (Plate 8, Ph. 7). This suggests that the dolomites post-dated the development of stylolites. The dolomitisation also post-dated the development of the CV as indicated by crosscutting relationships: the traces of the CV stop at the contact with the dolomite front. At this contact dolomite crystals substitute both the host limestone and the vein calcite (Plate 2, Ph. 5 and Plate 6, Ph. 4).

In the study area the youngest rocks affected by dolomitisation are Westphalian A limestones of the Valdeteja Fm. The age of these rocks gives a first lower constraint for the timing of dolomitisation.

Dolomite samples collected close to tectonic lineaments of Variscan age are not deformed. An example is given by the dolomite bodies which occur directly at the Correcilla Thrust (Plate 5, Ph. 1). Here the presence of open cavities and the lack of twins in the dolomite crystals suggest that the dolomitisation took place after thrust emplacement.

Absence of twins and crystal deformation also characterises dolomite samples from outcrops intensively folded by the Variscan Orogeny. Additionally, cavities and associated sparry dolomite sheets from folded outcrops have a relatively constant orientation, independent from the dip direction of the host layers (Plate 5, Phs. 2-4). In case the formation of cavities and sparry dolomite sheets pre-dated the Variscan folding, they should display various alignments in layers dipping differently. Therefore, the host rock underwent Variscan deformation and consequent folding prior to the formation of cavities and sparry dolomite sheets.

Outcrops where the dolomite is affected by tectonic disturbance are rare (Plate 6, Phs. 1 and 2). The faults responsible for dolomite deformation are of uncertain age and could have been activated anytime in the geological history of the study area.

All of the previous observations suggest that the dolomitisation likely occurred after the main compressional phase of the Variscan deformation in the study area, i.e. after thrust and fold emplacement. As reported in paragraph 2.4.3 thrust emplacement in the Bodón Unit occurred in the Wesphalian B. The deformation continued with the development of regional folds until the Stephanian B (Marcos et al. 1968b). Therefore, the dolomitisation possibly post-dated the Stephanian B. This interpretation is supported by the lack of massive dolomitisation in Stephanian sediments close to the study area (Ayllón, pers. commun.). The succession of the Ciñera-Matallana basin located S of the Bodón Unit (Fig. 3) begins with Stephanian B conglomerates containing carbonate clasts. These clasts derived from the erosion of Barcaliente and Valdeteja carbonates and do not show any dolomitisation. In case the dolomitisation affected the Barcaliente and Valdeteja carbonates prior to their exposure and consequent erosion, fully dolomitised clasts would be expected to occur in the conglomerates. The lack of dolomitised clasts suggests that the dolomitisation post-dated the Early Stephanian exposure.

In the study area ore minerals occur in the dolomite porosity in several mineralised localities (Plate 4, Ph. 6). This suggests that the mineralisation post-dated the dolomitisation. The ore fluids possibly used first the rock discontinuities and then the highly porous/permeable dolomites to circulate and to precipitate ore minerals.

Some of these dolomite-hosted mineralisations have been dated. Two U-Pb dating were accomplished by EPMA on Th-free uraninite grains associated to gesdorffite and vaesite in the Mina Profunda and to gersdorffite and pyrite in the Salamón gold deposit. These dating give ages of 273±11 Ma and 269±5 Ma respectively (Paniagua et al. 1993, Paniagua et al. 1996). Pb-Pb dating on samples of galena from the Mina Providencia and Mina Fontún give ages of 271±11 Ma and 269±11 Ma respectively (Paniagua et al. 1993, Paniagua et al. 1996). All of these deposits formed during the Early Permian, which represents, thus, the upper constraint for the timing of dolomitisation.

It can be concluded that the investigated dolomitisation occurred in a span of time comprised between the Late Stephanian and the Early Permian.

Each tectonic environment is accompanied by a specific style of strain cycling, manifested by the opening and closing of appropriately oriented fracture systems (Muir Wood 1994). The orientation of sheet-like cavities and associated sub-vertical cracks frequently reported in the studied dolomites (Plate 3, Ph. 7) can therefore reveal the particular tectonic style of deformation in which they generated. In an extensional tectonic environment high angle fractures undergo dilation as a result of horizontal strain. Following fault rupture these high-angle cracks partially close, expelling

fluid from the rock and forming sub-horizontal cracks (Fig. 43; Muir Wood 1994). Therefore, the geometric features reported from the studied samples suggest that they formed in a setting mainly governed by extensional tectonics.

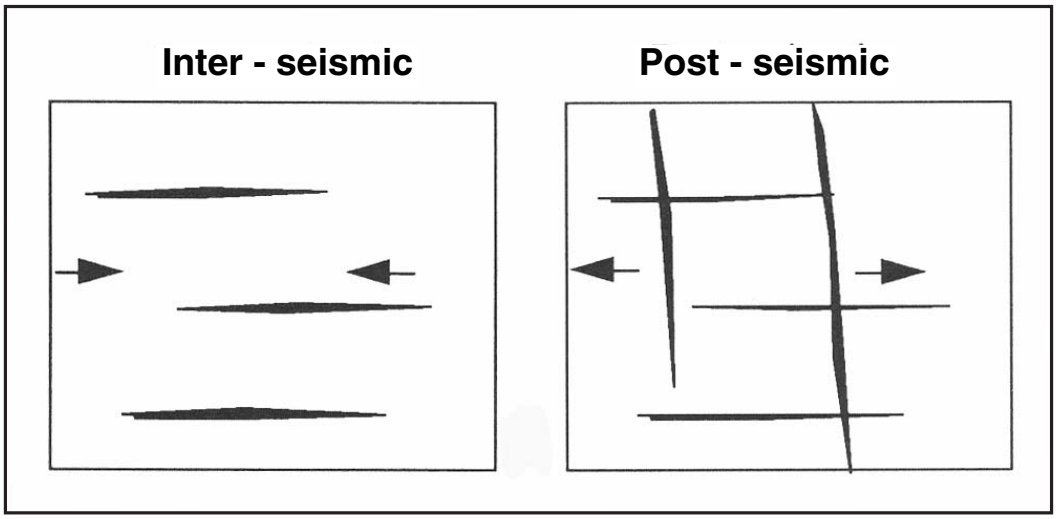

Fig. 43: View in section of idealised fracture dilation accompanying strain-cycling in an extensional tectonic environment (Muir Wood 1994).

8.11 "Openness" of the dolomitising system (water/rock ratio)

The distribution of trace elements can be uniform through a mineral phase if the trace/major ion ratios do not change during precipitation (Machel and Burton 1991). This is governed by the "openness" of the fluid system. In open systems where the water supply is considered unlimited and the rates of flow can be relatively high, carbonate cementation and replacement have no relevant effect on the fluid composition (Machel and Burton 1991). As a consequence trace element variation in the fluid will be negligible and the resulting mineral will show a constant and unzoned CL. On the other hand, trace element contents in the mineral phase will change during crystal growth if the system is closed. Consequently, the crystals will have a zoned CL.

The different dolomite phases analysed exhibit constant CL colour and intensity in all of the studied samples. The only exception is represented by the outermost part of the Dol B2 crystals, which is commonly zoned. The latter is, however, volumetrically insignificant relative to the whole amount of dolomite.

Regional or stratigraphic trends in the geochemistry of the studied dolomites are not observed: dolomite samples from different localities and formations have similar elemental and isotopic geochemical compositions (see Chapter 6). Therefore, neither the different mineralogy of the

precursor rocks nor the various depths at which the rocks were buried at the time of dolomitisation influenced the geochemistry of the fluids.

All of the previous observations lead to the conclusion that the dolomitising fluids were characterised by homogeneous composition and circulated in an open system, thus characterised by relatively high water/rock ratios. This is confirmed by the Sr-$^{87}Sr/^{86}Sr$ and $\delta^{18}O$-$^{87}Sr/^{86}Sr$ inverse covariations observed from the host limestones towards the dolomites (Figs. 23 and 24). These covariations are considered typical of fluid dominated systems (Banner et al. 1990, Banner 1995). The lack of $\delta^{13}C$-$^{87}Sr/^{86}Sr$ covariation (Fig. 25) indicates that the $\delta^{13}C$ of the dolomites was inherited from the host limestones in spite of the high water/rock ratios of the system, since C has a relatively low abundance in most aqueous fluids (e.g. White et al. 1963).

8.12 Thermal conditions of the dolomitising fluids

A first estimation of the thermal conditions which characterised the dolomitisation is given by the dolomite textures. The temperature of crystal growth is an important control on dolomite texture (Gregg and Sibley 1984). According to the crystal growth theory, a smooth crystal surface is energetically favoured at low temperatures. This results in planar-e to planar-s crystal mosaics. Above a “critical roughening temperature” (CRT), a rough surface is energetically favoured resulting in non-planar crystal mosaics. The CRT for dolomite is fixed above 50 °C. Therefore, non-planar dolomites form at temperatures above 50 °C (Gregg and Sibley 1984).

Saddle dolomite is frequently associated with hydrocarbon reservoirs. This suggested temperature of formation within the oil window (60-150 °C, Radke and Mathis 1980). At present it is believed that saddle dolomite requires minimum temperatures of 60-80 °C, although most occurrences formed between 90 and 160 °C (Machel 1987, Spötl and Pitman 1998).

Thin section microscopy revealed a dominant non-planar texture for Dol A1 and Dol A2. The latter exhibits a saddle nature in coarser crystalline samples. Dol B has a dominant non-planar texture and is always of the saddle type regardless of the crystal size (see paragraph. 5.2). Therefore, temperatures of formation higher than 50 °C are suggested for both replacive and void-filling dolomite phases, with the saddle occurrences pointing to even higher temperatures.

This temperature estimation from dolomite textures is in agreement with microthermometry results for both Dol A2 and Dol B: most of the primary FIs measured in these two phases have Th higher than 100 °C (Fig. 28).

The dolomitisation occurred at depths of a few kilometres at most (see Table 9), where the rocks are characterised by relatively high porosity. This suggests that hydrostatic pressure conditions may have prevailed during dolomitisation. Therefore, FI trapping temperatures calculated by

assuming a hydrostatic gradient approximate the real conditions of dolomitisation better than the temperatures calculated by assuming a lithostatic gradient (see paragraphs 7.10).

Further considerations on the geothermal gradient in the study area are necessary to better constrain the thermal conditions of dolomitisation. FI trapping conditions were calculated using a geothermal gradient of 35 °C/km (see paragraphs 7.10). García-López et al. (1997) and Brime et al. (2001) suggested the same gradient for the Sobia-Bodón Unit at the time of peak burial in the Westphalian. In the CZ a thermal peak occurred in Late Stephanian and especially Early Permian times, when crustal thinning, intense volcanism and sparse magmatism took place in a predominantly extensional setting (see paragraphs 2.3.3 and 2.3.5). Aller (1986) invoked a "high geothermal gradient at the transition from Carboniferous to Permian" to explain metamorphism and cleavage in the Central Coal Basin Unit. However, this author does not give any estimation of the gradient. Frings (2002) investigated palaeotemperature anomalies of the Stephanian Ciñera-Matallana basin and proposed a geothermal gradient for the Stephanian succession approaching 85 °C/km. This high gradient is thought to be related to Permian magmatic activity localised within the Stephanian succession and cannot be extrapolated to areas outside the basin.

The timing inferred for the dolomitisation (see paragraph 8.10) coincides with the occurrence of this thermal peak. Consequently, the geothermal gradient of the study area at the time of dolomitisation was likely higher than the gradient of 35 °C/km used for the calculation of pressure correction. 35 °C/km is the lowest possible gradient for the study area at the time of dolomitisation and the trapping temperatures (Tt) calculated by means of this gradient are the maximum possible temperatures for the dolomitising fluids. This is illustrated in Fig. 44, where the P-T trapping conditions of a FI of known density and Th are graphically derived for two different geothermal gradients (G1<G2). It can be seen that the lower the gradient chosen for the calculation, the higher the obtained P-T trapping conditions ($Pt_1>Pt_2$, $Tt_1>Tt_2$). Therefore, the real temperatures of dolomite formation in the study area were comprised between the measured Th and the temperatures corrected for the hydrostatic pressure with a gradient of 35 °C/km (see Table 9). This has to be considered when using the "corrected" Th values to characterise the O isotope composition of the dolomitising fluids (see paragraph 8.13).

Regional comparison of FI data indicated relatively homogeneous thermal conditions for the dolomitisation process. Only slight differences in Th from one locality to another are recorded by FIs in Dol B (see paragraph 7.4). The trapping temperatures for these FIs calculated in hydrostatic conditions are higher in the middle of the study area compared to the western and southeastern extremities by 35 and 17 °C respectively (see paragraph 7.10.2). This difference in trapping temperatures could have been caused by:

1. Difference in burial depths of the samples collected at the different localities;

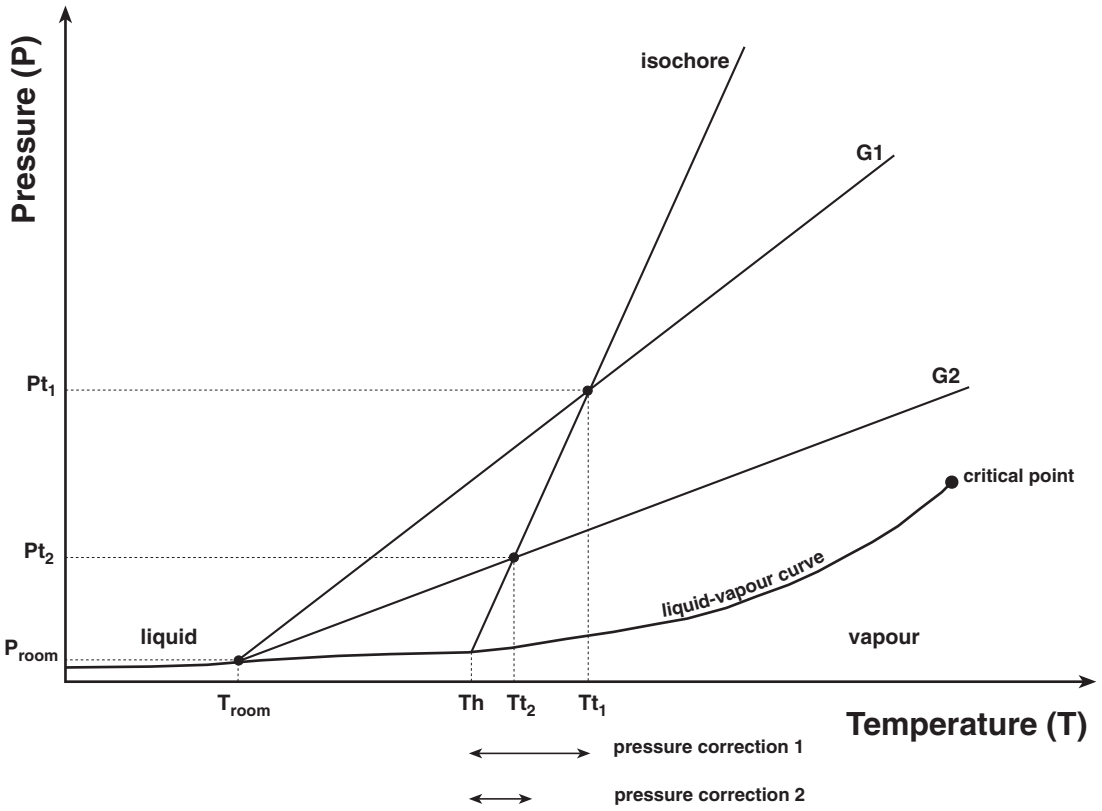

Fig. 44: P-T trapping conditions of a FI of known density and Th for two different geothermal gradients (G1<G2).

2. Difference in the geothermal gradient in correspondence of the different localities;
3. Difference in distance of the different localities from the source of the fluids.

In case 1. the higher temperatures of the fluid would reflect greater burial depth of the samples. There is lack of information in literature on the sedimentation and exhumation history of the study area after the Variscan nappe emplacement. Due to the complex superposition of the nappes, the different areas were affected after Stephanian exposure by differential erosion (Aramburu and Bastida 1995). Additionally, the scarcity of Stephanian and Permian deposits in the study area prevents the evaluation of their original thickness. Consequently, the burial depth of the samples in the different localities at the time of dolomitisation cannot be constrained.

In case 2. the higher temperatures of the fluid would reflect a higher geothermal gradient. Differences in the geothermal gradient from one locality to an other at the time of dolomitisation should be invoked. This cannot be proved because, as previously mentioned, there is lack of information on the geothermal gradient in the CZ during Stephanian and Permian times.

In case 3. the different temperatures would reflect the fluid-flow provenance, with the higher temperatures corresponding to the areas closer to the source of the fluids.

With the present knowledge none of the three mentioned possibilities can be demonstrated to be the most realistic, and any combination of the three is possible.

Whatever the cause of the difference in trapping temperatures, it is interesting to note that the middle of the study area, where the highest temperatures were reported, coincides with the most dolomitised region (see paragraph 4.1). This region is close to an important net of fractures associated with the León Fault.

8.13 Nature of the dolomitising fluids

The study of primary FIs indicated that the dolomitising fluids were highly saline brines with important concentrations of Mg, Na and Ca (see paragraph 7.8.1). The salinity calculated for FIs in both Dol A2 and Dol B is several times greater than salinity of modern seawater (≈3,5 eq. wt % NaCl).

Sr isotopes can be of great utility in constraining the source of dolomitising fluids (e.g. Mountjoy and Qing 1992, Mountjoy and Amthor 1994, Machel and Cavell 1999). The Sr isotope ratios measured in the studied carbonates can be better interpreted if compared to the ratios of potential Sr reservoirs (Fig. 45).

The $^{87}Sr/^{86}Sr$ ratios of Late Carboniferous - Early Permian seawater range between 0,7080 and 0,7085 (Burke et al. 1982, Smalley et al. 1994). The $^{87}Sr/^{86}Sr$ ratios calculated for the Peña Prieta stock and corrected to 270-275 Ma range between 0,7045 and 0,7069 (Gallastegui, written commun.). These low values are in agreement with the intermediate to basic nature of the intrusions. Precambrian to Middle Devonian shales which crop out all over the CZ have $^{87}Sr/^{86}Sr$ ratios corrected to 270-275 Ma, which range between 0,7090 and 0,7731 (Nägler 1990).

Both replacive and void-filling dolomites from the study area are slightly richer in radiogenic ^{87}Sr than the host limestones, which in turn reflect the Sr isotope composition of Late Carboniferous seawater (Fig. 42). The same is reported for Carboniferous carbonates hosting a talc deposit in the southeastern Central Coal Basin Unit (Tornos and Spiro 2000). It can be inferred that crustal materials, rich in Rb-bearing minerals, contributed with radiogenic ^{87}Sr to the dolomitising fluids. The $^{87}Sr/^{86}Sr$ ratios measured for the igneous rocks are distinctly lower than those of the investigated dolomites. Therefore, a contribution of Sr derived from igneous rocks could not explain the radiogenic character of the dolomites. Only the Precambrian to Middle Devonian shales have $^{87}Sr/^{86}Sr$ ratios distinctly higher than those of the studied dolomites. These siliciclastic materials were the most possible source of radiogenic ^{87}Sr.

It is not possible to determine the O isotope composition of a mother fluid only from the isotope composition of the precipitated mineral phase, since O isotope fractionation depends on both composition and temperature of the fluid. However, if the precipitation temperature of the mineral phase is also known, the isotope composition of the fluid can be determined.

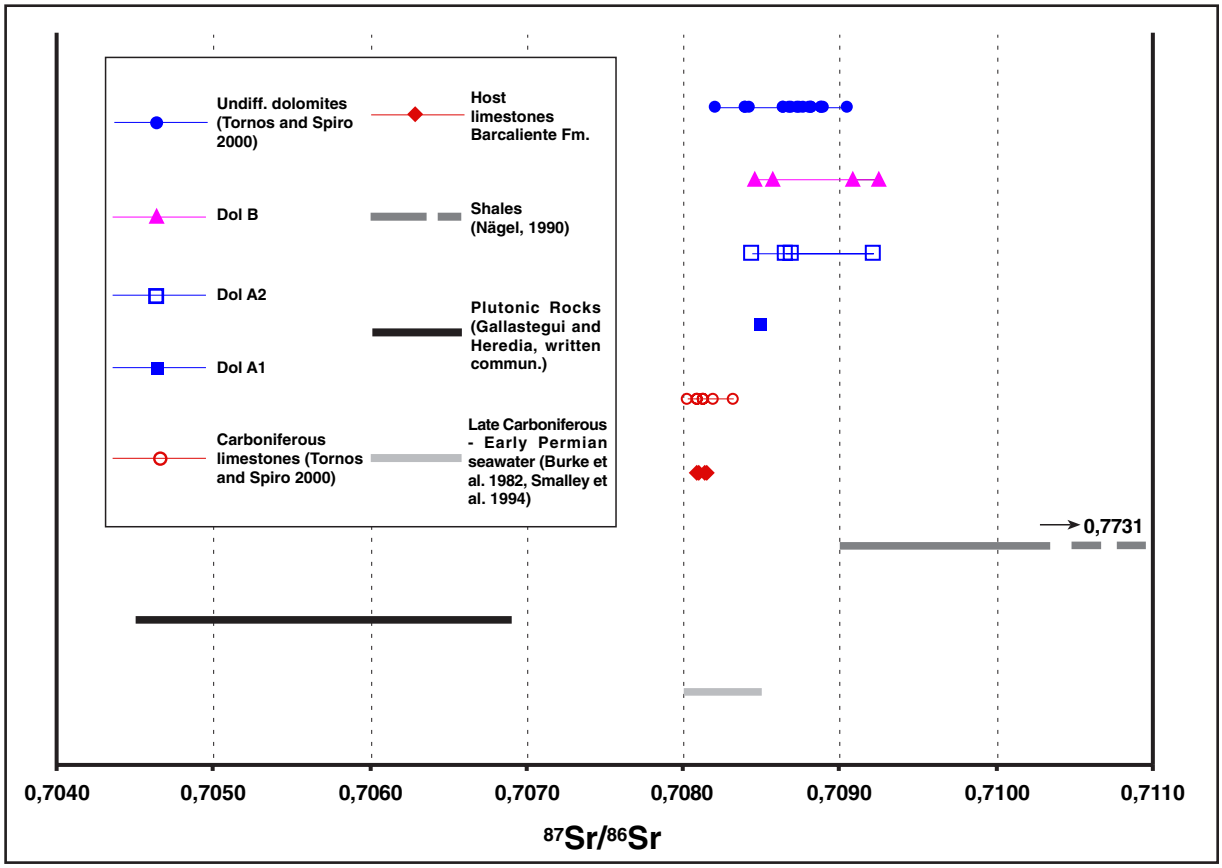

Fig. 45: The $^{87}Sr/^{86}Sr$ ratios of the different analysed phases are compared with the ratios of possible Sr reservoirs corrected to 270-275 Ma. $^{87}Sr/^{86}Sr$ ratios for Carboniferous carbonates from the Central Coal Basin Unit are also reported.

The temperatures of dolomite precipitation were estimated from FI microthermometry (see paragraph 7.10). It is therefore possible to combine microthermometry and isotope data to characterise the O isotope composition of the dolomitising fluids.

The relationship between the $\delta^{18}O$ of dolomite, the temperature of dolomite precipitation and the $\delta^{18}O$ of the dolomitising fluid was calculated using the equation of Land (1983):

$$10^3 \, \mathrm{Ln} \, \alpha_{\text{dolomite-water}} = 3{,}20 \cdot 10^6 \, T^{-2} \, (°K) - 3{,}30 \qquad (9)$$

where α is the O isotope fractionation coefficient between dolomite and water.

The range of FI trapping temperatures calculated in hydrostatic conditions for a geothermal gradient of 35 °C/km (see Table 9) was plotted versus the range of $\delta^{18}O$ values of dolomite samples, for which microthermometry was accomplished (Fig. 46).

$\delta^{18}O$ of Dol A1 mother fluid cannot be calculated as no FI data are available for this phase (see paragraph 7.1.2). The mother fluid of Dol A2 had $\delta^{18}O$ between about 2 and 9‰ SMOW. The mother fluid of Dol B had $\delta^{18}O$ between about 0 and 10‰ SMOW (Fig. 46). Therefore, the fluids which formed Dol A2 and Dol B had similar O isotope composition.

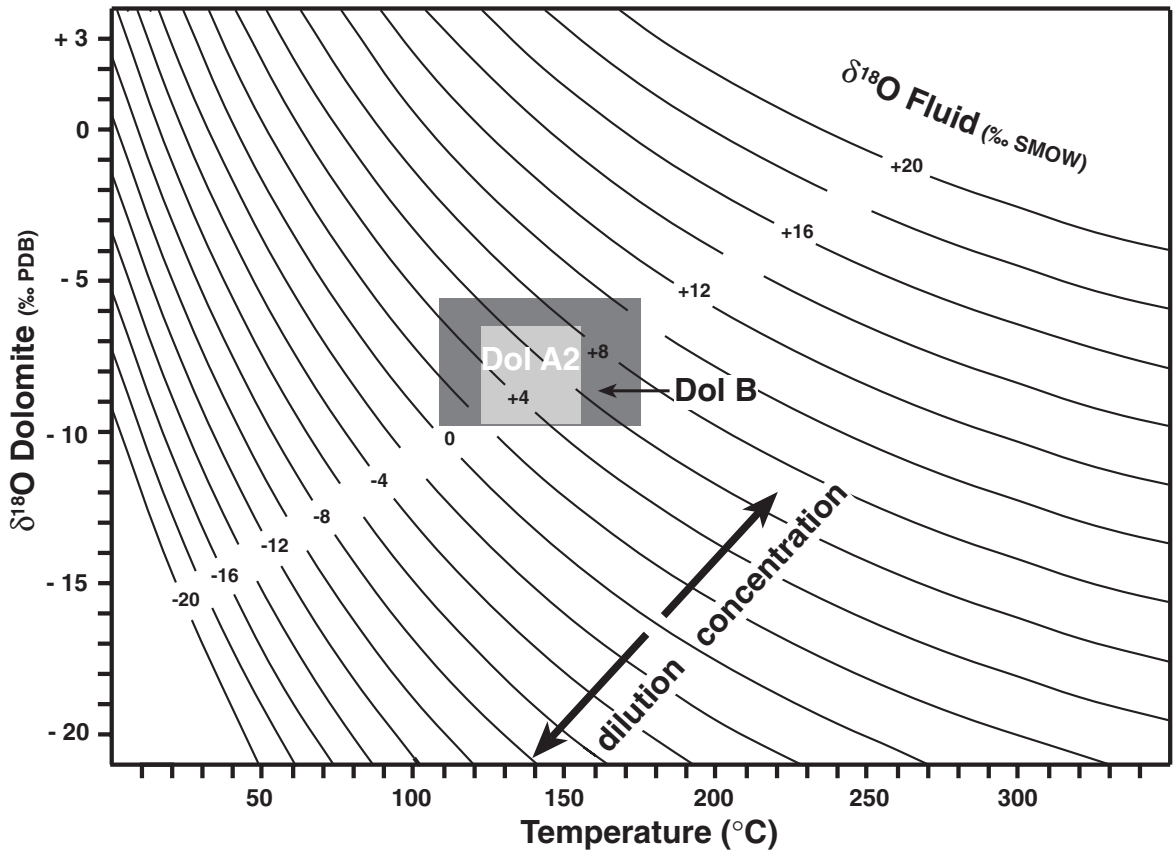

Fig. 46: Plot of precipitation temperature versus $\delta^{18}O$ values of Dol A2 and Dol B. The $\delta^{18}O$ composition of the fluid in equilibrium with dolomite as function of the temperature was calculated using the fractionation equation of Land (1983).

These $\delta^{18}O$ values have to be compared with those of different possible sources of fluid. The $\delta^{18}O$ of Late Carboniferous - Early Permian meteoric water from the Iberian Central System was between –10 and –6‰ SMOW (Tornos et al. 2000). Late Carboniferous – Early Permian seawater was characterised by $\delta^{18}O$ in the range –3 to 1‰ SMOW (Grossmann 1994). The $\delta^{18}O$ of magmatic waters associated with Early Permian intrusions was between 7,0 and 9,2‰ SMOW. The latter values were calculated from $\delta^{18}O$ of igneous rocks from the Carlés intrusion (Arcos 1996), using the fractionation factor between granodiorite and water from Cole (1994).

Meteoric waters can be ruled out as possible source of fluids for the studied dolomitisation because of their strongly negative $\delta^{18}O$ values, which are inconsistent with those reported for the dolomitising fluids. Moreover, meteoric waters carry soil CO_2 and commonly have a negative $\delta^{13}C$ signature, which is not recorded by any of the studied dolomite samples.

Although with some overlap, the $\delta^{18}O$ values of the dolomitising fluids are mostly lower than $\delta^{18}O$ values of the magmatic waters. This fact together with the scarcity of igneous rocks close to the study area and with their already mentioned low $^{87}Sr/^{86}Sr$ ratios rule out a magmatic origin for the dolomitising fluids.

Therefore, the $\delta^{18}O$ values of the dolomitising fluids could more likely reflect an origin from Late

Carboniferous – Early Permian seawater enriched in ^{18}O. This enrichment in ^{18}O is consistent with the fluids having salinity higher than normal seawater, as there is a good covariation between salinity and ^{18}O abundance in natural waters. Fluids with $\delta^{18}O$ higher than modern seawater (0‰ SMOW) commonly reflect concentration, whereas fluids with $\delta^{18}O$ values lower than this are the result of dilution (e.g. Hitchon et al. 1971). Main processes to explain the concentration of ^{18}O and salts in natural waters are evaporation and water-rock interaction.

Strong evaporation may occur in restricted basins especially in arid climatic conditions. Evaporation involves mainly the lighter ^{16}O. Consequently, ^{16}O is concentrated in the vapour, whereas the liquid is relatively enriched in ^{18}O (Lloyd 1966, Knauth and Beeunas 1986). Contemporaneously, seawater becomes more concentrated. As evaporation proceeds precipitation of gypsum may occur creating hypersaline brines. These are characterised by higher densities and Mg/Ca ratios than normal seawater (Morrow 1978, Land 1985).

Formation waters become progressively more saline and enriched in ^{18}O because of fluid-rock interaction at high temperatures with ^{18}O-rich carbonate and silicate minerals (Clayton et al. 1966, Hitchon et al. 1971, 1990, Land and Prezbindowski 1981, Kharaka and Carothers 1986, Morton and Land 1987). Dewatering of detrital rocks and shale membrane filtration can produce saline fluids (Graf 1982). Significant amounts of Mg^{2+}, Na^{+}, Ca^{2+}, Fe^{2+} and Cl^{-} can be released from clay mineral diagenesis (Perry and Hower 1970, Weaver and Beck 1971, Hiltabrand et al. 1973, Michalik 1997).

In conclusion, the dolomitising fluids were marine-derived solutions with high $\delta^{18}O$ values and high salinities relative to normal Late Carboniferous – Early Permian seawater. They were hypersaline brines comparable to formation waters or evaporated seawater, which acquired radiogenic ^{87}Sr by interaction with siliciclastic rocks.

8.14 Replacive versus void-filling dolomitisation

As already stated the studied dolomitisation resulted in replacive and void-filling events. The former produced Dol A1 and Dol A2, whereas the latter gave origin to Dol B. The aim of the following paragraphs is to interpret peculiarities of these dolomite phases and to sketch their emplacement mechanisms.

8.14.1 Origin of Dol A1 and Dol A2

As the dark bands of Dol A1 are frequently associated with stylolite planes (Plate 4, Phs. 2 and 5) it could be inferred that Dol A1 originated as a consequence of pressure-solution. Dolomite crystals growing along stylolites have been frequently reported (e.g. Ohle 1951, Wanless 1979,

Mattes and Mountjoy 1980, Zenger 1983, Miller and Folk 1994). However, in many cases the dolomite formation is not related to the pressure-solution process and the stylolite planes are interpreted as the conduits for the dolomitising fluids (Zenger 1983, Miller and Folk 1994).

The stylolites in the studied samples display traces smoothened by the Dol A1 crystal growth (Plate 8, Phs. 4 and 6). Furthermore, dolomites related to pressure-solution are characteristically rhombic and ferroan (Wanless 1979). Neither of these two features are typical of Dol A1. Therefore, the origin of Dol A1 was not related to pressure-solution. In order to interpret the origin of the banding described in paragraph 4.2.3 emplacement mechanisms for Dol A1 other than pressure-solution have to be invoked. Two possible scenarios are proposed.

Scenario 1. The emplacement of Dol A1 was related to the circulation of fluids along discontinuities (e.g. stylolite planes), from which the process of dolomitisation started. Different dolomitising pulses produced Dol A1 and Dol A2 respectively. A first pulse affected only the rock volume close to the discontinuities (Plate 2, Phs. 2 and 3) and its efficiency decreased with distance from these starting planes. Consequently, Dol A1 crystals formed pervasively along the discontinuities and decreased in density away from them. A second and more important dolomitising pulse affected the whole precursor rock and formed Dol A2.

Dol A1 and Dol A2 are geochemically indistinguishable (see Chapter 6). They can be differentiated only by macroscopic and textural features (see Chapters 4 and 5). Consequently, the two invoked dolomitising pulses corresponded to fluids of similar composition, or alternatively the second pulse, which formed Dol A2, completely overprinted the geochemistry of the former Dol A1.

Scenario 2. Dol A1 and Dol A2 formed during a common dolomitising pulse by the circulation of the same fluid. This fluid interacted with a heterogeneous substrate due to variability in coarseness and/or impurity content of the precursor limestone particles. In this scenario the textural differences between Dol A1 and Dol A2 would reflect differences in nucleation sites of the parent limestone, prior to dolomitisation (see Gregg and Sibley 1984, Sibley and Gregg 1987).

The normal grading commonly reported in the Barcaliente Fm. limestones suggests the presence of particle size heterogeneity. This would also explain why the banding is found mostly in the dolomites of the lower Barcaliente Fm.: the grading is the predominant structure in the lower part of this formation and diminishes in importance in the upper part (see paragraph 2.4.2).

Scenario 2 is most likely the case as the emplacement mechanism for Dol A1 and Dol A2 based on different dolomitising pulses (scenario 1) would not fully explain the occurrence of Dol A1 bands almost exclusively in the lower part of the Barcaliente Fm.

Assuming scenario 2 as the most plausible, Dol A1 and Dol A2 can be considered as the products of the same replacive event, thus representing only two different textural types of the same dolomite phase.

8.14.2 Origin of Dol B

Reaction borders and corroded crystals were never observed at the contact between Dol A2 and Dol B. Furthermore, the transition from Dol A2 towards Dol B is frequently gradual (Plate 9, Phs. 1 and 2). The replacive and void-filling dolomites exhibit the same CL. Additionally, they have very similar elemental and isotopic composition. No consistent trend in $\delta^{13}C$ and $^{87}Sr/^{86}Sr$ values was observed when comparing different dolomite phases from the same rock sample (Figs. 21 and 22). Only more negative $\delta^{18}O$ values were commonly reported in the void-filling Dol B (Fig. 20). FI investigation indicated very similar composition and temperatures for the fluids which formed Dol A2 and Dol B (see paragraphs 7.3.1 and 7.3.2).

All of the previous observations indicate that the different dolomite phases have a very similar geochemical signature. This suggests rather constant physico-chemical conditions during their formation. A continuous dolomitisation process which evolved from a replacive stage towards a void-filling stage in a nearly isochemical system can be postulated. In this case, the studied replacive and void-filling dolomites formed from a common fluid in evolution.

The slight depletion in ^{18}O from replacive towards void-filling dolomites belonging to individual rock samples could be the result of:

1. Temperature increase of the dolomitising fluid;
2. Contamination of the dolomitising fluid by a solution more depleted in ^{18}O;
3. Increase in the water/rock ratio of the dolomitising system.

The possibility that the fluid became hotter during its evolution from replacive towards void-filling stage can be ruled out because FI microthermometry for Dol A2 and Dol B from the same rock sample did not indicate any consistent temperature variation.

The hypothesis that the fluid was contaminated while forming the different phases by a solution more depleted in ^{18}O has to be rejected because no contamination can be observed affecting the geochemistry and CL of the subsequent dolomite phases.

The depletion in ^{18}O of Dol B is better explained with increased water/rock ratios of the dolomitising system. Dol B precipitated in open spaces, thus in an environment characterised by greater permeability and possibly higher water/rock ratios. Therefore, Dol B received a greater contribution of O from the dolomitising fluid than the replacive dolomites (see also Spencer-Cervato and Mullis 1992).

8.14.3 Origin of Dol B2 “reentrants”

Saddle dolomite crystals with a stepwise shape like those observed in the studied samples (Plate 9, Phs. 6 and 7) have been interpreted to result from tectonic instability of the crystal growth environment (e.g. Nielsen et al. 1998). In the studied samples the reported “reentrants” are not

caused by tectonic instability because no real displacement of the crystal segments is developed. The “reentrants” possibly formed by inhibition of the crystal growth. This may be caused by a process of “poisoning” and/or by the presence of structural defects. “Poisoning” implies contamination of the dolomite growth surface (or part of it) by components, which are not easily incorporated into the dolomite lattice (Machel, pers. commun.). On the other hand, the presence of structural defects is very common in minerals growing in natural environments.

8.14.4 Origin of Dol B2 zones

The terminations of Dol B2 crystals are usually zoned. The most common type of CL zonation consists of a darker red zone, which may coincide with a clear inclusion-free rim or with a hydroxide zone (Plate 10, Phs. 1-3). The terminations of Dol B2 crystals contain therefore more Fe, as also indicated by the results of long duration staining (Plate 11, Ph. 3). This iron enrichment towards the last stage of Dol B2 crystal growth is also recorded in crystals which lack hydroxide zones (Plate 10, Ph. 2). Therefore, the higher Fe content is a primary feature of the Dol B2 crystal terminations and did not depend on the development of hydroxide zones.

It could be suggested that the hydroxide zones formed by direct precipitation from a fluid upon growing dolomite crystals. However, the crystallographic orientation of these zones is identical to the one of the host crystals. Since hydroxides cannot grow as rhombohedral zones (Katz 1971), an origin by direct precipitation is unlikely. The hydroxide zones formed possibly as pseudomorphs of dolomite zones relatively rich in Fe, by later oxidation. The occurrence of dolomite relics within the hydroxide zones (Plate 9, Phs. 6 and 7) confirms this interpretation: only a pseudomorphic origin of the hydroxides on dolomite under oxidation could explain the presence of dolomite relics floating in a hydroxide mass (see Katz 1971).

8.15 “Hydrothermal” dolomitisation?

As mentioned in paragraph 1.2 the term “hydrothermal” dolomitisation should be used only for those dolomites which formed from fluids hotter than the ambient rocks (Machel and Lonnee 2002).

In the study area it is not possible to determine the burial temperature of the ambient rocks at the time of dolomitisation. This is because neither the geothermal gradient nor the burial depth of these rocks is known (see paragraph 8.12). However, the maximum temperature ever reached by the undolomitised Carboniferous carbonates from the study area can be derived from CAI (Conodont Alteration Index) values. The colour alteration of conodonts changes progressively with increasing temperatures and is irreversible. It is used to determine the peak temperature

experienced by the rocks which host the conodonts (Epstein and Harris 1977).

Raven and Van der Pluijm (1986) published CAI values for Carboniferous carbonates from the study area. The Alba Fm. has CAI mean values of 2,9 at Caldas, 1,5 at Millaró, 1,3 at Genicera, 1,8 at Tolibia de Abajo, 1,5 at Valdecastillo, 1,3 at the Porma Lake, 2,8 at Piedrasecha and 1,7 at Valporquero. The Barcaliente Fm. has CAI mean value of 1,5 at the Porma Lake. The Valdeteja Fm. has CAI mean value of 1,6 at Valdeteja.

These CAI values were converted into temperatures by means of conversion tables (after Epstein and Harris 1977). The maximum temperatures experienced by the Carboniferous carbonates from the study area are mostly lower than 70-95 °C. These temperatures are distinctly lower than those of dolomite precipitation inferred from FI study (see Chapter 7).

In conclusion, the studied dolomitisation was due to the circulation of a “hydrothermal” fluid (sensu White 1957) through the subsurface rocks.

8.16 Comparison with dolomites from other tectonic units of the CZ

As underlined in paragraph 4.1 large dolomite bodies crop out in several other tectonic units of the CZ. These dolomites mainly occur in Carboniferous rocks. They are spatially related to tectonic discontinuities and shear many macroscopic features with the dolomites from the study area, such as sharp contacts with the precursor carbonates, coarse crystallinity, development of vuggy porosity, etc. They also exhibit a similar paragenesis with the development of replacive mosaic dolomites and sparry dolomites, filling cavities and fractures. The aim of the present paragraph is to compare the main features of these dolomites with those from the study area.

- In the southeasternmost Central Coal Basin Unit the organic-rich carbonates of the Lena Group (Namurian C - Westphalian D) and the carbonate breccias and olistolites of the Maraña Group (Westphalian D - Lower Cantabrian) are locally dolomitised. They are the host lithologies of As-Sb-Au deposits (Paniagua et al. 1996, Crespo et al. 2000). The Salamón gold deposit, located on the León Fault, is the most important. Here, the precursor limestones have $\delta^{18}O$ between –5,2 and –3,8‰ PDB and $\delta^{13}C$ between 3,0 and 5,5‰ PDB. The dolomites have $\delta^{18}O$ between –12,9 and –4,7‰ PDB and $\delta^{13}C$ between 3,9 and 4,1‰ PDB (Paniagua et al. 1996). The isotope geochemistry of both host limestones and dolomites is therefore similar to the one reported for the carbonates from the study area.
- The talc deposits of Puebla de Lillo are located close to the Cofiñal Fault at the contact between the Central Coal Basin and the Ponga units. They are mainly hosted in dolomitised Carboniferous carbonates of the Alba and Barcaliente Fms. (Tornos and Spiro 2000). The precursor limestones have highly variable $\delta^{18}O$ (–16,0 to 2,0 ‰ PDB) with most of the values

comprised between -8,7 and 1,0‰ PDB. The $\delta^{13}C$ values vary between –2 and 7‰ PDB but most of the values are in the range 3,0-5,5‰ PDB. The dolomites have most $\delta^{18}O$ values between –16,4 and –10,6‰ PDB, and most $\delta^{13}C$ values between 2,0 and 5,0‰ PDB. These dolomites have lower $\delta^{18}O$ and $\delta^{13}C$ values than the dolomites from the study area. This could reflect the lower $\delta^{18}O$ and $\delta^{13}C$ values of the precursor limestones.

Tornos and Spiro (2000) reported also Sr isotope ratios for both precursor limestones and dolomites (Fig. 45). These ratios overlap those reported from the study area. This suggests that the dolomites from the two regions formed from similar fluids. The dolomites hosting talc deposits are thought to be related to post-Variscan extensional tectonics (Tornos and Spiro 2000). A similar origin has been inferred for the dolomites of the study area.

- In the Picos de Europa Unit the dolomitisation affected Carboniferous carbonates from the Alba Fm. (Viséan) up to the Picos de Europa Fm. (Westphalian B - Cantabrian). These carbonates are the main host lithology of small Pb-Zn deposits. Gómez-Fernández et al. (1993, 2000) investigated the elemental and isotopic geochemistry of dolomites and precursor limestones hosting Pb-Zn mineralisations. All of the dolomites are nearly stoichiometric. They have Sr contents (range 14-49 ppm and mean at 24 ppm) lower than those of the precursor limestones (range 60-840 ppm and mean at 311 ppm). Na contents are comprised between 0 and 668 ppm (mean at 74 ppm). The dolomites have Fe contents between 1958 and 5526 ppm (mean at 4200 ppm). They are strongly enriched in Fe relative to the host limestones (range 280-3497 ppm and mean at 1300 ppm). These dolomites have therefore elemental geochemistry similar to the one reported for the dolomites of the study area (see paragraph. 6.3), although they carry higher Fe contents. This could indicate that the dolomitisation in the Picos de Europa Unit involved major amounts of this element.

  The host limestone have $\delta^{18}O$ values between –16,0 and –8,0‰ PDB. The $\delta^{13}C$ values are between 4,0 and 5,5‰ PDB. The dolomites have $\delta^{18}O$ values between –14,3 and –8,4‰ PDB, whereas $\delta^{13}C$ values range between 3,8 and 4,2‰ PDB. The dolomites from the Picos de Europa Unit have therefore $\delta^{18}O$ values more negative than those of dolomites from the study area. This could reflect the strongly negative $\delta^{18}O$ values of the host limestones.

  The dolomites from the Picos de Europa Unit are inferred to be Permian in age (Gómez-Fernández et al. 1993, 2000). The dolomitising fluids are thought to be Carboniferous seawater contained in sediments of the Pisuerga-Carrión and Picos de Europa units. However, an origin from Permian seawater cannot be excluded (Gómez-Fernández et al. 2000).

- Grimmer (2000) accomplished a geochemical and microthermometric survey on brecciated and dolomitised Carboniferous rocks along fault planes in the eastern CZ. This author reported precursor limestones of the Barcaliente Fm. having $\delta^{18}O$ values between –12,7 and 1,5‰ PDB and $\delta^{13}C$ values between 2,6 and 5,4‰ PDB. The dolomite phases have $\delta^{18}O$

values between –10,1 and –4,1‰ PDB. The $\delta^{13}C$ values vary between 2,2 and 3,7‰ PDB. Primary FIs in the dolomites have Th between 75 and 277 °C, with most of the values falling in the range 100-190 °C. The combination of isotope and microthermometry data allowed to calculate $\delta^{18}O$ values for the dolomitising fluids between 0 and 7 ‰ SMOW. These values overlap those reported for the dolomites of the study area (see Fig. 45).

It is proposed that the dolomites investigated in this study and those from other tectonic units of the CZ formed during the same dolomitising event and from fluids of similar composition. The differences in geochemistry between the dolomites of the various regions could be due to the fluids interacting with precursor carbonates of variable composition and/or diagenetic stage.

8.17 Origin of the calcite cements

Cal 1 and Cal 2 fill open cavities between two Dol B sheets (Plate 3, Phs. 5 and 6). They also fill veins, which depart from the cavities and crosscut the different dolomite phases (Plate 10, Ph. 3 and Plate 11, Ph. 1). Therefore, they are late diagenetic products relative to the dolomites.

Cal 1 and Cal 2 were never observed in the precursor limestones and were exclusively found in dolomitised rocks. This can be explained by the distinctly lower permeability of the tight limestones relative to the vuggy dolomites: the fluids, which precipitated the calcites, were more easily channelled into the dolomites than into the limestones.

The aim of the following paragraphs is to interpret the origin and the composition of the fluids, from which Cal 1 and Cal 2 precipitated.

8.17.1 Origin of Cal 1

Cal 1 possibly precipitated “shortly” after Dol B2. This assumption is based on the occurrence of regular boundaries of Dol B2 crystals in contact with Cal 1 (Plate 9, Phs. 2 and 4). In case Cal 1 was a later product, the previously formed dolomite would have been exposed to fluid circulation for a longer time and reaction borders, or corroded dolomite crystals, would be expected. The absence of reaction borders also suggests that the fluid precipitating Cal 1 was in chemical equilibrium with the dolomite.

Cal 1 is frequently associated with ore minerals but their relative timing is ambiguous.

Cal 1 most commonly displays an unzoned CL. As discussed for dolomites (see paragraph 8.11) this could indicate that Cal 1 formed in an open system characterised by a high water/rock ratio.

The bright orange CL of Cal 1 (Plate 10, Phs. 1-3) suggests high concentration in activator ions. A similar CL has been reported for high-Mg calcites (e.g. Moore 1989, Tucker and Wright 1990). The

latter commonly form in the burial environment. A burial origin for Cal 1 is also suggested by the negative $\delta^{18}O$ values (Fig. 41) and the high Th of primary FIs (Fig. 28C). FI investigation indicated that Cal 1 formed from Na-Ca rich brines. These brines were slightly cooler but even more saline than those which formed the dolomites.

Cal 1 formed at relatively low depths (see Table 9). Therefore, hydrostatic pressure conditions can be assumed for the precipitation of Cal 1.

The O composition of the fluid from which Cal 1 precipitated was calculated using the $\delta^{18}O$ values of the calcite, the Th of primary FIs corrected for hydrostatic pressure (see Table 9) and the equation of Friedman and O'Neil (1977):

$$10^3 \, \mathrm{Ln} \, \alpha_{\text{calcite-water}} = 2{,}78 \cdot 10^6 \, T^{-2} \, (°K) - 2{,}89 \qquad (10)$$

where α is the O isotope fractionation coefficient between calcite and water.

The mother fluid of Cal 1 had $\delta^{18}O$ between 1,8 and 9,5‰ SMOW (Fig. 47). These values are very similar to those reported for the dolomite mother fluids (Fig. 46) and could correspond to seawater modified by evaporation and/or fluid-rock interaction. The latter would explain also the slightly radiogenic $^{87}Sr/^{86}Sr$ ratios reported for Cal 1 (Fig. 42).

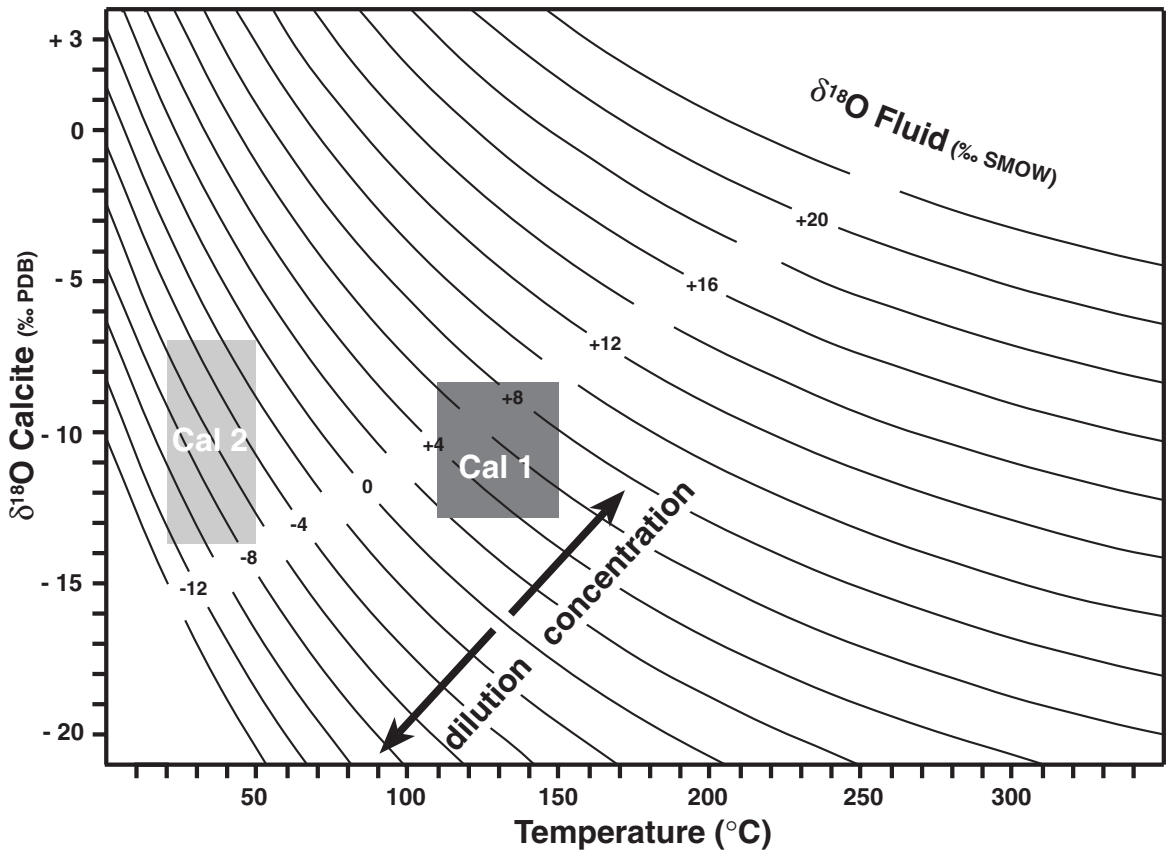

Fig. 47: Plot of precipitation temperature versus $\delta^{18}O$ values of Cal 1 and Cal 2. The $\delta^{18}O$ composition of the fluid in equilibrium with calcite as function of the temperature was calculated using the fractionation equation of Friedman and O´Neil (1977).

It is assumed that Cal 1 precipitated from fluids in the same hydraulic system than the dolomites. The fluids after dolomitisation evolved into slightly cooler, Na-Ca rich brines, progressively less rock buffered. The latter is suggested by the low $\delta^{13}C$ values of Cal 1. Incorporation of light C from organic matter diagenesis could have contributed to lower the $\delta^{13}C$ of the fluids (e.g. Carothers and Kharaka 1980). The evolution from Dol B cementation towards precipitation of Cal 1 could reflect a shift from the dolomite stability field into the calcite stability field, due to an increase in the Ca/Mg ratio and/or a decrease in temperature of the fluids (see Land 1985).

8.17.2 Origin of Cal 2

Cal 2 post-dated all of the investigated diagenetic phases. It precipitated from a fluid related to a different hydraulic system than the dolomites. Reaction borders and corroded Dol B2 crystals in contact with Cal 2 suggest that the calcite precipitated from fluids in chemical disequilibrium with the dolomite.

Cal 2 crystals display an intensively zoned CL characterised by thick non-luminescent and thin bright orange zones (Plate 11, Phs. 1 and 2). This kind of CL is typical of calcites which form in the most oxic portions of the groundwater system, thus near to meteoric recharge (Meyers 1991, Reeder 1991). The CL behaviour of meteoric calcites has been referred by many authors (e.g. Choquette and James 1988, Mussman et al. 1988, Neimann and Read 1988). They all agree that meteoric calcites are characteristically non-luminescent with minor bright zones. This kind of CL reflects the oxidised nature of the shallow meteoric environment.

Primary FIs in Cal 2 (see paragraphs 7.1.6 and 7.5) suggested trapping temperatures lower than 50 °C and a shallow environment for the precipitation of Cal 2 (e.g. Goldstein et al. 1990, Goldstein and Reynolds 1994).

The strongly negative $\delta^{13}C$ values of Cal 2 also indicate a meteoric water contribution: fluids with influx of meteoric waters, which are recharged through soil horizons, are strongly to moderately enriched in ^{12}C (Lohmann 1987, Clauer and Chaudhuri 1992, Hoefs 1997).

The O isotope composition of the fluid from which Cal 2 precipitated can be estimated from the $\delta^{18}O$ values of the calcite and assuming precipitation temperatures between 20 and 50 °C. The mother fluid of Cal 2 had $\delta^{18}O$ values between –14 and 0‰ SMOW (Fig. 47). These values are typical of fluids enriched in ^{16}O, such as fluids diluted by isotopically light meteoric waters (e.g. Lohmann 1987, Clauer and Chaudhuri 1992, Hoefs 1997).

It can be concluded that Cal 2 precipitated from fluids having a meteoric water signature. This suggests that the study area was exposed at the time of Cal 2 precipitation, since only after chain exposure fluids of surface origin could have entered the groundwater system. In the CZ main post-Variscan exposure periods occurred in the Late Permian and from the Tertiary onwards. However, also during the Mesozoic some areas of the CZ remained exposed (see paragraph

2.3.2). Consequently, a precise assessment of timing for Cal 2 is not possible.

Calcite cements with similar isotopic geochemistry are reported from several pre-Carboniferous lithologies of the Somiedo-Correcilla Unit. They are thought to have precipitated from meteoric fluids during the Late Cretaceous (Zeeh and Schneider in press). A similar timing could be inferred for Cal 2, although a more detailed comparative study is needed to prove this hypothesis.

8.18 Sequence of diagenetic events

The paragenetic sequence of the most important late diagenetic events recognised in the studied Carboniferous carbonates was reconstructed as follows (Fig. 48):

- Bedding parallel stylolites formed during burial prior to the onset of Variscan movements;
- Pervasive cracks developed as a consequence of Variscan compressional events. The cracks were filled with burial calcite and formed CV;
- Replacive burial dolomitisation clearly post-dated both stylolites and CV. It also post-dated the Variscan compressional events (see paragraph 8.10). It produced Dol A1 and Dol A2,

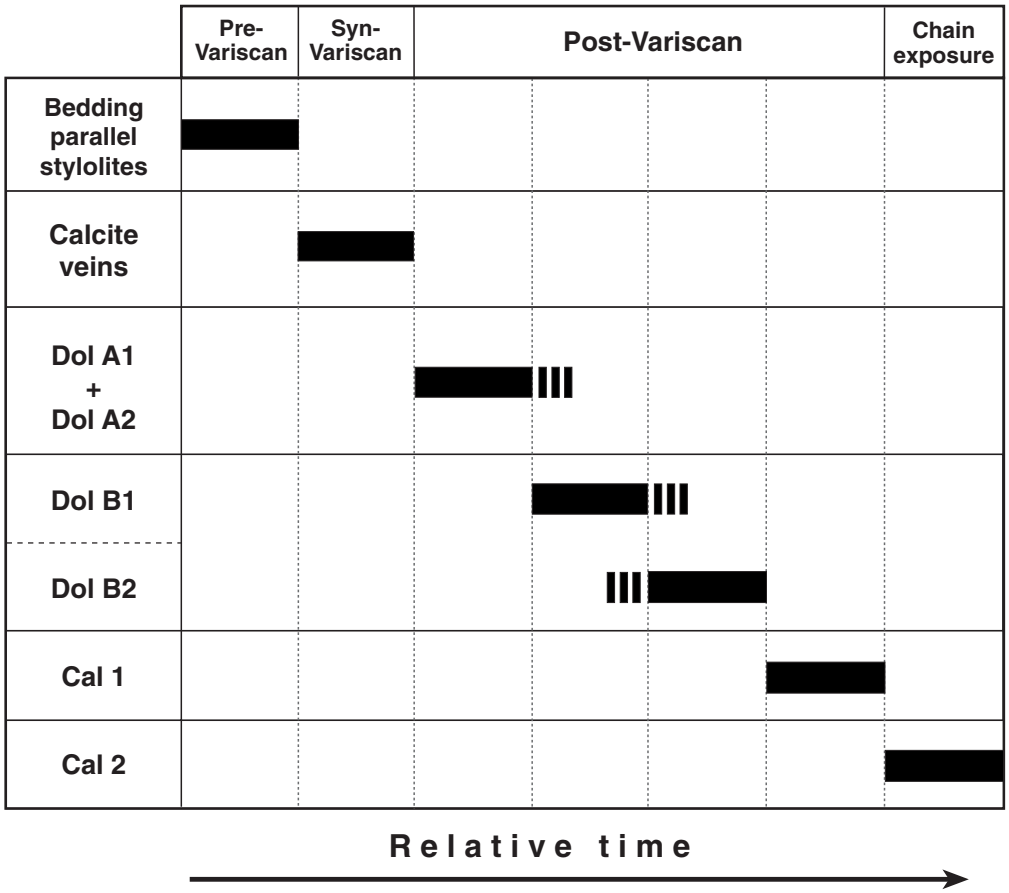

Fig. 48: Paragenetic sequence of the most important late diagenetic events recognised in the studied Carboniferous carbonates.

which possibly represent different textural types of the same dolomite phase. Cavities and sub-vertical cracks formed in an extensional field of stress;

- Void-filling burial dolomitisation followed according to a continuous and almost isochemical process. Dol B precipitated in cavities and cracks. The last generation of crystals (Dol B2) records an enrichment in Fe. Locally, a process of oxidation affected the terminations of Dol B2 crystals and formed hydroxide zones;
- Cal 1 precipitated after Dol B in the burial environment and likely from the same hydraulic system of the dolomites;
- Cal 2 precipitated from fluids with a meteoric signature, indicating the complete or partial exposure of the study area.

Chapter 9: Dolomitisation model

In Chapter 8 it has been proposed that the studied dolomitisation was due to one fluid in evolution, which first replaced the Carboniferous carbonates, creating new porosity, and then precipitated a void-filling dolomite. The dolomitisation occurred in the burial environment and was controlled by rock anisotropies and rock type. The dolomitising fluids were hydrothermal and hypersaline brines, with isotopic signature of chemically modified Late Palaeozoic seawater.

Any model for dolomitisation has to account for the regional extent and the late timing of the process, the supply of Mg and fluid to the site of dolomitisation, the moderately radiogenic Sr isotope composition of the dolomites and the highly saline and ^{18}O-enriched composition of the fluids. An effective hydraulic "pump" capable of moving the dolomitising fluids through the precursor rocks, as well as a source of heat to explain the high temperatures of the fluids, are also required to explain the origin of the studied dolomitisation.

9.1 Thermal convection and dolomitisation

The driving force for thermal convection is buoyancy: water rises upon heating and sinks upon cooling resulting in the formation of convection cells. This physical phenomenon has been observed also in natural geothermal systems (e.g. Elder 1965, Williams 1997, Oldenburg and Pruess 1998). Most of these systems are associated with structures determined by tectonic activity such as block faulting, graben formation and rift valleys. The water within geothermal systems may have several possible origins: it may be meteoric water or seawater that circulated to great depths, or formation waters trapped in the buried sediments.

Thermal convection in natural materials may arise if increased geothermal gradients create a sufficiently high density contrast between cool upper and warm lower fluids. This phenomenon can drive chemical reactions in a wide range of settings (Wilson et al. 2001 and reference therein). As mentioned in paragraph 1.2 a popular model to explain high temperature burial dolomites is the thermal convection model. Convective circulation can provide a long-lived, large-scale mechanism for the flow of Mg-rich fluids through subsurface carbonates. If the temperatures are sufficiently elevated to overcome kinetic limitations, dolomitisation may occur (Morrow 1998, Wilson et al. 2001). Thermal convection may account for more efficient dolomitisation than other mechanisms because the Mg-rich fluids can be recycled many times through the precursor carbonates (Morrow 1998).

Wilson et al. (1990) and Spencer-Cervato and Mullis (1992) reported examples of hydrothermal dolomitisation caused by thermal convection of seawater. The origin of extensive hydrothermal dolomites in northwestern Canada was interpreted with convective circulation of deep residual evaporitic brines (Aulstead et al. 1988, Morrow et al. 1990, Morrow and Aulstead 1995). Wendte et al. (1998) invoked a "thermoflux" model to explain hydrothermal dolomitisation in Alberta. These authors proposed convective circulation of residual brines derived from seawater evaporation which descended through fractures and were modified during burial. A similar model was proposed by Coniglio et al. (1994) to explain dolomitisation in Ontario. In all these examples the convective circulation of fluids was promoted by increased heat flow from the basement.

9.2 Proposed model of dolomitisation

It is proposed that the investigated dolomitisation occurred in Early Permian time (290-260 Ma). During this period extensional tectonics prevailed and the CZ underwent crustal thinning (see paragraph 2.3.3). Permian sediments crop out some tens of km N of the study area. They record the alternation of exposure and shallow water sedimentation in semiarid climatic conditions (see paragraph 2.3.2). Regional Variscan fractures (e.g. the León Fault) were reactivated and controlled the occurrence of alkaline volcanism and magmatic intrusions of mantle affinity. These phenomena coincided with the development of low temperature metamorphism affecting some areas of the CZ (see paragraph 2.3.5). In such a scenario increased heat flow from the basement could have induced thermal convection of subsurface fluids.

Criticism of extensive dolomitisation in the burial environment has focused on the Mg source and delivery mechanism in the subsurface (Land 1985, Morrow 1990b). Seawater (or modified seawater) is the only source of fluids sufficiently abundant and rich in Mg to cause widespread dolomitisation (Land 1985, Machel and Mountjoy 1986).

It can be imagined that Early Permian seawater percolated in depth along fractures (Fig. 49). These fluids formed in semiarid climatic conditions and in a shallow water environment, characterised by restricted circulation and high evaporation rate. Present-day seawater of the Red Sea has $\delta^{18}O$ values of 2‰ SMOW (Craig 1966). The seawater evaporation curve of Knauth and Beeunas (1986) indicates that evaporitic brines may have $\delta^{18}O$ values up to 7‰ SMOW. Therefore, prior to percolation in depth the Early Permian marine fluids had salinity and $\delta^{18}O$ values higher than normal seawater. This downward fluid-flow was density-driven. These fluids mixed with formation waters of marine origin, stored in the buried sediments. The formation waters were already equilibrated with ambient rocks and carried abundant ^{18}O, radiogenic ^{87}Sr and high salinity.

Thermal convection homogenised the surface seawater and the subsurface formation waters and

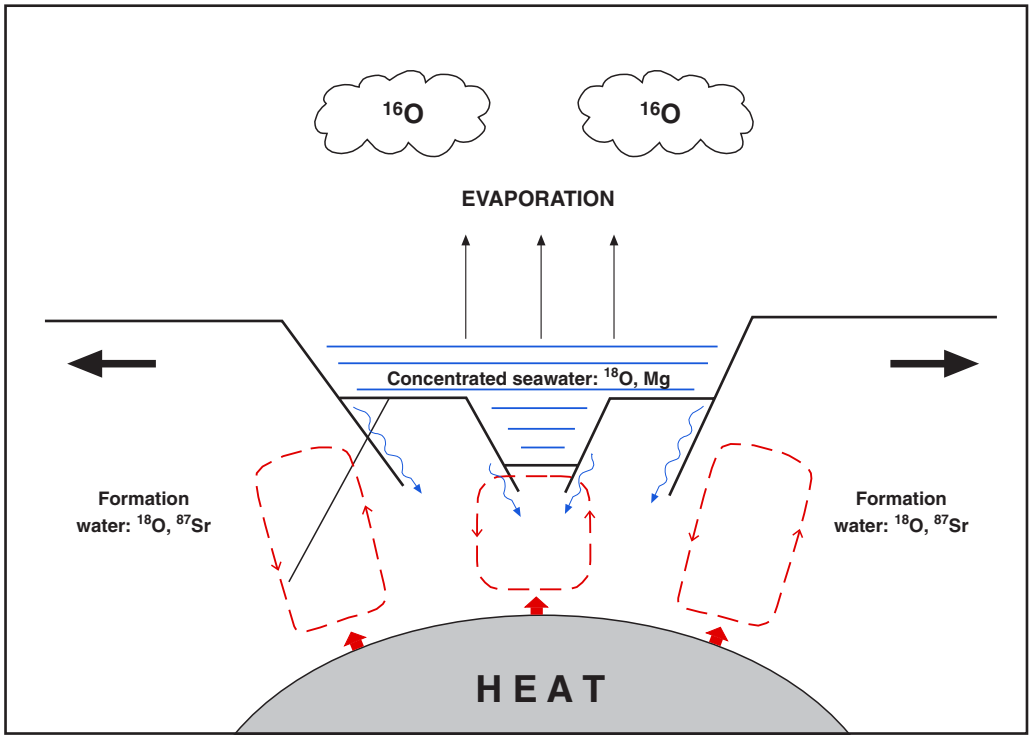

Fig. 49: Schematic representation of the proposed model of dolomitisation. Shallow water basins controlled by normal faults formed in Early Permian time. Concentrated seawater entered the sedimentary sequence through fractures. These brines already enriched in ^{18}O by evaporation mixed with formation waters, characterised by high salinity, abundant ^{18}O and radiogenic ^{87}Sr. Increased heat flow from the basement induced thermal convection of the fluids.

made them circulate in the fractured precursors. In this model convective recycling of seawater-derived brines occurred at depth, while additional concentrated seawater, formed at the surface, was introduced in the subsurface by percolation along deep fractures. The concentrated seawater would have furnished continuous supply of Mg to the convecting system (see Morrow 1998).

It has been widely documented that faults and fractures may significantly affect the movement of natural fluids (e.g. Sibson 1981, Knipe 1993, Hickman et al. 1995, Odling 1997). Highly permeable fault zones reactivated during Permian times may have facilitated fluid circulation in the study area. The net of fractures associated with the León Fault possibly played a major role as pathways for the dolomitising fluids, as suggested by the occurrence of more widespread dolomitisation in the region closer to this fault. Fluid circulation along the León Fault has also been invoked as an important agent responsible for the higher coal ranks and CAI values attained to the N of the fault (Raven and Van der Pluijm 1986, Colmenero and Prado 1993).

A modern analogue for the geothermal system inferred to have caused the studied dolomitisation occurs beneath the Salton Sea of southern California. In this geothermal system, located along the Gulf of California continental rift, hypersaline brines originated by evaporation of the Salton Sea water and percolated downwards into the subsurface until the depth of 5 km (Rex 1985,

McKibben 1987). Increased heat flow caused the brines to become less dense and to rise upwards. The brines circulated in the subsurface according to convective cells and precipitated high temperature carbonate cements (e.g. dolomite and ankerite) in fractures at depth of less than 1 km (McKibben et al. 1987).

9.3 Late to post-Variscan dolomites: a European perspective

Late to post-Variscan burial dolomites are reported from several regions of central and western Europe, like Spain (this study), Italy (Boni et al. 2000), Belgium (Nielsen et al. 1998), Germany (Grobe and Machel 1996), Ireland (Wright et al. 1999) and Czech Republic (Suchy et al. 1996). These dolomites are hosted in Palaeozoic carbonates, ranging in age from Early Cambrian to Late Carboniferous and mostly located in external zones of the Variscan orogen. These dolomites share many features such as comparable mineralogy and texture, pervasive replacement patterns, depletion in ^{18}O relative to their precursor carbonates, radiogenic Sr isotope ratios and high salinity FIs trapped at relatively high temperatures.

A comparative analysis of geochemical data, together with structural and petrographical evidence, allowed Iannace et al. (2001) and Boni et al. (2002) to distinguish site specific features from general characteristics of these dolomites. These authors concluded that due to the variable age and diagenetic stages of the precursor carbonates in the different districts, the resulting geochemical signatures of the dolomites may be quite distinct. However, they argued that the analogies among these dolomites could allow to relate the dolomitisation process to cogenetic fluid-flow events.

Post-Variscan migration of highly saline fluids was widespread in central and western Europe (Behr et al. 1987, 1993, Wilkinson et al. 1995, Heijlen et al. 2001). Movement of these fluids in the crust is thought to be fault controlled (Behr et al. 1993, Heijlen et al. 2001). One of the most important fluid-flow events was dated at 270 Ma in Western Europe (Schneider 2000, Boni et al. 2001), an age which coincides with post-thrusting Permian extensional tectonics and with the timing inferred for the dolomitisation in the CZ. It could be proposed that the investigated dolomitisation is analogous to dolomitisations affecting the other districts. However, this hypothesis requires further investigations to be proved.

References

Adams, J.E. and Rhodes, M.L., 1960. Dolomitisation by seepage refluxion. Bull. Am. Ass. Petrol. Geol., 44: 1912-1920.

Aller, J., 1986. La estructura del sector meridional de las unidades del Aramo y de la Cuenca Carbonífera. Consejería de Industria y Comercio, Oviedo, 180 pp.

Aller, J. and Brime, C., 1985. Deformación y metamorfismo en la parte sur de la Cuenca Carbonífera Central (NO de España), C.R. X Congr. Int. Strat. Géol. Carbonifère, Madrid, pp. 541-548.

Alonso, J.L. and Pulgar, J.A., 1995. La estructura de la Zona Cantábrica. In: C. Aramburu and F. Bastida (Eds.), Geología de Asturias. TREA, Gijón, pp. 103-112.

Alonso, J.L., Pulgar, J.A., García-Ramos, J.C. and Barba, P., 1996. Tertiary basins and Alpine tectonics in the Cantabrian Mountains (NW Spain). In: P.F. Friend and J.C. Dabrio (Eds.), Tertiary Basins of Spain: the stratigraphic record of crustal kinematics. Cambridge University Press, Cambridge, pp. 214-227.

Alonso, J.L., Suárez-Rodríguez, A., Rodríguez-Fernández, L.R., Farias, P. and Villegas, F.J., 1990. Hoja del Mapa Geológico Nacional de España (1: 50000), Memoria 104 (La Pola de Gordón). IGME, Madrid, 138 pp.

Alvarado, M., 1980. Introducción a la Geología general de España. Bol. Geol. Min., 91(1): 1-65.

Amthor, J.E., Mountjoy, E.W. and Machel, H.G., 1993. Subsurface dolomites in Upper Devonian Leduc Formation buildups, central part of Rimbey-Meadowbrook reef trend, Alberta, Canada. Bull. Can. Petrol. Geol., 41: 164-185.

Aramburu, C. and Bastida, F., 1995. Geología de Asturias. TREA, Gijón, 314 pp.

Aramburu, C., Truylos, J., Arbizu, M., Méndez-Bedia, I., Zamarreño, I., García-Ramos, J.C., Suárez de Centi, C. and Venezuela, C., 1992. El Paleozoico Inferior de la Zona Cantábrica. In: M.J. Liso-Rubio (Ed.), Palaeozoico Inferior de Ibero-América, Universidad de Extremadura, Badajoz, pp. 397-421.

Arcos, D., 1996. Las mineralizaciones asociadas a la granodiorita en el depósito de Cu-Au de Carlés, Asturias. Unpubl. Ph.D. Thesis, University of Barcelona, Spain, 360 pp.

Arne, D.C. and Kissin, S.A., 1989. The significance of "diagenetic crystallization rhythmites" at the Nanisivik Pb-Zn-Ag deposit, Baffin Island, Canada. Mineral. Deposita, 24: 230-232.

Aulstead, K.L., Spencer, R.J. and Krause, H.R., 1988. Fluid inclusion and isotopic evidence on dolomitisation, Devonian of western Canada. Geochim. Cosmochim. Acta, 52: 1027-1035.

Baadsgaard, H., Chaplin, C. and Griffin, W.L., 1986. Geochronology of the Gloserneia pegmatite, Froland, southern Norway. Nor. Geol. Tidsskr., 64: 111-119.

Baker, P.A. and Burns, S.J., 1985. Occurrence and formation of dolomite in organic-rich continental margin sediments. Bull. Am. Ass. Petrol. Geol., 69: 1917-930.

Bakker, R.J., 2001a. Combined Raman Spectroscopy and low temperature Microthermometry. In: F. Noronha, A. Dória and A. Guedes (Eds.), XVI ECROFI, Porto, pp. 15-18.

Bakker, R.J., 2001b. FLUIDS: new software package to handle microthermometric data and to calculate isochores. In: F. Noronha, A. Dória and A. Guedes (Eds.), XVI ECROFI, Porto, pp. 23-25.

Bakker R.J., 2002. Identification of salts in fluid inclusions by combined Raman Spectroscopy and low temperature Microthermometry. PACROFI VIII, Halifax, pp. 38-42.

Bakker, R.J., in press. Raman spectroscopic studies of pure H_2O, binary H_2O-NaCl and H_2O-$MgCl_2$ fluid systems at low temperatures: applications to fluid inclusion research. The Canadian Mineralogist.

Bakker, R.J., 2003. Package FLUIDS 1. Computer programs for analysis of fluid inclusion data and for modelling bulk fluid properties. Chem. Geol., 194(1-3): 3-23.

Banks, D.A. and Yardley, B.W.D., 1992. Crush-leach analysis of fluid inclusions in small natural and synthetic samples. Geochim. Cosmochim. Acta, 56: 245-248.

Banner, J.L., 1995. Application of the trace element and isotope geochemistry of strontium to studies of carbonate diagenesis. Sedimentology, 42: 805-824.

Banner, J.L. and Hanson, G.N., 1990. Calculation of simultaneous isotopic and trace element variations during water-rock interaction with application to carbonatic diagenesis. Geochim. Cosmochim. Acta, 54: 3123-3137.

Banner, J.L., Hanson, G.N. and Meyers, W.J., 1988. Water-rock interaction history of regionally extensive dolomites of the Burlington-Keokuk Formation (Mississippian): isotopic evidence. In: V. Shukla and P.A. Baker (Eds.), Sedimentology and geochemistry of dolostones. SEPM Spec. Publ. 43, pp. 97-114.

Barber, D.J., Reeder, R.J. and Smith, D.J., 1985. A TEM microstructural study of dolomite. Contrib. Mineral. Petrol., 91: 82-92.

Barnaby, R.J. and Read, J.F., 1992. Dolomitization of a carbonate platform during late burial: Lower to Middle Cambrian Shady Dolomite, Virginia Appalachians. J. Sed. Petrol., 62: 1023-1043.

Barnaby, R.J. and Rimstidt, D.J., 1989. Redox conditions of calcite cementation interpreted from Mn and Fe contents of authigenic calcites. Bull. Geol. Soc. America, 101: 795-804.

Barnes, I. and Back, W., 1964. Geochemistry of iron-rich ground water of southern Maryland. J. Geol., 72: 435-447.

Bastida, F., Brime, C., García-López, S. and Sarmiento, G.N., 1999. Tectono-thermal evolution in a region with thin-skinned tectonics: the western nappes in the Cantabrian Zone (Variscan belt of NW Spain). Int. J. Earth Sci., 88: 38-48.

Bastida, F., Marcos, A., Pérez-Estaún, A. and Pulgar, J.A., 1984. Geometría y evolución estructural del Manto de Somiedo (Zona Cantábrica, NO España). Bol. Geol. Min., 95(6): 517-539.

Bathurst, R.G.C., 1995. Burial diagenesis of limestones under simple overburden. Stylolites, cementation and feedback. Bull. Soc. Géol. France, 166(2): 181-192.

Beales, F.W. and Hardy, J.W., 1980. Criteria for recognition of diverse dolomite types with an emphasis on studies of host rock for Mississippi Valley-Type ore deposits. In: D.H. Zenger, J.B. Dunham and R.L. Ethington (Eds.), Concepts and models of dolomitization. SEPM Spec. Publ. 28, pp. 197-213.

Behr, H.J., Gerler, J., Hein, U.F. and Reutel, C., 1993. Tectonic Brines und Basement Brines in den mitteleuropäischen Variszіden: Herkunft, metallogenetische Bedeutung und geologische Aktivität. Göttinger Arb. Geol. Paläont., 58: 3-28.

Behr, H.J., Horn, E.E., Frentzel-Beyme, K. and Reutel, C., 1987. Fluid inclusion characteristics of the Variscan and post-Variscan mineralizing fluids in the Federal Republic of Germany. Chem. Geol., 61: 273-285.

Behrens, E.W. and Land, L.S., 1972. Subtidal Holocene dolomite, Baffin Bay, Texas. J. Sed. Petrol., 42(155-166).

Bein, A. and Land, L.S., 1983. Carbonate sedimentation and diagenesis associated with Mg-Ca-chloride brines: the Permian San Andreas Formation in the Texas Panhandle. J. Sed. Petrol., 53: 243-260.

Bird, P., 1979. Continental delamination and the Colorado plateau. J. Geoph. Res., 84(13): 7561-7571.

Bodnar, R.J., 1993. Revised equation and table for determining the freezing point depression of H_2O-NaCl solutions. Geochim. Cosmochim. Acta, 57: 683-684.

Bodnar, R.J. and Vityk, M.O., 1994. Interpretation of microthermometric data for H_2O-NaCl fluid inclusions. In: B. De Vivo and M.L. Frezzotti (Eds.), Fluid inclusions in minerals: methods and applications, Virginia Tech, Potignano-Siena, pp. 117-130.

Boni, M., Bechstädt, T. and Gasparrini, M., 2002. Post-Variscan hot dolomites in Europe: a “crustal scale hydrothermal palaeofield”?, 16th Int. Sedim. Congress, Johannesburg, pp. 1.

Boni, M., Iannace, A. and Villa, I.M., 2001. Multiple fluid-flow events and mineralizations in SW Sardinia: from Variscan onward, EUG XI, Strasbourg, pp. 272.

Boni, M., Parente, G., Bechstädt, T., De Vivo, B. and Iannace, A., 2000. Hydrothermal dolomites in SW Sardinia (Italy): evidence for a widespread late-Variscan fluid flow event. Sedim. Geol., 131: 181-200.

Braithwaite, C.J.R., 1991. Dolomites, a review of origins, geometries and textures. Trans. Roy. Soc. Edinburgh. Earth Sci., 82(2): 99-112.

Brand, U. and Veizer, J., 1980. Chemical diagenesis of a multi-component carbonate system. I. Trace elements. J. Sed. Petrol., 50: 1219-1236.

Brass, G.W., 1976. The variation of marine $^{87}Sr/^{86}Sr$ during Phanerozoic time: interpretation using a flux model. Geochim. Cosmochim. Acta, 40: 721-730.

Brime, C., García-López, S., Bastida, F., Valín, M.L., Sanz-López, J., Aller, J., 2001. Transition from diagenesis to metamorphism near the front of the Variscan regional metamorphism (Cantabrian Zone, northwestern Spain). J. Geol., 109: 363-379.

Bullen, S.B. and Sibley, D.F., 1984. Dolomite selectivity and mimic replacement. Geology, 12: 655-658.

Burke, E.A.J., 2001. Raman microspectrometry of fluid inclusions. Lithos, 55: 139-158.

Burke, W.H., Denison, R.E., Hetherington, E.A., Koepnick, R.B., Nelson, H.F., Otto, J.B., 1982. Variation of seawater $^{87}Sr/^{86}Sr$ throughout Phanerozoic time. Geology, 10: 516-519.

Burns, S.J. and Baker, P.A., 1987. A geochemical study of dolomite in the Monterey Formation, California. J. Sed. Petrol., 57: 128-139.

Butler, G.P. and Burns, S.J., 1969. Modern evaporite deposition and geochemistry of co-existing brines, the Sabkha, Trucial Coast, Arabian Gulf. J. Sed. Petrol., 39(1): 70-89.

Carballo, J.D., Land, L.S. and Miser, D.E., 1987. Holocene dolomitization of supratidal sediments by active tidal pumping, Sugarloaf Key, Florida. J. Sed. Petrol., 57: 153-165.

Carey, S.W., 1955. The orocline concept in geotectonics. Royal Society of Tasmania Proceedings, 89: 255-288.

Carothers, W.W. and Kharaka, Y.K., 1980. Stable carbon isotopes of HCO_3^- in oil-field waters - implications for the origin of CO_2. Geochim. Cosmochim. Acta, 44: 323-332.

Cepedál, M.A., Martín-Izard, A., Reguilon, R., Fuertes, M., Rodríguez-Pevida, L.S., Maldonado, C., Spiering, E., Gonzáles, S., Varela, A., 1998. Stable isotopic study of the “El Valle-Boinas” copper-gold deposits. Genetic implications and hydrothermal evolution. In: D. Arias, A. Martín-Izard and A. Paniagua (Eds.), Gold in NW Spain. Departamento de Geología, Oviedo, pp. 59-64.

Chaudhuri, S. and Clauer, N., 1993. Strontium isotopic composition and potassium and rubidium contents of formation waters in sedimentary basins: clues to the origin of the solutes. Geochim. Cosmochim. Acta, 57: 429-437.

Choquette, P.W. and James, N.P., 1988. Introduction. In: N.P. James and P.W. Choquette (Eds.), Paleokarst. Springer, New York, pp. 1-21.

Choquette, P.W. and James, N.P., 1990. Limestones - the burial diagenetic environment. In: I.A. McIlreath and D.W. Morrow (Eds.), Diagenesis. Geoscience Canada Reprint Series 4, Ottawa, pp. 75-111.

Choquette, P.W. and Pray, L.C., 1970. Geologic nomenclature and classification of porosity in sedimentary carbonates. Bull. Am. Ass. Petrol. Geol., 62: 207-250.

Clauer, N. and Chaudhuri, S., 1992. Isotopic signatures of sedimentary rocks. Lecture Notes in Earth Sciences 43, Springer, Berlin, 529 pp.

Clayton, R.N., Friedman, I., Graf, D.L., Mayeda, T.K., Meents, W.F., Shimp, N.F., 1966. The origin of saline formation waters: I. Isotopic composition. J. Geoph. Res., 71: 3869-3882.

Cole, D.R., 1994. Oxygen isotope exchange rates in mineral-fluid systems: correlations and predictions. Mineral. Mag., 58a: 189-190.

Colmenero, J.R., Agueda, J.A., Bahamonde, J.R., Barba, F.J., Barba, P., Fernández, L. P., Salvador, C.I., 1993. Evolocíon de la cuenca de antepaís Namuriense y Westfaliense de la Zona Cantábrica, noroeste de España, C.R. XII Inter. Congr. Carbonif. Perm. Stratigr. Geol., Buens Aires, pp. 175-190.

Colmenero, J.R. and Prado, J.C., 1993. Coal basins in the Cantabrian Mountains, northwestern Spain. Int. J. Coal

Geology, 23: 215-229.

Compton, J.S., 1988. Sediment composition and precipitation of dolomite and pyrite in the Neogene Monterey and Sisquoc Formations, Santa Maria Basin area, California. In: V. Shukla and P.A. Baker (Eds.), Sedimentology and geochemisry of dolostones. SEPM Spec. Publ. 43, pp. 53-65.

Coniglio, M., Sherlock, R., Williams-Jones, A.E., Middleton, K. and Frape, S.K., 1994. Burial and hydrothermal diagenesis of Ordovician carbonates from the Michigan Basin, Ontario, Canada. In: B.H. Purser, M.E. Tucker and D.H. Zenger (Eds.), Dolomites - A volume in honour of Dolomieu. IAS Spec. Publ. 21, pp. 231-254.

Coplen, T.B., Kendall, C. and Hopple, J., 1983. Comparison of stable isotope reference samples. Nature, 302(5905): 236-238.

Corretgé, L.G. and Suárez, O., 1990. Igneous rocks. In: R.D. Dallmeyer and E. Martínez-García (Eds.), Pre-Mesozoic geology of Iberia. Springer, Berlin, pp. 72-79.

Craig, H., 1963. The isotopic geochemistry of water and carbon in geothermal areas. In: E. Tongiorgi (Ed.), Nuclear geology on geothermal areas. C.N.R., Laboratorio di Geologia Nucleare, Spoleto, pp. 17-53.

Craig, H., 1966. Isotopic composition and origin of the Red Sea and Salton Sea geothermal brines. Science, 154: 1544-1548.

Crespo, J.L., Moro, M.C., Fadón, O., Cabrera, R. and Fernández, A., 2000. The Salamón gold deposit (León, Spain). J. Geochem. Explor., 71: 191-208.

Dallmeyer, R.D. and Martínez-García, E., 1990. Introduction to the pre-Mesozoic geology of Iberia. In: R.D. Dallmeyer and E. Martínez-García (Eds.), Pre-Mesozoic geology of Iberia. Springer, Berlin, pp. 3-4.

Davies, G.R., 1997. Hydrothermal dolomite (HTD) reservoir facies: global perspectives on tectonic-structural and temporal linkage between MVT and Sedex Pb-Zn ore bodies, and subsurface HTD reservoir facies, Can. Soc. Petrol. Geol. Short Course Notes, pp. 167.

Denison, R.E., Koepnick, R.B., Burke, W.H., Hetherington, E.A. and Fletcher, A., 1994. Construction of the Mississippian, Pennsylvanian and Permian seawater $^{87}Sr/^{86}Sr$ curve. Chem. Geol. (Isotope Geoscience Section), 112: 145-167.

Dickson, J.A.D., 1966. Carbonate identification and genesis as revealed by staining. J. Sedim. Petrol., 36(2): 491-505.

Dravis, J.J. and Muir, I.D., 1992. Case study of burial dissolution-dolomites, Devonian Upper Elk Point Group, western Canada. In: I.E. Hutcheon (Ed.), Subsurface dissolution porosity in carbonates: recognition, causes and implications. Am. Ass. Petrol. Geol. and Can. Soc. Petrol. Geol. Short Course Notes, pp. 55-117.

Drivet, E. and Mountjoy, E.W., 1997. Dolomitization of the Leduc Formation (Upper Devonian), southern Rimbey-Medowbrook reef trends, Alberta. J. Sed. Res., 67: 411-423.

Dubessy, J., Audeoud, D., Wilkins, R. and Kosztolanyi, C., 1982. The use of the Raman Microprobe Mole in the determination of the electrolytes dissolved in the aqueous phase of fluid inclusions. Chem. Geol., 37(1-2): 137-150.

Dubois, M. and Marignac, C., 1997. The H_2O-NaCl-$MgCl_2$ ternary phase diagram with special application to fluid inclusion studies. Econ. Geol., 92: 114-119.

Dunham, J.B. and Olson, E.R., 1980. Shallow subsurface dolomitization of subtidally deposited carbonate sediments in the Hanson Creek Formation (Ordovician - Silurian) of Central Nevada. In: D.H. Zenger, J.B. Dunham and R.L. Ethington (Eds.), Concepts and models of dolomitization. SEPM Spec. Publ. 28, pp. 139-161.

Dunnington, H.V., 1967. Aspects of diagenesis and shape change in stylolitic limestone reservoirs, 7th World Petroleum Congress, Mexico City, pp. 339-352.

Ebers, M.L. and Kopp, O.C., 1979. Cathodoluminescent microstratigraphy in gangue dolomite, the Mascot-Jefferson City District, Tennessee. Econ. Geol., 74: 908-918.

Edmunds, W.W., Miles, D.L. and Cook, J.M., 1984. Redox processes in aquifers. Geochim. Cosmochim. Acta, 46: 2069-2081.

Eichmüller, K., 1985. Die Valdeteja Formation: Aufbau und Geschichte einer oberkarbonischen Karbonatplattform (Kantabrisches Gebirge, Nordspanien). Facies, 13: 45-154.

Elder, J.W., 1965. Physical processes in geothermal areas. In: W.H.K. Lee (Ed.), Terrestrial heat flow. Am. Geoph. Union Geoph. Monograph Series, 8, pp. 211-239.

Elderfield, H., 1986. Strontium isotope stratigraphy. Palaeogeog. Palaeoclimatol. Palaeoecol., 57: 71-90.

Epstein, A.G., Epstein, J.B. and Harris, L.D., 1977. Conodont color alteration – an index to organic metamorphism. U.S. Geol. Surv. Prof. Paper, 995: 1-27.

Espina, R.G., 1992. La estructura del borde occidental de la Cuenca Vasco-Cantábrica en el área de Campoo (Cantabria-Palencia, norte de España), VIII Congreso Latinoamericano de Geología, Salamanca, pp. 149-178.

Evers, H.J., 1967. Geology of the Leonides between the Bernesga and Porma rivers, Cantabrian Mountains, NW Spain. Leidse Geol. Meded., 41: 83-151.

Fairbridge, R.W., 1957. The dolomite question. In: R.J. LeBlanc and J.G. Reeding (Eds.), Regional aspects of carbonate deposition. SEPM Spec. Publ. 5, pp. 125-178.

Faure, G., Hurley, P.M. and Fairbairn, H.W., 1963. An estimate of the isotopic composition of strontium in rocks of Precambrian Shield of North America. J. Geoph. Res., 68(8): 2323-2329.

Fernández, C.J., 1985. Las mineralizaciones (Cu)-Pb-Zn-Ba-(Hg) en rocas dominantemente calcáreas del Carbonífero, sector Norte de la Región de Picos de Europa, Asturias. Características metalogenéticas en relación al tipo plomo-cinc-caliza, C.R. X Congr. Int. Strat. Géol. Carbonifère, Madrid, pp. 105-119.

Fernández, C.J., Moreiras, D. and Paniagua, A., 1985. Mineralogía y paragénesis mineral de la Mina Providencia (Cármenes, León). Trab. Geol., 15: 239-247.

Fernández-Suárez, J., Dunning, G.R., Jenner, G.A. and Gutiérrez-Alonso, G., 2000. Variscan collisional magmatism and deformation in NW Iberia: constraints from U-Pb geocrhonology of granitoids. J. Geol. Soc.

London, 157: 565-576.

Fisher, W.L. and Rodda, P.U., 1969. Edwads Formation (Lower Cretaceous), Texas: dolomitization in a carbonate platform system. Bull. Am. Ass. Petrol. Geol., 53: 55-72.

Folk, R.J., 1965. Some aspects of recrystallisation in ancient limestones. In: L.C. Pray and R.C. Murray (Eds.), Dolomitization and limestone diagenesis - a symposium. SEPM Spec. Publ. 13, pp. 14-48.

Folk, R.J. and Land, L.S., 1975. Mg/Ca ratio and salinity, two controls over crystallisation of dolomite. Bull. Am. Ass. Petrol. Geol., 59: 60-68.

Fontboté, L., 1993. Self-organization fabrics in carbonate-hosted ore deposits: the example of diagenetic crystallization rhythmites (DCR´s). In: P. Fenoll Hach-Ali, J. Torres-Ruiz and F. Gervilla (Eds.), Current research in geology applied to ore deposits, Granada, 2nd biennal SGA Meeting, pp. 11-14.

Fontboté, L. and Amstutz, G.C., 1983. Facies and sequence analysis of diagenetic crystallization rhythmites in strata-bound Pb-Zn-(Ba-F-) deposits in the Triassic of Central and Southern Europe. In: H.J. Schneider (Ed.), Mineral Deposits of the Alps and of the Alpine Epoch in Europe. Springer, Heidelberg, pp. 347-358.

Fontboté, L. and Gorzawski, H., 1990. Genesis of the Mississippi Valley-Type Zn-Pb deposit of San Vicente Central Peru: geologic and isotopic (Sr, O, S, Pb) evidence. Econ. Geol., 85: 1402-1437.

Friedman, I. and O'Neil, J.R., 1977. Compilation of stable isotope fractionation factors of geochemical interest. U.S. Geol. Surv. Prof. Paper, 440 KK: 12.

Frings, K. 2002. Paläotemperatur-Anomalien in spätvariskisches Kohlenbecken am Beispiel des Ciñera-Matallana Beckens, Kantabrisches Gebirge, NW Spanien (CD-ROM). Gaea Heidelbergensis, 11: 136 pp.

Füchtbauer, H. and Goldschmidt, H., 1965. Beziehungen zwieschen Calcium-gehalt und Bildungsbedingungen der Dolomite. Geol. Rdsch., 55: 29-40.

Gaines, A.M., 1980. Dolomitization kinetics: recent experimental studies. In: D.H. Zenger, J.B. Dunham and R.L. Ethington (Eds.), Concepts and models of dolomitization. SEPM Spec. Publ. 28, pp. 81-86.

Galán, G., Pin, C. and Duthou, J.L., 1996. Sr-Nd isotopic record of multi-stage interactions between mantle-derived magmas and crustal components in a collision context. The ultramafic-granitoid association from Vivero (Hercynian belt, NW Spain). Chem. Geol., 131: 67-91.

Galán, G. and Suárez, O., 1989. Cortlanditic enclaves associated with calcalkaline granites from Tapia-Asturias (Hercynian Belt, northwestern Spain). Lithos, 23: 233-245.

Galán-Huertos, E. and Rodas, M., 1973. Contribución al estudio mineralógico de los depósitos de Talco de Puebla de Lillo (León, España). Bol. Geol. Min., 84(5): 347-365.

Gallastegui, G., Heredia, N., Rodríguez-Fernández, L.R. and Cuesta, A., 1990. El stock de Peña Prieta en el contexto del magmatismo de la Unidad del Pisuerga-Carrión (Zona Cantábrica, N de España). Cuad. Lab. Xeol. Laxe, 15: 203-217.

García-López, S., García-López, S., Bastida, F., Brime, C., Aller, J., Valín, M.L., Sanz-López, J., Méndez, C.A., Menéndez-Álvarez, J.R., 1999. Los episodios metamórficos de la Zona Cantábrica y su contexto estructural. Trab. Geol., 21: 177-187.

García-López, S., Brime, C., Bastida, F. and Sarmiento, G.N., 1997. Simultaneous use of thermal indicators to analyse the transition from diagenesis to metamorphism: an example from the Variscan Belt of northwest Spain. Geol. Mag., 143(3): 323-334.

García-Mondéjar, J., Pujalte, V. and Robles, S., 1986. Características sedimentológicas secuenciales y tectoestratigráficas del Triásico de Cantabria y norte de Palencia. Cuad. Geol. Ibérica, 10: 151-172.

Garrison, R.E., Kastner, M. and Zenger, D.H., 1984. Dolomites of the Monterey Formation and other organic-rich units. SEPM Spec. Publ., Pacific Section, 41, 215 pp.

Garven, G. and Freeze, R.A., 1984. Theoretical analysis of the role of groundwater flow in the genesis of stratabound ore deposits. 2. Quantitative results. Am. J. Sci., 284: 1125-1174.

Goldsmith, J.R. and Graf, D.L., 1958. Relations between lattice constants and compositions of the Ca-Mg carbonates. Amer. Miner., 43: 84-101.

Goldstein, R.H., Franseen, E.K. and Mills, M.S., 1990. Diagenesis associated with subaerial exposure of Miocene strata, southestern Spain: implications for sea-level change and preservation of low-temperature fluid inclusions in calcite cement. Geochim. Cosmochim. Acta, 54: 699-704.

Goldstein, R.H. and Reynolds, T.J., 1994. Systematics of fluid inclusions in diagenetic minerals. SEPM Short Course 31, 198 pp.

Gómez-Fernández, F., Both, R.A., Mangas, J. and Arribas, A., 2000. Metallogenesis of Zn-Pb carbonate-hosted mineralization in the southeastern region of the Picos de Europa (central northern Spain) province: geologic, fluid inclusion, and stable isotope studies. Econ. geol., 95: 19-40.

Gómez-Fernández, F., Escayo-Morán, M.A., Alonso-López, J.A. and Seebold Imbert, I., 1993. Caracterización y origen de las dolomías del sector sudeste de Picos de Europa (norte de España). Estudios Geol., 49: 343-350.

González-Lastra, J., 1978. Facies salinas en la Caliza de Montaña (Cordillera Cantábrica). Trab. Geol., 10: 249-259.

Graf, D.L., 1982. Chemical osmosis, reverse chemical osmosis and the origin of subsurface brines. Geochim. Cosmochim. Acta, 46: 1438-1441.

Gregg, J.M., 1985. Regional epigenetic dolomitization in the Bonneterre Dolomite (Cambrian), southeastern Missouri. Geology, 13: 503-506.

Gregg, J.M. and Sibley, D.F., 1984. Epigenetic dolomitization and the origin of xenotopic dolomite texture. J. Sed. Petrol., 54(3): 908-931.

Grimmer, J.O.W., 2000. Fluidassoziierte Brekzien als Monitor dolomitisierender und dedolomitisierender Lösungströme in der Kantabrischen Zone (Nordspanien). Unpubl. Ph.D. Thesis, University of Heidelberg, Germany, 148 pp.

Grobe, M. and Machel, H.G., 1996. Petrographische und stabile Isotopendaten (C und O) für störungskontrollierte hydrothermale Mineralisation im devonischen Briloner Riffkomplex, Deutschland. Zbl. Geol. Paläont., 1: 397-413.

Grossman, E.L., 1994. The carbon and oxygen isotope record during the evolution of Pangea: Carboniferous to Triassic. In: G.D. Klein (Ed.), Pangea: paleoclimate, tectonics, and sedimentation during accretion, zenith and breakup of a supercontinent. Geol. Soc. America, Spec. Paper 288, pp. 207-228.

Gutiérrez, J.L., Rodríguez-Pevida, L.S. and Paniagua, A., 1988. Las mineralizaciones poliminerálicas de Pb-Zn-Sb-Ag-Au de Escaro (Nordeste de León): controles geológicos, evolucíon mineralógica y implicaciones metalogénicas. Bol. Soc. Esp. Min., 11(2): 120-121.

Gutiérrez-Alonso, G., Fernández-Suárez, J. and Weil, A.B., submitted. Orocline triggered lithospheric delamination. Earth and Planetary Science Letters.

Gutiérrez-Claverol, M., 1984. Los depósitos evaporíticos del tránsito Permotrías-Lías en Asturias (Mina Felisa). Revista de Minas, 4: 37-49.

Hanshaw, B.B., Back, W. and Dieke, R.G., 1971. A geochemical hypothesis for dolomitization by groundwater. Econ. Geol., 66: 710-724.

Hardie, L.A., 1987. Dolomitization: a critical view of some current views. J. Sed. Petrol., 57: 166-183.

Hardy, J.W. and Tucker, M.E., 1988. X-ray powder diffraction of sediments. In: M.E. Tucker (Editor), Techniques in sedimentology. Blackwell, Oxford, pp. 191-228.

Hardy, M., Ildefonse, J.P., Fortune, J.P., Touray, J.C. and García-Iglesias, J., 1980. Genèse du talc par diffusion simultanée du magnésium et de la silice: cas des gites de Puebla de Lillo (Boñar, León, Espagne). Implications pour la prospection. C.R. Acad. Sc. Paris, 290(12): 731-734.

Heijlen, W., Muchez, P. and Banks, D.A., 2001. Origin and evolution of high-salinity, Zn-Pb mineralising fluids in the Variscides of Belgium. Mineral. Deposita, 36: 165-176.

Hemleben, C. and Reuther, C.D., 1980. Allodapic limestones of the Barcaliente Formation (Namurian A) between Luna and Cea Rivers (southern Cantabrian Mountains, Spain). N. Jb. Geol. Paläont. Abh., 159(2): 225-255.

Heward, H.P. and Reading, H.G., 1980. Deposits associated with a Hercynian to late Hercynian continental strike-slip system, Cantabrian Mountains, northern Spain, IAS Spec. Publ. 4, pp. 105-125.

Hickman, S., Sibson, R.H. and Bruhn, R., 1995. Introduction to special section: mechanical involvement of fluids in faulting. J. Geoph. Res., 100(7): 12.831-12.840.

Hiltabrand, R.R., Farrell, R.E. and Billings, G.K., 1973. Experimental diagenesis of Gulf Coast argillaceous sediment. Bull. Am. Ass. Petrol. Geol., 57: 338-348.

Hird, K., 1986. Petrography and geochemistry of some Carboniferous and Precambrian dolomites. Ph.D. Thesis, University of Durhan, U.K., 232 pp.

Hitchon, B., Bachu, S. and Underschulz, J.R., 1990. Regional subsurface hydrogeology, Peace River arch area, Alberta and British Columbia. Bull. Can. Petrol. Geol., 38(A): 196-217.

Hitchon, B., Billings, G.K. and Klovan, J.E., 1971. Geochemistry and origin of formation waters in the Western Canada Sedimentary Basin. Geochim. Cosmochim. Acta, 35: 567-598.

Hoefs, J., 1997. Stable isotope geochemistry. Springer, Heidelberg, 201 pp.

Iannace, A., Boni, M. and Bechstädt, T., 2001. Late Variscan fluid-flow and hydrothermal dolomitisation: a European perspective? In: Piestrzynsky et al. (Eds.), Sixth Biennial SGA Meeting, Mineral Deposits at the Beginning of the 21st Century, Krakow, pp. 197-200.

Illing, L.V., 1959. Deposition and diagenesis of some Upper Palaeozoic carbonate sediments in western Canada, Fifth World Petroleum Congress, New York, pp. 23-52.

Jacobson, R.L. and Usdowski, H.E., 1976. Partitioning of strontium between calcite, dolomite and liquids. Contrib. Mineral. Petrol., 59: 171-185.

Jones, G.D., Smart, P.L., Whitaker, F.F., Rostron, B.J. and Machel, H.G., in press. Numerical modeling of reflux dolomitisation in the Grosmont Platform complex (Upper Devonian), Western Canada Sedimentary Basin. Bull. Am. Ass. Petrol. Geol.

Jones, G.D., Whitaker, F.F., Rostron, B.J. and H.G., M., 2002. Fate of reflux brines in carbonate platforms. Geology, 30: 371-374.

Julivert, M., 1967. La ventana tectónica del río Color y la prolongación septentrional del manto del Ponga (Cordillera Cantábrica, España). Geología de la región de mantos al E de la Cuenca Carbonífera Central (cord. Cantábrica). Trab. Geol., 1: 1-26.

Julivert, M., 1971. Décollement tectonics in the Hercynian Cordillera of northwest Spain. Am. J. Sci., 270: 1-29.

Julivert, M., 1978. Hercynian orogeny and Carboniferous palaeogeography in northwestern Spain: a model of deformation-sedimentation relationships. Z. dt. geol. Ges., 29: 565-592.

Julivert, M., Fontboté, J.M., Ribeiro, A. and Conde, L.N., 1972. Mapa tectónico de la Península Ibérica y Baleares. IGME, Madrid.

Julivert, M. and Marcos, A., 1973. Superimposed folding under flexural conditions in the Cantabrian Zone (Hercynian Cordillera, northwest Spain). Am. J. Sci., 273: 353-375.

Julivert, M., Ramírez del Pozo, J. and Truyóls, J., 1971. Le réseau de failles et la couberture post-hercynienne dans les Asturies. Histoire structurale du Golfe de Gascogne. Publ. Inst. Fr. Pétrol. Ed. Technip., pp. 3.1-3.34.

Katz, A., 1971. Zoned dolomite crystals. J. Geology, 79: 38-51.

Keller, M. and Krumm, S., 1993. Variscan versus Caledonian and Precambrian metamorphic events in the Cantabrian Mountains, northern Spain. Z. dt. geol. Ges., 144: 88-103.

Kelts, K. and McKenzie, J.A., 1984. A comparison of anoxic dolomite from deep-sea sediments: Quaternary Gulf of California and Messinian Tripoli Formation of Sicily. In: R.E. Garrison, M. Kastner and D.H. Zenger (Eds.), Dolomites of the Monterey Formation and other organic-rich units. SEPM Publ., Pacific Section 41, pp. 119-140.

Kharaka, Y.K. and Carothers, W.W., 1986. Oxygen and hydrogen isotope geochemistry of deep basin brines. In: P. Fritz and J.P. Fontes (Eds.), Handbook of environmental isotope geochemistry. Elsevier, Amsterdam, pp. 305-360.

Knauth, L.P. and Beeunas, M.A., 1986. Isotope geochemistry of fluid inclusions in Permian halite with implications for the history of ocean water and the origin of saline formation waters. Geochim. Cosmochim. Acta, 50: 419-433.

Knipe, R.J., 1993. The influence of fault zone processes and diagenesis on fluid flow. In: A.D. Horbury and A. Robinson (Eds.), Diagenesis and basin development. AAPG Studies in Geology, 36. Am. Ass. Petrol. Geol., Tulsa, pp. 135-151.

Kretz, R., 1982. A model for the distribution of trace elements between calcite and dolomite. Geochim. Cosmochim. Acta, 46: 1979-1981.

Krumgalz, B.S., Pogorelsky, R. and Pitzer, K.S., 1996. Volumetric properties of single aqueous electrolytes from zero to saturation concentrations at 298,15 K represented by Pitzer´s Ion-Interaction Equation. Journal of Physical Chemistry Reference Data, 25: 663-689.

Kullmann, J., Reuther, C.D. and Schönenberg, R., 1977. La transicíon del estadio geosinclinal a la orogénesis en la formacíon varíscica de la Cordillera Cantábrica. Brev. Geol. Astur., 21(1): 4-11.

Land, L.S., 1980. The isotopic and trace element geochemistry of dolomite: the state of the art. In: D.H. Zenger, J.B. Dunham and R.L. Ethington (Eds.), Concepts and models of dolomitization. SEPM Spec. Publ. 28, pp. 87-110.

Land, L.S., 1983. The application of stable isotopes to studies of the origin of dolomite and to problems of diagenesis of clastic sediments. In: M.A. Arthur, T.F. Anderson, I.R. Kaplan, J. Veizer and L.S. Land (Eds.), Stable isotopes in sedimentary geology. SEPM Short Course 10, pp. 4.1-4.22.

Land, L.S., 1985. The origin of massive dolomite. J. Geol. Educ., 33: 112-125.

Land, L.S. and Hoops, G.K., 1973. Sodium in carbonate sediments and rocks: a possible index to the salinity of diagenetic solutions. J. Sed. Petrol., 43: 614-617.

Land, L.S. and Presbindowski, D.R., 1981. The origin and evolution of saline formation water, Lower Cretaceous carbonates, south-central Texas, U.S.A. J. Hydrology, 54: 51-74.

Lee, Y.I. and Friedman, G.M., 1987. Deep-burial dolomitisation in the Ordovician Ellenburger Group carbonates, western Texas and southeastern New Mexico. J. Sed. Petrol., 57: 544-557.

Lepvrier, C. and Martínez-García, E., 1990. Fault development and sress evolution of the post-Hercynian Asturian Basin (Asturias and Cantabria, NW Spain). Tectonophysics, 184: 345-356.

Lloyd, R.M., 1966. Oxigen isotope enrichment of seawater by evaporation. Geochim. Cosmochim. Acta, 30: 801-814.

Lobato, L., García-Alcalde, J.L., Sánchez de Posada, L.C., Truylos, J. and Villegas, F.J., 1984. Hoja del Mapa Geológico Nacional de España (1:50000), Memoria 104 (Boñar). IGME, Madrid, 77 pp.

Loeschke, J., 1982. Late Hercynian igneous rocks of the southeastern Cantabrian Mountains (NW Spain). In: J. Kullmann, R. Schönenberg and J. Wiedmann (Eds.), Subsidenz-Entwicklung im kantabrischen Variszikum und an passiven Kontinentalraendern der Kreide. N. Jb. Geol. Paläont. Abh., Tübingen, pp. 260-272.

Lohman, K.C., 1987. Geochemical patterns of meteoric diagenetic systems and their application to studies of paleokarst. In: N.P. James and P.W. Choquette (Eds.), Pleokarst. Springer, New York, pp. 58-80.

Long, J.V.P. and Agrell, S.O., 1965. The cathodo-luminescence of minerals in thin section. Mineral. Mag., 34: 318-326.

Loredo, J. and García-Iglesias, J., 1988. El yacimiento aurífero de Carlés (Asturias). Bol. Soc. Esp. Min., 11(1): 47-54.

Lotze, F., 1945. Zur Gliederung der Varisziden in der Iberischen Grundgebirges (Spanien). Geotekt. Forsch., 6: 78-92.

Lugli, S., Torres-Ruiz, J., Garuti, G. and Olmedo, F., 2000. Petrography and geochemistry of the Eugui magnesite deposit (Western Pyrenees, Spain): evidence for the development of a peculiar zebra banding by dolomite replacement. Econ. Geol., 95: 1775-1791.

Lumsden, D.N., 1979. Discrepancy between thin section and X-ray estimates of dolomite in limestone. J. Sed. Geol., 49: 429-436.

Lumsden, D.N. and Chimahusky, J.S., 1980. Relationship between dolomite nonstoichiometry and carbonate facies parameters. In: D.H. Zenger, J.B. Dunham and R.L. Ethington (Eds.), Concepts and models of dolomitization. SEPM Spec. Publ. 28, pp. 87-110.

Luque, C. and Martínez-García, E., 1983. Depósitos minerales en el Carbonífero en la Cordillera Cantábrica. In: C. Martínez-Diaz (Ed.), Carbonífero y Pérmico de España. IGME, Madrid, pp. 163-177.

Luque, C., Martínez-García, E. and Ruiz, F., 1990. Metallogenesis. In: R.D. Dallmeyer and E. Martínez-García (Eds.), Pre-Mesozoic geology of Iberia. Springer, Berlin, pp. 80-87.

Machel, H.G., 1987. Saddle dolomite as a by-product of chemical compaction and thermochemical sulfate reduction. Geology, 15: 936-940.

Machel, H.G., 1993. The “biogenic” origin of stylolites in the Mark Brandenburg, Germany. Ichnos, 2: 175-181.

Machel, H.G., 1988. Fluid flow direction during dolomite formation as deduced from trace-element trends. In: V. Shukla and P.A. Baker (Eds.), Sedimentology and geochemistry of dolostones. SEPM Spec. Publ. 43, pp. 115-125.

Machel, H.G. and Burton, E.A., 1991. Factors governing cathodoluminescence in calcite and dolomite and their implications for studies of carbonate diagenesis. In: C.E. Barker and O.C. Kopp (Eds.), Luminescence microscopy and spectroscopy: qualitative and quantitative applications. SEPM Short Course 25, pp. 37-57.

Machel, H.G. and Cavell, P.A., 1999. Low-flux, tectonically-induced squeegee fluid flow (“hot flash”) into the Rocky Mountain Foreland Basin. Bull. Can. Petrol. Geol., 47(4): 510-533.

Machel, H.G., Cavell, P.A., Buschkuehle, B.E. and Michael, K., 2000. Tectonically induced fluid flow in Devonian carbonate aquifers of the Western Canada Sedimentary Basin. J. Geochem. Explor., 69-70: 213-217.

Machel, H.G. and Lonnee, J., 2002. Hydrothermal dolomite – a product of poor definition and imagination. Sedim. Geol., 152: 163-171.

Machel, H.G., Mason, R.A., Mariano, A.N. and Mucci, A., 1991. Causes and emission of luminescence in calcite and dolomite. In: C.E. Barker and O.C. Kopp (Eds.), Luminescence microscopy and spectroscopy: qualitative and quantitative applications. SEPM Short Course 25, pp. 9-25.

Machel, H.G. and Mountjoy, E.W., 1986. Chemistry and environments of dolomitization: a reappraisal. Earth Sci. Rev., 23: 175-222.

Marcos, A., 1968a. Nota sobre el significado da la "Leon Line". Brev. Geol. Astur., 3: 1-5.

Marcos, A., 1968b. La tectónica de la Unidad de la Sobia-Bodón. Trab. Geol., 2: 59-87.

Marcos, A., Kullmann, J. and Schönenberg, R., 1979. Facies differentiation caused by wrench deformation along a deep-seated fault system (León Line, Cantabrian Mountains, North Spain) - Discussion and reply. Tectonophysics, 60: 303-309.

Marcos, A. and Pulgar, J.A., 1982. An approach to the tectonostratigraphic evolution in the Cantabrian foreland thrust and fold belt, Hercynian Cordillera of NW Spain. N. Jb. Geol. Paläont. Abh., 163(2): 256-260.

Marquínez, J., 1978. Estudio geológico del sector SE de los Picos de Europa (Cordillera Cantábrica, NW de España). Trab. Geol., 10: 295-315.

Martín, J.M., Torres-Ruiz, J. and Fontboté, L., 1987. Facies control of strata-bound ore deposits in carbonate rocks: the F-(Pb-Zn) deposits in the Alpine Triassic of the Alpujárrides, southern Spain. Mineral. Deposita, 22: 216-226.

Martinéz-García, E., 1981. Tectónica y mineralizaciones Pérmicas en la Cordillera Cantábrica Oriental (noroeste de España). Cuad. Lab. Xeol. Laxe, 2: 263-270.

Martínez-García, E., 1983. El Pérmico de la Cordillera Cantábrica. In: C. Martínez-Díaz (Ed.), Carbonífero y Pérmico de España. IGME, Madrid, pp. 389-402.

Martínez-García, E. and Wagner, R.H., 1982. Una cuenca marina del Estefaniense Superior en el Noroeste de España. Trab. Geol., 12: 119-124.

Matte, P., 1991. Accretionary history and crustal evolution of the Variscan belt in western Europe. Tectonophysics, 196: 309-337.

Matte, P. and Ribeiro, A., 1975. Forme et orientation de l´ellipsoide de déformation dans la viration hercynienne de Galicia: relation avec le plissement et hypothèses sur la génèse de l´arc ibéro-armoricain. C.R. Acad. Sc. Paris, 280: 2825-2828.

Mattes, B.W. and Mountjoy, E.W., 1980. Burial dolomitization of the Upper Devonian Miette buildup, Jasper National Park, Alberta. In: D.H. Zenger, J.B. Dunham and R.L. Ethington (Eds.), Concepts and models of dolomitization. SEPM Spec. Publ. 28, pp. 259-297.

Mazzullo, S.J., 1992. Geochemical and neomorphic alteration of dolomite: a review. Carbonates and evaporites, 7: 21-37.

Mazzullo, S.J., 2000. Organogenic dolomitisation in peritidal to deepsea sediments. J. Sed. Res., 70: 10-23.

McIntyre, W.L., 1963. Trace element partition coefficients - a review of theory and applications to geology. Geochim. Cosmochim. Acta, 27: 1209-1264.

McKenzie, J.A., 1981. Holocene dolomitization of calcium carbonate sediments from the coastal sabkhas of Abu Dhabi: a stable isotope study. J. Geol., 89: 185-198.

McKenzie, J.A., 1991. The dolomite problem: an outstanding controversy. In: D.W. Müller, J.A. McKenzie and H. Weissert (Eds.), Controversies in modern geology. Academic Press, London, pp. 37-54.

McKibben, M.A., Williams, A.E., Elders, W.A. and Eldridge, C.S., 1987. Saline brines and metallogenesis in a modern sediment-filled rift: the Salton Sea geothermal system, California, U.S.A. Appl. Geochem., 2(5/6): 563-578.

Meyers, W.J., 1991. Calcite cement stratigraphy. In: C.E. Barker and O.C. Kopp (Eds.), Luminescence microscopy and spectroscopy: qualitative and quantitative aspects. SEPM Short Course 25, pp. 133-148.

Michalik, M., 1997. Chlorine containing illites, copper chlorides and other chloride bearing minerals in the Fore-Sudetic copper deposit (Poland). In: H. Papunen (Ed.), Mineral deposits: research and exploration. Balkema, Rotterdam, pp. 543-546.

Miller, J., 1988. Cathodoluminescence microscopy. In: M.E. Tucker (Ed.), Techniques in sedimentology. Blackwell, Oxford, pp. 86-107.

Miller, J.K. and Folk, R.L., 1994. Petrographic, geochemical and structural constraints on the timing and distribution of postlithification dolomite in the Rhaetian Portoro ("Calcare nero") of the Portovenere Area, La Spezia, Italy. In: B.H. Purser, M.E. Tucker and D.H. Zenger (Eds.), Dolomites – A volume in honour of Dolomieu. IAS Spec. Publ. 21, pp. 187-202.

Montañez, I.P., 1994. Late diagenetic dolomitization of Lower Ordovician, Upper Knox Carbonates: a record of the hydrodynamic evolution of the southern Appalachian Basin. Bull. Am. Ass. Petrol. Geol., 78(8): 1210-1239.

Montañez, I.P. and Read, J.F., 1992. Fluid-rock interaction history during stabilization of early dolomites, Upper Knox Group (Lower Ordovician), US Appalachians. J. Sed. Petrol., 62: 753-778.

Moore, C.H., 1989. Carbonate diagenesis and porosity evolution. Developement in Sedimentology, 46, Elsevier, Amsterdam, 338 pp.

Morrow, D.W., 1978. The influence of the Mg/Ca ratio and salinity on dolomitization in evaporite basins. Bull. Can. Petrol. Geol., 26(3): 389-392.

Morrow, D.W., 1990a. Dolomite - Part 1: the chemistry of dolomitization and dolomite precipitation. In: I.A. McIlreath and D.W. Morrow (Eds.), Geoscience Canada Reprint Series, 4, Ottawa, pp. 113-124.

Morrow, D.W., 1990b. Dolomite - Part 2: dolomitization models and ancient dolostones. In: I.A. McIlreath and D.W. Morrow (Eds.), Diagenesis. Geoscience Canada Reprint Series, 4, Ottawa, pp. 125-139.

Morrow, D.W., 1998. Regional subsurface dolomitization: models and constraints. Geoscience Canada, 25(2): 57-70.

Morrow, D.W. and Aulstead, K.L., 1995. The Manetoe Dolomite - a Cretaceous-Tertiary or a Paleozoic event? Fluid inclusion and isotopic evidence. Bull. Can. Petrol. Geol., 43(3): 267-280.

Morrow, D.W., Cumming, G.L. and Aulstead, K.L., 1990. The gas-bearing Devonian Manetoe Facies, Yukon and Northwest Territories, Geol. Surv. Canada, Bulletin 400, pp. 54.

Morton, R.A. and Land, L.S., 1987. Regional variations in formation water chemistry, Frio Formation (Oligocene), Texas Gulf Coast. Bull. Am. Ass. Petrol. Geol., 71: 191-206.

Mountjoy, E.W. and Amthor, J.E., 1994. Has burial dolomitization come of age? Some answers from the Western Canada Sedimentary Basin. In: B.H. Purser, M.E. Tucker and D.H. Zenger (Eds.), Dolomites - A volume in honour of Dolomieu. IAS Spec. Publ. 21, pp. 203-229.

Mountjoy, W. and Qing, H., 1992. Strontium isotopic composition of Devonian dolomites, Western Canada Sedimentary Basin: significance of sources of dolomitizing fluids. Appl. Geochem., 7: 59-75.

M'Rabet, A., 1981. Differentiation of environments of dolomite formation, Lower Cretaceous of Central Tunisia. Sedimentology, 28: 331-352.

Muchez, P., Slobodnik, M., Viaene, W.A. and Keppens, E., 1995. Geochemical constraints of the origin and migration of palaeofluids in the northern margin of the Variscan foreland, southern Belgium. Sedim. Geol., 96: 191-200.

Muir Wood, R., 1994. Earthquakes, strain-cycling and the mobilization of fluids. In: J. Parnell (Ed.), Geofluids: origin, migration and evolution of fluids in sedimentary basins. Spec. Publ. Geol. Soc. London 78, pp. 85-98.

Murray, R.C. and Lucia, F.J., 1967. Cause and control of dolomite distribution by rock selectivity. Bull. Geol. Soc. America, 78: 21-36.

Mussman, W.J., Montañez, I.P. and Read, J.F., 1988. Ordovician Knox paleokarst unconformity, Appalachians. In: N.P. James and P.W. Choquette (Eds.), Paleokarst. Springer, New York, pp. 211-228.

Naden, J., 1996. *CalcicBrine*: a Microsoft Excel 5.0 Add-in for calculating salinities from microthermometric data in the system NaCl-$CaCl_2$-H_2O, PACROFI VI, Wisconsin, pp. 97-98.

Nägler, T., 1990. Sm-Nd, Rb-Sr and common lead isotope geochemistry on fine-grained sediments of the Iberian Massif. Unpubl. Ph.D. Thesis, Federal Technical Institute of Zurich, Swiss, 139 pp.

Neimann, J.C. and Read, J.F., 1988. Regional cementation associated with unconformity-sourced aquifers and burial fluids, Kentucky. J. Sed. Petrol., 58: 688-705.

Nelson, K.D., 1992. Are crustal thickness variations in old mountain belts like the Appalachians a consequence of lithospheric delamination? Geology, 20: 498-502.

Nielsen, P., Swennen, R., Muchez, P. and Keppens, E., 1998. Origin of Dinantian zebra-dolomites south of the Brabant-Wales Massif, Belgium. Sedimentology, 45: 727-743.

Odling, N.E., 1997. Fluid flow in fractured rocks at shallow levels in the Earth´s crust: an overview. In: M.B. Holness (Ed.), Deformation-enhanced fluid transport in the Earth´s crust and mantle. Chapman and Hall, London, pp. 333.

Ohle, E.L., 1951. The influence of permeability on ore distribution in limestone and dolomite. Econ. Geol., 46: 667-706, 871-908.

Oldenburg, C.M. and Pruess, K., 1998. Layered thermohaline convection in hypersaline geothermal systems. Geothermal Energy, 33(1-2): 29-63.

Oliver, J., 1986. Fluids expelled tectonically from orogenic belt: their role in hydrocarbon migration and other geologic phenomena. Geology, 14: 99-102.

Orti, F., García-Veigas, J., Rosell, L., Jurado, M.J. and Utrilla, R., 1996. Formaciónes salinas de la cuencas triásicas en la península Ibérica: caracterizacíon petrológica y geoquímica. Cuad. Geol. Ibérica, 20: 13-35.

Pagel, M., Barbin, V., Blanc, P. and Ohnenstetter, D., 2000. Cathodoluminescence in geosciences: an introduction. Springer, Heidelberg, 514 pp.

Paniagua, A., 1989. The pyrite-type Cu-rich disulfides in the Providencia mine, León, NW Spain. In: G.H. Moh (Ed.), Ore Minerals: an experimental approach and new observations. Neues. J. Mineral. Abh., Tübingen, pp. 8-11.

Paniagua, A., 1993. Mineralizaciones asociadas a estructuras tardihercínicas en la rama Sur de la Zona Cantábrica. Unpubl. Ph.D. Thesis, University of Oviedo, Spain, 377 pp.

Paniagua, A., 1998. Gold showings and deposits of the Palentian Zone (NW Spain). In: D. Arias, A. Martín-Izard and A. Paniagua (Eds.), Gold in NW Spain. Departamento de Geología, Oviedo, pp. 112-123.

Paniagua, A., Fontboté, L., Fenoll Hach-Alí, P., Fallick, A.E., Moreiras, D.B., Corretgé, L.G., 1993. Tectonic setting, mineralogical characteristics, geochemical signatures and age dating of a new type of epithermal carbonate-hosted, precious metal-five element deposits: the Villamanín area (Cantabrian Zone, northern Spain). In: P. Fenoll Hach-Alí, J. Torres-Ruiz and F. Gervilla (Eds.), Current research in geology applied to ore deposits, 2nd biennal SGA Meeting, Granada, pp. 531-534.

Paniagua, A., Loredo, J. and García-Iglesias, J., 1988a. Epithermal (Cu-Co-Ni) mineralization in the Aramo mine (Cantabrian Mountains, Spain). Bull. Minéral., 111: 383-391.

Paniagua, A., Loredo, J. and García-Iglesias, J., 1995. Epithermal carbonate-hosted Au-Cu-Ni-Co mineralization at the Villamanín area (Cantabrian Zone, N Spain). Bol. Soc. Esp. Min., 18(1): 172-173.

Paniagua, A. and Rodríguez-Pevida, L.S., 1988. Genesis y evolucíon de las mineralizaciones de Cu-Co-Ni-U-Pb-Zn-Au-Ag ligadas a las estructuras tardihercinicas en el area Pajares-Villamanín-Boñar (Norte de León). Bol. Soc. Esp. Min., 11(2): 118-119.

Paniagua, A., Rodríguez-Pevida, L.S., Garzón, L., Pérez, J.M. and Quintana, A., 1987. Presencia de una paragénesis Cu-Ni-U-As-S en la Zona Cantábrica: la Mina Profunda (Cármenes, León). Geogaceta, 2: 22-24.

Paniagua, A., Rodríguez-Pevida, L.S. and Gutiérrez-Villarias, J.L., 1988b. Mineralizaciones As-Sb-Au asociadas a rocas igneas filonianas del NE de León: las

minas de Burón. Bol. Soc. Esp. Min., 11(1): 35-46.

Paniagua, A., Rodríguez-Pevida, L.S., Loredo, J., Fontboté, L. and Fenoll Hach-Ali, P., 1996. Un yacimiento de Au en carbonatos del Orógeno Hercínico: el área de Salamón (N León). Geogaceta, 20(7): 1605-1608.

Patterson, R.J., 1972. Hydrology and carbonate diagenesis on a coastal sabkha in the Persian Gulf. Unpubl. Ph.D. Thesis, Princeston University, United States, 498 pp.

Pérez-Estaún, A. and Bastida, F., 1990. Structure, Cantabrian Zone. In: R.D. Dallmeyer and E. Martínez-García (Eds.), Pre-Mesozoic geology of Iberia. Springer, Berlin, pp. 55-69.

Pérez-Estaún, A., Bastida, F., Alonso, J.L., Marquinez, J., Aller, J., Alvarez-Marrón, J., Marcos, A., Pulgar, J.A., 1988. A thin-skinned tectonics model for an arcuate fold and thrust belt: the Cantabrian Zone (Variscan Ibero-Armorican Arc). Tectonics, 7(3): 517-537.

Perry, E.A. and Hower, J., 1970. Burial diagenesis in Gulf Coast pelitic sediments. Clays and Clay Min., 56: 2013-2021.

Perry, E.A.J. and Turekian, K.K., 1974. The effects of diagenesis on the redistribution of strontium isotopes in shales. Geochim. Cosmochim. Acta, 38(6): 929-935.

Pierson, B.J., 1981. The control of cathodoluminescence in dolomite by iron and manganese. Sedimentology, 28: 601-610.

Popp, B.A., Anderson, T.F. and Sandberg, P.A., 1986. Brachiopods as indicators of original isotopic compositions in some Paleozoic limestones. Bull. Geol. Soc. America, 97: 1262-1269.

Prado, J.G., 1972. Nota sobre la petrografía de la Zona de Viñon (Asturias). Stud. Geol. Salamanca, 3: 7-32.

Presbindowski, D.R. and Larese, R.E., 1987. Experimental stretching of fluid inclusions in calcite - implications for diagenetic studies. Geology, 15: 333-336.

Pulgar, J.A., Alonso, J.L., Espina, R.G. and Marín, J.A., 1999. La deformación alpina en el basamento varisco de la Zona Cantábrica. Trab. Geol., 21: 283-294.

Purser, B.H., Brown, A. and Aissaoui, D.M., 1994c. Nature, origin and evolution of porosity in dolomites. In: B.H. Purser, M.E. Tucker and D.H. Zenger (Eds.), Dolomites – A volume in honour of Dolomieu. IAS Spec. Publ. 21, pp. 283-308.

Purser, B.H., Tucker, M.E. and Zenger, D.H., 1994a. Problems, progress and future research concerning dolomites and dolomitization. In: B.H. Purser, M.E. Tucker and D.H. Zenger (Eds.), Dolomites – A volume in honour of Dolomieu. IAS Spec. Publ. 21, pp. 3-20.

Purser, B.H., Tucker, M.E. and Zenger, D.H., 1994b. Dolomites - A volume in honour of Dolomieu. IAS Spec. Publ., 21, 451 pp.

Qing, H. and Mountjoy, E.W., 1992. Large-scale fuid flow in the Middle Devonian Presquíle barrier, Western Canada Sedimentary Basin. Geology, 20: 903-906.

Qing, H. and Mountjoy, E.W., 1994a. Formation of coarsely crystalline, hydrothermal dolomite reservoirs in the Presqu´ile Barrier, Western Canada Sedimentary Basin. Bull. Am. Ass. Petrol. Geol., 78(1): 55-77.

Qing, H. and Mountjoy, E.W., 1994b. Origin of dissolution vugs, caverns, and breccias in the Middle Devonian Presqu´ile Barrier, host of the Pine Point Mississippi Valley-Type deposits. Econ. Geol., 89: 858-876.

Radke, B.M. and Mathis, R.L., 1980. On the formation and occurrence of saddle dolomite. J. Sed. Petrol., 50(4): 1149-1168.

Ramsay, J.G., 1980. The crack-seal mechanism of rock deformation. Nature, 284: 135-139.

Raven, J.G.M. and Van der Pluijm, B.A., 1986. Metamorphic fluids and transtention in the Cantabrian Mountains of northern Spain: an application of the conodont colour alteration index. Geol. Mag., 123(6): 673-681.

Reeder, R.J., 1991. An overview of zoning in carbonate minerals. In: C.E. Barker and O.C. Kopp (Eds.), Luminescence microscopy and spectroscopy: qualitative and quantitative applications. SEPM Short Course 25, pp. 77-82.

Reuther, C.D., 1977. Das Namur im südlichen Kantabrischen Gebirge (Nordspanien). Krustenbewegungen und Faciesdifferenzierung im Übergang Geosynklinale-Orogen. Clausth. geol. Abh., 28: 1-122.

Reuther, C.D., 1980. The Lower Carboniferous facies levelling and the first Upper Carboniferous tectonic events in the Cantabrian Mountains and the Pyrenees (Spain) - a comparison. In: J. Kullmann, R. Schönenberg and J. Wiedmann (Eds.), Subsidenz-Entwicklung im Kantabrischen Variszikum und an passiven Kontinentalraendern der Kreide. N. Jb. Geol. Paläont., Tübingen, pp. 244-250.

Rex, R.W., 1985. Temperature-chlorinity balance in the hypersaline brines of the Imperial Valley, California. In: C. Stone (Ed.), International Symposium on Geothermal Energy. Geothermal Resources Council, Davis, pp. 351-356.

Ries, A.C., Richardson, A. and Schackleton, R.M., 1980. Rotation of the Iberian arc: paleomagnetic results from north Spain. Earth and Planetary Science Letters, 50: 301-310.

Roedder, E., 1984. Fluid inclusions. Reviews in Mineralogy 12. Min. Soc. America, Chelsea, 644 pp.

Samson, I.M. and Walker, R.T., 2000. Cryogenic Raman Spectroscopy studies in the system NaCl-$CaCl_2$-H_2O. The Canadian Mineralogist, 38: 35-43.

Sánchez de la Torre, L., Águeda, J., Colmenero, J.R., García-Ramos, J.C. and González-Lastra, J., 1983. Evolución sedimentaria y paleogeográfica del Carbonífero en la Cordillera Cantábrica. In: D.C. Martínez (Ed.), Carbonífero y Pérmico de España. IGME, Madrid, pp. 133-150.

Sánchez de la Torre, L., Agueda-Villar, J.A., Colmenero, J.R. and Manjón, M., 1977. La serie Permotríasica en la región de Villaviciosa. Cuad. Geol. Ibérica, 4: 329-338.

Sanford, W.E., Whitaker, F.A., Smart, P.L. and Jones, G., 1998. Numerical analysis of seawater circulation in carbonate platforms: I. Geothermal convection. Am. J. Sci., 298: 801-828.

Sass-Gustkiewicz, M., Dzulynski, S. and Ridge, J.D., 1983. The emplacement of zinc-lead sulfide ores in the Upper Silesian district - a contribution to the understanding of Mississippi Valley-type deposits. Econ. Geol., 77: 392-412.

Schneider, J., 2000. Indirekte Rb-Sr-Chronometrie postorogener Hydrothermalsysteme und assoziierter Gangmineralisationen im Rhenohercynikum. Unpubl. Ph.D. Thesis, University of Giessen, Germany, 162 pp.

Schott, B. and Schmeling, H., 1998. Delamination and detachment of a lithospheric root. Tectonophysics, 296: 225-247.

Shepherd, T.J., Rankin, A.H. and Alderton, D.H.M., 1985. A practical guide to fluid inclusion studies. Blackie & Son, Glasgow, 239 pp.

Shukla, V. and Baker, P.A., 1988. Sedimentology and geochemistry of dolostones. SEPM Spec. Publ., 43, 266 pp.

Sibley, D.F. and Gregg, J.M., 1987. Classification of dolomite rock textures. J. Sed. Geol., 57(6): 967-975.

Sibson, R.H., 1981. Fluid flow accompanying faulting: field evidence and models. In: D.W. Simpson and P.G. Richards (Eds.), Earthquake prediction: an international review. American Geophysical Union, Washington, pp. 593-603.

Simo, J.A. et al., 1994. Burial dolomitization of the Middle Ordovician Glenwood Formation by evaporitic brines, Michigan Basin. In: B.H. Purser, M.E. Tucker and D.H. Zenger (Eds.), Dolomites - A volume in honour of Dolomieu. IAS Spec. Publ. 21, pp. 169-186.

Smalley, P.C., Higgins, A.C., Howarth, R.J., Nicholson, H., Jones, C.E., Swinburne, N.H.M., Bessa, J., 1994. Seawater Sr isotope variations through time: a procedure for constructing a reference curve to date and correlate marine sedimentary rocks. Geology, 22: 431-434.

Sommer, S.E., 1972. Cathodoluminescence of carbonates, 1. Characterization of cathodoluminescence from carbonate solid solutions. Chem. Geol., 9: 257-273.

Spencer-Cervato, C. and Mullis, J., 1992. Chemical study of tectonically controlled hydrothermal dolomitization: an example from the Lessini Mountains, Italy. Geol. Rdsch., 81(2): 347-370.

Sperber, C.M., Wilkinson, B.H. and Peacor, D.R., 1984. Rock composition, dolomite stoichiometry, and rock/water reactions in dolomitic carbonate rocks. J. Geology, 92: 609-622.

Spiro, B., Tornos, F. and Shepherd, T.J., 1995. Stable isotope characterization of barren and mineralized tardi-Hercynian hydrothermal carbonates in the Cantabrian Zone (N Spain). In: J. Pasava, B. Kríbek and K. Zák (Eds.), Mineral deposits: from their origin to environmental impacts. Balkema, Rotterdam, pp. 75-78.

Spötl, C. and Pitman, J.K., 1998. Saddle (baroque) dolomite in carbonates and sandstones: a reappraisal of a burial-diagenetic concept, IAS Spec. Publ. 26, pp. 437-460.

Stueber, A.M., Pushkar, P. and Hetherington, E.A., 1987. A strontium isotopic study of formation waters from the Illinois basin, USA. Appl. Geochem., 2: 477-494.

Suchy, V., Rozkosny, I., Zák, K. and Francu, J., 1996. Epigenetic dolomitization of the Prídolí formation (Upper Silurian), the Barrandian basin, Czech Republic: implications for burial history of Lower Paleozoic strata. Geol. Rdsch., 85(264-277).

Sun, S.Q., 1992. Skeletal aragonite dissolution from hypersaline seawater: a hypothesis. Sedim. Geol., 77: 249-257.

Taylor, T.R. and Sibley, D.F., 1986. Petrographic and geochemical characteristics of dolomite types and the origin of ferroan dolomite in the Treton Formation, Ordovician, Michigan Basin, USA. Sedimentology, 33: 61-86.

Tompkins, L.A., Murray, J.R. and Groves, D.I., 1994. Evaporites: in situ source for rhythmically banded ore in the Cadjebut Mississippi Valley-Type Zn-Pb deposit, Western Australia. Econ. Geol., 89: 467-492.

Tornos, F., Delgado, A., Casquet, C. and Galindo, C., 2000. 300 Million years of episodic hydrothermal activity: stable isotope evidence from hydrothermal rocks of the Eastern Iberian Central System. Mineral. Deposita, 35: 551-569.

Tornos, F. and Spiro, B.F., 2000. The geology and isotope geochemistry of the talc deposits of Puebla de Lillo (Cantabrian Zone, northern Spain). Econ. Geol., 95: 1277-1296.

Tucker, M.E. and Wright, V.P., 1990. Carbonate sedimentology. Blackwell, Oxford, 482 pp.

Usdowski, E., 1994. Synthesis of dolomite and geochemical implications. In: B.H. Purser, M.E. Tucker and D.H. Zenger (Eds.), Dolomites - A volume in honour of Dolomieu. IAS Spec. Publ. 21, pp. 345-360.

Vahrenkamp, V.C., Swart, P.K. and Ruiz, J., 1991. Episodic dolomitisation of Late Cenozoic carbonates in the Bahamas: evidence from strontium isotopes. J. Sed. Petrol., 61: 1002-1014.

Valverde-Vaquero, P., Cuesta-Fernández, A., Gallastegui, G., Suárez, O., Corretgé, L.G., Dunning, G.R., 1999. U-Pb dating of late-Variscan magmatism in the Cantabrian Zone (northern Spain), EUG X, Strasbourg, pp. 101.

Van der Voo, R., Stamatakos, J.A. and Parés, J.M., 1997. Kinematic constraints on thrust-belt curvature from syndeformational magnetisations in Lagos de Valle Syncline in the Cantabrian arc, Spain. J. Geoph. Res., 102(10): 105-120.

Veizer, J., 1983. Chemical diagenesis of carbonates: theory and application of trace element technique. In: M.A. Arthur, T.F. Anderson, I.R. Kaplan, J. Veizer and L.S. Land (Eds.), Stable isotopes in sedimentary geology. SEPM Short Course 10, pp. 3.1-3.100.

Veizer, J., Ala, D., Azmy, K., Bruckschen, P., Dieter, B., Bruhn, F., Carden, G.A.F., Diener, A., Ebneth, S., Godderis, Y., Jasper, T., Korte, C., Pawellek, F., Podlaha, O.G., Strauss, H., 1999. $^{87}Sr/^{86}Sr$, $\delta^{13}C$ and $\delta^{18}O$ evolution of Phanerozoic seawater. Chem. Geol., 161: 59-88.

Veizer, J. and Compton, W., 1974. $^{87}Sr/^{86}Sr$ composition of seawater during the Phanerozoic. Geochim. Cosmochim. Acta, 38: 1461-1484.

Veizer, J. and Demovic, R., 1974. Strontium as a tool in facies analysis. J. Sed. Petrol., 44: 93-115.

Veizer, J., Fritz, P. and Jones, B., 1986. Geochemistry of brachiopods: oxygen and carbon isotopic records of Paleozoic oceans. Geochim. Cosmochim. Acta, 50: 1679-1696.

Veizer, J. and Hoefes, J., 1976. The nature of $^{18}O/^{16}O$ and $^{13}C/^{12}C$ secular trend in sedimentary carbonate rocks. Geochim. Cosmochim. Acta, 40: 1387-1395.

Veizer, J., Lemieux, J., Jones, B., Gibling, M.R. and Savelle, J., 1977. Sodium: paleosalinity indication in ancient carbonate rocks. Geology, 5: 177-179.

Von der Borch, C.C. and Lock, D., 1979. Geological significance of Coorong dolomites. Sedimentology, 23: 587-591.

Wachter, E. and Hayes, J.M., 1985. Exchange of oxygen isotopes in carbon-dioxide - phosphoric acid systems. Chem. Geol., 52: 365-374.

Wagner, R.H., Winkler Prins, C.F. and Riding, R.E., 1971. Lithostratigraphic units of the lower part of the Carboniferous in northern León, Spain. Trab. Geol., 4: 603-663.

Wallace, M.W., Both, R.A., Morales Ruano, S., Hach-Ali, P.F. and Lees, T., 1994. Zebra textures from carbonate-hosted sulfide deposits: sheet cavity networks produced by fracture and solution enlargement. Econ. Geol., 89: 1183-1191.

Wanless, H.R., 1979. Limestone response to stress: pressure solution and dolomitization. J. Sed. Petrol., 49: 437-462.

Weaver, C.E. and Beck, K.C., 1971. Clay-water diagenesis during burial: how mud becomes gneiss, Geol. Soc. America, Spec. Paper 134, pp. 96.

Weil, A.B., Van der Voo, R. and Van der Pluijm, B.A., 2001. Oroclinal bending and evidence against the Pangea megashear: the Cantabria-Asturias arc (northern Spain). Geology, 29: 991-994.

Weil, A.B., Van der Voo, R., Van der Pluijm, B.A. and Parés, J.M., 2000. The formation of an orocline by multiphased deformation: a paleomagnetic investigation of the Cantabria-Asturias arc hinge-zone (northern Spain). J. Struct. Geol., 22: 735-756.

Wendte, J., Qing, H., Dravis, J.J., Moore, S.L.O., Stasiuk, L.D., Ward, G., 1998. High temperature saline (thermoflux) dolomitization of Devonian Swan Hills platform and bank carbonates, Wild River area, west-central Alberta. Bull. Can. Petrol. Geol., 46(2): 210-265.

Weyl, P.K., 1959. Pressure solution and the force of crystallisation - a phenomenological theory. J. Geoph. Res., 64: 2001-2025.

Whitaker, F.F., Smart, P.L., Vahrenkamp, V.C., Nicholson, H. and Wogelius, R.A., 1994. Dolomitization by near-normal seawater? Field evidence from the Bahamas. In: B.H. Purser, M.E. Tucker and D.H. Zenger (Eds.), Dolomites – A volume in honour of Dolomieu. IAS Spec. Publ. 21, pp. 111-132.

White, D.E., 1957. Thermal waters of volcanic origin. Bull. Geol. Soc. America, 68: 1637-1658.

White, D.E., Hem, J.D. and Waring, G.A., 1963. Chemical composition of subsurface waters, U.S. Geol. Surv. Prof. Paper 44, pp. 67.

Wilkinson, J.J., Jenkin, G.R.T. and Fallick, R.P., 1995. Oxygen and hydrogen isotopic evolution of Variscan crustal fluids, U.K. Chem. Geol., 123: 239-254.

Williams, A.E., 1997. Fluid density distribution in high temperature, stratified thermohaline system: implications for saline hydrothermal circulation. Earth and Planetary Science Letters, 146(1-2): 121-136.

Wilson, A.M., Sanford, W.E., Whitaker, F.A. and Smart, P.L., 2001. Spatial patterns of diagenesis during geothermal circulation in carbonate platforms. Am. J. Sci., 301: 727-752.

Wilson, E.N., Lawrence, A.H. and Phillips, O.M., 1990. Dolomitization front geometry, fluid flow patterns, and the origin of massive dolomite: the Triassic Latemar buildup, northern Italy. Am. J. Sci., 290: 741-796.

Wood, J. and Hewett, T.A., 1982. Fluid convection and mass transfer in porous sandstones - a theoretical model. Geochim. Cosmochim. Acta, 46: 1707-1713.

Wopenka, B., Pasteris, J.D. and Freeman, J.J., 1990. Analysis of individual fluid inclusions by Fourier transform infrared and Raman microspectroscopy. Geochim. Cosmochim. Acta, 54: 519-533.

Wright, W.R., Somerville, I.D., J.M., G. and Shelton, K.L., 1999. Dolomite CL and $\delta^{18}O$ $\delta^{13}C$ data from Irish Midlands and Dublin Basin, Carboniferous. In: Stanley et al. (Eds.), Mineral Deposits: Processes to Processing, pp. 913-916.

Ypma, J.M., Evers, H.J. and Woensdergt, C.F., 1968. Mineralogy and geology of the Providence Mine (León, Spain), type-locality of Villamaninite. N. Jb. Miner. Monaths., 6: 174-191.

Zeeh, S., 1995. Complex replacement of saddle dolomite by fluorite within zebra dolomites. An example from Radnig, Carinthia, Austria. Mineral. Deposita, 30: 469-475.

Zeeh, S. and Schneider, J., in press. Fluid-Flow in S-Frankreich und N-Spanien im Zeitraum Oberkreide - Eozän, Sediment 2003, Wilhelmshaven.

Zenger, D.H., 1983. Burial dolomitization in the Lost Burro Formation (Devonian), east-central California, and the significance of late diagenetic dolomitization. Geology, 11: 519-522.

Zenger, D.H., Dunham, J.B. and Ethington, R.L., 1980. Concepts and models of dolomitization. SEPM Spec. Publ., 28, 320 pp.

Appendix

Appendix 1

Geological map of the central and eastern Bodón Unit (modified from Lobato et al. 1984, Alonso et al. 1990), stratigraphy of the different nappes and location of the sampled sites.

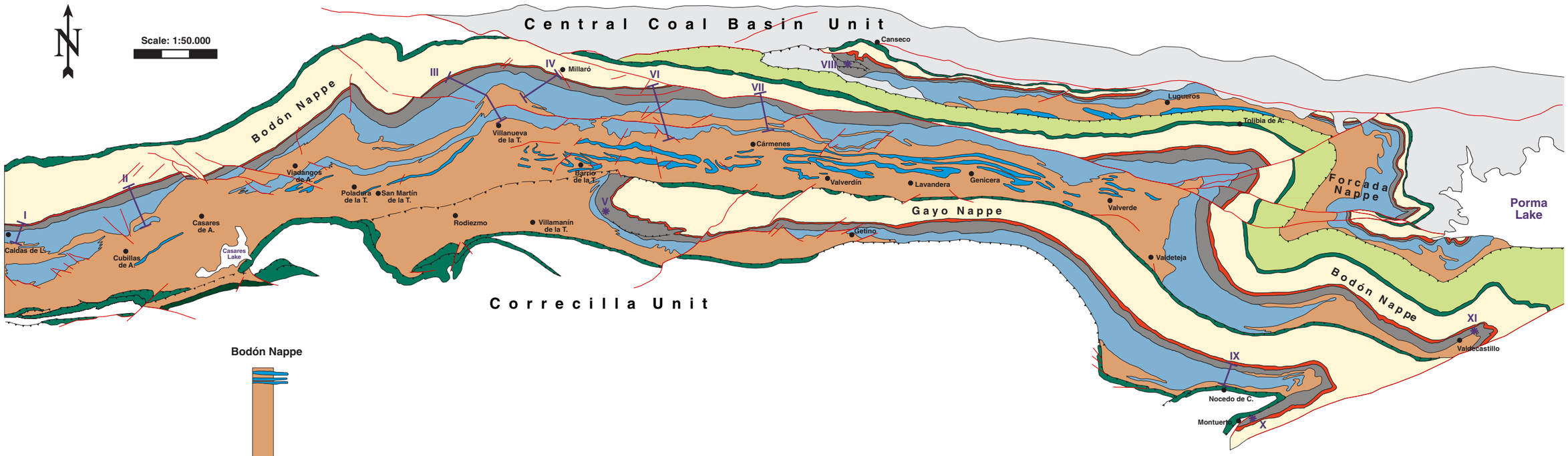

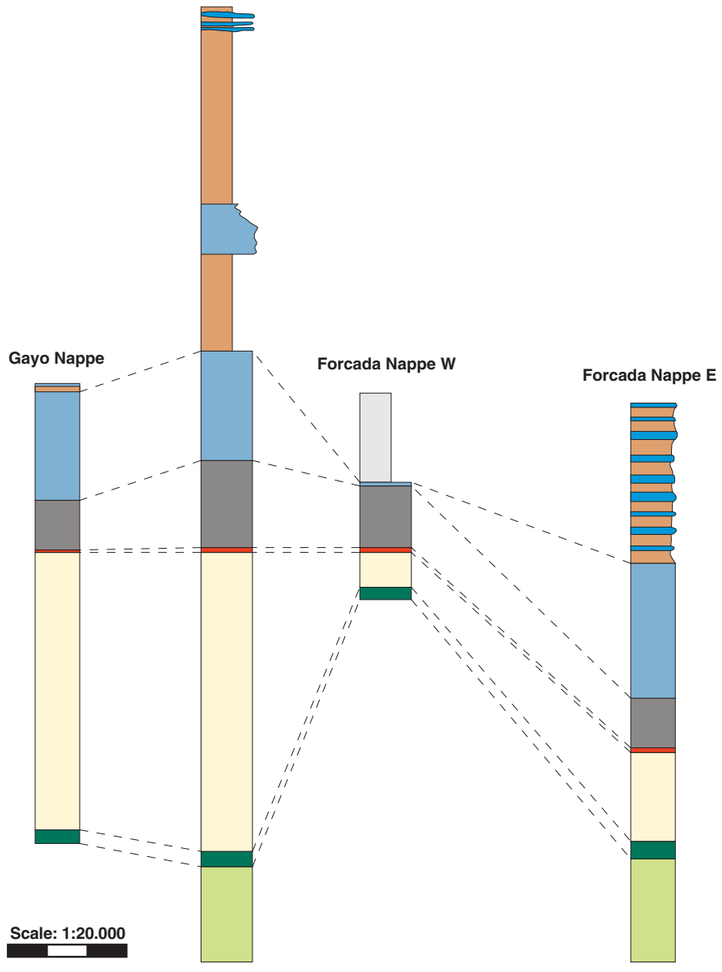

LEGEND

- Undifferentiated Upper Carboniferous (Lena and Sama groups, Stephanian B molasse)
- Light grey, massive, bioclastic limestone (Valdeteja Fm.)
- Undifferentiated Upper Cambrian - Devonian
- Carbonate levels (San Emiliano Fm.)
- Black, laminated, bitouminous limestone (Barcaliente Fm.)
- Limestones, dolomites, red nodular limestones (Láncara Fm.)
- Sandstones and shales (San Emiliano Fm.)
- Fossiliferous reddish nodular limestone (Alba Fm.)
- Sandstones, quarzites lutites and shales (Herrería Fm.)
- Faults
- Thrusts
- Sampled profiles
- Sampled points
- Towns, villages
- Artificial lakes

SAMPLED SITES

I	Caldas			VIII	Canseco
II	Cubillas	V	Villamanín	IX	Nocedo
III	Villanueva	VI	Mina Profunda	X	Montuerto
IV	Millaró	VII	Cármenes	XI	Valdecastillo

Appendix 2

Analysed samples and results of geochemical analyses: stoichiometry, degree of order, and elemental and isotopic geochemistry.

In the column “Formation” the stratigraphic level of the collected samples is reported as “base”, “middle” and “top”. The stratigraphic level of the samples from the Valdeteja Fm. interfingered with the San Emiliano Fm. is reported as “interf.”.

In the column “Phase” the grey and white colours group the mineral phases, which refer to the same sampled site.

Locality	Sample	Formation	Phase	$CaCO_3$ mol %	OR	$\delta^{18}O$	$\delta^{13}C$	$^{87}Sr/^{86}Sr$	Ca (%)	Mg (%)	Sr (ppm)	Na (ppm)	Fe (ppm)	Mn (ppm)
Caldas I	134	Alba (top)	H	-	-	-2.02	3.14	-	36.49	0.33	256	200	2000	463
	136	Alba (top)	Dol A2	50.14	0.67	-9.83	3.61	-	18.35	10.62	23	500	3400	558
	"	"	Dol B	50.01	0.6	-9.85	3.57	-	19.24	10.29	25	400	3200	553
	"	"	Cal 1	-	-	-8.12	-2.64	-	-	-	-	-	-	-
	ClBL1M	Barcaliente (middle)	H	-	-	1.12	4.54	-	32.57	0.17	450	200	3100	117
	138	Barcaliente (middle)	Dol A2	48.99	0.87	-3.61	4.66	-	17.43	10.69	19	500	1000	230
	"	"	Dol B	48.9	0.97	-4.48	3.65	-	17.48	10.71	15	300	1000	364
	147	Barcaliente (middle)	Cal 2	-	-	-11.72	-3.18	-	-	-	-	-	-	-
	ClVL1B	Valdeteja (base)	H	-	-	-1.55	3.32	-	-	-	-	-	-	-
	144l	Valdeteja (base)	Dol A2	49.43	0.77	-2.96	3.16	-	-	-	-	-	-	-
	143	Valdeteja (base)	Cal 2	-	-	-6.77	-7.93	-	-	-	-	-	-	-
Cubillas II	CuBL3M	Barcaliente (middle)	H	-	-	2.05	4.55	0.708105	39.43	0.25	725	200	200	12
	"	"	CV	-	-	-9.76	2.33	-	-	-	-	-	-	-
	CuBD1M	Barcaliente (middle)	Dol A1	49.50	0.91	-5.30	4.00	0.708491	18.00	10.55	30	300	1400	222
	"	"	Dol A2	49.47	1	-5.34	3.96	0.708687	17.93	10.65	17	200	1300	179
	"	"	Dol B	49.51	0.87	-6.75	4.02	0.708576	18.11	10.6	15	300	1800	391
	CuBL4T	Barcaliente (top)	H	-	-	0.36	5.13	-	-	-	-	-	-	-
	CuBD2T	Barcaliente (top)	Dol A1	-	-	-7.2	5.25	-	-	-	-	-	-	-
	"	"	Dol A2	-	-	-7.28	5.23	-	-	-	-	-	-	-
	CuVL2T	Valdeteja (top)	H	-	-	-2.74	4.48	-	-	-	-	-	-	-
	CuVD2T	Valdeteja (top)	Dol A2	-	-	-5.44	4.46	-	-	-	-	-	-	-
	VaVL4	Valdeteja (interf.)	H	-	-	-4.09	5.29	-	38.52	0.31	335	100	500	39
	VaVD2	Valdeteja (interf.)	Dol A2	49.89	0.75	-8.71	4.39	-	19.05	9.89	20	200	3300	514
	"	"	Dol B	50.08	0.76	-9.07	5.23	-	20.21	10.16	22	200	4600	655
	"	"	Cal 1	-	-	-14.23	2.52	-	-	-	-	-	-	-

Locality	Sample	Formation	Phase	$CaCO_3$ mol %	OR	$\delta^{18}O$	$\delta^{13}C$	$^{87}Sr/^{86}Sr$	Ca (%)	Mg (%)	Sr (ppm)	Na (ppm)	Fe (ppm)	Mn (ppm)
Villanueva III	VC172	Alba (top)	Dol A2	-	-	-8.53	3.87	-	-	-	-	-	-	-
	"	"	Dol B	-	-	-8.48	3.71	-	-	-	-	-	-	-
	"	"	Cal 1	-	-	-15.39	0.76	-	-	-	-	-	-	-
	VCAD1T	Alba (top)	Dol A2	49.7	0.77	-	-	-	18.57	10.94	17	500	1700	326
	"	"	Dol B	49.3	0.75	-	-	-	18.95	10.41	24	300	1900	338
	"	"	Cal 1	-	-	-	-	-	-	-	-	-	-	-
	46	Barcaliente (base)	Dol A2	-	-	-9.63	4.02	-	-	-	-	-	-	-
	"	"	Dol B	-	-	-7.79	4.54	-	-	-	-	-	-	-
	VCBD1B	Barcaliente (base)	Dol A2	49.65	0.82	-7.96	4.26	0.708646	19.37	10.99	16	300	2300	361
	"	"	Dol B	49.01	0.96	-8.23	3.06	0.708458	18.75	11.1	16	300	2100	263
	"	"	Cal 1	-	-	-8.42	0.18	0.708738	-	-	-	-	-	-
	153	Valdeteja (top)	H	-	-	-4.2	3.82	-	38	0.2	600	300	900	80
	"	"	CV	-	-	-6.51	3.85	-	-	-	-	-	-	-
	31	Valdeteja (top)	Dol A2	49.4	0.87	-4.38	4.53	-	18.83	11.23	25	400	1000	268
	"	Valdeteja (top)	Dol B	49.49	0.74	-6.4	4.45	-	18.29	10.69	24	600	1400	320
	"	"	Cal 2	-	-	-13.45	-7.6	-	-	-	-	-	-	-
	VCVL3	Valdeteja (middle interf.)	H	-	-	-3.25	5.13	-	-	-	-	-	-	-
	29	Valdeteja (middle interf.)	Dol A2	-	-	-5.27	4.19	-	-	-	-	-	-	-
	"	"	Dol B	-	-	-5.55	4.1	-	-	-	-	-	-	-
	"	"	Cal 1	-	-	-8.54	0.21	-	-	-	-	-	-	-
	VCVL2	Valdeteja (top interf.)	H	-	-	-4.86	4.57	-	33.58	0.45	749	400	1300	130
	26	Valdeteja (top interf.)	Dol A2	48.88	0.79	-8.43	5.03	-	18.61	10.6	20	400	1800	316
	"	"	Dol B	49.6	0.87	-8.28	4.97	-	19.01	11.15	17	300	1900	317
	"	"	Cal 1	-	-	-9.3	1.05	-	-	-	-	-	-	-

Locality	Sample	Formation	Phase	$CaCO_3$ mol %	OR	$\delta^{18}O$	$\delta^{13}C$	$^{87}Sr/^{86}Sr$	Ca (%)	Mg (%)	Sr (ppm)	Na (ppm)	Fe (ppm)	Mn (ppm)
Millaró IV	MAL1T	Alba (top)	H	-	-	0.28	3.73	-	-	-	-	-	-	-
	MAD1T	Alba (top)	Dol A2	-	-	-7.76	3.16	-	-	-	-	-	-	-
	"	"	Dol B	-	-	-9.43	2.41	-	-	-	-	-	-	-
	MBL1B	Barcaliente (base)	H	-	-	1.56	4.53	0.708137	37.68	0.04	802	100	100	9
	MBD1B	Barcaliente (base)	Dol A2	-	-	-7.53	4.69	-	-	-	-	-	-	-
	"	"	Dol B	-	-	-8.59	3.87	-	-	-	-	-	-	-
	"	"	Cal 1	-	-	-10.5	1.97	-	-	-	-	-	-	-
	40	Barcaliente (base)	Dol A1	-	-	-6.53	4.91	-	-	-	-	-	-	-
	"	"	Dol A2	-	-	-6.52	4.82	-	-	-	-	-	-	-
	"	"	Dol B	-	-	-6.91	4.77	-	-	-	-	-	-	-
	MBL2M	Barcaliente (middle)	H	-	-	0.77	4.44	-	39.95	0.24	950	400	-	8
	173	Barcaliente (middle)	Dol A2	-	-	-7.72	4.4	-	18.91	11.29	23	500	800	167
	"	"	Dol B	-	-	-7.93	3.54	-	19.48	11.69	20	500	600	213
	172	Barcaliente (middle)	Cal 2	-	-	-9.53	-1.82	-	-	-	-	-	-	-
	38	Valdeteja (base)	DolA2	-	-	-4.97	4.37	-	-	-	-	-	-	-
	"	"	Dol B	-	-	-5.41	4.4	-	-	-	-	-	-	-
Villamanín V	ViBL1	Barcaliente	H	-	-	-0.05	5.21	-	37.18	0.13	699	200	200	15
	ViBD1	Barcaliente	Dol A2	-	-	-6.18	4.44	-	20.61	12.25	16	400	800	226
	"	"	Dol B	-	-	-6.18	4.38	-	19.29	11.62	14	300	600	221

Locality	Sample	Formation	Phase	$CaCO_3$ mol %	OR	$\delta^{18}O$	$\delta^{13}C$	$^{87}Sr/^{86}Sr$	Ca (%)	Mg (%)	Sr (ppm)	Na (ppm)	Fe (ppm)	Mn (ppm)
Mina Profunda VI	MPAL1M	Alba (top)	H	-	-	-0.72	3.08	-	-	-	-	-	-	-
	MPAD1M	Alba (top)	Dol A2	49.76	0.54	-6.66	3.26	-	-	-	-	-	-	-
	MPBL1M	Barcaliente (middle)	H	-	-	-0.46	4.75	0.708082	38.39	0.25	806	300	900	56
	"	"	CV	-	-	-9.28	3.62	-	-	-	-	-	-	-
	MPBD2M	Barcaliente (middle)	Dol A2	49.23	0.91	-5.72	4.19	0.708097	17.72	10.47	16	200	2900	411
	"	"	Dol B	49.41	0.82	-5.63	4.07	0.709081	19.41	10.34	16	200	4600	412
	"	"	Cal 1	-	-	-12.72	1.95	0.708502	-	-	-	-	-	-
	MPVL1B	Valdeteja (base)	H	-	-	-2.96	4.45	-	-	-	-	-	-	-
	MPVD1B	Valdeteja (base)	Dol A2	51.06	0.59	-8.74	3.99	-	-	-	-	-	-	-
	"	"	Cal 2	-	-	-6.98	-4.47	-	-	-	-	-	-	-
	MPVD2M	Valdeteja (base)	Dol B	51.12	0.84	-9.26	-1.71	-	-	-	-	-	-	-
	MPVL2	Valdeteja (interf.)	H	-	-	-2.99	4.16	-	39.1	0.34	254	100	300	57
	MPVD3	Valdeteja (interf.)	Dol A2	-	-	-7.47	3.39	-	19.16	11.48	12	300	1200	274
	"	"	Dol B	-	-	-7.25	3.44	-	19.73	10.65	12	200	2700	301
	"	"	Cal 2	-	-	-7.35	-5.75	-	-	-	-	-	-	-
	CBM15	Valdeteja (interf.)	Dol A2	-	-	-6.6	4.67	-	-	-	-	-	-	-
	"	"	Dol B	-	-	-8.82	4.77	-	-	-	-	-	-	-
	"	"	Cal 2	-	-	-9.23	-2.44	-	-	-	-	-	-	-

Locality	Sample	Formation	Phase	$CaCO_3$ mol %	OR	$\delta^{18}O$	$\delta^{13}C$	$^{87}Sr/^{86}Sr$	Ca (%)	Mg (%)	Sr (ppm)	Na (ppm)	Fe (ppm)	Mn (ppm)
Cármenes VII	CaBL2B	Barcaliente (base)	H	-	-	-0.24	4.5	0.708147	39.26	0.28	752	300	300	15
	"	"	CV	-	-	-14.82	3.78	-	-	-	-	-	-	-
	CaBD2B	Barcaliente (base)	Dol A2	49.42	0.6	-7.24	4.17	0.709207	18.69	11.02	24	500	2000	359
	"	"	Dol B	49.78	0.85	-9.06	4.16	0.709251	18.77	11.1	20	200	1700	346
	"	"	Cal 2	-	-	-12.77	-4.11	0.708416	-	-	-	-	-	-
	CaBL1T	Barcaliente (top)	H	-	-	-3.8	3.75	-	-	-	-	-	-	-
	42	Barcaliente (top)	Dol A2	-	-	-9.52	3.69	-	-	-	-	-	-	-
	CaVL4T	Valdeteja (top)	H	-	-	-2.88	4.26	-	-	-	-	-	-	-
	"	"	CV	-	-	-8.03	3.72	-	-	-	-	-	-	-
	CaVD4T	Valdeteja (top)	Dol A2	-	-	-11.86	1.86	-	-	-	-	-	-	-
	"	"	Dol B	-	-	-11.97	1.74	-	-	-	-	-	-	-
	CaVL1	Valdeteja (interf.)	H	-	-	-3.91	4.33	-	-	-	-	-	-	-
	CaVD1	Valdeteja (interf.)	Dol A2	-	-	-8.8	3.22	-	-	-	-	-	-	-
	"	"	Dol B	-	-	-8.66	2.97	-	-	-	-	-	-	-
Canseco VIII	CBL3T	Barcaliente (top)	H	-	-	-4.52	4.19	-	33.08	0.07	459	100	800	131
	"	"	CV	-	-	-6.79	2.1	-	-	-	-	-	-	-
	CBD1T	Barcaliente (top)	Dol A1	-	-	-5.36	5.28	-	17.21	10.56	28	300	5200	716
	"	"	Dol A2	-	-	-5.73	5.42	-	-	-	-	-	-	-
	"	"	Dol B	-	-	-5.84	5.3	-	-	-	-	-	-	-
	45	Barcaliente (top)	Dol A2	49.41	0.82	-6.49	4.42	-	18.4	10.7	41	200	6100	814
	"	"	Dol B	50.06	0.72	-8.69	3.91	-	22.73	10.86	102	100	5500	901
	"	"	Cal 1	-	-	-13.44	-0.79	-	-	-	-	-	-	-

Locality	Sample	Formation	Phase	$CaCO_3$ mol %	OR	$\delta^{18}O$	$\delta^{13}C$	$^{87}Sr/^{86}Sr$	Ca (%)	Mg (%)	Sr (ppm)	Na (ppm)	Fe (ppm)	Mn (ppm)
Nocedo IX	NBL1B	Barcaliente (base)	H	-	-	-5.09	3.24	-	-	-	-	-	-	-
	101	Barcaliente (base)	Dol A1	-	-	-2.99	4.2	-	-	-	-	-	-	-
	"		Dol B	-	-	-5.56	3.07	-	-	-	-	-	-	-
	NBL2M	Barcaliente (middle)	H	-	-	-0.41	4.61	-	-	-	-	-	-	-
	"	"	CV	-	-	-10.06	3.86	-	-	-	-	-	-	-
	NBD1M	Barcaliente (middle)	Dol A1	-	-	-4.07	4.2	-	-	-	-	-	-	-
	"	"	Cal 2	-	-	-11.1	-6.65	-	-	-	-	-	-	-
	NBL3T	Barcaliente (top)	H	-	-	-1.63	4.63	-	-	-	-	-	-	-
	NBD2T	Barcaliente (top)	Dol A1	49.87	0.75	-3.67	4.6	-	-	-	-	-	-	-
	"	"	Dol A2	49.36	0.77	-3.22	4.48	-	-	-	-	-	-	-
	"	"	Dol B	-	-	-4.19	4.52	-	-	-	-	-	-	-
	NVL1B	Valdeteja (base)	H	-	-	-2.68	4.14	-	35.87	0.31	179	200	200	49
	NVD1B	Valdeteja (base)	Dol A2	-	-	-8.15	4.7	-	19.21	11.33	16	300	1400	310
	"	"	Dol B	-	-	-6.71	4.4	-	-	-	-	-	-	-
	"	"	Cal 2	-	-	-11.08	-2.12	-	-	-	-	-	-	-
	NVL2M	Valdeteja (middle)	H	-	-	-7.73	3.55	-	-	-	-	-	-	-
	NVD2M	Valdeteja (middle)	Dol A2	-	-	-6.86	4.68	-	-	-	-	-	-	-
	NVL3T	Valdeteja (top)	H	-	-	-4.66	4.49	-	-	-	-	-	-	-
	"	"	CV	-	-	-6.36	4.48	-	-	-	-	-	-	-
	NVD3T	Valdeteja (top)	Dol A2	-	-	-5.09	4.33	-	-	-	-	-	-	-

Locality	Sample	Formation	Phase	$CaCO_3$ mol %	OR	$\delta^{18}O$	$\delta^{13}C$	$^{87}Sr/^{86}Sr$	Ca (%)	Mg (%)	Sr (ppm)	Na (ppm)	Fe (ppm)	Mn (ppm)
Montuerto X	1	Barcaliente	H	-	-	0.65	4.67	-	-	-	-	-	-	-
	3	Barcaliente	Dol A1	-	-	-5.38	4.87	-	-	-	-	-	-	-
	"	"	Dol A2	-	-	-5.41	4.74	-	-	-	-	-	-	-
	5	Barcaliente	Dol B	-	-	-5.88	2.19	-	-	-	-	-	-	-
Valdecastillo XI	109 I	Barcaliente (middle)	H	-	-	-6.3	3.3	-	-	-	-	-	-	-
	109 II	Barcaliente (middle)	Dol A2	-	-	-10.58	3.85	-	-	-	-	-	-	-
	"	"	Dol B	-	-	-10.37	4	-	-	-	-	-	-	-
	"	"	CV	-	-	-11.01	2.8	-	-	-	-	-	-	-
	108 II	Barcaliente (middle)	Dol A1	49.87	0.77	-6.84	4.95	-	-	-	-	-	-	-
	"	"	Dol A2	49.4	0.86	-7.01	5.21	-	-	-	-	-	-	-
Piedrasecha	PSBL1	Barcaliente	H	-	-	0.39	4.78	-	35.09	0.12	949	300	1800	36
	PSBD1	Barcaliente	Dol A1	-	-	-10.48	3.45	-	21.9	10.22	20	200	2200	315
	"	"	Dol A2	49.74	0.86	-10.52	3.19	-	20.55	11.88	22	300	2100	348
	"	"	Dol B	49.86	0.85	-10.52	3.2	-	-	-	-	-	-	-
	"	"	Cal 2	-	-	-8.24	-4.89	-	-	-	-	-	-	-
Valporquero	VVD4M	Valdeteja (middle)	Dol A1	49.62	0.88	-	-	-	-	-	-	-	-	-
	"	"	Dol A2	49.55	0.76	-	-	-	-	-	-	-	-	-

Appendix 3

Results of FI microthermometry.

Locality: Caldas					Sample: 136											
Phase	Fl	F	Th	Tn_{gas}	Tn_{ice}	T_{liq}	Tm_{ice}	Salinity (eq. wt %)			Molar Vol.	Bulk composition				
			°C	°C	°C	°C	°C	$MgCl_2$	NaCl	$CaCl_2$	cm^3/mol	xH_2O	xMg^{2+}	xNa^+	xCa^{2+}	xCl^-
Dol A2	fi1	0.90	121.5	-62.0	-62.0		-34.0	21.1			18.43	0.868	0.044			0.088
Dol A2	fi2	0.89	138.3	>30			-34.0	21.1			18.63	0.868	0.044			0.088
Dol A2	fi3	0.86	110.8	-60.0	-60.0		-32.5	20.7			19.32	0.871	0.043			0.086
Dol A2	fi4		129.5													
Dol A2	fi5	0.89	118.5	-75.0	-70.0		-32.5	20.7			18.67	0.871	0.043			0.086
Dol B	fi1	0.93	124.7	-45.0	-81.5	-34.4	-33.0	20.8			17.86	0.870	0.043			0.087
Dol B	fi2		112.4	66.0	-78.0		-32.0	20.5								
Dol B	fi3	0.86	122.2		-74.0		-31.5	20.4			19.30	0.870	0.040			0.080
Dol B	fi4	0.89	114.3	-75.0	-70.0	-36.4	-32.5	20.7			18.70	0.870	0.040			0.090
Dol B	fi5		116.5		-75.0	-35.9	-30.5	20.1								
Dol B	fi6	0.94	108.5	-62.0	-82.0		-32.5	20.7			17.70	0.870	0.040			0.090
Dol B	fi7	0.91	99.2		-67.0		-32.9	20.8			18.20	0.870	0.040			0.090
Dol B	fi8	0.93	99.2		-69.0		-33.0	20.8			17.86	0.870	0.043			0.087
Dol B	fi9	0.91	106.5	-62.0	-83.0		-32.6	20.7			18.30	0.870	0.040			0.090
Dol B	fi10	0.92	106.6		-76.0		-31.3	20.3			18.09	0.874	0.042			0.084
Dol B	fi11	0.92	105.4		-75.0	-33.5	-31.2	20.3			18.09	0.874	0.042			0.084
Dol B	fi12	0.92	105.4	-57.0	-75.0		-31.2	20.3			18.09	0.874	0.040			0.084
Dol B	fi13	0.93	102.7		-75.0		-31.2	20.3			17.89	0.874	0.042			0.084
Dol B	fi14	0.87	103.2			-34.4	-30.2	20.0			19.15	0.876	0.041			0.083
Dol B	fi15	0.93	107.1				-33.3	20.9			17.85	0.870	0.044			0.087
Dol B	fi16	0.90	112.3	55.0	-75.0	-33.5	-30.8	20.2			18.50	0.874	0.042			0.084
Dol B	fi17	0.88	112.8	-57.0	-57.0	-34.4	-30.8	20.2			18.92	0.874	0.042			0.084
Dol B	fi18	0.88	107.1	-60.0	-60.0	-33.9	-31.4	20.3			18.91	0.874	0.042			0.084
Dol B	fi19	0.90	104.8	-58.0	-58.0	-32.5	-31.4	20.3			18.49	0.874	0.042			0.084
Dol B	fi20	0.94	104.8				-30.4	20.1			17.72	0.875	0.042			0.083
Dol B	fi21	0.90	108.3				-31.4	20.3			18.49	0.874	0.042			0.084
Dol B	fi22	0.89	143.7	>10	-77.0	-34.4	-31.4	20.3			18.70	0.874	0.042			0.084
Dol B	fi23	0.83	136.4	>30			-29.5	19.8			20.09	0.877	0.041			0.082

Locality: Caldas Sample: 136 (continued)

Phase	FI	F	Th °C	Tn_{gas} °C	Tn_{ice} °C	T_{liq} °C	Tm_{ice} °C	Salinity (eq. wt %)			Molar Vol.	Bulk composition				
								$MgCl_2$	NaCl	$CaCl_2$	cm^3/mol	xH_2O	xMg^{2+}	xNa^+	xCa^{2+}	xCl^-
Dol B	fi24	0.83	115.1	5.0		-33.5	-31.9	20.5			20.03	0.872	0.043			0.085
Dol B	fi25	0.89	114.1				-32.2	20.6			18.67	0.872	0.043			0.086
Dol B	fi26	0.91	128.9	75.0	-76.0	-37.4	-32.9	20.8			18.25	0.870	0.043			0.087
Dol B	fi27	0.89	119.8	55.0	-74.0		-32.4	20.7			18.67	0.871	0.043			0.086
Dol B	fi28	0.89	113.7	59.0			-32.4	20.7			18.67	0.871	0.043			0.086
Cal 1	fi1	0.94	102.6	48.0	-83.0	-32.0	-21.6		23.4		17.72	0.842		0.079		0.079
Cal 1	fi2	0.93	133.9	>0	-68.0	-31.0	-23.7		24.8		17.82	0.831		0.085		0.085
Cal 1	fi3	0.92	112.5	>0	-80.0	-28.5	-23.7		24.8		18.01	0.831		0.085		0.085

Locality: Cubillas Sample: CuBD1M

Phase	FI	F	Th °C	Tn_{gas} °C	Tn_{ice} °C	T_{liq} °C	Tm_{ice} °C	Salinity (eq. wt %)			Molar Vol.	Bulk composition				
								$MgCl_2$	NaCl	$CaCl_2$	cm^3/mol	xH_2O	xMg^{2+}	xNa^+	xCa^{2+}	xCl^-
Dol B	fi1	0.92	110.9			-52.8	-37.2	22.0			17.96	0.862	0.046			0.092
Dol B	fi2	0.89	106.4			-52.8	-36.7	21.8			18.58	0.863	0.046			0.091
Dol B	fi3	0.93	101.4			-39.1	-37.1	21.9			17.77	0.863	0.046			0.092
Dol B	fi4	0.94	106.4			-37.1										
Dol B	fi5	0.95	96.6			-45.9	-36.3	21.7			17.41	0.864	0.045			0.091
Dol B	fi6	0.96	104.9			-40.1	-37.4	22.0			17.21	0.862	0.046			0.092
Dol B	fi7	0.94	108.0			-48.9	-37.3	22.0			17.57	0.862	0.046			0.092
Dol B	fi8		109.4													
Dol B	fi9		95.8													
Dol B	fi10	0.90	109.1			-46.4	-36.9	21.9			18.36	0.863	0.046			0.092
Dol B	fi11	0.92	106.6			-45.9	-37.3	22.0			17.96	0.862	0.046			0.092
Dol B	fi12	0.81	114.9			-45.0	-37.1	21.9			20.40	0.863	0.046			0.092
Dol B	fi13	0.92	109.7			-47.9	-37.6	22.1			17.95	0.861	0.046			0.092
Dol B	fi14	0.92	107.5													
Dol B	fi15	0.94	107.5				-37.8	22.1			17.57	0.861	0.046			0.092
Dol B	fi16	0.91	107.8				-37.8	22.1			18.15	0.861	0.046			0.092

Locality: Villanueva								Sample: VC-172								
Phase	Fl	F	Th	Tn_{gas}	Tn_{ice}	T_{liq}	Tm_{ice}	Salinity (eq. wt %)			Molar Vol.	Bulk composition				
			°C	°C	°C	°C	°C	$MgCl_2$	NaCl	$CaCl_2$	cm^3/mol	xH_2O	xMg^{2+}	xNa^+	xCa^{2+}	xCl^-
Dol B	fi1	0.80	140.5													
Dol B	fi2	0.91	136.6			-41.1	-34.8	21.3			18.21	0.867	0.044			0.089
Dol B	fi3	0.90	126.8				-33.7	21.0			18.43	0.869	0.044			0.087
Dol B	fi4	0.93	129.7				-35.2	21.4			17.81	0.866	0.045			0.089
Dol B	fi5	0.87	147.6				-35.7	21.6			19.02	0.865	0.045			0.090
Dol B	fi6	0.86	139.4	10.0			-33.8	21.1			19.28	0.868	0.044			0.088
Dol B	fi7	0.89	142.7	64.0			-33.8	21.1			18.63	0.868	0.044			0.088
Dol B	fi8	0.83	142.0	70.0			-33.8	21.1			19.98	0.868	0.044			0.088
Dol B	fi9	0.86					-36.7									
Dol B	fi10	0.83	114.9				-33.8	21.1			19.98	0.868	0.044			0.088
Dol B	fi11	0.92	115.4				-33.8	21.1			18.03	0.868	0.044			0.088
Dol B	fi12	0.86	134.9	76.5			-33.7	21.0			19.29	0.869	0.044			0.087
Dol B	fi13	0.87	138.7	88.0			-33.7	21.0			19.07	0.869	0.437			0.087
Dol B	fi14	0.91	135.2			-46.9	-32.7	20.7			18.26	0.871	0.043			0.086
Dol B	fi15	0.87	138.1			-48.9	-32.7	20.7			19.09	0.871	0.043			0.086
Dol B	fi16	0.87	140.5	67.0		-39.1	-33.5	21.0			19.07	0.869	0.044			0.087
Dol B	fi17	0.92	131.0	78.0			-27.1	19.0			18.19	0.883	0.039			0.078
Dol B	fi18	0.93	141.6	64.0												
Dol B	fi19	0.87	142.3	95.0			-34.5	21.3			19.05	0.867	0.044			0.089
Dol B	fi20	0.88	143.4	95.0		-42.0	-33.5	21.0			18.85	0.869	0.044			0.087
Dol B	fi21	0.86	139.4	52.0		-41.1	-34.2	21.2			19.28	0.868	0.044			0.088
Dol B	fi22	0.91	142.5	22.0		-41.1	-34.2	21.2			18.22	0.868	0.044			0.088
Dol B	fi23	0.87	133.0			-42.0	-34.2	21.2			19.05	0.868	0.044			0.088
Dol B	fi24		144.6				-34.5	21.3								
Dol B	fi25	0.91				-44.0	-37.1	21.9			18.16	0.863	0.046			0.092
Dol B	fi26	0.89	142.2				-33.6	21.0			18.64	0.870	0.044			0.087
Dol B	fi27	0.89	140.1	69.0		-44.0	-32.7	20.7			18.67	0.871	0.043			0.086
Dol B	fi28		135.4				-34.6	21.3								

Locality: Villanueva			Sample: VCBD1B													
Phase	Fl	F	Th °C	Tn_{gas} °C	Tn_{ice} °C	T_{liq} °C	Tm_{hy} °C	Tm_{ice} °C	Salinity (eq. wt %)			Molar Vol.	Bulk composition				
									$MgCl_2$	NaCl	$CaCl_2$	cm^3/mol	xH_2O	xMg^{2+}	xNa^+	xCa^{2+}	xCl^-
Dol A2	fi1	0.86	126.3	-77.0	-77.0	-34.0		-33.0	20.8			19.31	0.870	0.043			0.087
Dol A2	fi2	0.84	132.5					-34.5	21.3			19.73	0.867	0.044			0.089
Dol A2	fi3	0.83	134.5			-31.0		-32.0	20.5			20.03	0.872	0.043			0.085
Dol A2	fi4	0.91	137.7	5.0		≤-51,5		-35.0	21.4			18.20	0.866	0.045			0.089
Dol A2	fi5	0.85	135.5	-15.0				-35.3	21.5			19.48	0.866	0.045			0.090
Dol A2	fi6	0.86	139.7					-34.5	21.3			19.27	0.867	0.044			0.089
Dol A2	fi7	0.88	138.3	>0		-48.5		-35.3	21.5			18.81	0.866	0.045			0.090
Dol A2	fi8	0.92	120.5	>4		-48.0		-34.0	21.1			18.03	0.868	0.044			0.088
Dol A2	fi9	0.90	196.5	>4		-48.8		-34.0	21.1			18.43	0.868	0.044			0.088
Dol A2	fi10	0.92	138.5	15.0		-42.5		-34.5	21.3			18.01	0.867	0.044			0.089
Dol A2	fi11	0.91	135.8					-36.5	21.8			18.17	0.863	0.046			0.091
Dol A2	fi12	0.93	117.5					-34.5	21.3			17.82	0.867	0.044			0.089
Dol A2	fi13	0.91	127.5					-34.5	21.3			18.21	0.867	0.044			0.089
Dol A2	fi14	0.94	125.5					-36.5	21.8			17.59	0.863	0.046			0.091
Dol A2	fi15	0.91	126.5					-34.5	21.3			18.21	0.867	0.044			0.089
Dol A2	fi16	0.91	128.5														
Dol A2	fi17	0.90	133.3														
Dol B	fi1	0.91	127.5	60.0		-49.0		-34.5	21.3			18.21	0.867	0.044			0.089
Dol B	fi2	0.92	131.5	-80.0	-80.0	-44.0		-34.3	21.2			18.02	0.868	0.044			0.088
Dol B	fi3	0.91	137.5	50.0		-42.0		-33.8	21.1			18.22	0.868	0.044			0.088
Dol B	fi4	0.90	123.0	43.0		-42.0		-33.8	21.1			18.43	0.868	0.044			0.088
Dol B	fi5	0.92	129.5	70.0				-33.8	21.1			18.03	0.868	0.044			0.088
Dol B	fi6	0.93	130.5	-74.0	-74.0	-49.0		-34.0	21.1			17.83	0.868	0.044			0.088
Dol B	fi7	0.90	155.0	40.0		-42.0		-33.5	21.0			18.43	0.869	0.044			0.087
Dol B	fi8	0.91	113.0			-46.0		-34.1	21.1			18.22	0.868	0.044			0.088
Dol B	fi9	0.88															
Dol B	fi10	0.92															

Locality: Villanueva Sample: VCBD1B (continued)

Phase	Fl	F	Th	Tn_{gas}	Tn_{ice}	T_{liq}	Tm_{hy}	Tm_{ice}	Salinity (eq. wt %)			Molar Vol.	Bulk composition				
			°C	°C	°C	°C	°C	°C	$MgCl_2$	NaCl	$CaCl_2$	cm^3/mol	xH_2O	xMg^{2+}	xNa^+	xCa^{2+}	xCl^-
Dol B	fi11	0.86	136.5			-40.0		-36.2	21.7			19.23	0.864	0.045			0.091
Dol B	fi12	0.88	123.5			-48.0		-34.2	21.2			18.84	0.868	0.044			0.088
Dol B	fi13	0.92	129.5					-33.7	21.0			18.03	0.869	0.044			0.087
Dol B	fi14	0.90	127.5														
Dol B	fi15	0.90	133.5	-36.0		-42.0		-34.0	21.1			18.43	0.868	0.044			0.088
Dol B	fi16	0.92	129.2	-73.3	-73.3	-51,6±1	-43,2	-34.4	21.2			18.02	0.868	0.044			0.088
Dol B	fi17	0.94	127.5	86.0				-34.1	21.1			17.64	0.868	0.044			0.088
Dol B	fi18	0.91	127.5	-76.0	-76.0			-35.5	21.5			18.19	0.866	0.045			0.090
Dol B	fi19	0.85	133.5		-2.0			-34.7	21.3			19.49	0.867	0.044			0.089
Dol B	fi20	0.89	139.5	12.0				-34.1	21.1			16.63	0.868	0.044			0.088
Dol B	fi21	0.91	133.5	57.0				-34.1	21.1			18.22	0.868	0.044			0.088
Dol B	fi22	0.90	136.5	2.0				-34.1	21.1			18.43	0.868	0.044			0.088
Dol B	fi23	0.89	134.5	4.0				-33.7	21.0			18.64	0.869	0.044			0.087
Dol B	fi24	0.83	136.5	80.0				-34.1	21.1			19.98	0.868	0.044			0.088
Dol B	fi25	0.88	136.5	5.0				-33.7	21.0			18.85	0.869	0.044			0.087
Dol B	fi26	0.84	140.8	38.0				-34.1	21.1			19.74	0.868	0.044			0.088
Dol B	fi27	0.91	140.3	22.0				-34.1	21.1			18.22	0.868	0.044			0.088
Dol B	fi28	0.91	134.0	-2.0				-34.1	21.1			18.22	0.868	0.044			0.088

Locality: Mina Profunda									Sample: MPBD2M									
Phase	Fl	F	Th °C	Tn_{gas} °C	Tn_{ice} °C	T_{liq} °C	Tm_{hy} °C	Tm_{ice} °C	Salinity (eq. wt %)			Molar Vol.	Bulk composition				
									$MgCl_2$	NaCl	$CaCl_2$	cm^3/mol	xH_2O	xMg^{2+}	xNa^+	xCa^{2+}	xCl^-
Dol B	fi1	0.92	126.9														
Dol B	fi2	0.84	127.5														
Dol B	fi3	0.92	121.3														
Dol B	fi4	0.92	120.5	60.0													
Dol B	fi5	0.94	118.8														
Dol B	fi6	0.93	112.5				-33.5		21.0			17.84	0.869	0.044			0.087
Dol B	fi7	0.91															
Dol B	fi8	0.92															
Dol B	fi9	0.93															
Dol B	fi10	0.94															
Dol B	fi11	0.92															
Dol B	fi12	0.85															
Dol B	fi13	0.93															
Dol B	fi14	0.90															
Dol B	fi15	0.89															
Dol B	fi16	0.90															
Dol B	fi17	0.91															
Dol B	fi18	0.83	129.1	28.0		-50.0	-34.0		21.1			19.98	0.868	0.044			0.088
Dol B	fi19	0.95	118.9	35.0			-34.7		21.3			17.44	0.867	0.044			0.089
Dol B	fi20	0.87	158.8														
Dol B	fi21	0.93	129.5	60.0			-39.5		22.6			17.72	0.858	0.047			0.095
Dol B	fi22	0.92															
Dol B	fi23	0.97	93.1				-35.0		21.4			17.07	0.866	0.045			0.089
Cal 1	fi1	0.97	125.5	-8.0	-59.2		-23.9			24.9		17.08	0.830		0.085		0.085
Cal 1	fi2	0.96	117.6	-40.0	-62.0	-45.3	-24.7	-16.3		17.4	10.0	17.33	0.845		0.055	0.015	0.085
Cal 1	fi3	0.94	113.5														
Cal 1	fi4	0.93	116.5	65.5													
Cal 1	fi5	0.95	113.9														

Locality: Mina Profunda Sample: MPBD2M (continued)

Phase	Fl	F	Th °C	Tn_{gas} °C	Tn_{ice} °C	T_{liq} °C	Tm_{hy} °C	Tm_{ice} °C	Salinity (eq. wt %)			Molar Vol.	Bulk composition				
									$MgCl_2$	NaCl	$CaCl_2$	cm^3/mol	xH_2O	xMg^{2+}	xNa^+	xCa^{2+}	xCl^-
Cal 1	fi7	0.94															
Cal 1	fi8	0.95	113.2	-63.0	-81.0		-24.2			25.1		17.43	0.829		0.086		0.086
Cal 1	fi9	0.91	114.5	32.0	-81.5		-24.0			25.0		18.20	0.830		0.085		0.085
Cal 1	fi10	0.97	108.3	25.5	-73.0	-44.9	-20.1			22.4		17.24	0.849		0.076		0.076
Cal 1	fi11	0.95	116.3		-73.9		-19.5			22.0		17.63	0.852		0.074		0.074
Cal 1	fi12	0.95	145.6	43.0	-81.6		-23.8			24.8		17.45	0.831		0.085		0.085
Cal 1	fi13	0.95	100.0		-59.8		-23.5			24.6		17.46	0.833		0.084		0.084
Cal 1	fi14	0.93															
Cal 1	fi15	0.95	111.0		-65.4		-26.4			26.4		17.34	0.819		0.091		0.091
Cal 1	fi16	0.95	115.8		-75.1		-24.1			25.0		17.43	0.830		0.085		0.085
Cal 1	fi17	0.95															
Cal 1	fi18	0.95	112.5		-83.3		-24.5			25.3		17.41	0.827		0.086		0.086
Cal 1	fi19	0.92	113.5		-69.1		-24.5			25.3		17.98	0.827		0.086		0.086
Cal 1	fi20	0.96	100.0		-80.4		-23.9			24.9		17.26	0.830		0.085		0.085
Cal 1	fi21	0.92															
Cal 1	fi22	0.88	107.5		-88.3	-34.2	-19.9			22.3		19.01	0.850		0.075		0.075
Cal 1	fi23	0.88	103.6		-81.5	-35.2	-22.3			23.9		18.90	0.838		0.081		0.081
Cal 1	fi24	0.87	120.8		-64.3	-39.1	-21.5	-17.1		24.1	1.0	19.06	0.833		0.082	0.001	0.084
Cal 1	fi25	0.89	118.7		~-60		-21.0			23.0		18.75	0.845		0.078		0.078
Cal 1	fi26	0.91	120.2	55.0	-65.0	-46.9	-26.5			26.5		18.09	0.818		0.091		0.091
Cal 1	fi27	0.88	110.5		-65.0		-24.4			25.2		18.80	0.828		0.086		0.086
Cal 1	fi28	0.92	120.3		-86.2	-34.2	-24.2			25.1		17.99	0.829		0.856		0.856
Cal 1	fi29	0.89	120.3		-65.3	-34.2	-24.6	-17.6		17.5	9.8	18.69	0.845		0.055	0.015	0.085
Cal 1	fi30	0.93	112.4	>0	-83.0	-27.6	-22.6	-24.0		16.1	7.4	18.08	0.864		0.051	0.011	0.074
Cal 1	fi31	0.93	110.5	35.0	-87.0	-36.0	-24.5	-17.2		17.8	9.5	17.89	0.844		0.056	0.014	0.085
Cal 1	fi32	0.91	113.3	-65.0	-65.0	-33.0	-24.7	-16.8		17.3	10.0	18.29	0.845		0.055	0.015	0.085
Cal 1	fi33	0.85	120.5	-65.0	-65.0	-32.0	-24.7	-16.8		17.3	10.0	19.58	0.845		0.055	0.015	0.085

Locality: Cármenes							Sample: CaBD2B								
Phase	FI	F	Th	Tn_{gas}	Tn_{ice}	T_{liq}	Tm_{ice}	Salinity (eq. wt %)			Molar Vol.	Bulk composition				
			°C	°C	°C	°C	°C	$MgCl_2$	NaCl	$CaCl_2$	cm^3/mol	xH_2O	xMg^{2+}	xNa^+	xCa^{2+}	xCl^-
Dol B	fi1	0.88	148.5	~60		-41.0										
Dol B	fi2	0.92	152.5	~50												
Dol B	fi3		149.5	~50												
Dol B	fi4	0.87	146.0	61.0												
Dol B	fi5	0.87	163.3	~60												
Dol B	fi6	0.90	175.8	~99												
Dol B	fi7	0.90	159.3	46.0												
Dol B	fi8		205.5	129.0												

Locality: Canseco							Sample: 45								
Phase	FI	F	Th	Tn_{gas}	Tn_{ice}	T_{liq}	Tm_{ice}	Salinity (eq. wt %)			Molar Vol.	Bulk composition				
			°C	°C	°C	°C	°C	$MgCl_2$	NaCl	$CaCl_2$	cm^3/mol	xH_2O	xMg^{2+}	xNa^+	xCa^{2+}	xCl^-
Dol A2	fi1		78.8													
Dol A2	fi2		98.0													
Dol A2	fi3		109.0													
Dol A2	fi4		111.0													
Dol B	fi1		118.5													
Dol B	fi2		124.5													
Dol B	fi3		133.0													
Dol B	fi4		123.5													

Locality: Nocedo							Sample: NVD1B								
Phase	FI	F	Th	Tn_{gas}	Tn_{ice}	T_{liq}	Tm_{ice}	Salinity (eq. wt %)			Molar Vol.	Bulk composition				
			°C	°C	°C	°C	°C	$MgCl_2$	NaCl	$CaCl_2$	cm^3/mol	xH_2O	xMg^{2+}	xNa^+	xCa^{2+}	xCl^-
Dol B	fi1	0.89	121.2	~70		-41.1	-34.2	21.2			18.63	0.868	0.044			0.088
Dol B	fi2	0.90	124.2	~7		$\leq$-44.5	-35.2	21.4			18.40	0.866	0.045			0.089
Dol B	fi3	0.92	118.5	~50	-84.9		-35.1	21.4			18.00	0.866	0.045			0.089
Dol B	fi4	0.91														

Locality: Nocedo Sample: NVD1B (continued)

Phase	FI	F	Th °C	Tn_{gas} °C	Tn_{ice} °C	T_{liq} °C	Tm_{ice} °C	Salinity (eq. wt %)			Molar Vol.	Bulk composition				
								$MgCl_2$	NaCl	$CaCl_2$	cm^3/mol	xH_2O	xMg^{2+}	xNa^+	xCa^{2+}	xCl^-
Dol B	fi6	0.90	126.1	>60		-40.1	-34.7	21.3			18.41	0.867	0.044			0.089
Dol B	fi7	0.86	130.5	>60		≤-40,4	-36.2	21.7			19.23	0.864	0.045			0.091
Dol B	fi8	0.88	126.6	>60		-38.1	-35.8	21.6			18.80	0.865	0.045			0.090
Dol B	fi9	0.91														
Dol B	fi10	0.78														
Dol B	fi11	0.87														
Dol B	fi12	0.89	126.1													
Dol B	fi13	0.90	133.2	20.0												
Dol B	fi14	0.86	126.7	43.0		-42.0	-36.2	21.7			19.23	0.864	0.045			0.091
Dol B	fi15	0.91	139.8	70.0			-35.5	21.4			18.20	0.866	0.045			0.089
Dol B	fi16	0.89	123.7	~20			-35.7	21.4			18.61	0.866	0.045			0.089
Dol B	fi17	0.87	124.2	~27												
Dol B	fi18	0.90	122.2			-40.1	-35.7	21.4			18.40	0.866	0.045			0.089
Dol B	fi19	0.91	124.6	~20			-35.7	21.4			18.20	0.866	0.045			0.089
Dol B	fi20	0.91	125.3	>60			-35.7	21.4			18.20	0.866	0.045			0.089
Dol B	fi21	0.88	125.4				-36.3	21.7			18.80	0.864	0.045			0.091
Dol B	fi22	0.90	123.2			-41.1	-36.3	21.7			18.37	0.864	0.045			0.091
Dol B	fi23	0.89	120.7				-36.3	21.7			18.59	0.864	0.045			0.091
Dol B	fi24	0.90	126.1				-36.3	21.7			18.38	0.864	0.045			0.091
Dol B	fi25	0.90	119.3				-36.3	21.7			18.38	0.864	0.045			0.091
Dol B	fi26	0.85	120.7	<25		≤-47,6	-35.6	21.6			19.47	0.865	0.045			0.090
Dol B	fi27	0.89	123.7	~34			-35.6	21.6			18.59	0.865	0.045			0.090
Dol B	fi28	0.87	126.6	45.0		-41.1	-35.7	21.4			19.04	0.866	0.045			0.089
Dol B	fi29	0.89	122.9	38.0			-35.6	21.6			18.59	0.865	0.045			0.090
Dol B	fi30	0.89	122.9													
Dol B	fi31	0.89	124.4	~50		-42.3	-35.7	21.4			18.61	0.866	0.045			0.089
Dol B	fi32	0.89	122.9	~45			-35.7	21.4			18.61	0.866	0.045			0.089

Plates of photos

Plate 1

Ph. 1: Colour contrast between the dark grey dolomite (D) and the light grey limestone (L). The light spot in the circle represents the dumps of an abandoned Cu-mine. Casares Lake.

Ph. 2: Light grey limestone (L) is in contact with dolomite (D). The dolomite has different surface colours: light pink in correspondence of the fresh cut and dark grey where the dolomite is covered by lichens (upper right corner). Nocedo de Curueño. Hammer for scale is 28 cm.

Ph. 3: The dolomite (D) occurs as sub-vertical bodies with a dyke-like geometry “intruding” the limestone (L). Nocedo de Curueño.

Ph. 4: Sharp contact between limestone (L) and dolomite (D). The latter has a more brittle behaviour as indicated by the presence of fractures which do not propagate into the limestone. Nocedo de Curueño. Hammer for scale is 28 cm.

Ph. 5: Limestone (L) - dolomite (D) contact sharply cuts bedding planes. Canseco. Scale is 14 cm.

Ph. 6: A yellowish dolomite body is spatially related to a sub-horizontal fault plane (dashed line). Correscilla Unit. Hammer for scale is 40 cm.

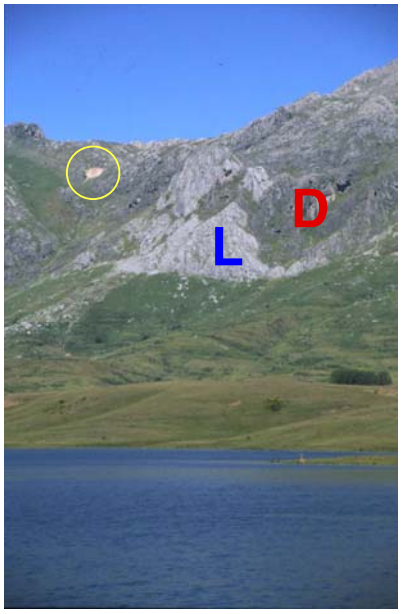

1

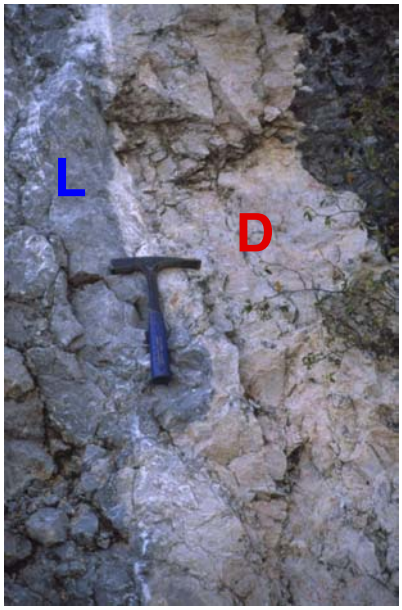

2

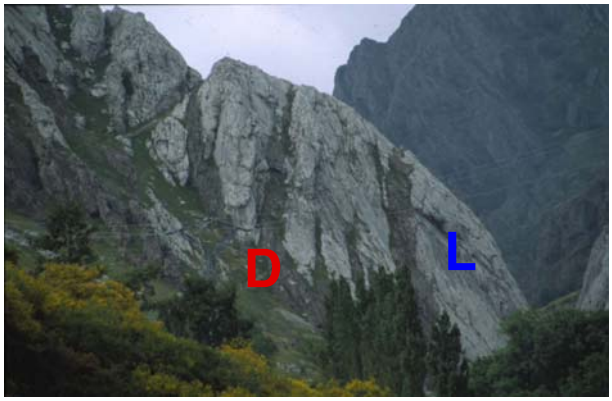

3

4

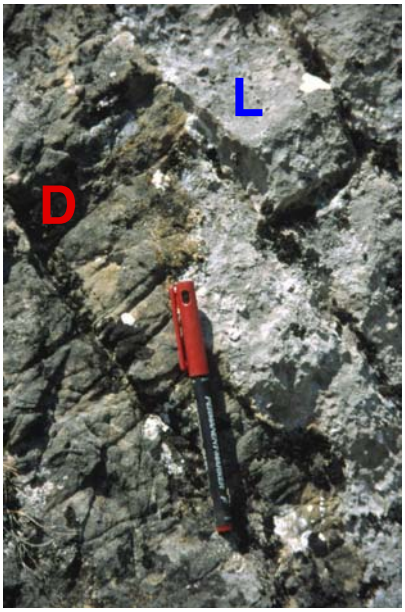

5

6

Plate 2

Ph. 1: Irregular contact between limestone (L) and dolomite (D). The dolomitisation front is constrained by primary discontinuity planes. Canseco. Hammer for scale is 28 cm.

Ph. 2: Particular of the outcrop in photo 1. The dolomite (arrow) is found along bedding and lamination planes as wavy and elongated bodies. Scale is 14 cm.

Ph. 3: The dolomitisation affects less than 1 cm of the host rock on both sides of lamination/ stylolite planes (arrows). Montuerto. Scale is 14 cm.

Ph. 4: A halo of yellowish dolomite crystals is found at the contact between limestone (L) and massive dolomite (D). Valdecastillo. Scale is 20 cm.

Ph. 5: Rock slice from the outcrop of photo 4. The yellow dolomite crystals are scattered within the lime mud. A thin calcite vein (arrow) stops at the dolomite front and is partly replaced by yellow dolomite crystals. Scale bar is 1 cm.

Ph. 6: Rock slice of fully dolomitised crinoidal limestone from the Valdeteja Fm. The dolomitised matrix displays a pink coloration. The crinoids in equatorial section are grey in colour. Getino. Scale bar is 1 cm.

Ph. 7: Selectively dolomitised Porma Breccia. The breccia matrix is dolomitised, whereas most of the breccia clasts were not affected by dolomitisation and maintained the original grey colour. Valporquero. Scale bar is 5 cm.

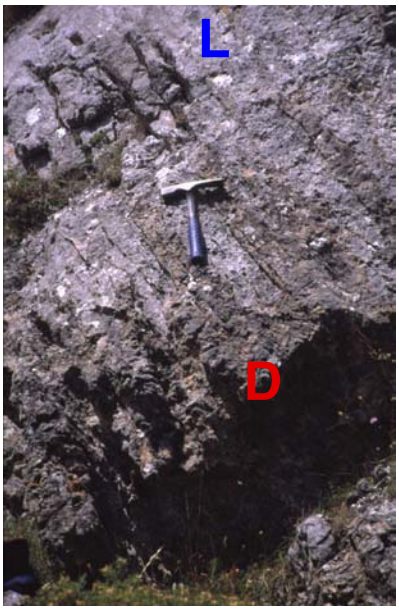

1

2

3

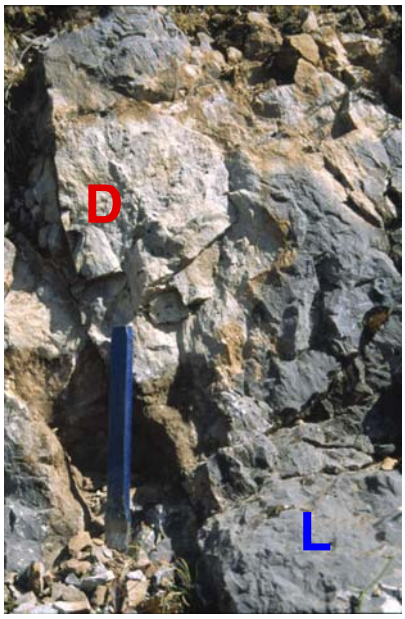

4

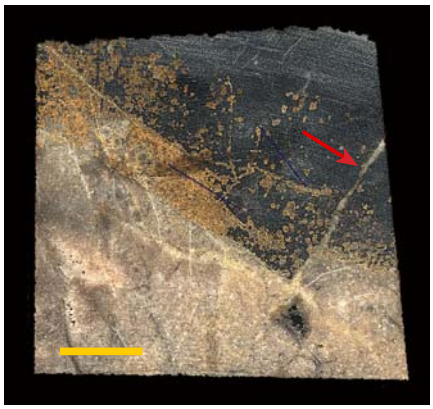

5

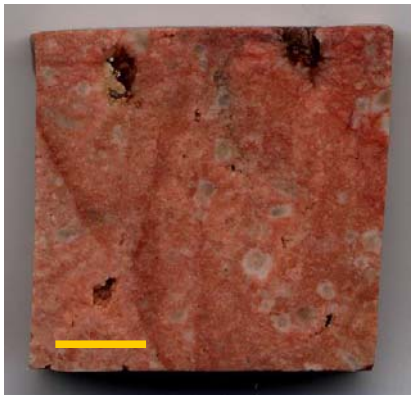

6

7

Plate 3

Ph. 1: Dolomite hosted in well bedded limestone of the Barcaliente Fm. exhibits linear and sub-horizontal cavities. Valporquero. Scale is 14 cm.

Ph. 2: Dolomite hosted in massive limestone of the Valdeteja Fm. exhibits large and irregular cavities. Millaró. Scale is 14 cm.

Ph. 3: Grey mosaic dolomite and white sparry dolomite associated with linear to roundish cavities in a sub-vertically dipping host rock. Sub-horizontal sheet-like cavities follow the orientation of fissure planes (arrow). Villanueva de la Tercia. Scale is 14 cm.

Ph. 4: Grey mosaic dolomite and white sparry dolomite form sub-horizontal zebra-structures in a sub-vertically dipping host rock. Open space is present between two subsequent white sparry dolomite sheets. Caldas de Luna. Scale is 16 cm.

Ph. 5: Rock sample showing zebra-structures. The cavities are completely filled with a transparent calcite (arrow). Caldas de Luna. Scale bar is 2 cm.

Ph. 6: Rock sample showing zebra-structures. The cavities between two sparry dolomite sheets are filled by a milky white calcite (arrow). Canseco. Scale bar is 2 cm.

Ph. 7: Rock sample showing zebra-structures associated with sub-vertical sparry dolomite veins. Some of the cavities are filled with white calcite. Villanueva de la Tercia. Scale bar is 2 cm.

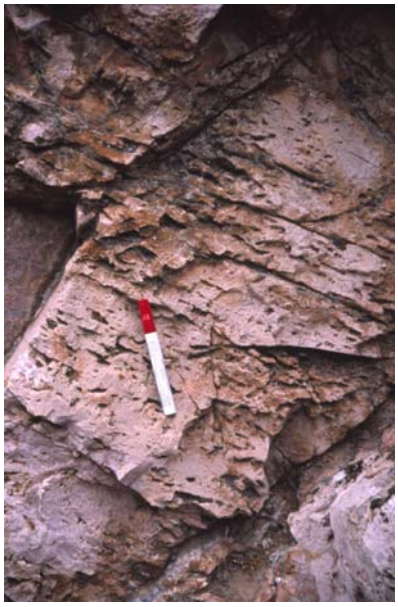

1

2

3

4

5

6

7

Plate 4

Ph. 1: Dolomitised outcrop at the base of Barcaliente Fm. exhibits a bedding parallel alternation of light grey and dark grey dolomite bands. Millaró. Hammer for scale is 28 cm.

Ph. 2: Rock sample showing alternation of light brown and dark grey dolomite bands. The dark bands have a wavy trace and develop on both sides of stylolites (S). A thin sparry dolomite vein (arrow) cuts both the light and the dark dolomite bands. Cubillas de Arbas. Scale bar is 2 cm.

Ph. 3: Rock sample showing alternation of brown and dark grey dolomite bands. Cavities filled with white sparry dolomite are exclusively hosted in the brown dolomite bands. Canseco. Scale bar is 1 cm.

Ph. 4: Rock slice showing alternation of pink and dark grey dolomite bands. The grey dolomite is coarser crystalline. A white sparry dolomite vein (arrow) crosscuts the dark grey dolomite. Caldas de Luna. Scale bar is 1 cm.

Ph. 5: Rock sample showing alternation of dark grey and pink dolomite bands. The dark crystals are coarser crystalline and associated with low amplitude stylolites (S). Many dark dolomite crystals float within the pink dolomite. Cavities are seen exclusively in the pink dolomite bands. Valporquero. Scale bar is 1 cm.

Ph. 6: Rock sample showing light grey mosaic and white sparry dolomites. The cavities are completely filled by ore minerals which consist mainly of malachite and oxides (arrow). Mina Profunda. Scale is 5 cm.

1

2

3

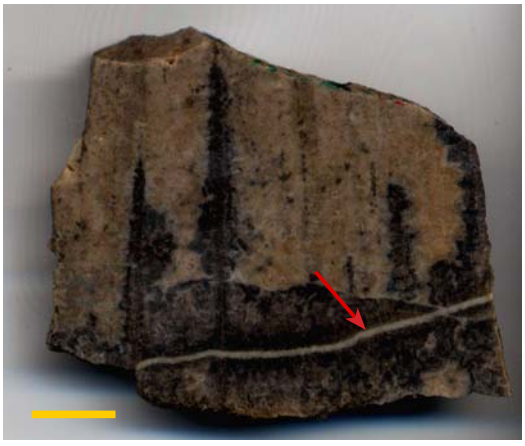

4

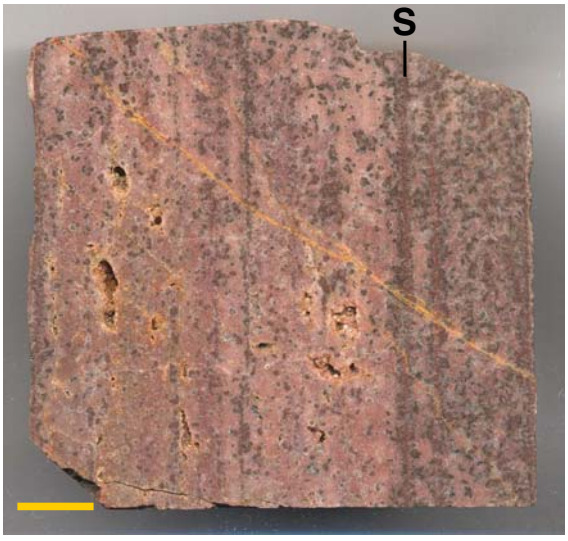

5

6

Plate 5

Ph. 1: The Correcilla Thrust puts in contact partly dolomitised Láncara carbonates (on the left) with black shales of the San Emiliano Fm. S of Poladura de la Tercia. Hammer for scale is 40 cm.

Ph. 2: Folded and dolomitised outcrop. The yellow and red frames represent the areas shown in photos 3 and 4 respectively. Piedrasecha. Hammer for scale is 40 cm.

Ph. 3: Particular of the outcrop in photo 2 (yellow frame). Sub-horizontal layers host sub-horizontally aligned cavities. Scale is 14 cm.

Ph. 4: Particular of the outcrop in photo 2 (red frame). Sub-vertical layers host small and sub-horizontally aligned cavities. Scale is 14 cm.

1

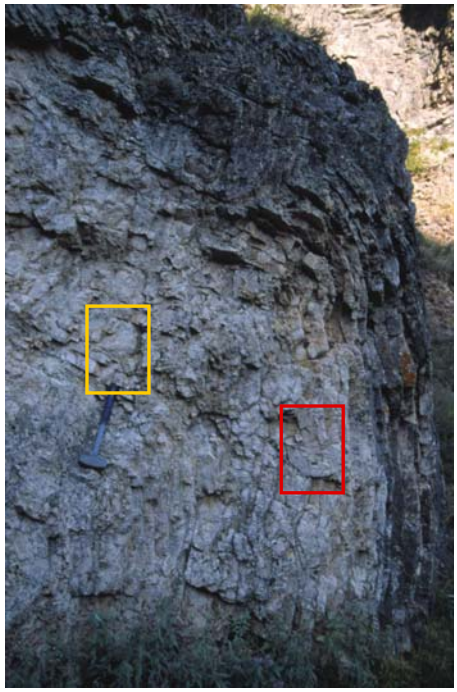

2

3

4

Plate 6

Ph. 1: Fault contact between dolomitised Valdeteja carbonates and San Emiliano siliciclastics. A planar and striated slickenside surface is developed in the dolomite. Villanueva de la Tercia. Scale is 20 cm.

Ph. 2: Deformed dolomite sample from a fault zone. The sample displays a curved and glassy slickenside surface (arrow). Getino. Scale is 5 cm.

Ph. 3: Rock slice from the Barcaliente Fm. Calcite veins form a tangled net cutting through the dark grey limestone. Montuerto. Scale bar is 0,1 cm.

Ph. 4: Limestone (L) is crosscut by a calcite vein (arrow) which stops at the contact with massive dolomite (D). Scattered dolomite crystals are found both in the lime mud and in the calcite vein. Scale is 14 cm.

1

2

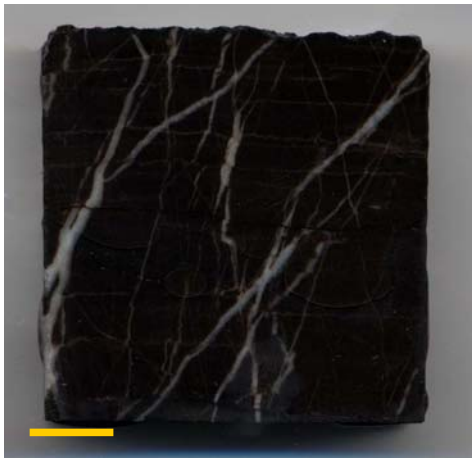

3

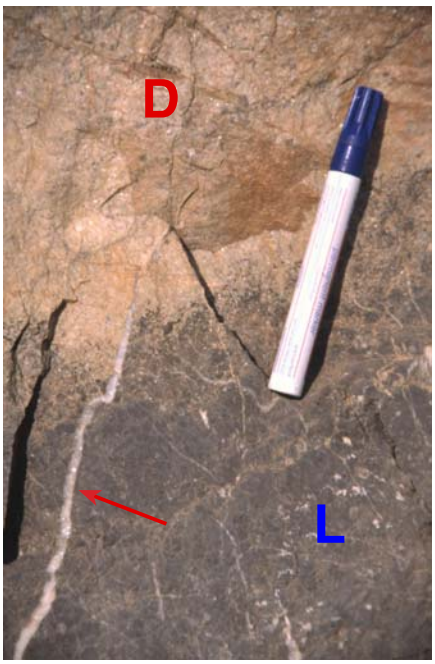

4

Plate 7

Ph. 1: Low amplitude, bedding parallel stylolite in the micrite of the Barcaliente Fm. shows opaque phases along its trace. Calcite veins crosscut the stylolite plane. Scalebar is 0,4 mm. Plane light.

Ph. 2: Thick CV propagates through the micrite of the Barcaliente Fm. The calcite crystals are twinned and become coarser from the walls towards the vein centre. Scalebar is 0,2 mm. Cross-polarised light.

Ph. 3: **A.** A CV propagates through the micrite of the Alba Fm. Scalebar is 0,2 mm. Cross-polarised light. **B.** The same picture under CL. The vein calcite has a dull orange CL, almost indistinguishable from the CL of the host micrite.

Ph. 4: **A.** Dol A2 is composed of a mosaic of interlocked and cloudy crystals of various size. Scalebar is 0,4 mm. Plane light. **B.** The same picture under CL. Dol A2 has a dull red and unzoned CL, with brighter reds spots.

Ph. 5: Pseudo-rhombohedra of Dol A2 are disseminated within the micrite of the Barcaliente Fm. The crystal borders are coated by a brownish ferroan phase. Scalebar is 0,2 mm. Plane light.

Ph. 6: A mosaic of Dol A2 crystals encloses remnants of relic stylolite (S). The dolomite displays a polymodal crystal size distribution. Scalebar is 0,4 mm. Plane light.

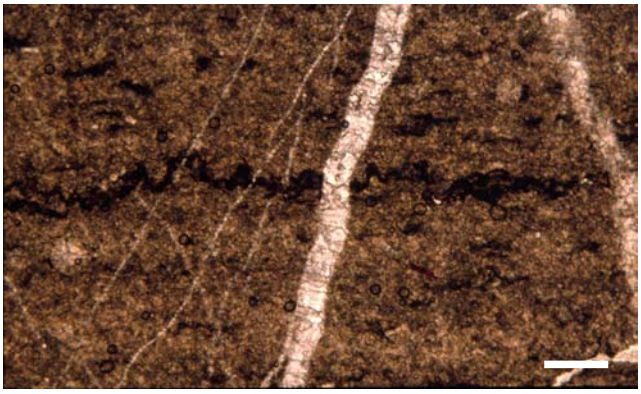

1

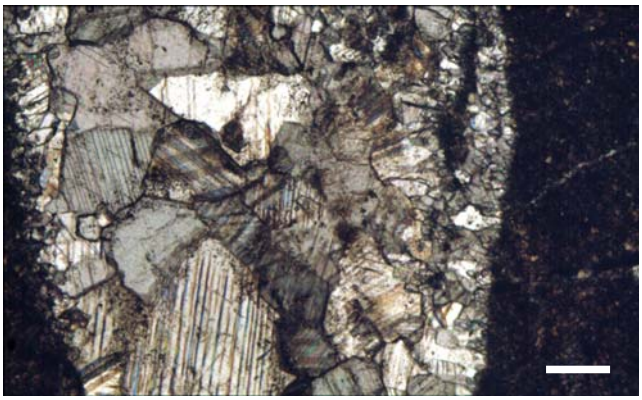

2

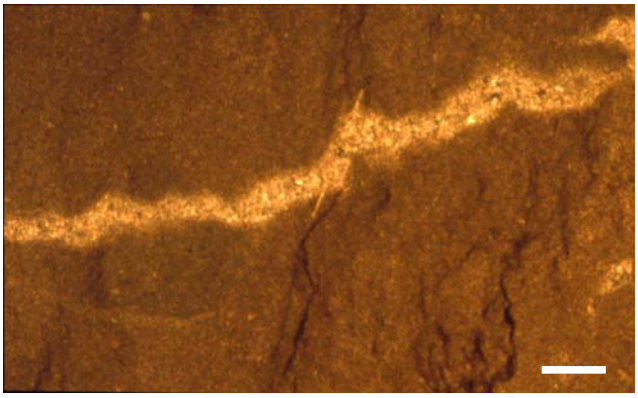

3A

3B

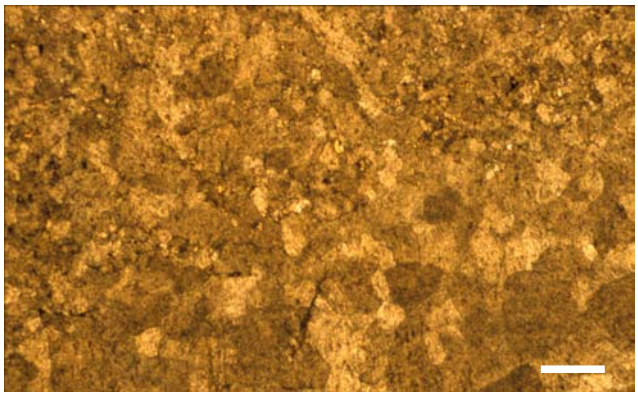

4A

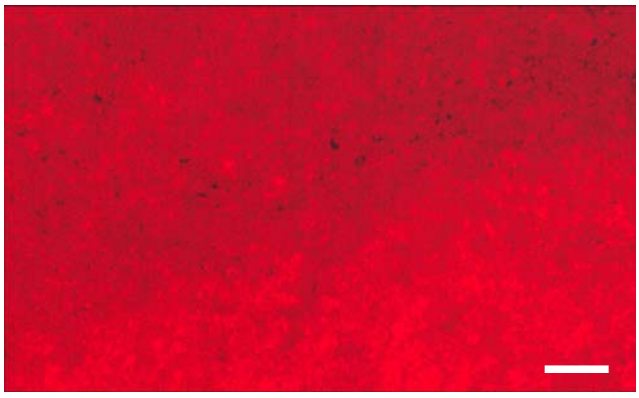

4B

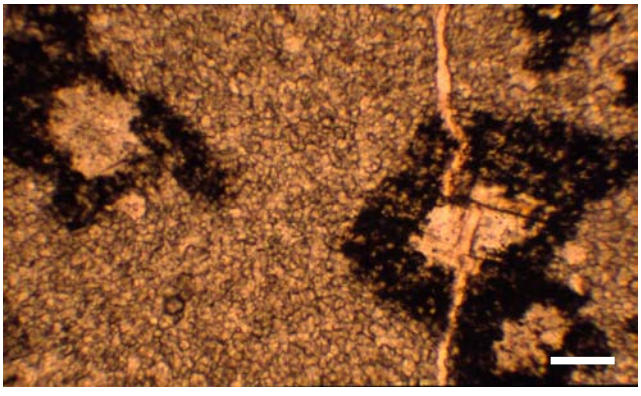

5

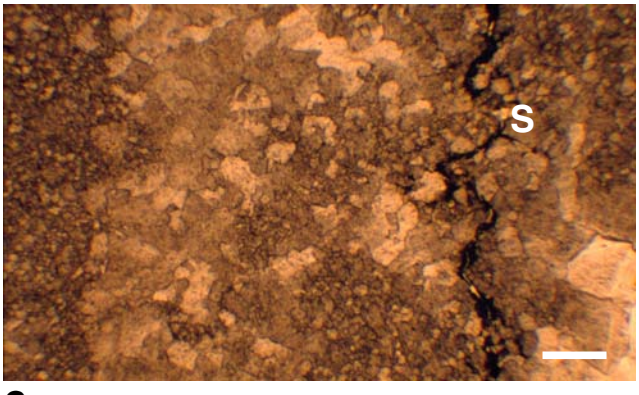

6

Plate 8

Ph. 1: Recrystallised crinoid (arrows) in equatorial section. The crinoid is hardly distinguishable from the matrix. Scalebar is 0,4 mm. Cross-polarised light.

Ph. 2: Dol A2 crystal mosaic associated with framboidal pyrite. Scalebar is 0,2 mm. Plane light.

Ph. 3: **A.** Dolomite A2 crystal mosaic associated with light yellow patches of microcrystalline quartz. Scalebar is 0,2 mm. Plane light. **B.** The same picture in cross-polarised light.

Ph. 4: Contact between Dol A1 and Dol A2. The trace of a stylolite (S) is still recognisable within the Dol A1 crystals. Scalebar is 0,4 mm. Plane light.

Ph. 5: Dol A1 crystal mosaic on one side of a stylolite plane (S). The crystal size increases towards the stylolite plane. Scalebar is 0,4 mm. Plane light.

Ph. 6: Dol A1 on both sides of a stylolite plane (S). On the left away from the stylolite Dol A1 passes gradually into Dol A2. Scalebar is 0,4 mm. Plane light.

Ph. 7: Contact between Dol A2 to Dol B. The Dol B crystals are coarser and clearer. They also truncate the trace of a stylolite (S). Scalebar is 0,2 mm. Plane light.

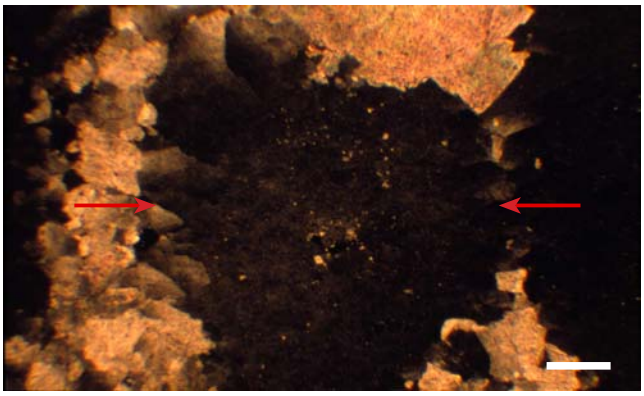

1

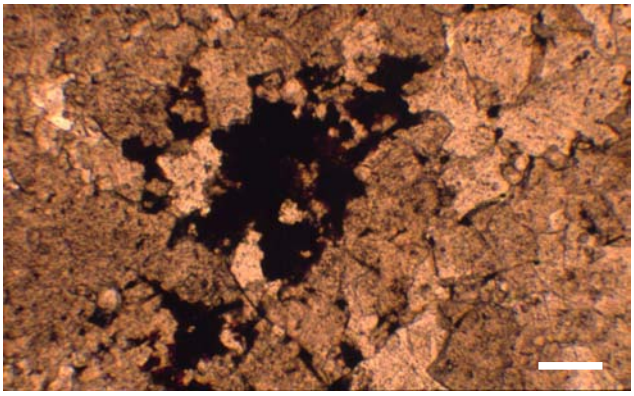

2

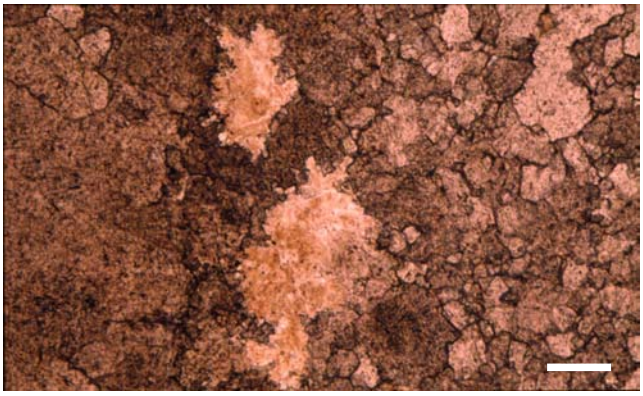

3A

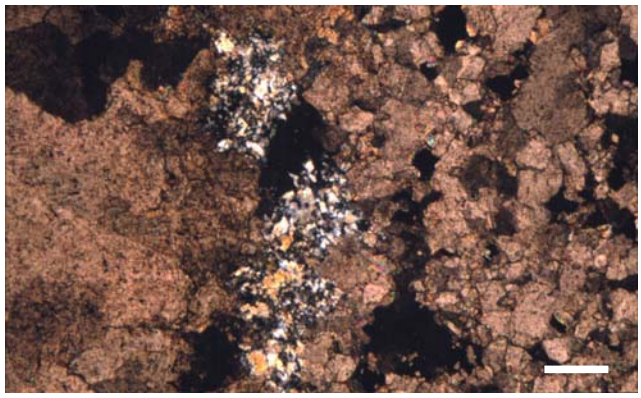

3B

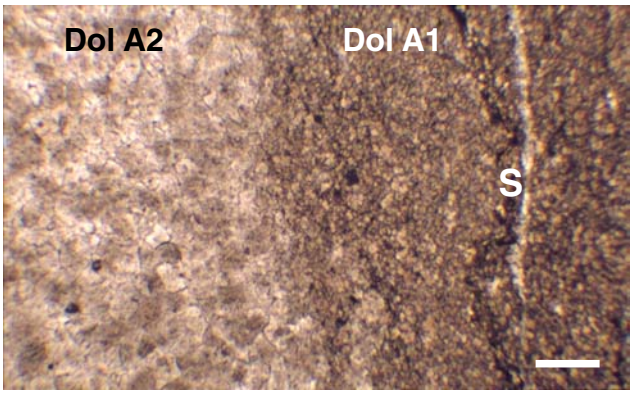

4

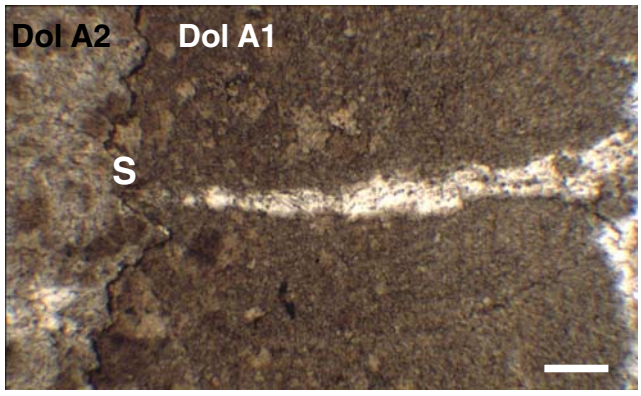

5

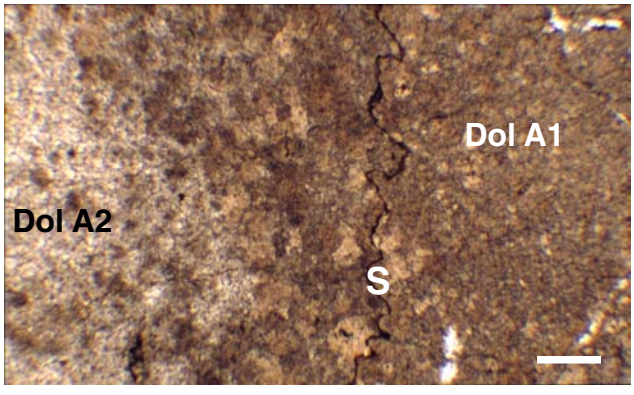

6

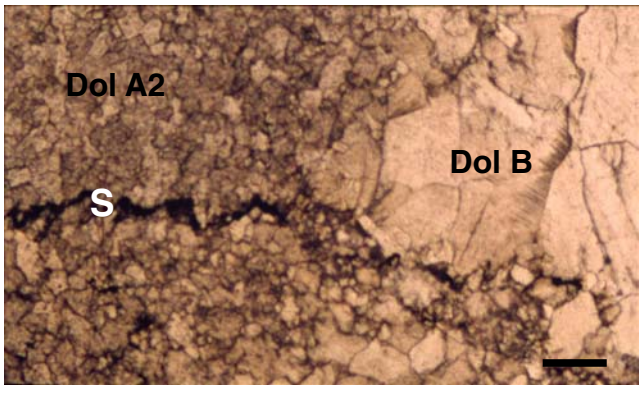

7

Plate 9

Ph. 1: Transition from the replacive to the cement dolomite phases. The size of the Dol B crystals increases towards the cavity, which is filled by calcite. Note the stylolite (S) which still persists in Dol A2. Scalebar is 0,4 mm. Plane light.

Ph. 2: Crystal size increase from the replacive to the cement dolomite phases. Note the sweeping extinction of the Dol B and the twinned calcite which fills the cavity. Scalebar is 0,4 mm. Cross-polarised light.

Ph. 3: **A.** Dol B1 fills a vein which cuts through the Dol A2 mosaic. The contact between the two phases is not sharp. The vein is recognised only by the coarser crystallinity of Dol B1. Scalebar is 0,2 mm. Plane light. **B.** The same picture in cross-polarised light. Dol B1 displays sweeping extinction.

Ph. 4: Dol B2 crystals with straight crystal boundaries and inclusion-rich cores. Only the most external rim of the crystal is clear and inclusion-free. Twinned calcite crystals are in contact with Dol B2. Scalebar is 0,2 mm. Plane light.

Ph. 5: Dol B2 crystal displays a regular alternation of inclusion-rich and inclusion-free concentric zones. Scalebar is 0,1 mm. Plane light.

Ph. 6: Dol B2 crystal is inclusion-rich in the core and inclusion-free in the external part. The crystal is coated by hydroxides and has a stepwise shape. Scalebar is 0,1 mm. Plane light.

Ph. 7: The termination of a clear Dol B2 crystal consists of dolomite and hydroxide concentric zones. The crystal has a stepwise shape. Scalebar is 0,2. Plane light.

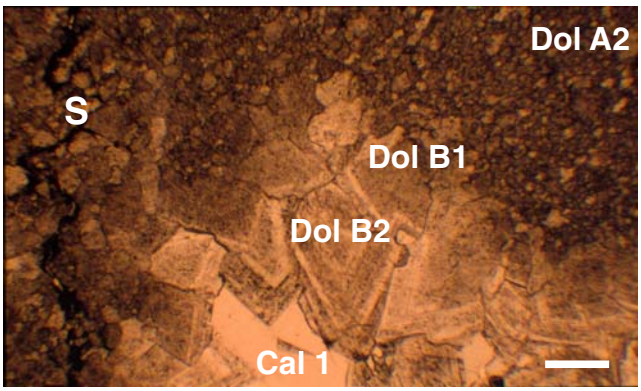
Dol A2
S
Dol B1
Dol B2
Cal 1

1

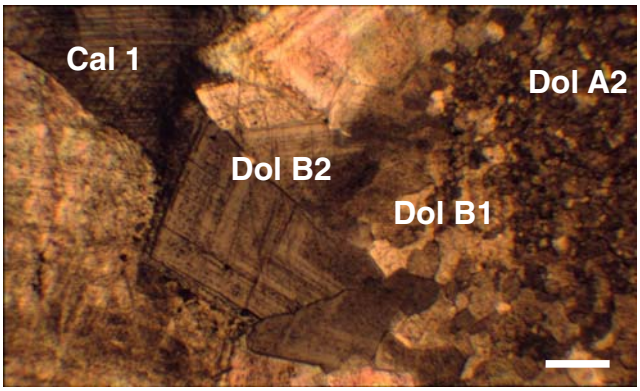
Cal 1
Dol A2
Dol B2
Dol B1

2

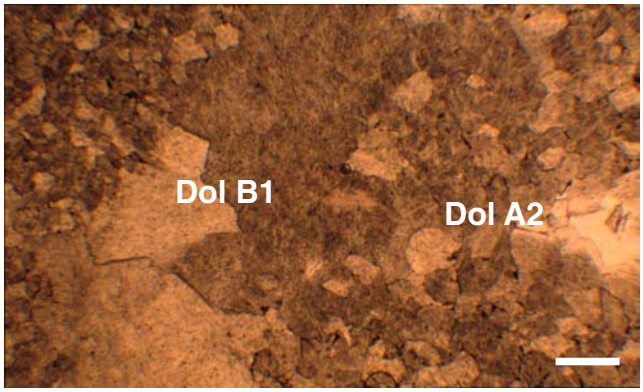
Dol B1
Dol A2

3A

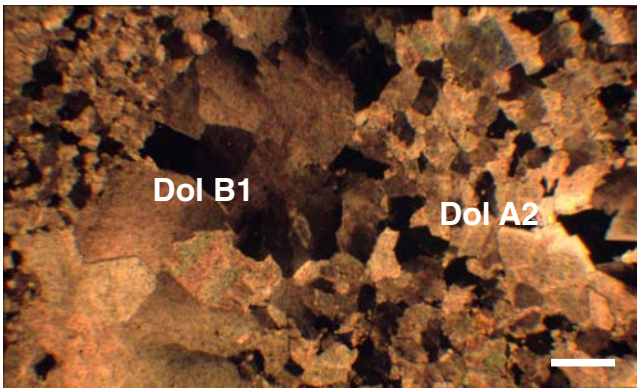
Dol B1
Dol A2

3B

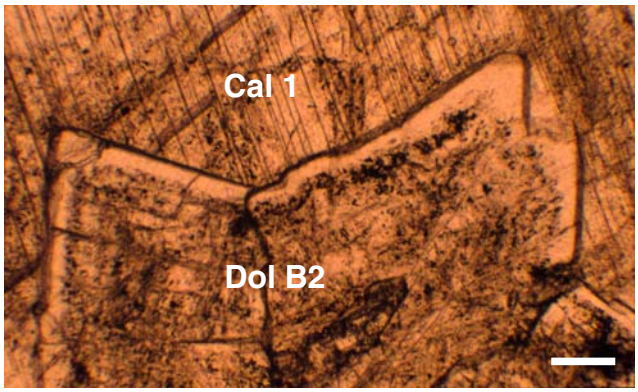
Cal 1
Dol B2

4

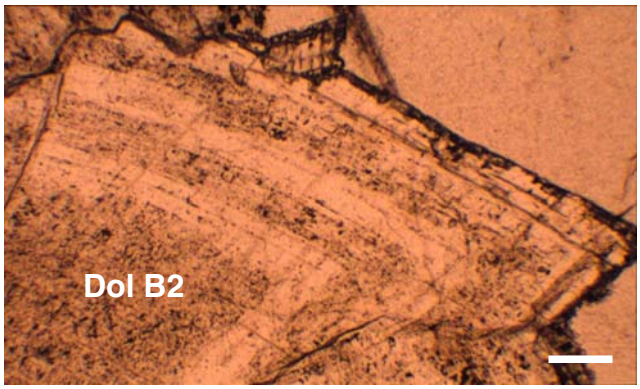
Dol B2

5

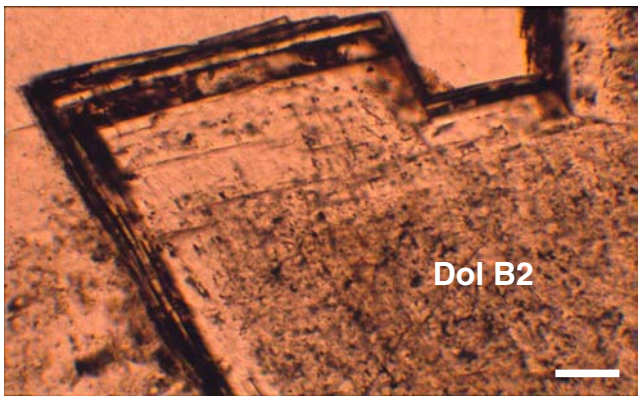
Dol B2

6

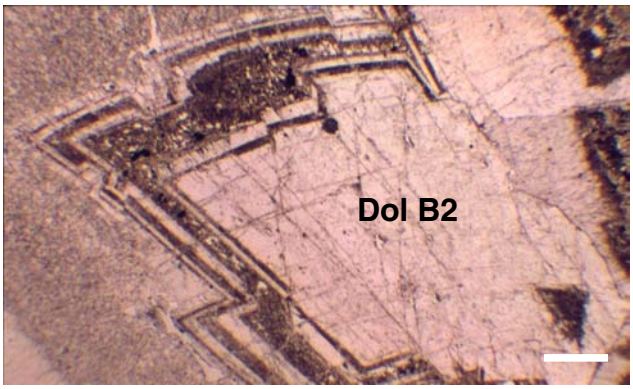
Dol B2

7

Plate 10

Ph. 1: **A.** Dol B2 crystals border a cavity filled with calcite. The Dol B2 crystal terminations are coated by brownish hydroxides. Scalebar is 0,2 mm. Plane light. **B.** The same picture under CL. Dol B2 crystals display a dull red CL with only a darker red zone, which coincides with the hydroxide coating observed in plane light. The calcite has a uniform bright-orange CL.

Ph. 2: **A.** Dol B2 crystals display curved borders. The terminations of the crystals are inclusion-free. Scalebar is 0,4 mm. Plane light. **B.** The same picture under CL. The Dol B2 crystals luminesce red in the core and have zoned, darker red, terminations. The concentric zones have a stepwise shape. The Dol B2 crystals are in contact with calcite having a uniform orange CL.

Ph. 3: **A.** Dol B2 crystals show a brownish hydroxide coating and are in contact with twinned Cal 1 crystals. Scalebar is 0,2 mm. Plane light. **B.** The same picture under CL. Dol B2 crystals have a dull red CL with only a darker red rim. The latter coincides with the hydroxide coating observed in plane light. Cal 1 has a bright orange, zoned CL and also fills a vein (arrow) which cuts through the dolomite.

Ph. 4: Dol B2 crystals close to an open cavity. The cavity is partly filled with green malachite. Scalebar is 0,2 mm. Cross-polarised light.

Ph. 5: Dol B2 crystals close to a cavity filled with Cal 1. Note the opaque mineral grown in the cavity between Dol B2 and Cal 1. Scalebar is 0,2 mm. Cross-polarised light.

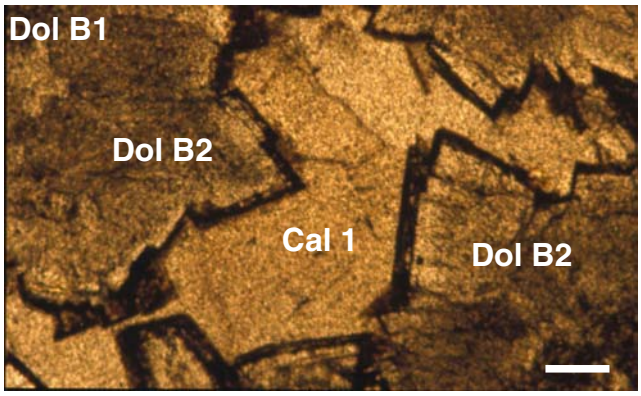

1A

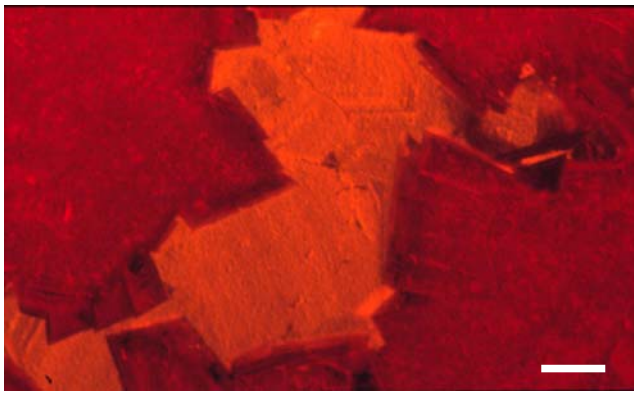

1B

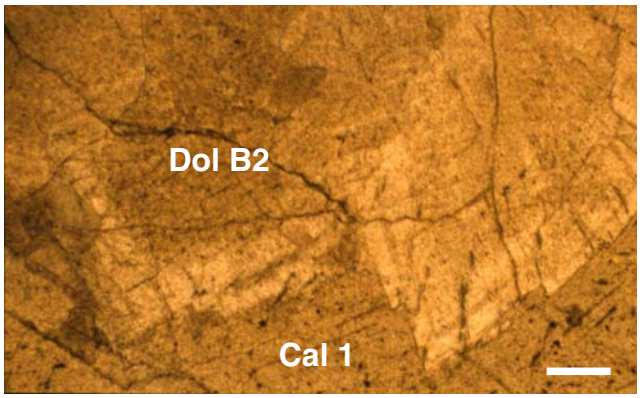

2A

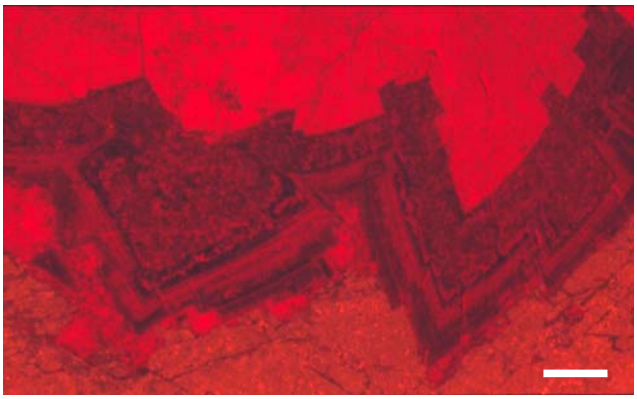

2B

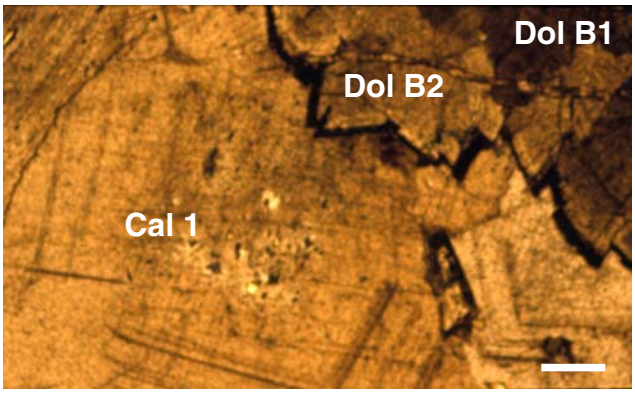

3A

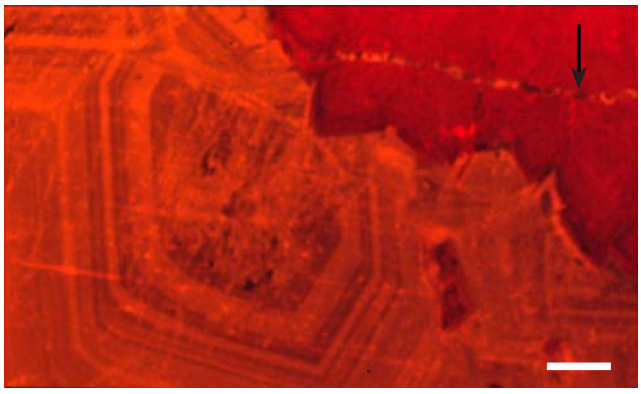

3B

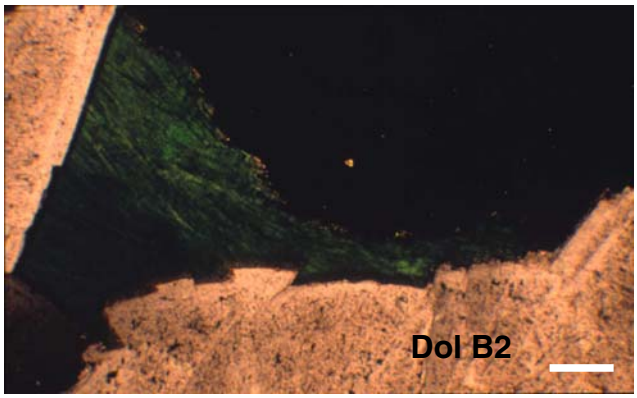

4

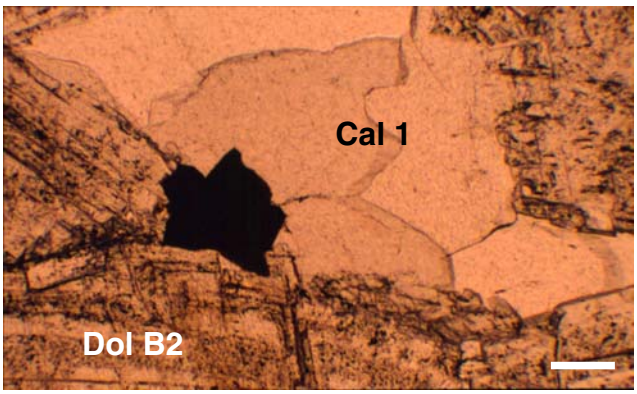

5

Plate 11

Ph. 1: **A.** Cal 2 partially fills a cavity in the dolomite. Scalebar is 0,4 mm. Plane light. **B.** The same picture under CL. Cal 2 is mostly non-luminescent and displays only some thin and bright orange luminescing zones. Non-luminescent Cal 2 is found also in a thin vein crosscutting the dolomite.

Ph. 2: **A.** Coarse and interlocked crystals of Cal 2 fill a cavity and are in contact with Dol B2. Scalebar is 0,4 mm. Plane light. **B.** The same picture under CL. Cal 2 has a zoned CL given by the alternation of thick non-luminescent and thin bright orange zones.

Ph. 3: **A.** Rock slice with Dol A2, Dol B and Cal 1. **B.** The same rock slice after long duration staining. The terminations of the Dol B2 crystals display a deeper blue colour relative to the other dolomite phases. Cal 1 remains unstained. Scalebar is 1cm.

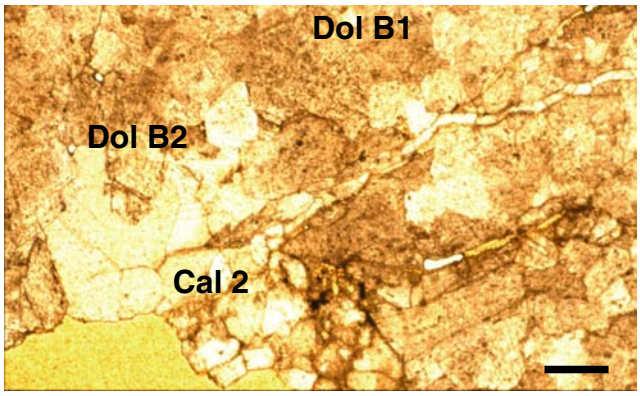

1A

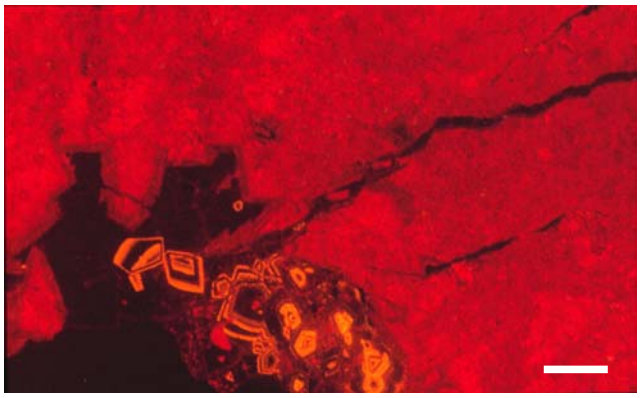

1B

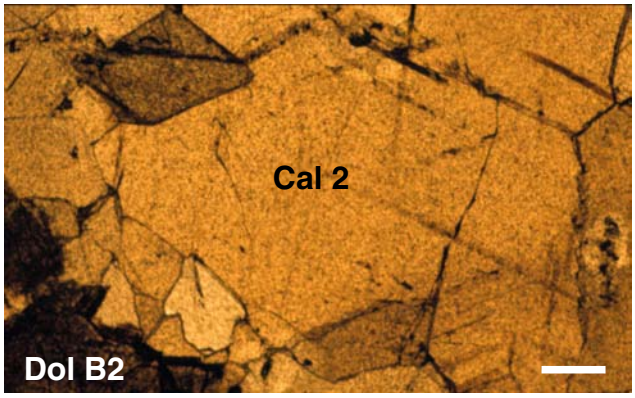

2A

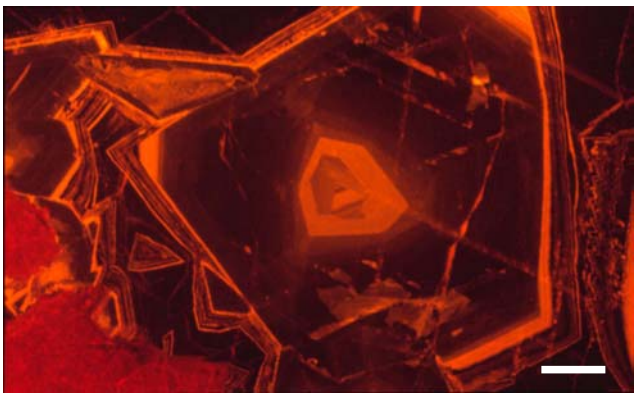

2B

3A

3B

Plate 12

Ph. 1: Irregular shaped, 2-phase, liquid-rich FIs in Dol A2 (type I).

Ph. 2: Negative crystal shaped, 2-phase, liquid-rich FIs in Dol A2 (type I) coexist together with 1-phase all liquid FIs (type II).

Ph. 3: Particular of a Dol B crystal having an inclusion-rich crystal core and a clear, almost inclusion-free outermost rim.

Ph. 4: Lobate, 2-phase, liquid-rich FI in Dol B (type III).

Ph. 5: Particular of a Cal 1 crystal showing the alternation of inclusion-rich and inclusion-free concentric zones of variable thickness.

Ph. 6: Lobate, 2-phase, liquid-rich FI in Cal 1 (type IV).

Ph. 7: Irregular shaped, empty FI in Cal 2 (type VI).

Ph. 8: Negative crystal shaped, empty FI in Cal 2 (type VI).

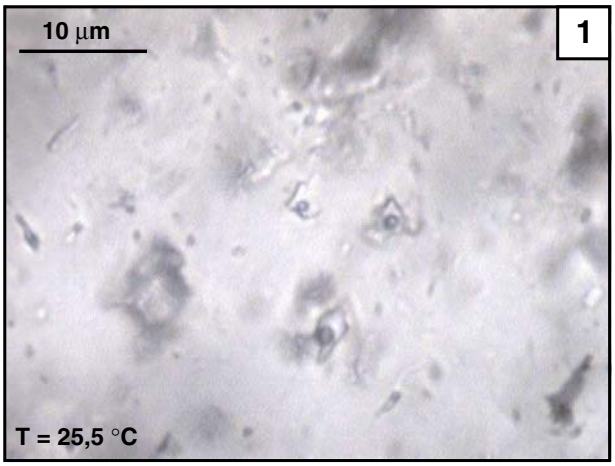
10 μm
1
T = 25,5 °C

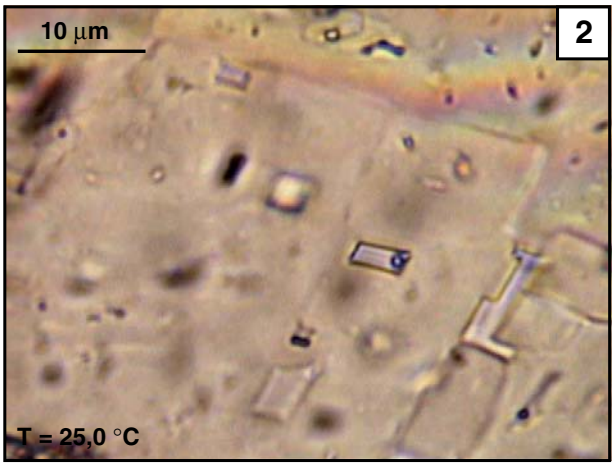
10 μm
2
T = 25,0 °C

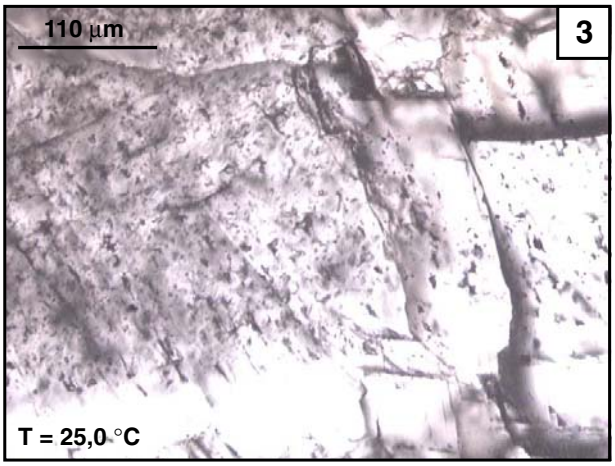
110 μm
3
T = 25,0 °C


10 μm
4
T = 25,0 °C

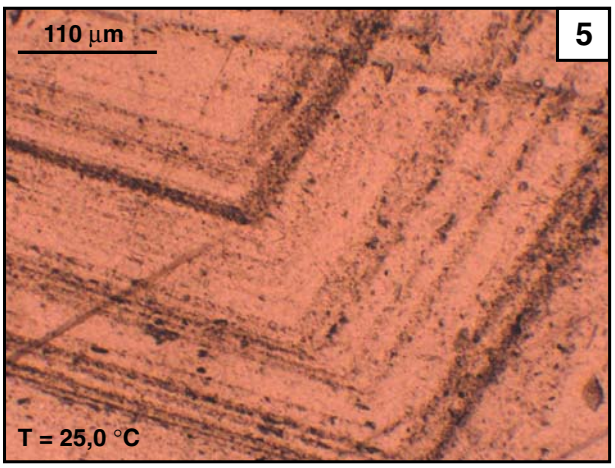
110 μm
5
T = 25,0 °C


10 μm
6
T = 25,0 °C

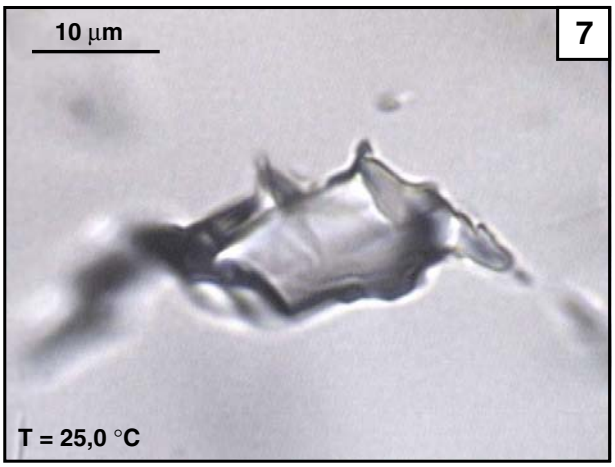
10 μm
7
T = 25,0 °C

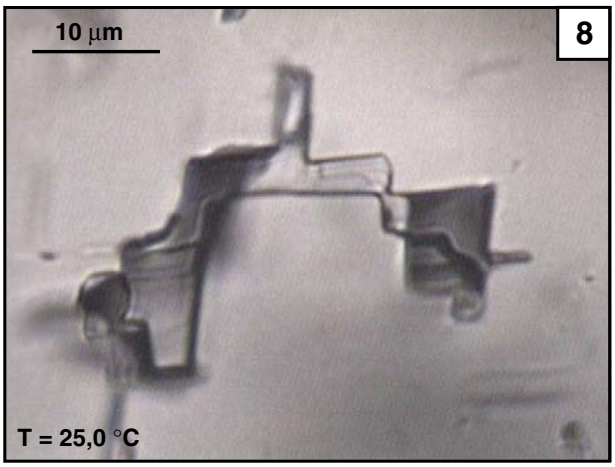
10 μm
8
T = 25,0 °C

Plate 13

Ph. 1: Sequence of photographs showing the major phase changes observed in FI 16 (type III) during a heating/freezing cycle. **A.** At room temperature aqueous liquid coexists with a vapour bubble. **B.** At 130,0 °C homogenisation has occurred in the liquid phase. **C.** At –150,0 °C after ice nucleation has occurred, the FI developed a dark mosaic texture. The vapour bubble is distorted. **D.** After several minutes at –60,0 °C the mosaic texture disappeared and the solid phases developed coarse crystallinity. The vapour bubble is hardly recognisable. **E.** At –45,0 °C after first melting has occurred, ice and salt hydrate crystals coexist together with aqueous liquid and a vapour bubble. **F.** At –43,0 °C the last salt hydrate crystal has molten. Ice crystals coexist together with aqueous liquid and a vapour bubble.

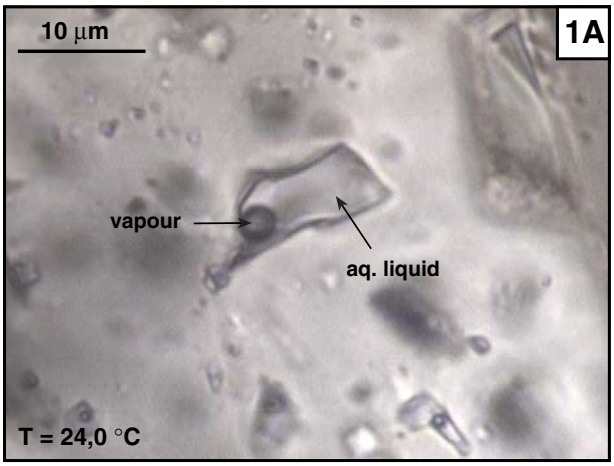
10 μm
1A
vapour
aq. liquid
T = 24,0 °C

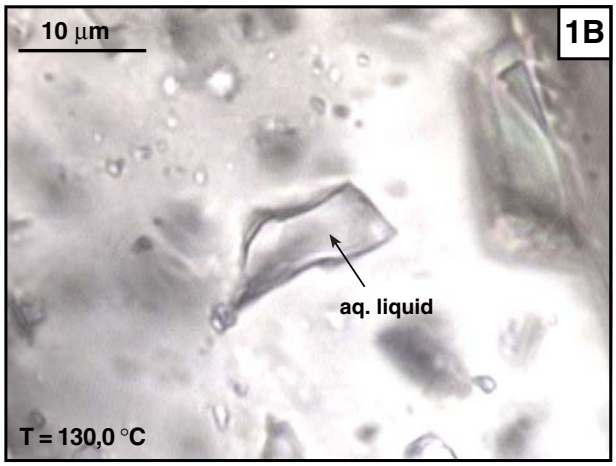
10 μm
1B
aq. liquid
T = 130,0 °C

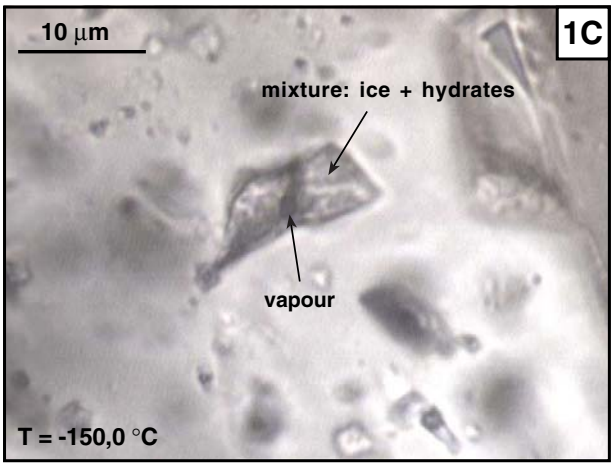
10 μm
1C
mixture: ice + hydrates
vapour
T = -150,0 °C

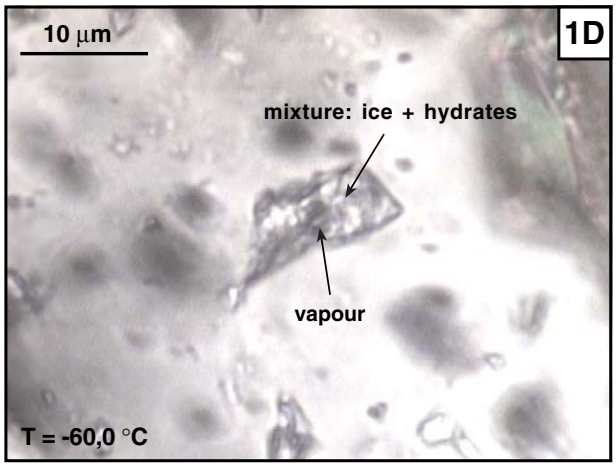
10 μm
1D
mixture: ice + hydrates
vapour
T = -60,0 °C

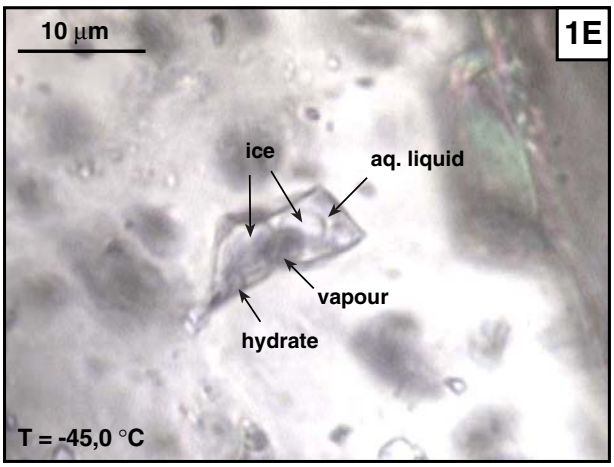
10 μm
1E
ice
aq. liquid
vapour
hydrate
T = -45,0 °C

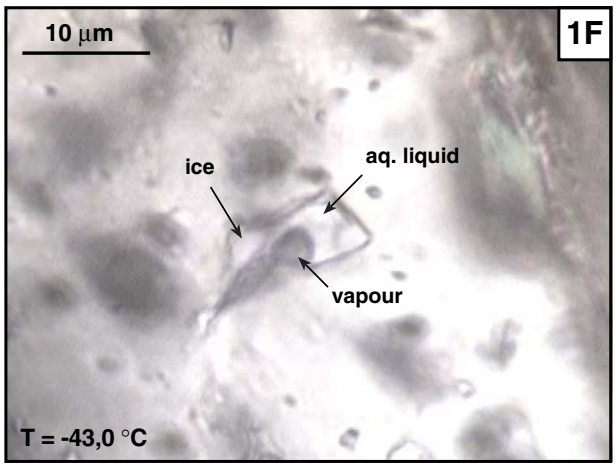
10 μm
1F
ice
aq. liquid
vapour
T = -43,0 °C

Plate 14

Ph. 1: Sequence of photographs showing the major phase changes observed in a type IV FI during a heating/freezing cycle. **A.** At room temperature aqueous liquid and a vapour bubble coexist. **B.** At 110,5 °C the FI homogenised in the liquid phase. **C.** At –36,0 °C, after occurrence of the first melting, the FI consists of a mixture of aqueous liquid, ice and hydrohalite coexisting with a distorted vapour bubble. **D.** At –30,0 °C aqueous liquid, ice and hydrohalite crystals are fairly distinguishable. The vapour bubble expanded. **E.** At –25,5 °C aqueous liquid and vapour bubble still coexist with ice and hydrohalite crystals. **F.** At –24,5 °C the last ice crystal melted and a large hydrohalite crystal coexists with aqueous liquid and a vapour bubble.

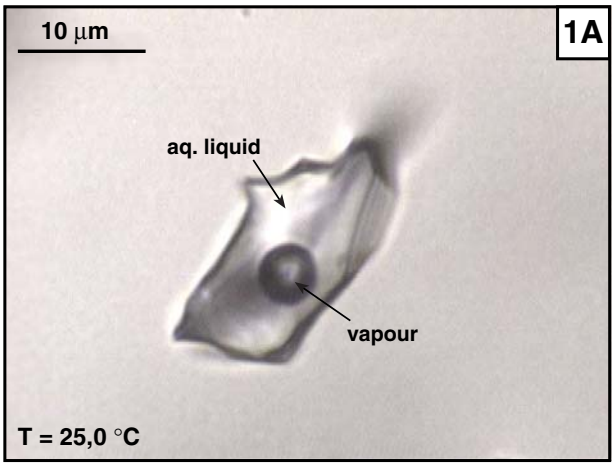
10 μm
1A
aq. liquid
vapour
T = 25,0 °C

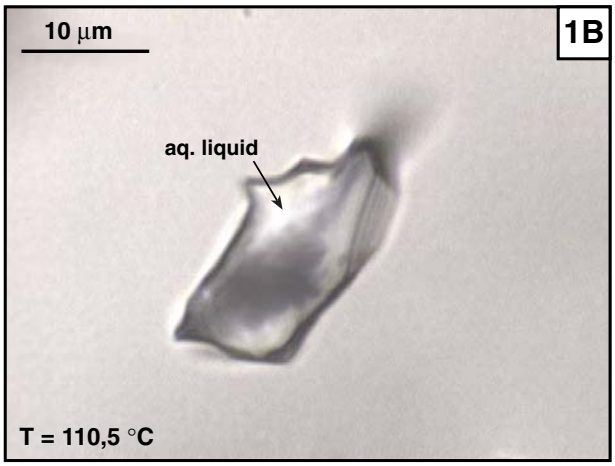
10 μm
1B
aq. liquid
T = 110,5 °C

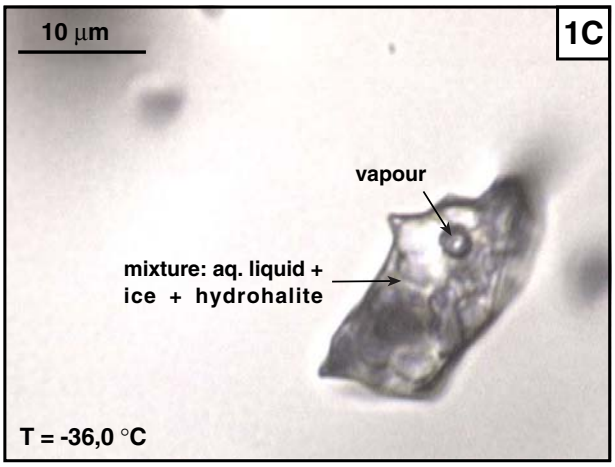
10 μm
1C
vapour
mixture: aq. liquid +
ice + hydrohalite
T = -36,0 °C

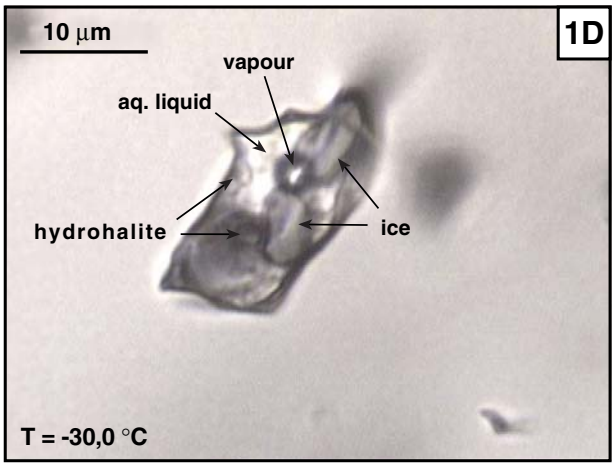
10 μm
1D
vapour
aq. liquid
hydrohalite
ice
T = -30,0 °C

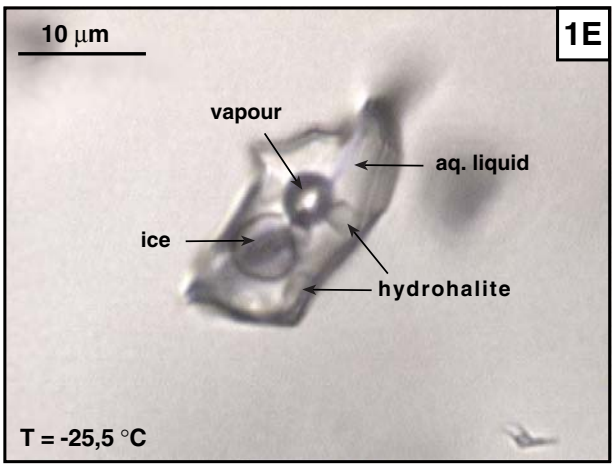
10 μm
1E
vapour
aq. liquid
ice
hydrohalite
T = -25,5 °C

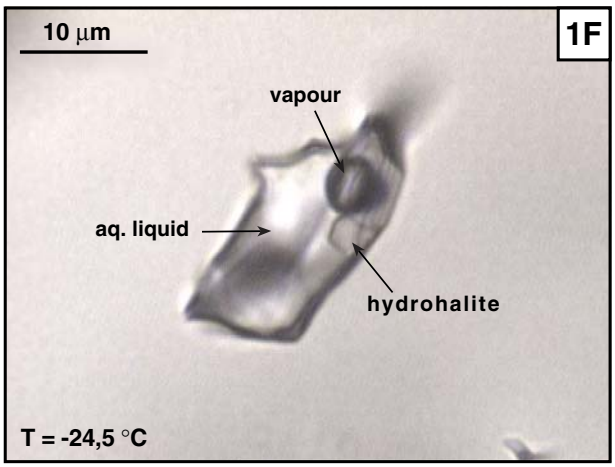
10 μm
1F
vapour
aq. liquid
hydrohalite
T = -24,5 °C

Hiermit erkläre ich, dss ich die vorgelegte Dissertation selbst verfsst und mich dabei keiner anderen als den von mir ausdrücklich bezeichneten Quellen und Hilfsmittel bedient habe.
Weiterhin erkläre ich, dass ich an keiner anderen Stelle ein Prüfungsverfahren beantragt bzw. die Dissertation in dieser oder anderer Form bereits anderweitig als Prüfungsarbeit verwendet oder einer anderen Fakultät als Dissertation vorgelegt habe.

Heidelberg, den 17.04.2003